Polymer 150 (2018) 130–137

Contents lists available at ScienceDirect

Polymer

journal homepage: www.elsevier.com/locate/polymer

Synergistic conductivity increase in polypyrrole/molybdenum disulfide composite

Udit Acharya [a, b], Patrycja Bober [a], Miroslava Trchová [a], Alexander Zhigunov [a], Jaroslav Stejskal [a], Jiří Pfleger [a, *]

[a] Institute of Macromolecular Chemistry, Academy of Sciences of the Czech Republic, 162 06 Prague 6, Czech Republic
[b] Faculty of Mathematics and Physics, Charles University, 121 16 Prague 2, Czech Republic

ARTICLE INFO

Article history:
Received 15 February 2018
Received in revised form
8 June 2018
Accepted 1 July 2018
Available online 3 July 2018

Keywords:
Polypyrrole
Molybdenum disulfide
Polymer composites
Electrical conductivity
Variable-range hopping

ABSTRACT

Polypyrrole/molybdenum disulfide (PPy/MoS_2) composites were synthesized by *in-situ* chemical polymerization of pyrrole in the presence of MoS_2 flakes. The conductivity of the composite with a moderate content of PPy (15–30 wt%) reached 13 S cm^{-1}, which is markedly higher than the conductivity of both the pristine PPy and MoS_2, 1 and 10^{-6} S cm^{-1}, respectively. The improved conductivity was explained by the formation of ordered thin PPy films with high conductivity at the MoS_2 surface. At higher pyrrole content, globular PPy was formed in the bulk of the composite resulting in an increase of a disordered polymer fraction, and the conductivity decreased. The composite conductivity is thus controlled not only by content of PPy but also by the proportions between ordered and disordered PPy phases. The structural and morphological characterization of composite materials is based on Fourier-transform infrared and Raman spectroscopies, wide-angle X-ray diffraction, and scanning and transmission electron microscopies. The charge-carrier transport in the composites fits the Mott variable-range hopping mechanism.

1. Introduction

The last decade has seen an increased interest in the area of conducting polymers due to the increasing demand for related applications in printed organic electronics. Among the known conducting polymers, particularly polypyrrole (PPy) or polyaniline have attracted an attention due to their high and controllable conductivity, excellent environmental stability [1], simple preparation and a lucrative production cost [2–4]. Their properties can be further improved when preparing composite materials with various fillers, for example, noble metals increase catalytic activity [5–7], silver particles bring antibacterial properties [8], graphene, carbon nanotubes and graphite increase electrical conductivity [9], cellulose or other polymer additives improve mechanical properties [10]. The development of hybrid inorganic–organic conducting polymer composites with transition metal oxides and dichalcogenides (molybdenum disulfide, molybdenum diselenide, tungsten disulfide, *etc.*) gained enormous significance due to their possible application abilities [11–15]. Such composites were prepared by an *in-situ* [13,16–18] or *ex-situ* [19,20] preparation of conducting polymers as well as simultaneous one-pot synthesis of both components [21].

Molybdenum disulfide (MoS_2) has a layered structure composed of S-Mo-S sheets, in which a plane of molybdenum atoms is sandwiched between two sulfur-planes and each atom of molybdenum is connected by strong S–Mo covalent bonds with six S atoms in the adjacent S-containing layers either in a trigonal prismatic (for 2H-MoS_2) or octahedral (for 1T-MoS_2) arrangement. These layers are mutually bound by much weaker van der Waals forces. MoS_2 has been applied in supercapacitors, photonics, photovoltaics *etc.* [22,23] Also a memristor-like behaviour of MoS_2 was reported showing the voltage-dependent resistance change [24,25]. In most of the applications, however, the low conductivity and specific capacitance of MoS_2 limit its performance.

The preparation of PPy/MoS_2 composites, mostly by electrochemical method or two-step procedure (exfoliation of MoS_2 followed by polymerization of pyrrole), has recently been described in the literature and their properties were tested in supercapacitors [12,18], as electrode material in lithium-ion batteries [12], electrochemical sensors [12,26] and as a catalyst for the electrochemical hydrogen evolution [21]. However, there is no detailed study on the conductivity of PPy/MoS_2 composites available in the literature.

* Corresponding author.
E-mail address: pfleger@imc.cas.cz (J. Pfleger).

https://doi.org/10.1016/j.polymer.2018.07.004
0032-3861/

Wang et al. [16] reported that such conducting polymer composites have higher conductivity with respect to pristine MoS_2 as expected but the comparison with neat PPy was missing. The purpose of the present paper is to develop a single-step method for the PPy/MoS_2 composite preparation and to study its fundamental charge-transport properties. We found that the conductivity of the composite was higher compared to that of both pristine components and the reason for such behaviour has been sought.

2. Experimental

2.1. Synthesis of polypyrrole/molybdenum disulfide composites

Molybdenum disulfide (MoS_2; Sigma-Aldrich, powder with particle size <2 μm) was coated with PPy by the surface polymerization of pyrrole (0.2 M; Sigma-Aldrich) with iron(III) chloride hexahydrate (0.5 M; Penta, Czech Republic) in aqueous medium at room temperature. The oxidant-to-pyrrole mole ratio was thus 2.5. First, pyrrole was added to the aqueous suspension of MoS_2 and left for 1 h to intercalate under stirring. The solution of iron(III) chloride hexahydrate was added in the next step. Polymerization of pyrrole was completed within tens of minutes. After 24 h, the polypyrrole powder was collected on a filter, rinsed with 0.2 M hydrochloric acid and acetone, and dried at room temperature over silica gel. The content of PPy in composites was varied from 10 to 50 wt%, and calculated from the yield of resulting composites and also confirmed by thermogravimetric analysis. For the preparation of each composite, fixed amount of MoS_2 (4 g) was used and various volumes of prepared aqueous reaction mixture (from 25 to 225 mL) were added in the next step. The fact that 100 mL of reaction mixture generates ≈ 1.1 g of PPy was used in the design of experiments.

2.2. Characterization

The morphology of the composites was investigated with the scanning electron microscopy (SEM) using a JEOL 6400 microscope (JEOL) and with a transmission electron microscope (TEM) JEM 2000 FX. Fourier-transform infrared (FTIR) spectra of the powders dispersed in potassium bromide pellets have been acquired with a Thermo Nicolet NEXUS 870 FTIR Spectrometer. Raman spectra were recorded with a Renishaw InVia Reflex Raman microspectrometer. The spectra were excited with NIR diode laser emitting at 785 nm. Diffraction patterns were obtained using a high resolution diffractometer Explorer (GNR Analytical Instruments, Italy). The instrument was equipped with one-dimensional silicon strip detector Mythen 1K (Dectris, Switzerland). Samples were measured in reflection mode. The radiation (CuKα line, wavelength 1.54 Å) monochromatized with Ni foil (β filter) was used for diffraction measurements performed in 2θ range from 2° to 40° with 0.1° steps. Exposure time at each step was 10 s. The specific surface area of the samples was determined using Gemini VII 2390 (Micromiretics, Instruments Corp, Norcross, USA) with nitrogen as the sorbate. The samples were vacuum-dried at 130 °C for ~80 h.

DC electrical conductivity was determined by a van der Pauw method on compressed pellets (diameter 13 mm, thickness 1.0 ± 0.2 mm) prepared under pressure 530 MPa using a hydraulic press Trystom H-62 (Trystom, Czech Republic). A Keithley 230 Programmable Voltage Source in serial connection with a Keithley 196 System DMM served as a current source, the potential difference between the potential probes was measured with a Keithley 181 Nanovoltmeter (Keithley, USA). Measurements have been carried out at constant ambient conditions at 24 ± 1 °C and relative humidity 35 ± 5%. The electrical conductivity σ was calculated from the applied current I and the measured potential difference U in the linear part of the current-voltage characteristics as

$$\sigma = \frac{\ln 2 \times I}{\pi U D k} \quad (1)$$

where D is sample thickness and k is the correction factor. For temperature dependence of DC conductivity, the above process was repeated at different temperatures. The temperature was controlled by Novocontrol Alpha Analyzer BDS in nitrogen atmosphere.

For frequency and temperature dependences of the real part of the conductivity, 35 nm gold electrodes were deposited on both sides of the pellets by vacuum evaporation. The conductivity was determined with a Novocontrol Alpha Analyzer BDS under applied AC voltage 1 V_{rms} in the temperature range 115–435 K with varying frequency from 10^7 to 10^{-2} Hz. The pellets were placed in the sample holder between the gold-plated brass disk electrodes 13 mm in diameter.

3. Results and discussion

Series of PPy/MoS_2 composites were prepared by the *in-situ* polymerization of pyrrole in the presence of MoS_2 flakes (Fig. 1). The pyrrole oligomers produced in the oxidation of pyrrole are insoluble in aqueous reaction medium, and adsorb at MoS_2 surface. They subsequently start the growth of PPy chains that produce the conducting polymer coating (Fig. 1b). Some PPy is also generated outside MoS_2 particles but, in analogy with polyaniline [27], the coating takes place with preference.

3.1. Morphology

SEM was employed for obtaining insights into the surface morphology of PPy/MoS_2 composites (Fig. 2). Molybdenum disulfide is represented by micrometre-sized flakes (Figs. 1a and 2a). Polymerization of pyrrole with iron(III) chloride as an oxidant yields PPy with globular morphology (Fig. 2b). PPy/MoS_2 composites are composed of the filler particles covered with PPy (Fig. 2c), accompanied with free PPy at high polymer content (Fig. 2d). This is not surprising since, similarly to closely related polymer polyaniline [3,28], PPy films grow on any surface immersed in reaction mixture.

The coating of MoS_2 surface with PPy is clearly demonstrated by TEM (Fig. 3). The micrograph of PPy/MoS_2 composites with 15 wt% of PPy shows relatively smooth PPy film on the surface of MoS_2 particles with a thickness ~30 nm (Fig. 3a). When the amount of pyrrole in the reaction mixture is increased the PPy coating becomes thicker (100–140 nm) and the secondary growth of PPy particles appeared (Fig. 3b).

3.2. Wide-angle X-ray diffraction

In Fig. 4 we present a selected part of X-ray diffractogram with intensity normalized by the amount of MoS_2 content. Observed diffraction pattern coincides with entry 9009144 from Crystallography Open Database. The peak at $2\Theta = 14.41°$ corresponds to (002) direction in MoS_2 structure. The (002) peak is attributed to the interplanar spacing between the nanosheets, which, according to Bragg's law, is equal to 6.14 Å. Peak position remains the same for all measured fractions of PPy. This means that polymerization of pyrrole does not lead to permanent intercalation of MoS_2 sheets. Nevertheless we have observed decrease in (002) peak intensity. This is the sign of the presence of exfoliated layers (Fig. 1). The change was approximately the same regardless of pyrrole content.

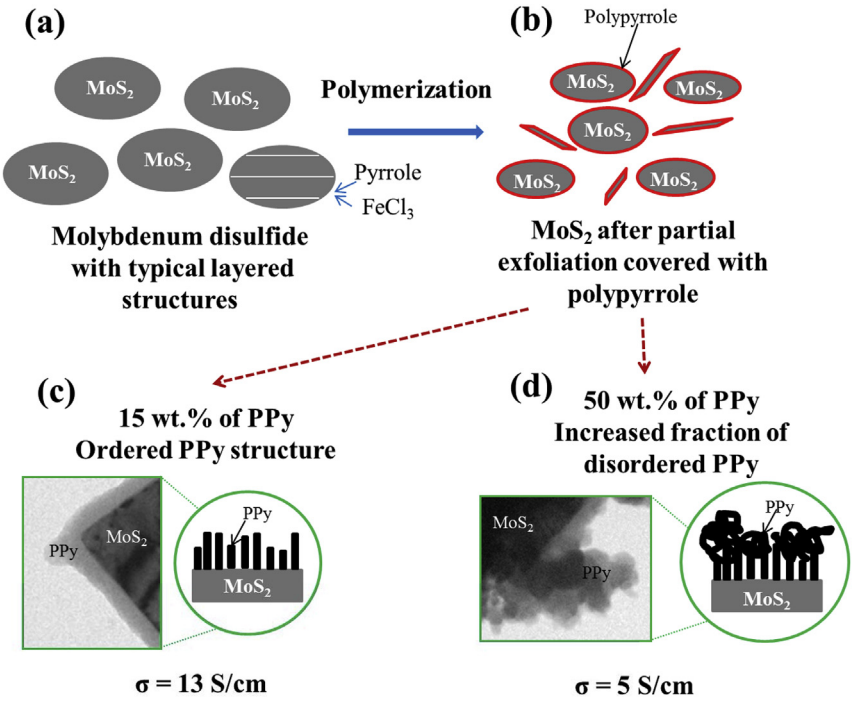

Fig. 1. Schematic diagram of (a, b) preparation and obtained PPy/MoS_2 composite with (c) ordered and (d) disordered PPy structure.

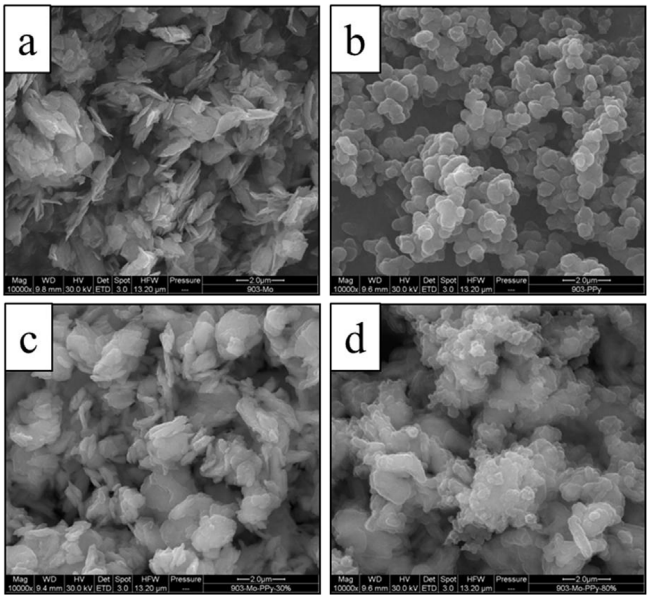

Fig. 2. Scanning electron micrographs of (a) neat MoS_2 powder, (b) globular PPy, and PPy/MoS_2 composites with (c) 15 wt% of PPy and (d) 45 wt% of PPy, respectively.

3.3. FTIR spectra

According to the shape of the infrared spectra, the PPy/MoS_2 composites may be divided into three groups (Fig. 5). In all groups we detected the bands of protonated PPy, which were previously described [29–32]. They are situated at 1537 cm^{-1} (C–C stretching vibrations in the pyrrole ring), 1450 cm^{-1} (C–N stretching vibration in the pyrrole rings), 1298 cm^{-1} (C–H or C–N in-plane deformation modes), 1160 cm^{-1} (breathing vibrations of the pyrrole rings), 1088 cm^{-1} ($N–H^+$ deformation vibrations), 1040 cm^{-1} (C–H and

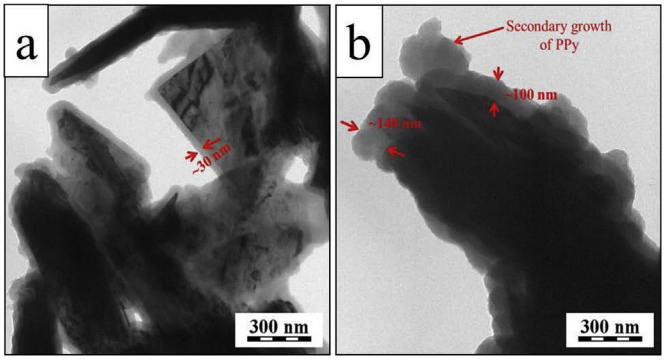

Fig. 3. Transmission electron micrographs of PPy/MoS_2 composites with (a) 15 wt% of PPy and (b) 45 wt% of PPy. The PPy coating is indicated with arrows.

N–H in-plane deformation vibrations), and 895 cm^{-1} (C–H out-of-plane deformation vibrations of the ring.

The spectra of composites corresponding to 10 and 15 wt% of PPy concentration exhibit the highest absorption bands close to the absorption of neat PPy and with the highest broad absorption band above 1800 cm^{-1}, which is in agreement with the higher conductivity of these samples. This may be connected with more ordered brush-like structure of the polymer chains in the thin layer of PPy deposited on the surface of MoS_2 nanoparticles. The spectra of the samples with the PPy contents from 20 to 38 wt% exhibit the lower absorption band observed above 1800 cm^{-1}. In the spectra of this group of composites, we detect a small sharp peak of neat molybdenum disulfide marked with asterisks in Fig. 5. Finally, the samples with the PPy content above 40 wt% exhibit very small absorption caused by a compact stone-like structure which was difficult to disperse in potassium bromide pellets. This may be connected with the presence of strong hydrogen bonding in secondary growth of PPy globules. The spectrum of neat disulfide is featureless with only a small sharp band at about 470 cm^{-1}.

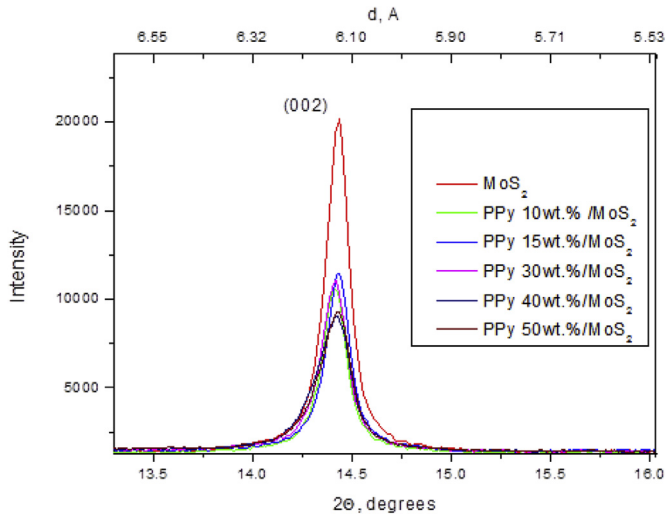

Fig. 4. XRD of selected region of MoS_2 (red line) and samples containing different fractions of PPy. (For interpretation of the references to colour in this figure legend, the reader is referred to the Web version of this article.)

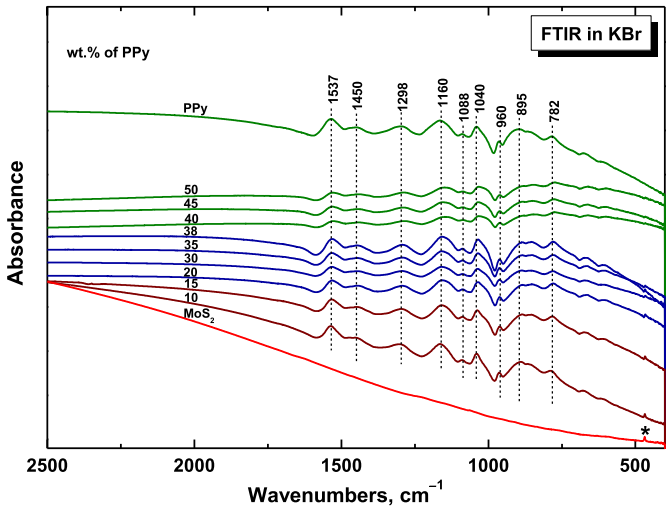

Fig. 5. Infrared spectra of PPy/MoS_2 composites with various PPy contents.

3.4. Raman spectra

Raman spectroscopy is a method convenient for the surface analysis. Energy of the absorption in a polaron electronic state of PPy corresponds to the energy of the laser excitation of 785 nm. In this case the penetration depth is reduced to a few tens of nanometers [33]. The spectra of all samples correspond to the spectrum of globular protonated PPy [29,34–36]. They contain the bands at 1595 cm^{-1} (C=C in-ring of C–C inter-ring vibrations and of the stretching vibrations in cation of the PPy backbone), at 1490 cm^{-1} (C–C and C=N stretching skeletal vibrations), the double peak at 1380 and 1333 cm^{-1} (ring-stretching vibrations of pyrrole at 1245 cm^{-1} (C–H antisymmetric in-plane bending vibrations), the double peak at 1087 and 1052 cm^{-1} (C–H in-plane deformation vibrations), and at 934 cm^{-1} (C–C ring deformation vibrations within dication unit).

At the same conditions of experiment the intensity of scattered light is decreasing with increasing the concentration of PPy from 10 to 50 wt% of PPy. We can speculate that this is connected with the formation of ordered PPy structure on MoS_2 particles for low PPy concentration. The spectrum of neat sulfide contains the sharp peaks at lower wavenumbers which are detected in the spectra till 30 wt% (marked with asterisks in Fig. 6). This signifies that the thickness of the uniform PPy film is either low or the surface of MoS_2 particles is patchy. The former hypothesis is preferred due to the hydrophobicity of MoS_2 [3]. At higher PPy contents the coating with PPy is sufficiently thick and complete.

3.5. DC conductivity

The DC conductivity of the composites was always considerably higher than that of neat semiconducting MoS_2 powder or PPy alone (Fig. 7) thus illustrating the pronounced synergistic effect. Table 1 summarizes the electrical conductivities of various composites based on PPy or MoS_2 from previous studies. A similar but much less pronounced increase of the DC conductivity was reported already for the composite of polyaniline and MoS_2, in which the polymer was intercalated in MoS_2 structure [37]. The effect was explained by an impact of the interlayer growth of the polymer on its conformation and stereo-regular characteristics. Zhong et al. [38] has reported a similar conductivity enhancement in the composites of PPy with graphene oxide, and discussed the results in terms of polaron/bipolaron equilibria in PPy affected by graphene oxide.

From the XRD spectra (Fig. 4) we see that no intercalation takes place during the polymerization. However, there is clear evidence about the different morphology of the polymer grown in bulk and as a thin film on the MoS_2 surface. At low polymer contents, PPy forms a compact shell composed of PPy chains grown from the oligomeric nucleates adsorbed at MoS_2 surface. The surface thus acts as a template on which well-ordered polymer structure is formed, similarly as reported previously on polyaniline [46]. At higher polymer concentration, when no free MoS_2 template surface is available, a secondary nucleation can occur on the already grown polymer yielding disordered less conducting PPy. This explanation corresponds well with previously reported decrease in electrical conductivity with increasing thickness of conducting polymer films [47] or with increasing thickness of conducting polymer nanotubes prepared with membrane templates [48] or organic dyes [49]. The decrease in the DC conductivity of the composite with PPy content increasing above certain limiting value can be thus attributed to the generation of PPy with random orientation of polymer chains. Such

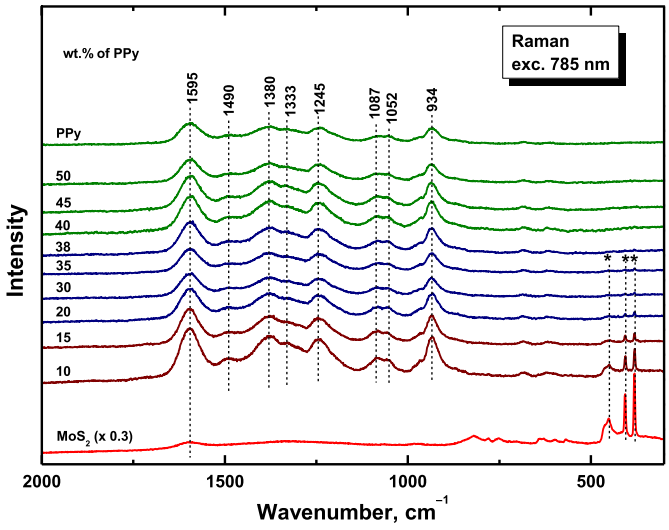

Fig. 6. Raman spectra of PPy/MoS_2 composites with various PPy contents.

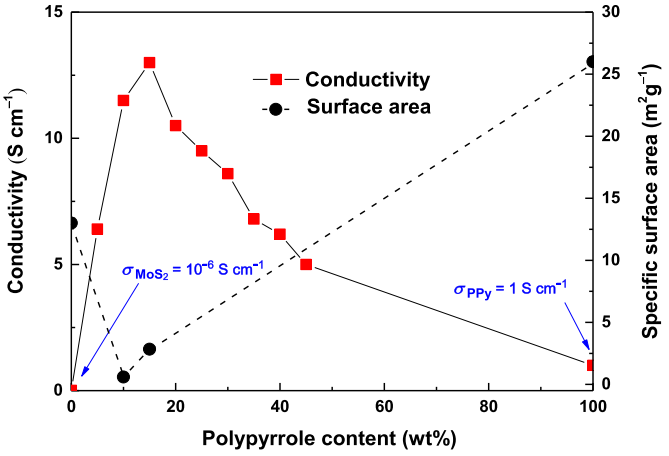

Fig. 7. Dependence of conductivity of PPy/MoS_2 composites and the specific surface area on PPy content.

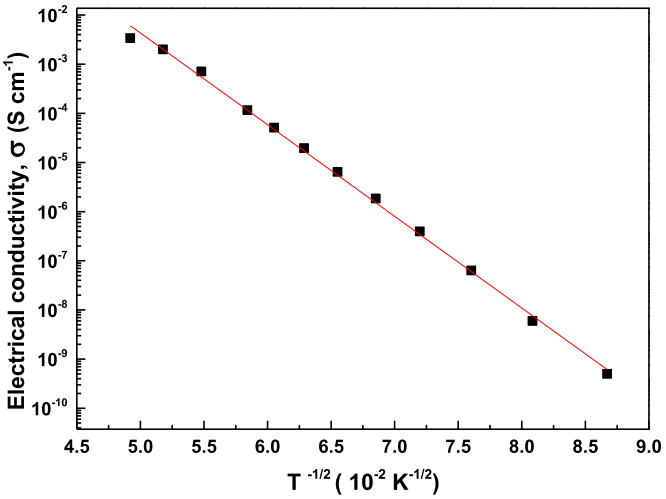

Fig. 9. Dependence of the electrical conductivity σ, on $T^{-1/2}$ for pristine MoS_2.

Table 1
Comparision of electrical conductivity of PPy/MoS_2 composites with other MoS_2-based, PPy-based and related composites.

Samples	Conductivity (S cm^{-1}) [reference]
Globular PPy	1 [this report]; 0.3 [31]
MoS_2	10^{-6} [this report]; 5×10^{-7} [39]
PPy/Ag/boron nitride	0.42 [40]
PPy/montmorillonite	4 [41]
PPy/Ag/montmorillonite	1.08 [42]
PPy/SiO_2	6.8×10^{-4} [43]
PPy/WS_2	3.25×10^{-2} [17]
PANI/MoS_2	1.01×10^{-2} [13]; 0.3 [44]
Chitosan/MoS_2	5×10^{-5} [39]
Polythiophene/MoS_2	5.3×10^{-2} [45]
PPy/MoS_2	13 [this report]; 0.1 [16]

globular structure is less conducting due to poor electrical connection between the disordered globular boundaries.

In order to justify the above concept, the following simple calculation can be made. Let us consider PPy/MoS_2 composite with a weight fraction of PPy being w_P. The specific surface area of MoS_2 powder determined by BET technique was $S_{MoS2} = 13.7$ m^{2}g^{-1} (Fig. 7). This gives the total surface of MoS_2 particles $S = S_{MoS2}(1-w_P)$ per 1 g of the composite. If we assume a homogeneous coating of this surface by PPy, it represents a PPy volume $V_P = w_P/d_P$, where $d = 1.47$ g cm^{-3} is the density of PPy [50]. Then the thickness of the PPy layer is D_P [nm] $= V_P/S = 52\ w_P/(1-w_P)$. When the conductivity is plotted against such calculated thickness of the layer (Fig. 8) instead of the weight fraction of PPy, the maximum conductivity is expected at the thickness $D_P \approx 10$ nm. This is the thickness which can be associated with the highly conducting ordered PPy film (Fig. 3a). When the thickness becomes higher (Fig. 3b), this is due to the disordered secondary growth of PPy on the top of the ordered phase [28]. The disordered PPy is less conducting and the further growth of polymer coating results in the decrease of the composite conductivity (Fig. 8).

The specific surface area for the most conducting sample was 2.84 m^{2}g^{-1} (Fig. 7). This is below the value of specific surface areas for pristine PPy and MoS_2, 26 and 13 m^{2}g^{-1}, respectively (Fig. 7). This signifies that the composites are non-porous and more compact which is in good agreement with the higher value of conductivity making charge transfer easier. Similar effect was also previously observed by Muller et al. [43].

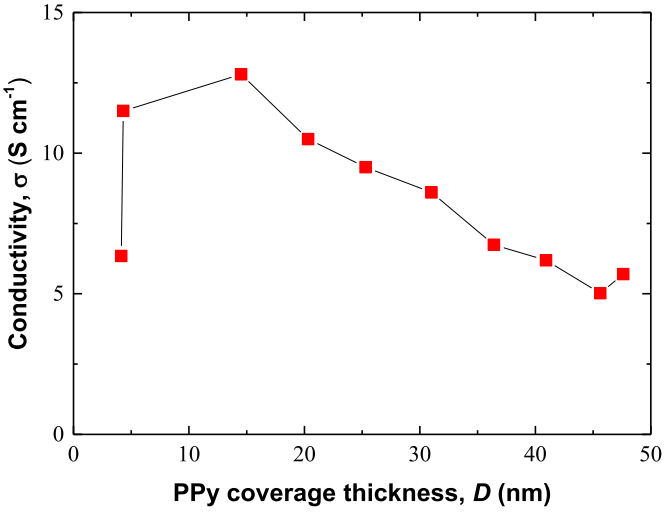

Fig. 8. The dependence of experimental DC conductivity on the thickness of polypyrrole grown on MoS_2 particles, calculated from the polypyrrole content by assuming the uniform coating.

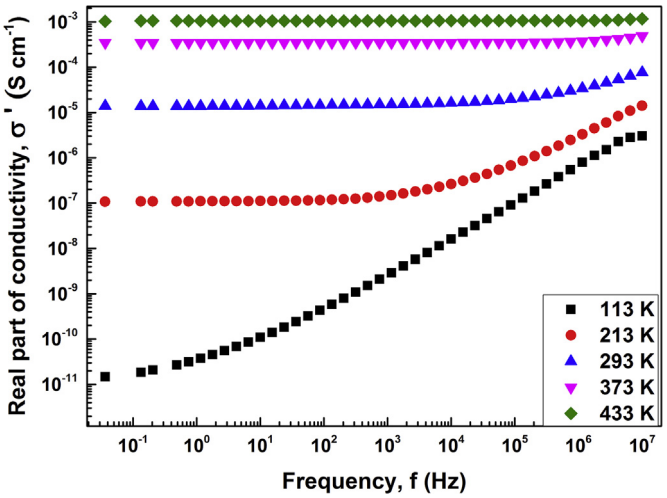

Fig. 10. Frequency spectrum of the real part of conductivity of MoS_2 pellets at various temperatures.

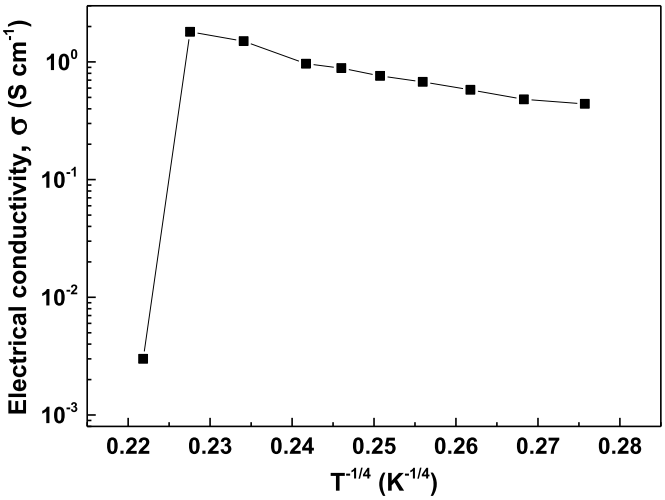

Fig. 11. Temperature dependence of the DC conductivity σ of PPy as a function of $T^{-1/4}$.

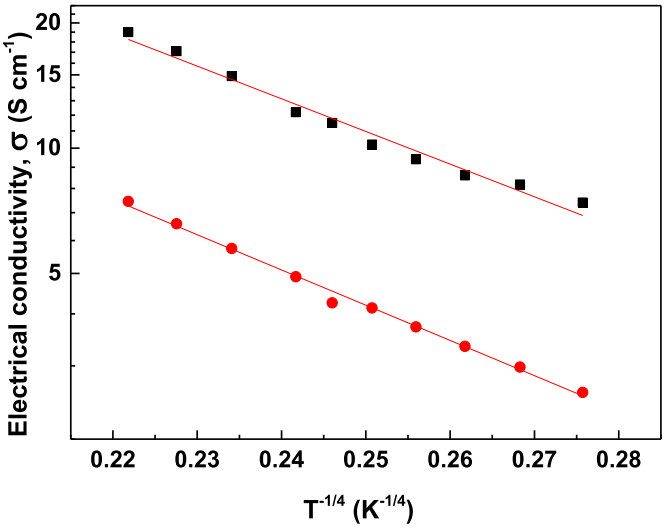

Fig. 12. Temperature dependence of the DC conductivity σ of PPy/MoS_2 composites as a function of $T^{-1/4}$ PPy content 15 wt% (black squares) and 45 wt% (red circles). (For interpretation of the references to colour in this figure legend, the reader is referred to the Web version of this article.)

3.6. Charge transport in MoS_2

In order to investigate the charge transport mechanism in the composites and pristine components in more detail, temperature dependence of DC conductivity was determined in the range from 130 to 415 K. As can be seen from Fig. 9, this dependence can be well fitted (the lowest value of the linear regression coefficient from least-squares fitting, R^2) by a straight line in log σ *vs.* $T^{-1/2}$ plot.

The electrical conductivity of disordered inorganic semiconductors is usually assessed within a Mott theory, which describes the temperature dependence of conductivity in the case of disordered semiconducting materials, according to which conductivity is given by:

$$\sigma(T) = \sigma_0 \exp\left[-\frac{T_0}{T}\right]^{\gamma} \quad (2)$$

where σ_0 is high temperature limit of conductivity, T_0 is the Mott characteristic temperature and $\gamma = 1/(n+1)$, n being the dimension in which the charge transport takes place. From Fig. 9 we get the value $n = 1$, which suggests the transport proceeds via one-dimensional hopping mechanism. When the experimental data were approximated by the Boltzmann dependence, an activation energy $E_a = 0.27$ eV was obtained, which is in a good agreement with literature, where experimental value $E_a = 0.32$ eV and theoretically calculated activation energy $E_a = 0.23–0.31$ eV, were found, respectively [51].

AC conductivity in pristine MoS_2 (Fig. 10) in high frequency range is only weakly dependent on temperature, which suggests that the bulk of the sample is not homogeneous. At low frequency range, $f < 10^3$ Hz, conductivity approaches a constant value, which might indicate that the material is composed of small relatively compact grains. The grains play a greater role in the low-frequency limit since the grain boundary limits the long-range transport of charges.

3.7. Electrical properties of composites

Due to the large difference in the electrical conductivity of both components of the composite, the charge transport proceeds *via* PPy. As previously described in the literature [52–54] charge transport in conducting polymers, such as PPy, is controlled by different mechanisms in different temperature ranges. Above room temperature, the prevailing transport is of intra-chain nature and below the room temperature it is *via* isoenergetic hopping and fluctuation-assisted tunnelling mechanism. The observed dependence of the DC conductivity on temperature follows Mott three-dimensional variable-range hopping (ref to Eq. (2) with $n = 3$; Fig. 11). Above 410 K the conductivity of pristine PPy drastically decreased from ~2 to ~10^{-2} S cm^{-1} due to partial deprotonation of PPy salt [52,54], and consequent conversion to less conducting PPy base [29].

The data of DC conductivity acquired on the PPy/MoS_2 pellets follow the same tendency (Fig. 12). A log $\sigma \sim T^{-1/4}$ dependence found for the composites with various composition corresponds to a 3-D variable-range hopping charge-transport mechanism but lower value of activation energy was found (Table 2). Different values of the activation energy at different temperature ranges indicate different limiting charge-transport mechanisms taking place in the bulk of these composites. At low temperature the transport between grains limits the conductivity whereas with increasing temperature it is mainly inter-chain hopping and intra-chain transport. For all the composites the electrical properties were stable to much higher temperature compared with neat PPy, no decrease in the conductivity was observed up to 150 °C.

Table 2
Activation energy (eV) of PPy and PPy/MoS_2 composites at different temperature ranges.

Temperature range (K)	Neat PPy	PPy/MoS_2 composite 15 wt% of PPy	PPy/MoS_2 composite 45 wt% of PPy
300–400	0.074	0.038	0.037
200–300	0.034	0.024	0.023
130–200	0.027	0.015	0.015

4. Conclusions

Series of PPy/MoS_2 composites were successfully prepared and characterized by various methods. The DC conductivity was significantly improved (5–13 S cm^{-1}) for all the composites compared with the conductivity of neat PPy, 1 S cm^{-1}, and MoS_2, 10^{-6} S cm^{-1} and preserved even above 410 K, where neat PPy already loses its high conductivity. The composites with 15–30 wt% of PPy showed the highest conductivity due to growth of ordered thin PPy film on MoS_2 surface. The chain ordering is favourable for the transport of charge carriers. When the amount of PPy was higher, the secondary growth of PPy onto ordered film occurred, leading to more disordered globular PPy structure and resulting in a decrease of the overall conductivity of the composite. The level of conductivity thus depends on the proportions between the ordered and disordered PPy phases. The temperature dependences of the DC conductivity of the composites point to the variable-range hopping as the main charge transport mechanism. Higher electrical conductivity of the composite makes the material more suitable for many potential electronic applications like photovoltaics and memristors.

Conflicts of interest

There are no conflicts of interest to declare.

Acknowledgements

The financial support of the Czech Science Foundation (17-03984S) is gratefully acknowledged.

References

[1] L. Brožová, P. Holler, J. Kovářová, J. Stejskal, M. Trchová, The stability of polyaniline in strongly alkaline or acidic aqueous media, Polym. Degrad. Stabil. 93 (2008) 592–600.
[2] J.R. Aggas, W. Harrell, J. Lutkenhaus, A. Guiseppi-Elie, Metal-polymer interface influences apparent electrical properties of nano-structured polyaniline films, Nanoscale 10 (2018) 672–682.
[3] J. Stejskal, I. Sapurina, M. Trchová, Polyaniline nanostructures and the role of aniline oligomers in their formation, Prog. Polym. Sci. 35 (2010) 1420–1481.
[4] G. Ćirić-Marjanović, Recent advances in polyaniline research: polymerization mechanisms, structural aspects, properties and applications, Synth. Met. 177 (2013) 1–47.
[5] I. Sapurina, J. Stejskal, Ternary composites of multi-wall carbon nanotubes, polyaniline, and noble-metal nanoparticles for potential applications in electrocatalysis, Chem. Pap. 63 (2009) 579–585.
[6] J. Han, M. Wang, Y. Hu, C. Zhou, R. Guo, Conducting polymer-noble metal nanoparticle hybrids: synthesis mechanism application, Prog. Polym. Sci. 70 (2017) 52–91.
[7] M.G. Abd El-Moghny, H.H. Alalawy, A.M. Mohammad, A.A. Mazhar, M.S. El-Deab, B.E. El-Anadouli, Conducting polymers inducing catalysis: enhanced formic acid electro-oxidation at a Pt/polyaniline nanocatalyst, Int. J. Hydrogen Energy 42 (2017) 11166–11176.
[8] J. Stejskal, Conducting polymer-silver composites, Chem. Pap. 67 (2013) 814–848.
[9] Y. Sun, G. Shi, Graphene/polymer composites for energy applications, J. Polym. Sci. B Polym. Phys. 51 (2013) 231–253.
[10] P. Bober, J. Liu, K.S. Mikkonen, P. Ihalainen, M. Pesonen, C. Plumed-Ferrer, A. von Wright, T. Lindfors, C. Xu, R.-M. Latonen, Biocomposites of nanofibrillated cellulose, polypyrrole, and silver nanoparticles with electroconductive and antimicrobial properties, Biomacromolecules 15 (2014) 3655–3663.
[11] T. Alamro, M.K. Ram, Polyethylenedioxythiophene and molybdenum disulfide nanocomposite electrodes for supercapacitor applications, Electrochim. Acta 235 (2017) 623–631.
[12] A. Sajedi-Moghaddam, E. Saievar-Iranizad, M. Pumera, Two-dimensional transition metal dichalcogenide/conducting polymer composites: synthesis and applications, Nanoscale 9 (2017) 8052–8065.
[13] J. Stejskal, M. Mrlík, T. Plachý, M. Trchová, J. Kovářová, Y. Li, Molybdenum and tungsten disulfides surface-modified with a conducting polymer, polyaniline, for application in electrorheology, React. Funct. Polym. 120 (2017) 30–37.
[14] Y. Liu, B.H. Zhang, Y.Q. Yang, Z. Chang, Z.B. Wen, Y.P. Wu, Polypyrrole-coated alpha-MoO_3 nanobelts with good electrochemical performance as anode materials for aqueous supercapacitors, J. Mater. Chem. A 1 (2013) 13582–13587.
[15] F. Yu, Y. Liu, Y.J. Zhu, F. Dai, L. Zhang, Z.B. Wen, Polypyrrole@MoO_3/reductive graphite oxide nanocomposites as anode material for aqueous supercapacitors with high performance, Mater. Lett. 171 (2016) 104–107.
[16] L. Wang, J. Schindler, J.A. Thomas, C.R. Kannewurf, M.G. Kanatzidis, Entrapment of polypyrrole chains between MoS_2 layers via an in situ oxidative polymerization encapsulation reaction, Chem. Mater. 7 (1995) 1753–1755.
[17] B.-H. Xu, B.-Z. Lin, Z.-J. Chen, X.-L. Li, Q.-Q. Wang, Preparation and electrical conductivity of polypyrrole/WS_2 layered nanocomposites, J. Colloid Interface Sci. 330 (2009) 220–226.
[18] Y. Chen, W. Ma, K. Cai, X. Yang, C. Huang, In situ growth of polypyrrole onto three-dimensional tubular MoS_2 as an advanced negative electrode material for supercapacitor, Electrochim. Acta 246 (2017) 615–624.
[19] R. Bissessur, P.K.Y. Liu, Direct insertion of polypyrrole into molybdenum disulphide, Solid State Ionics 177 (2006) 191–196.
[20] C. Chan, X. Yang, S. Xiang, H. Que, M. Li, Layered MoS2/PPy nanotube composites with enhanced performance for supercapacitors, J. Mater. Sci. Mater. Electron. 28 (2017) 1777–1784.
[21] J. Lei, X. Lu, G. Nie, Z. Jiang, C. Wang, One-pot synthesis of algae-like MoS_2/PPy nanocomposite: a synergistic catalyst with superior peroxidase-like catalytic activity for H_2O_2 detection, Part. Part. Syst. Char. 32 (2015) 886–892.
[22] K. Krishnamoorthy, P. Pazhamalai, G.K. Veerasubramani, S.J. Kim, Mechanically delaminated few layered MoS_2 nanosheets based high performance wire type solid-state symmetric supercapacitors, J. Power Sources 321 (2016) 112–119.
[23] X. Li, X. Li, J. Cheng, D. Yuan, W. Ni, Q. Guan, L. Gao, B. Wang, Fiber-shaped solid-state supercapacitors based on molybdenum disulfide nanosheets for a self-powered photodetecting system, Nano Energy 21 (2016) 228–237.
[24] P. Cheng, K. Sun, Y.H. Hu, Memristive behavior and ideal memristor of 1T phase MoS_2 nanosheets, Nano Lett. 16 (2016) 572–576.
[25] V.K. Sangwan, D. Jariwala, I.S. Kim, K.-S. Chen, T.J. Marks, L.J. Lauhon, M.C. Hersam, Gate-tunable memristive phenomena mediated by grain boundaries in single-layer MoS_2, Nat. Nanotechnol. 10 (2015) 403–406.
[26] K. Vijayaraj, T. Dinakaran, Y. Lee, S. Kim, H.S. Kim, J. Lee, S.C. Chang, One-step construction of a molybdenum disulfide/multi-walled carbon nanotubes/polypyrrole nanocomposite biosensor for the ex-vivo detection of dopamine in mouse brain tissue, Biochem. Biophys. Res. Commun. 494 (2017) 181–187.
[27] S. Fedorova, J. Stejskal, Surface and precipitation polymerization of aniline, Langmuir 18 (2002) 5630–5632.
[28] I. Sapurina, A. Riede, J. Stejskal, In-situ polymerized polyaniline films 3. Film formation, Synth. Met. 123 (2001) 503–507.
[29] J. Stejskal, M. Trchová, Z. Morávková, P. Bober, D. Kopecký, J. Kopecká, E. Watzlová, M. Varga, J. Prokeš, Polypyrrole salts and bases: superior conductivity of nanotubes and their stability towards the loss of conductivity by deprotonation, RSC Adv. 6 (2016) 88382–88391.
[30] G. Ćirić-Marjanović, S. Mentus, I. Pašti, N. Gavrilov, J. Krstić, J. Travas-Sejdic, L. Strover, J. Kopecká, Z. Morávková, M. Trchová, J. Stejskal, Synthesis, characterization and electrochemistry of nanotubular polypyrrole and polypyrrole-derived carbon nanotubes, J. Phys. Chem. C 118 (2014) 14770–14784.
[31] N.V. Blinova, J. Stejskal, M. Trchová, J. Prokeš, M. Omastová, Polyaniline and polypyrrole: a comparative study of the preparation, Eur. Polym. J. 43 (2007) 2331–2341.
[32] M. Omastová, M. Trchová, J. Kovářová, J. Stejskal, Synthesis and structural study of polypyrrole prepared in the presence of surfactants, Synth. Met. 138 (2003) 447–455.
[33] Ph. Colomban, S. Folch, A. Gruger, Vibrational study of short-range order and structure of polyaniline bases and salts, Macromolecules 32 (1999) 3080–3092.
[34] S. Gupta, Hydrogen bubble-assisted syntheses of polypyrrole micro/nanostructures using electrochemistry: structural and physical property characterization, J. Raman Spectrosc. 39 (2008) 1343–1355.
[35] Y.C. Liu, Characteristics of vibration modes of polypyrrole on surface-enhanced Raman scattering spectra, J. Electroanal. Chem. 571 (2004) 255–264.
[36] K. Crowley, J. Cassidy, In situ resonance Raman spectroelectrochemistry of polypyrrole doped with dodecylbenzenesulfonate, J. Electroanal. Chem. 547 (2003) 75–82.
[37] J. Wang, Z.C. Wu, K.H. Hu, X.Y. Chen, H.B. Yin, High conductivity graphene-like MoS_2/polyaniline nanocomposites and its application in supercapacitor, J. Alloy. Comp. 69 (2015) 38–43.
[38] J. Zhong, S. Gao, G.B. Xue, B. Wang, Study of enhancement mechanism of condcutivity induced by graphene oxide for polypyrrole nanocomposites, Macromolecules 48 (2015) 1592–1597.
[39] I. Saada, R. Bissessur, Nanocomposite materials based on chitosan and molybdenum disulphide, J. Mater. Sci. 47 (2012) 5861–5866.
[40] A. Sultan Adil, F. Mohammad, Chemical sensing, thermal stability, electrochemistry and electrical conductivity of silver nanoparticles decorated and polypyrrole enwrapped boron nitride nanocomposite, Polymer 113 (2017) 221–232.
[41] Y.Q. Han, Synthesis and characterization of montmorillonite/polypyrrole nanocomposite, Polym. Compos. 30 (2009) 66–69.
[42] X.T. Tran, S.S. Park, M. Hussain, H.T. Kim, Electroconductive and catalytic performance of polypyrrole/montmorillonite/silver composites synthesized through in situ oxidative polymerization, J. Appl. Polym. Sci. 135 (2018)

45986.
[43] D. Muller, G.K. Pinheiro, T. Bendo, A.J. Gutierrez Aguayo, G.M.O. Barra, C.R. Rambo, Synthesis of conductive PPy/SiO_2 aerogels nanocomposites by *in situ* polymerization of pyrrole, J. Nanomater. (2015) 658476.
[44] R. Bissessur, W. White, D.C. Dahn, Electrical characterization of conductive polymers and their intercalated nanocomposites with molybdenum disulphide, Mater. Lett. 60 (2006) 248–251.
[45] B.Z. Lin, C. Ding, B.H. Xu, Z.J. Chen, Y.L. Chen, Preparation and characterization of polythiophene/molybdenum disulfide intercalation material, Mater. Res. Bull. 44 (2009) 719–723.
[46] I. Sapurina, A. Yu. Osadchev, B.Z. Volchek, M. Trchová, A. Riede, J. Stejskal, In-situ polymerized polyaniline films 5. Brush-like chain ordering, Synth. Met. 129 (2002) 29–37.
[47] A. Riede, M. Helmstedt, I. Sapurina, J. Stejskal, In situ polymerized polyaniline films 4. Film formation in dispersion polymerization of aniline, J. Colloid Interface Sci. 248 (2002) 413–418.
[48] Z.H. Cai, J.T. Lei, W.B. Liang, V. Menon, C.R. Martin, Molecular and supramolecular origins of enhanced electronic conductivity in template-synthesized polyheterocyclic fibrils. 1. Supermolecular effects, Chem. Mater. 3 (1991) 960–967.
[49] D. Kopecký, M. Varga, J. Prokeš, M. Vrňata, M. Trchová, J. Kopecká, M. Václavík, Optimization routes for high electrical conductivity of polypyrrole nanotubes prepared in presence of methyl orange, Synth. Met. 230 (2017) 89–96.
[50] J.J. López-Cascales, A.J. Fernández, T.F. Otero, Characterization of the reduced and oxidized polypyrrole/water interface: a molecular dynamics simulation study, J. Phys. Chem. B 107 (2003) 9339–9343.
[51] O. El Beqqali, I. Zorkani, F. Rogemond, H. Chermette, R. Ben Chaabane, M. Gamoudi, G. Guillaud, Electrical properties of molybdenum disulfide MoS_2. Experimental study and density functional calculation results, Synth. Met. 90 (1997) 165–172.
[52] M. Taunk, E. Kapil, S. Chand, Hopping and tunneling transport over a wide temperature range in chemically synthesized doped and undoped polypyrrole, Solid State Commun. 150 (2010) 1766–1769.
[53] S.D. Kang, G.J. Snyder, Charge-transport model for conducting polymers, Nat. Mater. 16 (2017) 252–257.
[54] A. Imani, G. Farzi, Low temperature process of electronic charge transport mechanism in PANi/MWCNT nanocomposites: tubular morphology, J. Mater. Sci. Mater. Electron. 28 (2017) 10684–10692.

Synthetic Metals 237 (2018) 40–49

Contents lists available at ScienceDirect

Synthetic Metals

journal homepage: www.elsevier.com/locate/synmet

Acid Blue dyes in polypyrrole synthesis: The control of polymer morphology at nanoscale in the promotion of high conductivity and the reduction of cytotoxicity

Patrycja Bober[a,*], Yu Li[a,b], Udit Acharya[a,c], Yaduram Panthi[a], Jiří Pfleger[a], Petr Humpolíček[d], Miroslava Trchová[a], Jaroslav Stejskal[a]

[a] Institute of Macromolecular Chemistry, Academy of Sciences of the Czech Republic, 162 06 Prague 6, Czech Republic
[b] Department of Applied Chemistry, School of Science, Xi'an Jiaotong University, Xi'an, 710049, People's Republic of China
[c] Faculty of Mathematics and Physics, Charles University, 121 16 Prague 2, Czech Republic
[d] Centre of Polymer Systems, Tomas Bata University in Zlin, 760 01 Zlin, Czech Republic

ARTICLE INFO

Keywords:
Acid Blue
Conducting polymer
Conductivity
Cytotoxicity
Nanowires
Polypyrrole

ABSTRACT

Polypyrrole has been prepared by facile single-step chemical oxidative polymerization of the monomer in aqueous medium containing an anthraquinone dye, Acid Blue 25 or Acid Blue 129. The addition of the former structure-guiding agent results in the formation of polypyrrole nanowires with conductivity improved up from the units S cm^{-1} to 60 S cm^{-1}. The second closely related dye, Acid Blue 129, had no impact on polymer morphology but in its presence the conductivity of polypyrrole also increased. It has been shown that the pyrrole concentration and oxidant-to-pyrrole mole ratio significantly affect the conductivity of synthesized polypyrrole. Polypyrroles have been characterized by FTIR and Raman spectroscopies to assess their molecular structure and intermolecular interactions. Considering the applications in biomedicine, the cytotoxicity of the samples has also been tested. Polypyrrole prepared with Acid Blue 129 has significantly lower cytotoxicity compared to that prepared with Acid Blue 25. The cytotoxicity of both polypyrroles can be eliminated by purification step. Low cytotoxicity combined with high conductivity enables application of these conducting polymers in biomedicine.

1. Introduction

The preparation of conducting polymer materials has become an important branch of materials research. Nanostructured conducting polymers [1], such as polypyrrole (PPy) [2–4] or polyaniline [5,6], are fabricated by various chemical-oxidation methods. The preparation of one-dimensional polymer morphologies requires the presence of structure-guiding additives that produce hard templates [7,8], soft templates [9,10], reactive-templates [11], or self-degraded templates [12]. Template-free method has also been demonstrated in the preparation of polyaniline nanotubes [13]. The understanding of the processes underlying the formation of a specific morphology and its relation to the conductivity, however, is still a challenge.

Polypyrrole [14,15] in various nanostructures (e.g., nanoparticles, nanotubes, nanowires, thin films, etc.) has been prepared by oxidation of pyrrole in aqueous media and it has subsequently been used in supercapacitors [4,16–19], sensors [20–23], corrosion protection [24], as catalysts supports [25], and as anodes for high-performance lithium-ion batteries [26,27]. The promising applications are expected in biomedicine, where conducting polymers will be used in electrical monitoring or stimulation of biological objects. For example, polypyrrole and its composites can promote neurite outgrowth [28,29], be used as electrically controlled drug-delivery systems [30] or as artificial muscles [31,32].

A substantial effort has recently been exerted on the preparation of polypyrrole nanotubes, in order to increase the conductivity of resulting materials from units S cm^{-1}, which is typical for globular PPy, to 60 S cm^{-1} [2], and even above 100 S cm^{-1} [33]. The most common way how to convert the morphology in favour of nanotubes is represented by addition of methyl orange (MO) to the polymerization mixture [2,12,34,35]. The use of resulting materials in biological application, however, is difficult due to the toxicity of MO. Other dyes, such as Acid Blue 25 [36], Acid Blue 41 [37], Acid Red G [38], Acid Violet 19 [39], or methylene blue [40] have also been studied as structure-guiding agents for PPy preparation. The morphology of PPy prepared in the presence of Acid Blue 25 turned to clusters of nanowires with simultaneous increase in conductivity from units S cm^{-1} up to ≈20 S cm^{-1}. Such one-dimensional structures have successfully been

* Corresponding author.
E-mail address: bober@imc.cas.cz (P. Bober).

https://doi.org/10.1016/j.synthmet.2018.01.010
Received 10 October 2017; Received in revised form 16 January 2018; Accepted 24 January 2018
Available online 07 February 2018
0379-6779/

tested as electrode material in supercapacitors [36]. Also the addition of Acid Violet 19 improved conductivity of PPy nanoparticles to ≈40 S cm^{-1} [39]. However, the presence of some other dyes, such as Acid Green 25, Reactive Black 5, Thymol blue or Indigo carmine, led to a significant decrease in conductivity of PPy [40].

The biocompatibility is a complex materials property for applications pertaining the field of biomedicine. The cytotoxicity is generally believed to be the test of the first choice when the biocompatibility of any material is considered. This is due to the fact that many biological tests can be predicted by the results of cytotoxicity. There are only few studies focused on the biocompatibility of PPy [41–43], especially in form of powders. It is generally accepted, that the biocompatibility of conducting polymers is influenced especially by protonating acids and the presence of residual precursors or oligomers rather than by the polymer itself [44]. The effort to find alternative dopants is therefore obvious in the literature. Also the study focusing on the purification of conducting polymers has been published [45]. The nanostructured conducting polymers possess physicochemical properties which enable their biomedical applications. Their cytotoxicity assessments, however, have been generally neglected in the literature and this motivated the present work.

In the present paper, the influence of two closely related anthraquinone dyes, Acid Blue 25 and Acid Blue 129 (Fig. 1a), on the morphology and electrical conductivity of PPy has been studied. It is shown for the first time that, despite the similarity in molecular structure, their influence on PPy formation substantially differs. Acid Blue 25 acts as a template to produce PPy nanowires during the oxidation of pyrrole with iron(III) chloride as oxidant (Fig. 1b), with enhanced conductivity up to 60 S cm^{-1}, which is three times higher than that reported for this dye in the literature [30]. The presence of the second dye also improved the conductivity but it had no impact on morphology of PPy, which remained globular. The special attention was paid to investigate the cytotoxicity of new highly conducting polypyrroles.

2. Experimental

2.1. Preparation

Pyrrole (≥98%), iron(III) chloride hexahydrate, Acid Blue 25 (AB 25; sodium 1-amino-4-anilinoanthraquinone-2-sulfonate, dye content 45%) and Acid Blue 129 (AB 129; sodium 1-amino-4-(2,4,6-trimethylanilino)anthraquinone-2-sulfonate, dye content 25%), all from Sigma-Aldrich, have been used as supplied without any correction for true dye content.

Polypyrrole was prepared by the oxidation of pyrrole with iron(III) chloride in aqueous medium [40] (Fig. 1b). In a typical synthesis, 0.2 M pyrrole was oxidized with 0.2 M iron(III) chloride in the presence of 0.01 M dye. The AB 25 or AB 129 was dissolved in 50 mL of deionized water and treated in ultrasonic bath for 15 min until complete dissolution. Pyrrole monomer was added. Iron(III) chloride hexahydrate was separately dissolved in deionized water to 50 mL of solution. Then the monomer and oxidant solutions were mixed and left undisturbed at room temperature for 24 h. The reaction mixture was filtered and solid products were rinsed with 200 mL of 0.1 M hydrochloric acid, followed by 100 mL of ethanol. The products were left in air to dry at room temperature until their weights were constant.

Two series of experiments have been carried out. In the first series (*Series 1*), the concentration of pyrrole, [Py], was varied from 0.05 M to

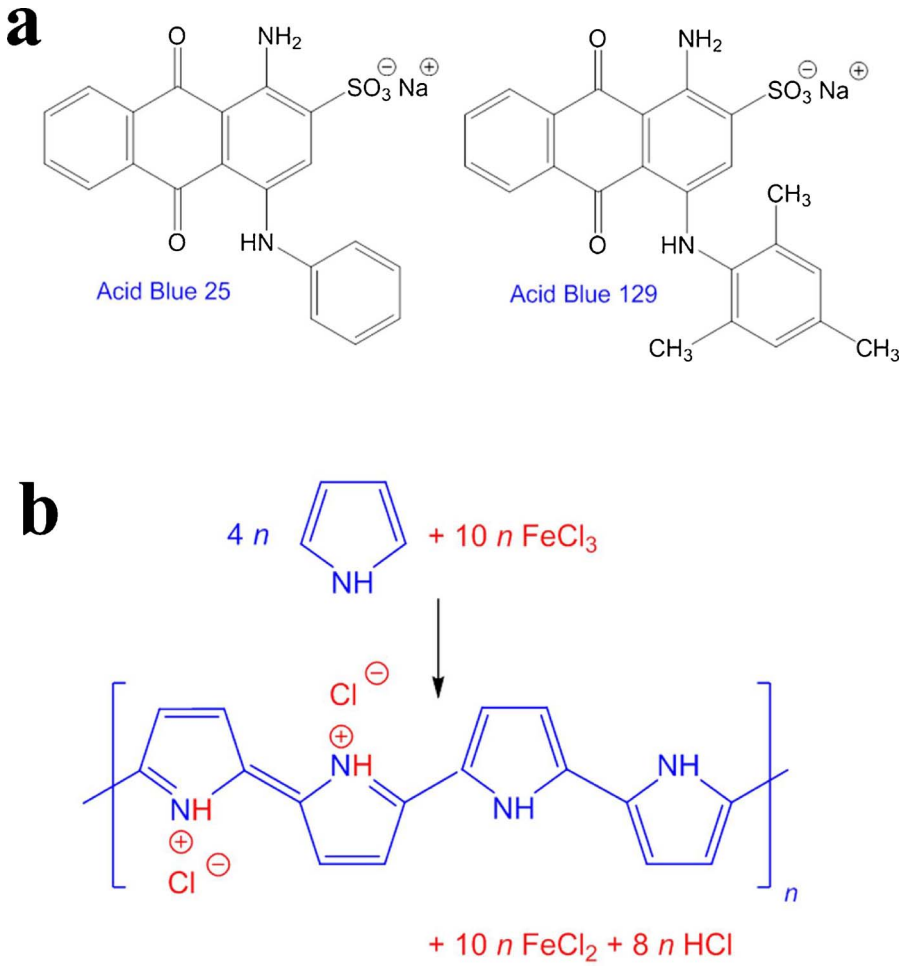

Fig. 1. (a) Formulae of Acid Blue 25 and Acid Blue 129. (b) Pyrrole was oxidized with iron(III) chloride to polypyrrole; stoichiometric oxidant-to-pyrrole mole ratio is 2.5.

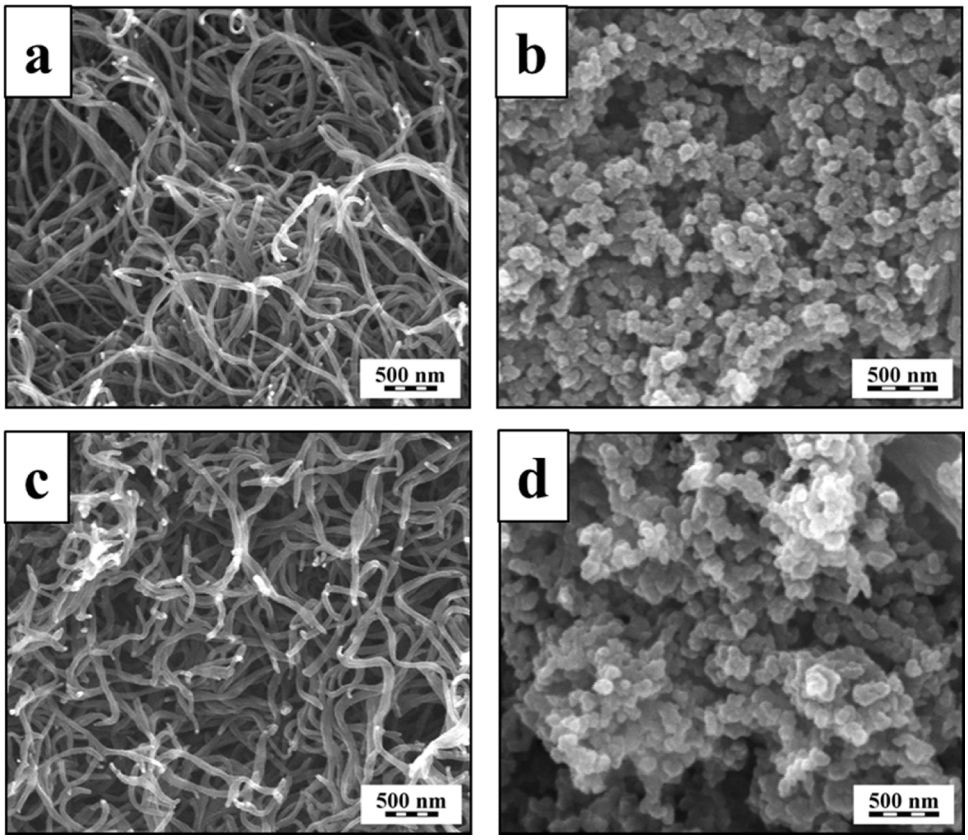

Fig. 2. *Series 1*: SEM images of polypyrrole prepared with Acid Blue 25 (a, c) and Acid Blue 129 (b, d) with pyrrole concentration [Py] = 0.1 M (a, b) and 0.2 M (c, d). [Ox]/[Py] = 1.

0.2 M at equimolar mole ratio of oxidant to monomer and dye-to-pyrrole mole ratio [Dye]/[Py] = 0.05. In the second series (*Series 2*) of experiments, pyrrole concentration was fixed to 0.2 M and the dye concentration to 0.01 M, i.e. dye-to-monomer mole ratio was 0.05, and the oxidant-to-pyrrole mole ratio was varied. The both series have a common sample prepared by the oxidation of 0.2 M pyrrole, 0.2 M iron (III) chloride and 0.01 M dye. The globular PPy (PPy G) was prepared in the absence of any dye at [Py] = 0.2 M and [Ox]/[Py] = 2.5 for comparison.

2.2. Characterization

Polypyrroles were compressed into pellets with a 13 mm diameter and thickness 1 ± 0.2 mm with a manual hydraulic press Trystom H-62 for the conductivity measurement using van der Pauw method. A Keithley 230 Programmable Voltage Source, a Keithley 196 System DMM, and a Keithley 181 Nanovoltmeter (Keithley, USA) were used as voltage supply for current measurement, and voltage measurement, respectively. Measurements have been carried out at constant environmental conditions at 24 ± 1 °C and relative humidity 35 ± 5%. At least four pellets of each sample were prepared and were measured 3 times, then the results were averaged. Morphology of the products was characterized with a scanning electron microscope (SEM) JEOL 6400 and with a transmission electron microscope (TEM) JEM 2000 FX (JEOL, Japan). Elemental composition was determined with a Perkin Elmer CHNS/O Analyzer 2400.

Fourier-transform infrared (FTIR) spectra of the powdered samples were recorded in the transmission mode in potassium bromide pellets using a Thermo Nicolet NEXUS 870 FTIR Spectrometer (Nicolet, USA) with a DTGS TEC detector in the 400–4000 cm^{-1} wavenumber region. All spectra were corrected for the presence of moisture and carbon dioxide in the optical path. Raman spectra excited with HeNe 633 nm and near infrared diode 785 nm lasers were collected on a Renishaw inVia Reflex Raman microspectrometer (Renishaw, UK). A research-grade Leica DM LM microscope with an objective magnification ×50 was used to focus the laser beam on the sample placed on an X–Y motorized sample stage. The scattered light was analysed by the spectroscope with holographic gratings 1800 and 1200 lines mm^{-1} for corresponding lasers, respectively. A Peltier-cooled CCD detector (576 × 384 pixels) registered the dispersed light.

According to the ISO series 10993, the cytotoxicity was determined using the NIH/3T3 cells (ATCC CRL-1658 NIH/3T3, USA). The ATCC-formulated Dulbecco's Modified Eagle's Medium (PAA Laboratories GmbH, Austria) containing 10% of calf serum (BioSera, France) and 100 U mL^{-1} penicillin/streptomycin (GE Healthcare HyClone, UK), was used as the culture medium. The test of cytotoxicity was performed using the extracts from polypyrrole powders. These were prepared according to ISO standard 10993-12 with one modification consisting of extraction of lower amount of material (0.04 g mL^{-1} instead of prescribed 0.2 g mL^{-1} of media) because of the absorbability of polypyrrole. The polymer was incubated in DMEM medium with calf serum for 24 h at 37 °C with stirring. The parent extracts (100%) were then diluted in culture medium to obtain a series of dilutions with concentrations of 75, 50, 25, 10, and 1%. All extracts were used within 24 h for evaluation of cytotoxicity by the decrease in viability of cells cultivated under individual dilutions of extracts for 24 h. The cell viability was evaluated by MTT assay (MTT cell proliferation assay kit, Duchefa Biochemie, Netherlands). The absorbance was measured at 570 nm and the reference wavelength was adjusted at 690 nm. The results are reported as the reduction of cell viability in percentage when compared to cell cultivated in reference medium without the extracts of tested materials.

The native PPy powders were subjected to the purification to evaluate the possibility of cytotoxicity improvement. This was performed by the additional extraction of sample in cultivation media as defined above for 4 days with 0.04 g of PPy powder in 1 mL of

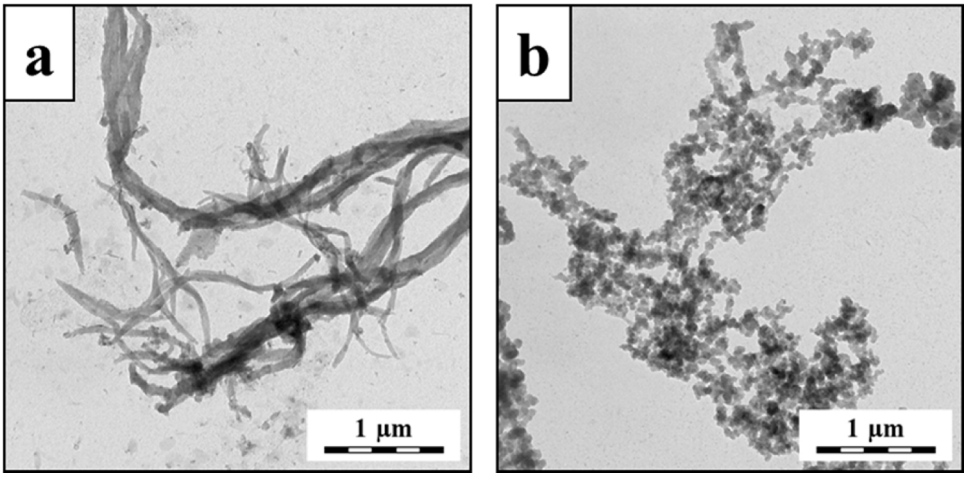

Fig. 3. *Series 1*: TEM images of polypyrrole prepared with (a) Acid Blue 25 and (b) Acid Blue 129. [Py] = 0.2 M, [Ox]/[Py] = 1.

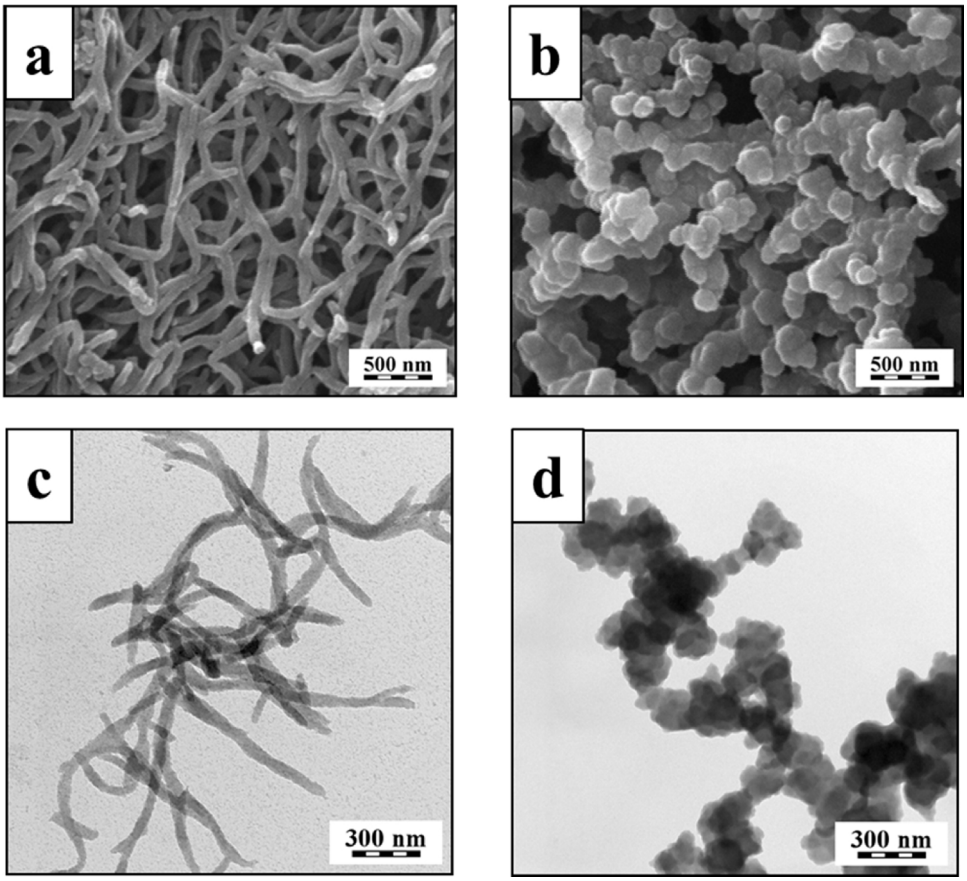

Fig. 4. *Series 2*: SEM (a, b) and TEM images (c, d) of polypyrrole prepared with Acid Blue 25 (a, c) and Acid Blue 129 (b, d). [Py] = 0.2 M, [Ox]/[Py] = 3.

cultivation media. The cytotoxicity of purified PPy was subsequently determined in the same way as described above.

To reveal the effect of AB dyes on the cytotoxicity of PPy, the cytotoxicity of AB 25 and AB 129 alone was determined using the same methodology as described above. The cytotoxicity of concentrations 0.5, 0.75, 1 and 2.5 mM of individual AB dyes in the cultivation media was determined.

3. Results and discussion

3.1. Morphology

The typical polymerization of pyrrole led to a globular morphology which is well known from literature [14,15,40,46]. After introducing a structure-guiding agent AB 25 to the synthesis, PPy nanowires were produced (Fig. 2Figs. 2a,c, Fig. 33a and Fig. 44a,c). In the presence of AB 129 at all oxidant-to-pyrrole mole ratios, the globular PPy has exclusively been obtained (Fig. 2Figs. 2b,d, Fig. 33b and Fig. 44b,d). When the ratio increased, the small increase in PPy particle size was visible.

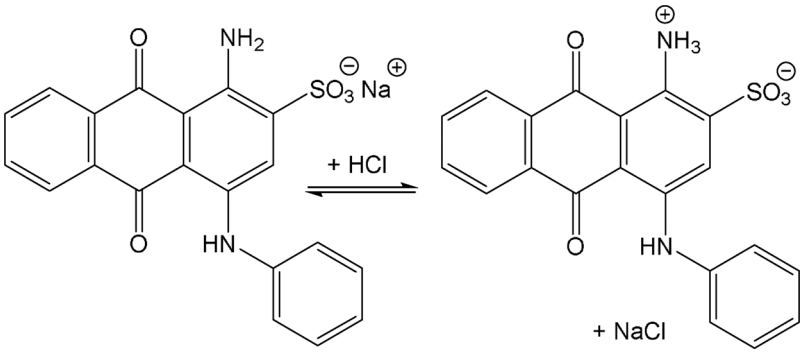

Fig. 5. The conversion of Acid Blue 25 salt to an acid under acidic conditions.

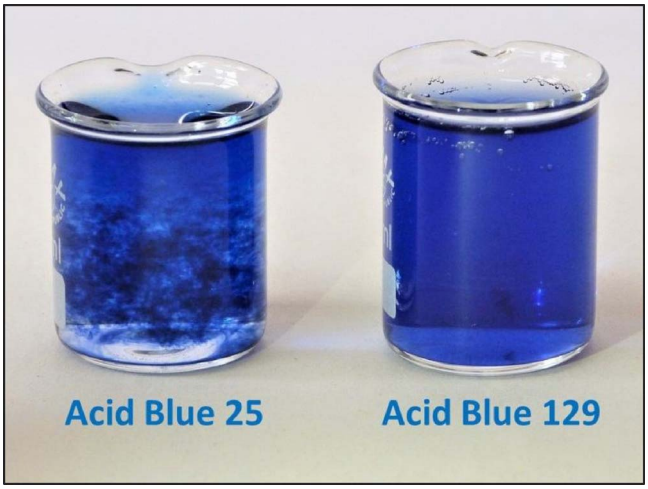

Fig. 6. Aqueous solution of Acid Blue 25 precipitates after acidification with hydrochloric acid and affords the templates (left) while Acid Blue 129 remains soluble (right).

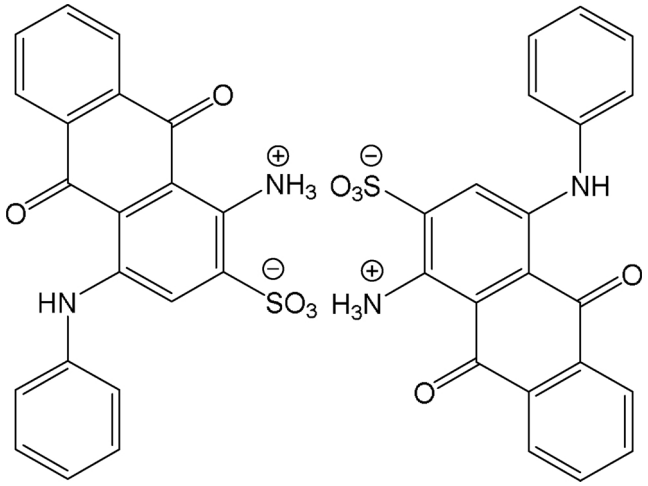

Fig. 7. The dimer of Acid Blue 25.

3.2. The role of dyes

The influence of dyes on the morphology of PPy has been documented in the literature, however, the understanding of the processes underlying the generation of a specific morphology is still a challenge [2]. The formation of the template during the polymerization seems to be the most important step. In analogy with recent report comparing the performance of methyl orange and ethyl orange dyes [33], it is assumed that AB 25 converts from salt to acid form when the pH of reaction mixture drops to pH 1 after the addition of iron(III) chloride oxidant (Fig. 5). The sodium salt of the dye is well-soluble, the acid form is not, and it separates from the solution after its acidification within seconds (Fig. 6). We expect that this is due to the formation of an insoluble dimer (Fig. 7). Indeed, the proposed dimer is based on the analogy with *o*-aminobenzenesulfonic acid which, in the contrast to its sodium salt, is completely insoluble in water due to the formation of internal salt which prevents the standard dissociation and consequent solubility. As the dye separates from the solution, it affords the template for the adsorption of the pyrrole oligomers generated at the same time, followed by the growth of PPy chains.

The second dye, AB 129 does not separate at the same time scale (Fig. 6), no template was formed before polymerization of pyrrole occured, and globular PPy was therefore obtained (Fig. 5). It has to be noted that even AB 129 starts to precipitate after tens of minutes but the polymerization of pyrrole was completed by that time. This means that the formation of the template and the polymerization of pyrrole has to proceed in the accord, and only then PPy nanowires are produced.

Table 1
Series 1: Effects of pyrrole concentration [Py] on the conductivity and the yield of polypyrrole prepared in the presence of Acid Blue 25 and 129. [Dye]/[Py] = 0.05, [Ox]/[Py] = 1.

[Py] (M)	Conductivity (S cm^{-1})		Yield (g g^{-1} pyrrole)	
	AB 25	AB 129	AB 25	AB 129
0.05	20 ± 0.3	18 ± 0.2	0.71	0.16
0.1	43 ± 0.6	31 ± 0.5	0.72	0.32
0.15	45 ± 0.4	38 ± 0.6	0.73	0.50
0.2	52 ± 0.4	40 ± 0.2	0.76	0.67

Table 2
Series 2: Effects of oxidant-to-pyrrole mole ratio, [Ox]/[Py], on the conductivity and the yield of polypyrrole prepared at various oxidant-to-pyrrole mole ratios. [Py] = 0.2 M, [Dye] = 0.01 M.

[Ox]/[Py]	Conductivity (S cm^{-1})		Yield (g g^{-1} pyrrole)	
	AB 25	AB 129	AB 25	AB 129
1.5	45 ± 0.3	39 ± 0.4	1.10	0.95
2	55 ± 0.3	36 ± 0.5	1.41	1.20
2.5	60 ± 0.5	35 ± 0.2	1.53	1.40
3	62 ± 0.7	40 ± 0.4	1.55	1.43

3.3. Conductivity

The addition of AB 25 or AB 129 during the polymerization of pyrrole has led to significant increase in conductivity of PPy. The globular PPy prepared by polymerization of pyrrole with iron(III) chloride had conductivity of ≈1 S cm^{-1} [46]. For the systems including AB 25, the increase in the PPy conductivity was observed with increasing pyrrole concentration from 0.05 to 0.2 M (Table 1). When the

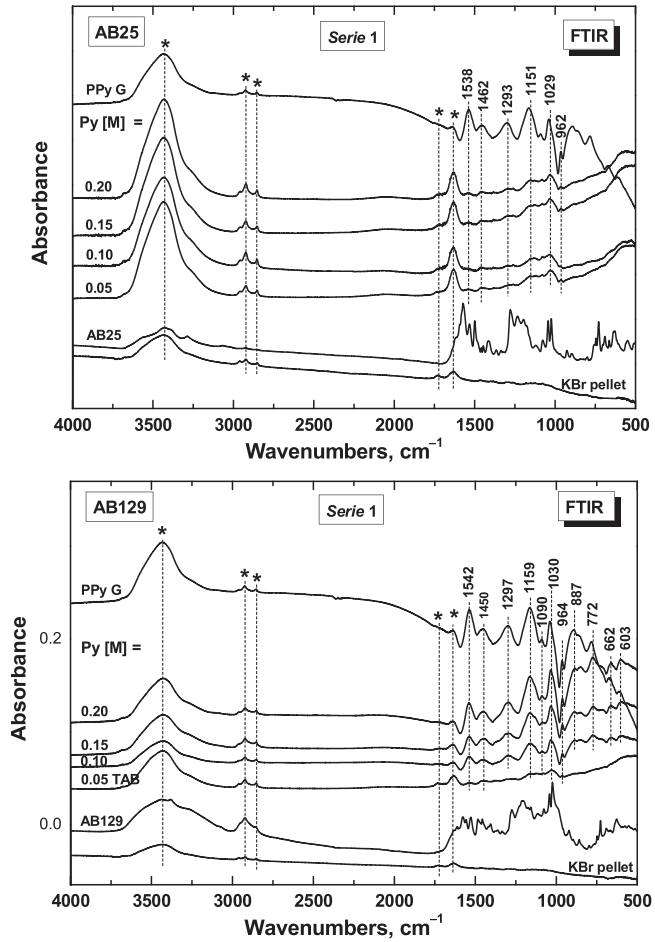

Fig. 8. *Series 1:* FTIR spectra of polypyrrole prepared in the presence of Acid Blue 25 (top) and Acid Blue 129 (bottom) at fixed the mole ratios of a dye to pyrrole, [Dye]/[Py] = 0.05, and oxidant to pyrrole, [Ox]/[Py] = 1. The spectra of the pure dyes and of the globular PPy (PPy G) prepared in the absence of any dye for [Py] = 0.2 and [Ox]/[Py] = 2.5 are also displayed. The spectrum of potassium bromide pellet is shown for comparison.

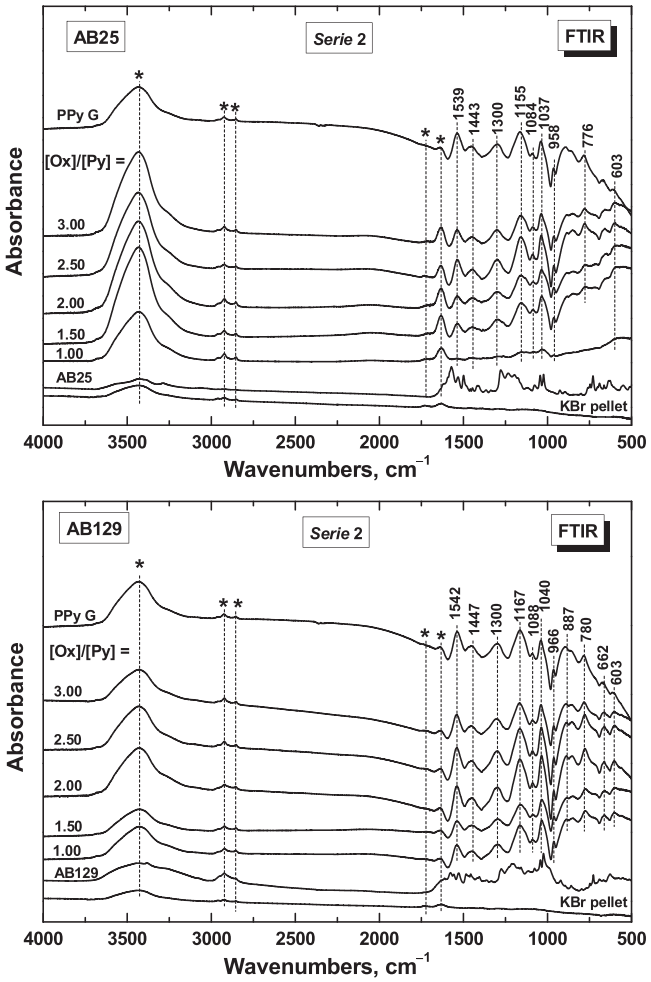

Fig. 9. *Series 2*: FTIR spectra of polypyrrole prepared in the presence of Acid Blue 25 (top) and Acid Blue 129 (bottom) at various oxidant-to-pyrrole mole ratios, [Ox]/[Py], at fixed concentrations of pyrrole, [Py] = 0.2 M, and of a dye, [Dye] = 0.01 M. The spectra of pure dyes and of the globular PPy (PPy G) prepared in the absence of any dye for [Py] = 0.2 and [Ox]/[Py] = 2.5 are also displayed. The spectrum of potassium bromide pellet is shown for comparison.

pyrrole concentration was fixed at 0.2 M, the conductivity was further improved with oxidant-to-pyrrole mole ratio increasing from 1.5 to 3 (Table 2). We can spot the same trends with AB 129 dye (Table 1Tables 1 and Table 22). The conductivity of the one-dimensional PPy prepared with AB 25 was always somewhat higher than that prepared with AB 129, but still small compared with the dramatic difference in morphology. We therefore conclude that the one-dimensional morphology alone is not an automatic prerequisite for the high conductivity.

3.4. Yield

The yield of the reaction is another parameter of practical importance. When 1 g of pyrrole was oxidized with iron(III) chloride, it theoretically produces 1.1 g of PPy chloride according to the reaction scheme when oxidant to pyrrole mole ratio [Ox]/[Py] = 2.5 (Fig. 1b). The yield is lower than theoretical one only in the case of the ratio [Ox]/[Py] = 1 (Table 1), and it became higher when oxidant-to-pyrrole mole ratio increased (Table 2). This indicates the incorporation of the dye into polymer structure [40]. Elemental analysis also confirmed the presence of dyes in PPy, which manifersts itself by 3 and 2 wt.% of sulfur in polypyrrole ([Dye]/[Py] = 0.05, [Ox]/[Py] = 1) prepared with Acid Blue 25 and Acid Blue 129, respectively. Both polypyrroles contained 22 wt% of carbon, 3.5 wt% of nitrogen and 8 wt% of hydrogen.

It should be also noted that even though the yields calculated per gram of pyrrole are comparable for, e.g., AB 129 (Table 1), the yields calculated per unit volume of reaction mixture are about four time higher at [Py] = 0.2 M than at [Py] = 0.05. This means that the synthesis at higher monomer concentrations is more efficient with respect to both the yield and the conductivity. The increase in the [Ox]/[Py] ratio further improves these parameters (Table 2).

3.5. Infrared spectra

FTIR spectra provide important information on the molecular structure of PPy and on its interactions with dyes. FTIR spectra of PPy prepared in presence of AB 25 or AB 129 at fixed mole ratios of a dye to pyrrole, [Dye]/[Py] = 0.05, and oxidant to pyrrole, [Ox]/[Py] = 1 (*Series 1*, Fig. 8) differ. In the spectra of samples prepared with AB 25, the absorption bands in the region of stretching and bending vibrations of water molecules and of aliphatic impurities coming from potassium bromide pellets are relatively high (marked with asterisks in Fig. 8). This is caused by their compact stone-like structure which was very difficult to disperse in potassium bromide pellets. The better dispersion in the case of AB 129 may be explained by the presence of methyl groups in its structure (Fig. 1a), which does not allow the dye to form a rigid template, and by strong hydrogen bonding in the nanowires structure obtained with AB 25. This fact may explain the higher yield and conductivity of the PPy nanowires prepared with AB 25. As a

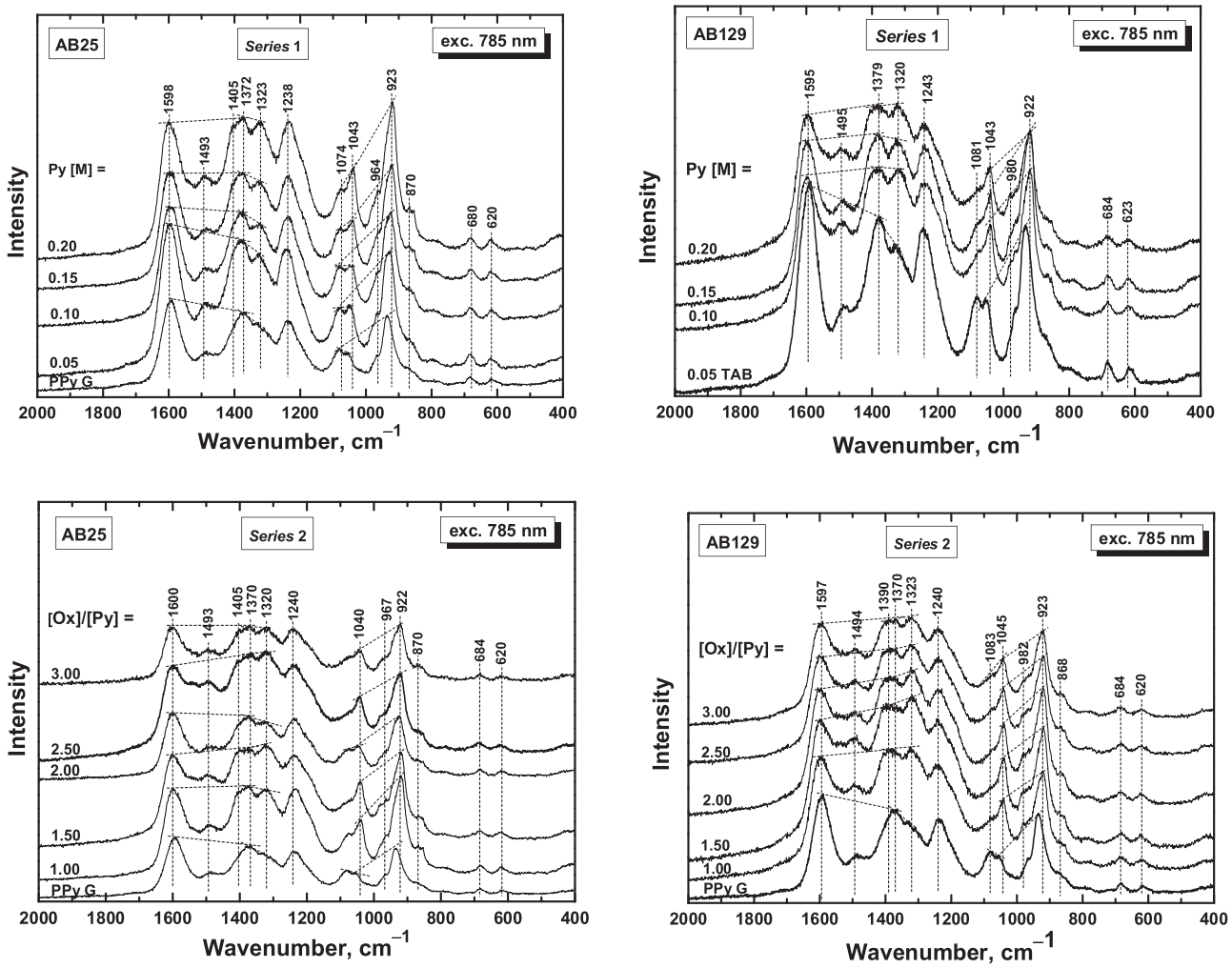

Fig. 10. Raman spectra of polypyrrole prepared in the presence of Acid Blue 25 and Acid Blue 129 at fixed the mole ratios of a dye to pyrrole, [Dye]/[Py] = 0.05, and oxidant to pyrrole, [Ox]/[Py] = 1 (*Series 1*, top) and at various oxidant to pyrrole mole ratio, [Ox]/[Py], at fixed concentration of pyrrole, [Py] = 0.2 M, and a dye, [Dye] = 0.01 M (Series 2, bottom) excited with laser wavelength 785 nm.

consequence the bands of PPy are better resolved for samples prepared in presence of AB 129 dye. We detect the main bands of globular PPy (spectrum PPy G in Fig. 8) that have been interpreted in the literature [3,15,40,47]. The band of C—C stretching vibrations in the pyrrole ring at 1542 cm^{-1}, the band of the C—N stretching vibrations in the ring at 1450 cm^{-1}, the broad band attributed to C—H or C—N in-plane deformation modes with a maximum at about 1297 cm^{-1}, and the band in the region of the C—H and N—H inplane deformation vibrations with maximum at 1158 cm^{-1} are all observed in the spectrum. The band with maximum at 1030 cm^{-1} corresponds to the C—H and N—H in-plane deformation vibrations, and the peak at 964 cm^{-1} to the C—H out of plane deformation vibrations of the ring. It should be stressed that, contrary to the PPy nanotubes prepared in presence of MO [47], the peaks of AB 25 or AB 129 are not detected in the spectra (the spectra of the dyes in Fig. 8). The absorption of the bands of PPy slightly increases with increasing concentration of pyrrole when [Ox]/[Py] = 1 for both dyes in the *Series 1*. This corresponds to the increase of yield and conductivity (Table 1).

FTIR spectra of PPy prepared in presence of AB 25 and AB 129 at various oxidant to pyrrole mole ratios, [Ox]/[Py], at fixed concentration of pyrrole, [Py] = 0.2 M, and a dye, [Dye] = 0.01 M, are better resolved for both dyes (*Series 2* in Fig. 9). The sample for [Py] = 0.2 M prepared in *Series 1* corresponds to the sample for [Ox]/[Py] = 1 in *Series 2*. The bands of PPy and the absorption in the region above 2000 cm^{-1} increase with increasing [Ox]/[Py] ratio for both dyes in the *Series 2*. This corresponds well to the increasing yield and conductivity of the samples (Table 2).

3.6. Raman spectra

3.6.1. 785 nm laser excitation line

Energy of laser excitation wavelength 785 nm is in resonance with the energy of delocalized polarons and bipolarons in PPy. Raman spectra of PPy prepared in presence of AB 25 and AB 129 at fixed the mole ratios of a dye to pyrrole, [Dye]/[Py] = 0.05, and oxidant to pyrrole, [Ox]/[Py] = 1 (*Series 1* in Fig. 10) display the main bands of PPy [3,47–50]. When the concentration of pyrrole increased, the intensity of the band of C=C stretching vibrations of PPy backbone observed at 1598 cm^{-1} decreased. The relative intensity of the second band of the twin band of ring-stretching vibrations situated at 1372 and 1323 cm^{-1} increased. The band of antisymmetric C—H deformation vibrations is observed at 1240 cm^{-1}. In the double peak corresponding to the C—H out-of-plane deformation vibrations with local maxima at 1074 and 1043 cm^{-1}, the second peak becomes sharper. All these changes are usually observed after partial deprotonation [3]. The band at 984 cm^{-1} of the ring-deformation vibrations of neutral PPy units and the sharp peak at 923 cm^{-1} of the ring-deformation vibrations in dication (bipolaron) units (Fig. 1b) are detected in the spectra. The changes of the spectra are at variance with the increasing of the conductivity of the samples with increasing concentration of pyrrole in the

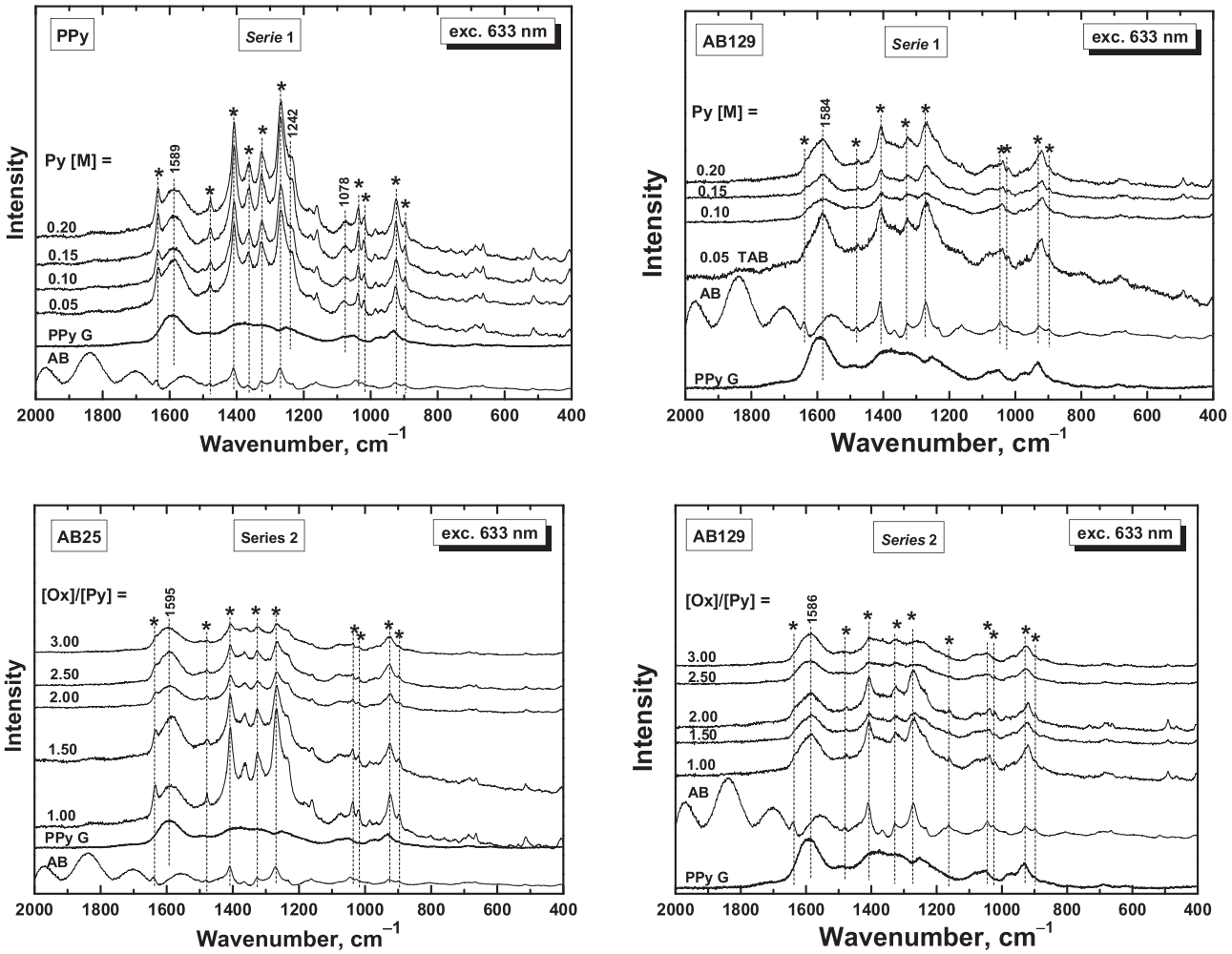

Fig. 11. Raman spectra of polypyrrole prepared in the presence of Acid Blue 25 and 129 at fixed the mole ratios of a dye to pyrrole, [Dye]/[Py] = 0.05, and oxidant to pyrrole, [Ox]/[Py] = 1 (*Series 1*, top) and at various oxidant to pyrrole mole ratio, [Ox]/[Py], at fixed concentration of pyrrole, [Py] = 0.2 M, and a dye, [Dye] = 0.01 M (*Series 2*, bottom) excited with laser wavelength 633 nm.

reaction mixture (Table 1). This paradox has been also detected in the case of PPy nanotubes prepared in presence of MO [40]. The changes in the spectra with increasing molar concentration of MO were also similar to those after treatment of globular PPy with 0.1 M ammonium hydroxide. It should be stressed that the peaks of partially protonated PPy were detected in the spectra of the regions rich in MO [40]. Due to the resonance character of the Raman scattering, the spectrum obtained with the laser excitation at 785 nm corresponds especially to the surface of PPy nanotubes.

Raman spectra of PPy prepared in presence of AB 25 and AB 129 at various oxidant-to-pyrrole mole ratio, [Ox]/[Py], at fixed concentration of pyrrole, [Py] = 0.2 M, and a dye, [Dye] = 0.01 M (*Series 2* in Fig. 10) also exhibit some features corresponding to the spectra of standard PPy after deprotonation with 0.1 M ammonium hydroxide (compare with spectrum of standard globular PPy in Fig. 10) [3].

3.6.2. 633 nm laser excitation line

Raman spectra of PPy prepared in presence of AB 25 and AB 129 recorded with 633 nm excitation wavelength display prevailing spectral features of the dyes (*Series 1,* Fig. 11). The peaks of dye are more pronounced in the case of AB 25, and they are marked with asterisks in Fig. 11. The intensity of the bands of dye increased with increasing pyrrole concentration. Some bands of PPy are also detected especially in the spectra of samples prepared with AB 129. It is interesting that the bands of PPy detected in the spectra with laser excitation line 633 nm correspond to the protonated samples.

In the Raman spectra of PPy prepared in presence of AB 25 and AB 129 at various oxidant-to-pyrrole mole ratio, [Ox]/[Py], at fixed concentration of pyrrole, [Py] = 0.2 M, and a dye, [Dye] = 0.01 M (*Series 2* in Fig. 11), the intensity of the bands of dyes decreased with increasing of the [Ox]/[Py] ratio. The bands of PPy correspond also to protonated samples.

The excitation line in NIR region (785 nm) is in resonance with the energy of transitions in polarons in PPy (globular or nanowires) and so the spectrum corresponds especially to the surface of the nanowires which is formed by PPy. It follows from the UV–vis spectra of PPy [51,52]. The spectrum obtained with laser excitation light of 633 nm, which penetrates inside the nanowires, corresponds to PPy which is in contact with dyes. It is in resonance with the energy of the electronic transition in the dyes. The peaks of the corresponding dyes are well detected in the spectra in Fig. 9. These facts may explain the different protonation state of PPy observed in the Raman spectra for two different laser excitation wavelengths. The spectrum obtained with laser excitation of 633 nm, which penetrates inside the nanowires, corresponds to PPy, which is in contact with dyes. This observation may explain the paradox of the lower protonation state of PPy observed on the surface of PPy nanowires with a 785 nm laser. We conclude that the profile of nanowires is not uniform and the structure of surface region differs from the nanowires interior. This may be due to the local difference in the degree of protonation or chain-organization or both resulting in the gradient of polaron concentration. The Raman spectroscopy itself is not able to provide more detailed information.

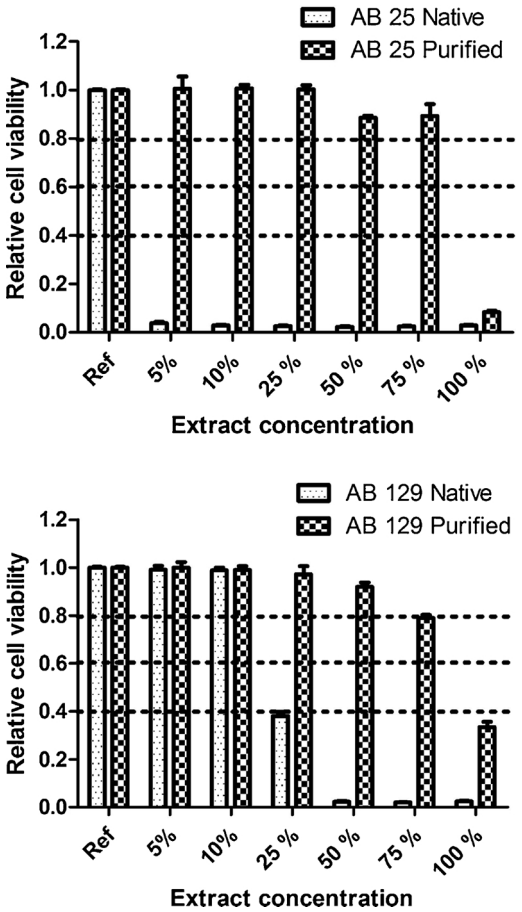

Fig. 12. Cytotoxicity of native and purified polypyrrole powders prepared with Acid Blue 25 or Acid Blue 129.

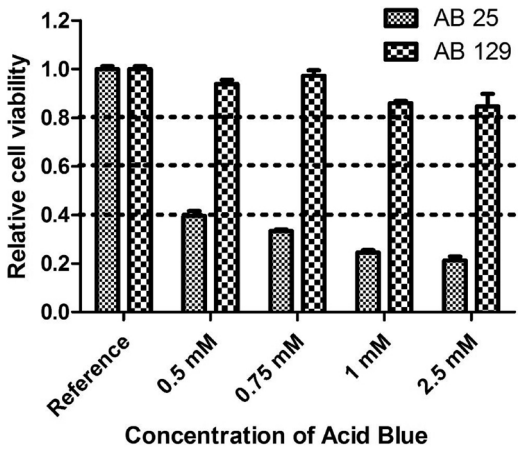

Fig. 13. Cytotoxicity of Acid Blue 25 and Acid Blue 129.

3.7. Cytotoxicity

The cytotoxicity of PPy in its native as well as in purified forms is illustrated in Fig. 12. It is obvious that native PPy prepared with AB 129 dye displays smaller cytotoxicity than that prepared with AB 25. The PPy with AB 129 became cytotoxic at concentration higher than 10% of extracts in cultivation medium while PPy with AB 25 was in its native form cytotoxic even at the 5% of extract in cultivation medium. Considering the fact that the lower ratio between the PPy powder and cultivation medium was used for preparation of extracts (see the methodology), it can be concluded that cytotoxicity of PPy with Acid Blue is comparable to, for example, the second most studied conducting polymer, polyaniline prepared according to IUPAC-recommended procedure [53]. Regarding the PPy, the only study focused on the cytotoxicity of PPy powder extracted according to ISO protocol 10993 was published by Wang et al. [54]. Their study, however, used special Schwann cells line. By using this line, the authors declare that no cytotoxicity was observed if they cultivated 100 µL of 50% extract and 100 µL of cultivation medium. The standard PPy can be therefore considered as similarly cytotoxic on Schwann cells as AB 25.

The cytotoxicity of native samples can be related to either the residual precursors or oligomers or to the used type of Acid Blue dye. Polypyrrole itself is believed to be biocompatible, thus, the cytotoxicity of dyes alone used for preparation of PPy powders was tested (Fig. 13). It is clear that the cytotoxicity of PPy is connected to the used Acid Blue dyes, as cytotoxicity of AB 129 is significantly lower than AB 25 in all tested concentrations. In addition, the purification step consisting in double extraction in cultivation medium significantly reduces the cytotoxicity of PPy as after the purification neither PPy prepared with AB 129 nor polypyrrole with AB 25 shows cytotoxicity at all concentrations of extracts in cultivation medium except of 100%. It can be therefore concluded that extractions lead to the leaching of non-bound Acid Blues and therefore the PPy became less cytotoxic.

4. Conclusions

The preparation of polypyrrole nanowires by the oxidation of pyrrole with iron(III) chloride in the presence of structure-guiding dye, Acid Blue 25, is reported. The dye produces a template for the growth of polypyrrole under acidic conditions afforded by iron(III) chloride oxidant. The conductivity was improved from units S cm^{-1}, which is typical for globular polypyrrole prepared in the absence of dyes, to *ca* 60 S cm^{-1}, for polypyrrole prepared in the presence of Acid Blue 25. Both the yield and conductivity increased with increasing concentration of pyrrole and oxidant-to-pyrrole mole ratio.

The similar syntheses with a closely related dye, Acid Blue 129, displayed similar trends with respect to improved conductivity and higher yield compared with the preparation in the absence of a dye. The conductivity was only slightly lower compared with the samples prepared with Acid Blue 25 dye. The morphology of polypyrrole, however, was exclusively globular, i.e. completely different. This was explained and demonstrated by the inability of this dye to produce a template for nanotubular growth of polypyrrole in time. We also conclude that the one-dimensional morphology does not directly imply the high conductivity, which rather depends on the degree of polymer-chain ordering.

FTIR and Raman spectra demonstrate that the molecular structure of polypyrrole prepared in presence of Acid Blue 25 and Acid Blue 129 corresponds to the molecular structure of standard polypyrrole. Raman spectra also suggest that the degree protonation of polypyrrole is lower at the surface of nanowires than in its body. The incorporation of the dyes is confirmed by the Raman spectroscopy when the 633 nm laser excitation was used.

Polypyrrole prepared with Acid Blue 129 is in its native form less cytotoxic compared to Acid Blue 25. It has therefore a higher application potential in biomedical applications, such as in the engineering of electrosensitive tissues (e.g., cardiac or neuronal), biosensors and bioactuators. A simple purification by pouring in extraction medium, however, substantially reduced the cytotoxicity in both cases.

Acknowledgments

The authors thank the Czech Science Foundation (17-04109S) for financial support. Y. L. and Y. P. participated in the Postgraduate Course in Polymer Science 2015/6 and 2016/7, respectively, organized by the Institute of Macromolecular Chemistry in Prague. J. Hromádková is acknowledged for SEM and TEM micrographs.

References

[1] Y.Z. Long, M.M. Li, C.Z. Gu, M.X. Wan, J.L. Duvail, Z.W. Liu, Z.Y. Fan, Recent advances in synthesis, physical properties and applications of conducting polymer nanotubes and nanofibers, Prog. Polym. Sci. 36 (2011) 1415–1442.

[2] J. Kopecká, D. Kopecký, M. Vrňata, P. Fitl, J. Stejskal, M. Trchová, P. Bober, Z. Morávková, J. Prokeš, I. Sapurina, Polypyrrole nanotubes: mechanism of formation, RSC Adv. 4 (2014) 1551–1558.

[3] J. Stejskal, M. Trchová, P. Bober, Z. Morávková, D. Kopecký, M. Vrňata, J. Prokeš, M. Varga, E. Watzlová, Polypyrrole salts and bases: superior conductivity of nanotubes and their stability towards the loss of conductivity by deprotonation, RSC Adv. 6 (2016) 88382–88391.

[4] Y. Huang, H.F. Li, Z.F. Wang, M.S. Zhu, Z.X. Pei, Q. Xu, Y. Huang, C.Y. Zhi, Nanostructured polypyrrole as a flexible electrode material of supercapacitor, Nano Energy 22 (2016) 422–438.

[5] S. Virji, J. Huang, R.B. Kaner, B.H. Weiller, Polyaniline nanofiber gas sensors: examination of response mechanisms, Nano Lett. 4 (2004) 491–496.

[6] J. Stejskal, I. Sapurina, M. Trchová, Polyaniline nanostructures and the role of aniline oligomers in their formation, Prog. Polym. Sci. 35 (2010) 1420–1481.

[7] B. Schulz, I. Orgzall, I. Diez, B. Dietzel, K. Tauer, Template mediated formation of shaped polypyrrole particles, Colloids Surf. A 354 (2010) 368–376.

[8] M. Radoicić, G. Ćirić-Marjanović, Z.V. Saponjić, M. Mitrić, Z. Konstantinović, M. Stoiljković, J.M. Nedeljković, Structural and magnetic properties of nanocomposites based on nanostructured polyaniline and titania nanotubes, J. Mater. Sci. 48 (2013) 5776–5787.

[9] Y. Wang, C.H. Yu, Z. Li, D.S. Zhou, W. Chen, G. Xue, Synthesis of ordered spiral and ring-like polypyrrole nanowires in cetyltrimethylammonium bromide crystalline suspension, Colloid Polym. Sci. 287 (2009) 1325–1330.

[10] Y.J. Wang, W.B. Zhong, X.T. Ning, Y.T. Li, X.H. Chen, Y.X. Wang, W.T. Yang, The controlled preparation of polypyrrole nanostructures via tuning the concentration of acrylic acid, J. Nanosci. Nanotechnol. 13 (2013) 2382–2390.

[11] H. Farrokhi, O. Khani, F. Nemati, M. Jazirehpour, Synthesis and investigation of microwave characteristics of polypyrrole nanostructures prepared via self-reactive flower-like MnO_2 template, Synth. Met. 215 (2016) 142–149.

[12] X.M. Yang, Z.X. Zhu, T.Y. Dai, Y. Lu, Facile fabrication of functional polypyrrole nanotubes via a reactive self-degraded template, Macromol. Rapid Commun. 26 (2005) 1736–1740.

[13] M. Trchová, I. Šeděnková, E.N. Konyushenko, J. Stejskal, P. Holler, G. Ćirić-Marjanović, Evolution of polyaniline nanotubes: the oxidation of aniline in water, J. Phys. Chem. B 110 (2006) 9461–9468.

[14] L.-X. Wang, X.-G. Li, Y.-L. Yang, Preparation, properties and applications of polypyrroles, React. Funct. Polym. 47 (2001) 125–139.

[15] M. Omastová, M. Trchová, J. Kovářová, J. Stejskal, Synthesis and structural study of polypyrroles prepared in the presence of surfactants, Synth. Met. 138 (2003) 447–455.

[16] X. Wang, C. Yang, P. Liu, Facile decoration of polypyrrole nanoparticles onto graphene nanosheets for supercapacitors, Synth. Met. 162 (2012) 2349–2354.

[17] S. Chen, I. Zhitomirsky, Polypyrrole electrodes doped with sulfanilic acid azochromotrop for electrochemical supercapacitors, J. Power Sources 243 (2013) 865–871.

[18] C. Shen, Y. Sun, W. Yao, Y. Lu, Facile synthesis of polypyrrole nanospheres and their carbonized products for potential application in high-performance supercapacitors, Polymer 55 (2014) 2817–2824.

[19] L.L. Zhang, H.H. Li, C.Y. Fan, K. Wang, X.L. Wu, H.Z. Sun, H.M. Xie, J.P. Zhang, Polypyrrole nanosphere embedded in wrinkled graphene layers to obtain cross-linking network for high performance supercapacitors, Electrochim. Acta 184 (2015) 179–185.

[20] O.Y. Posudievsky, N.V. Konoschuk, A.L. Kukla, A.S. Pavluchenko, Y.M. Shirshov, V.D. Pokhodenko, Comparative analysis of sensor responses of thin conducting polymer films to organic solvent vapors, Sens. Actuators B Chem. 151 (2011) 351–359.

[21] J.S. Lee, J. Jun, D.H. Shin, J. Jang, Urchin-like polypyrrole nanoparticles for highly sensitive and selective chemiresistive sensor application, Nanoscale 6 (2014) 4188–4194.

[22] M.R. Mahmoudian, W.J. Basirun, Y. Alias, A sensitive electrochemical Hg^{2+} ions sensor based on polypyrrole coated nanospherical platinum, RSC Adv. 6 (2016) 36459–36466.

[23] J. Kopecká, M. Mrlík, R. Olejník, D. Kopecký, M. Vrňata, J. Prokeš, P. Bober, Z. Morávková, M. Trchová, J. Stejskal, Polypyrrole nanotubes and their carbonized analogs: synthesis, characterization, gas sensing properties, Sensors 16 (2016) 1917.

[24] M. Ates, A review on conducting polymer coatings for corrosion protection, J. Adhes. Sci. Technol. 30 (2016) 1510–1536.

[25] I. Sapurina, J. Stejskal, I. Šeděnková, M. Trchová, J. Kovářová, J. Hromádková, J. Kopecká, M. Cieslar, A. Abu El-Nasr, M.M. Ayad, Catalytic activity of polypyrrole nanotubes decorated with noble-metal nanoparticles and their conversion to carbonized analogues, Synth. Met. 214 (2016) 14–22.

[26] X.-B. Zhong, H.-Y. Wang, Zh.-Z. Yang, B. Jin, Q.-C. Jiang, Facile synthesis of mesoporous $ZnCo_2O_4$ coated with polypyrrole as an anode material for lithium-ion batteries, J. Power Sources 296 (2015) 298–304.

[27] G. Li, R. Han, X. Xu, M. Ren, Facile synthesis of Mn-doped hollow Fe_2O_3 nanospheres coated with polypyrrole as anodes for high-performance lithium-ion batteries, RSC Adv. 6 (2016) 48199–48204.

[28] A. Kotwal, C.E. Schmidt, Electrical stimulation alters protein adsorption and nerve cell interactions with electrically conducting biomaterials, Biomaterials 22 (2001) 1055–1064.

[29] K.-H. Park, E.A. Jo, K. Na, Heparin/polypyrrole (PPy) composite on gold-coated matrix for the neurite outgrowth of PC12 cells by electrical stimulation, Biotechnol. Bioprocess Eng. 12 (2007) 463–469.

[30] P.M. George, D.A. LaVan, J.A. Burdick, C.-Y. Chen, E. Liang, R. Langer, Electrically controlled drug delivery from biotin-doped conductive polypyrrole, Adv. Mater. 18 (2006) 557–581.

[31] T. Mirfakhrai, J.D.W. Madden, R.H. Baughman, Polymer artificial muscles, Mater. Today 10 (2007) 30–38.

[32] T.F. Otero, J.G. Martinez, J. Arias-Pardilla, Biomimetic electrochemistry from conducting polymers. A review. Artificial muscles, smart membranes, smart drug delivery and computer/neuron interfaces, Electrochim. Acta 84 (2012) 112–128.

[33] Y. Li, P. Bober, M. Trchová, J. Stejskal, Polypyrrole prepared in the presence of methyl orange and ethyl orange: nanotubes versus globules in conductivity enhancement, J. Mater. Chem. C 5 (2017) 4236–4245.

[34] J. Škodová, D. Kopecký, M. Vrňata, M. Varga, J. Prokeš, M. Cieslar, P. Bober, J. Stejskal, Polypyrrole-silver composites prepared by the reduction of silver ions with polypyrrole nanotubes, Polym. Chem. 4 (2013) 3610–3616.

[35] S. Misra, M. Bharti, A. Singh, A.K. Debnath, D.K. Aswal, Y. Hayakawa, Nanostructured polypyrrole: enhancement in thermoelectric figure of merit through suppression of thermal conductivity, Mater. Res. Express 4 (2017) 085007.

[36] Y. Wang, C. Yang, P. Liu, Acid blue AS doped polypyrrole (PPy/AS) nanomaterials with different morphologies as electrode materials for supercapacitors, Chem. Eng. J. 172 (2011) 1137–1144.

[37] Y. Wang, X. Wang, C. Yang, B. Mu, P. Liu, Effect of Acid Blue BRL on morphology and electrochemical properties of polypyrrole nanomaterials, Powder Technol. 235 (2013) 901–908.

[38] J. Han, W. Yan, Y.B. Xu, Synthesis of long polypyrrole micro/nanotubules with rectangular sections, Chem. Lett. 35 (2006) 306–307.

[39] L. Zang, J. Qiu, C. Yang, E. Sakai, Enhanced conductivity and electrochemical performance of electrode material based on multifunctional dye doped polypyrrole, J. Nanosci. Nanotechnol. 16 (2016) 2564–2570.

[40] I. Sapurina, Y. Li, E. Alekseeva, P. Bober, M. Trchová, M. Morávková, J. Stejskal, Polypyrrole nanotubes: the tuning of morphology and conductivity, Polymer 113 (2017) 247–258.

[41] A. Ramanaviciene, A. Kausaite, S. Tautkus, A. Ramanavicius, Biocompatibility of polypyrrole particles: an in-vivo study in mice, J. Pharm. Pharmacol. 59 (2007) 311–315.

[42] S. Kim, W. Oh, Y.S. Jeong, J. Hong, B. Cho, J. Hahn, J. Jang, Cytotoxicity of, and innate immune response to, size-controlled polypyrrole nanoparticles in mammalian cells, Biomaterials 32 (2011) 2342–2350.

[43] A. Ramtin, A. Seyfoddin, F. Coutinho, G. Waterhouse, I. Rupenthal, D. Svirskis, Cytotoxicity considerations and electrically tunable release of dexamethasone from polypyrrole for the treatment of back-of-the-eye conditions, Drug Deliv. Transl. Res. 6 (2016) 793–799.

[44] V. Kašpárková, P. Humpolíček, J. Stejskal, J. Kopecká, Z. Kuceková, R. Moučka, Conductivity, impurity profile, and cytotoxicity of solvent-extracted polyaniline, Polym. Adv. Technol. 27 (2016) 156–161.

[45] J. Stejskal, M. Hajná, V. Kašpárková, P. Humpolíček, A. Zhigunov, M. Trchová, Purification of a conducting polymer, polyaniline, for biomedical applications, Synth. Met. 195 (2014) 286–293.

[46] N.V. Blinova, J. Stejskal, M. Trchová, J. Prokeš, M. Omastová, Polyaniline and polypyrrole: a comparative study of the preparation, Eur. Polym. J. 43 (2007) 2331–2341.

[47] G. Ćirić-Marjanović, S. Mentus, I. Pašti, N. Gavrilov, J. Krstić, J. Travas-Sejdic, L.T. Strover, J. Kopecká, Z. Morávková, M. Trchová, J. Stejskal, Synthesis, characterization, and electrochemistry of nanotubular polypyrrole and polypyrrole-derived carbon nanotubes, J. Phys. Chem. C 118 (2014) 14770–14784.

[48] K. Crowley, J. Cassidy, In situ resonance Raman spectroelectrochemistry of polypyrrole doped with dodecylbenzenesulfonate, J. Electroanal. Chem. 547 (2003) 75–82.

[49] Y.-C. Liu, Characteristics of vibration modes of polypyrrole on surface-enhanced Raman scattering spectra, J. Electroanal. Chem. 571 (2004) 255–264.

[50] S. Gupta, Hydrogen bubble-assisted syntheses of polypyrrole micro/nanostructures using electrochemistry: structural and physical property characterization, J. Raman Spectrosc. 39 (2008) 1343–1355.

[51] Y. Li, P. Bober, D.H. Apaydin, T. Syrový, N.S. Sariciftci, J. Hromádková, I. Sapurina, M. Trchová, J. Stejskal, Colloids of polypyrrole nanotubes/nanorods: a promising conducting ink, Synth. Met. 221 (2016) 67–74.

[52] J.L. Bredas, J.C. Scott, K. Yakushi, G.B. Street, Polarons and bipolarons in polypyrrole: evolution of the band structure and optical spectrum upon doping, Phys. Rev. B 30 (1984) 1023–1025.

[53] P. Humpolíček, V. Kašpárková, P. Sáha, J. Stejskal, Biocompatibility of polyaniline, Synth. Met. 162 (2012) 722–727.

[54] X. Wang, X. Gu, C. Yuan, S. Chen, P. Zhang, T. Zhang, J. Yao, F. Chen, G. Chen, Evaluation of biocompatibility of polypyrrole in vitro and in vivo, J. Biomed. Mater. Res. Part A 68 (2004) 411–422.

Polymer 174 (2019) 11–17

Contents lists available at ScienceDirect

Polymer

journal homepage: www.elsevier.com/locate/polymer

Cationic dyes as morphology-guiding agents for one-dimensional polypyrrole with improved conductivity

Islam M. Minisy[a,b], Patrycja Bober[a,*], Udit Acharya[a,c], Miroslava Trchová[a], Jiřina Hromádková[a], Jiří Pfleger[a], Jaroslav Stejskal[a]

[a] Institute of Macromolecular Chemistry, Academy of Sciences of the Czech Republic, 162 06 Prague 6, Czech Republic
[b] Faculty of Science, Charles University, 128 43 Prague 2, Czech Republic
[c] Faculty of Mathematics and Physics, Charles University, 182 00 Prague 8, Czech Republic

HIGHLIGHTS

- 1D polypyrrole was prepared in the presence of two cationic dyes.
- Conductivity and morphology of polypyrrole was significantly affected by the dyes.
- Conductivity was enhanced to 35 S cm^{-1} in the presence of safranin.

ARTICLE INFO

Keywords:
Polypyrrole
Safranin
Phenosafranin
Nanofibers
Nanotubes
Conductivity

ABSTRACT

Polypyrrole was prepared in the presence of cationic dyes, safranin and phenosafranin. The safranin supported the one-dimensional growth of polypyrrole, converting globules to nanorods and later also to nanotubes, particularly at higher dye concentrations. In the case of phenosafranin, the produced nanotubes were considerably thicker and were always accompanied by globules. Upon oxidation both dyes are expected to generate insoluble oligomeric templates that serve as loci for the deposition of polypyrrole. The formation of globular morphology takes place when the dye becomes depleted, due to its low concentration for safranin, or because of robust templates produced by phenosafranin. In addition to scanning and transmission electron microscopies, the resultant polypyrroles were characterized by FTIR and Raman spectroscopies, and DC conductivity measurements. The conversion of globular morphology to nanotubes/nanofibers was accompanied by the increase in conductivity from 5 to 35 S cm^{-1}, which was explained by the improved ordering of polypyrrole chains more preferable for charge transport. The series of syntheses at varying oxidant-to-pyrrole mole ratios confirmed the stoichiometric ratio 2.5 to be the best for pyrrole oxidation but a good stability of polypyrrole was demonstrated even at extremely high stoichiometric ratio 15.

1. Introduction

Conducting polymers with tunable morphology and electroactivity can be easily synthesized by oxidative polymerization of corresponding monomers [1]. They can be obtained with conventional globular morphology or as various nanostructures, such as nanorods [2], nanowires [3], nanofibers [4,5] or nanotubes [6–8]. Among them, polypyrrole (PPy) is one of the most promising conducting polymers due to its unique physical and electrochemical properties. Its processability can be improved by the formation of various morphologies [9], composites [10], colloids [11,12] or hydrogels [13]. Different additives in the polymerization medium can affect the morphology and conductivity as well; they could be used as morphology directing agents which work as templates to produce polymers with different nanomorphologies. Basically, two main types of structure-directing agents have been used: soft templates represented by micellar aggregates [14] and hard templates, such as porous membranes [15] or *in-situ*-generated solid dye templates. Anionic dyes, such as methyl orange [6], Acid Red 1 [16], Acid Red B [17], and Acid Blue 25 [4], have been reported as templates guiding one-dimensional growth of polypyrrole. Cationic dyes, such as rhodamine B [18,19] and methylene blue complex with heparin [2], have been applied only exceptionally. It has recently been observed that also another cationic dye, safranin, promotes the formation of one-dimensional PPy [20].

* Corresponding author.
E-mail address: bober@imc.cas.cz (P. Bober).

https://doi.org/10.1016/j.polymer.2019.04.045
Received 7 January 2019; Received in revised form 16 April 2019; Accepted 18 April 2019
Available online 23 April 2019

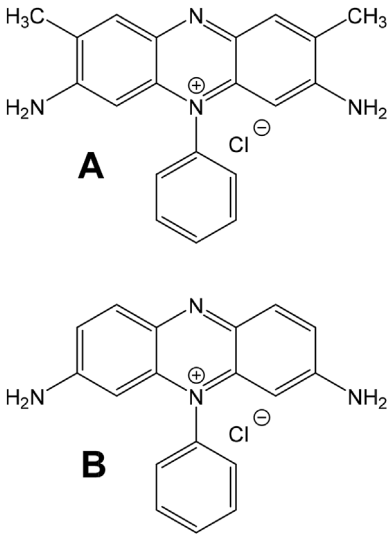

Scheme 1. Chemical formulae of (A) safranin and (B) phenosafranin.

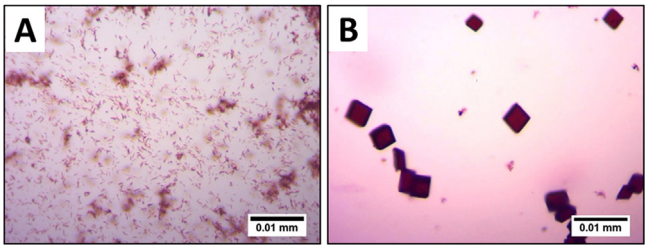

Fig. 1. Optical microscope images of formed templates by mixing (A) 4 mM of safranin and (B) 4 mM of phenosafranin with 0.25 M iron(III) chloride.

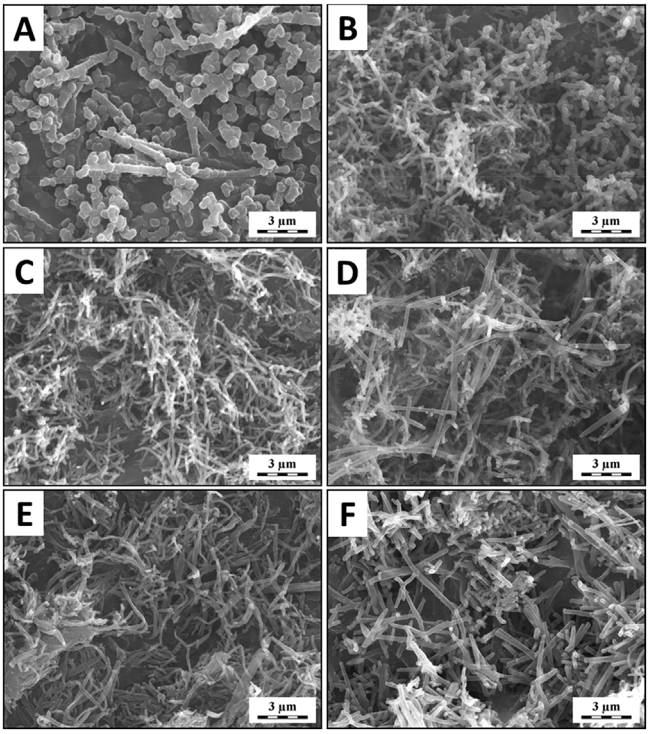

Fig. 2. SEM micrographs of polypyrrole prepared in the presence of safranin with different concentrations: (A) 0.5 mM, (B) 2 mM, (C) 4 mM, (D) 10 mM, (E) 20 mM, and (F) 40 mM.

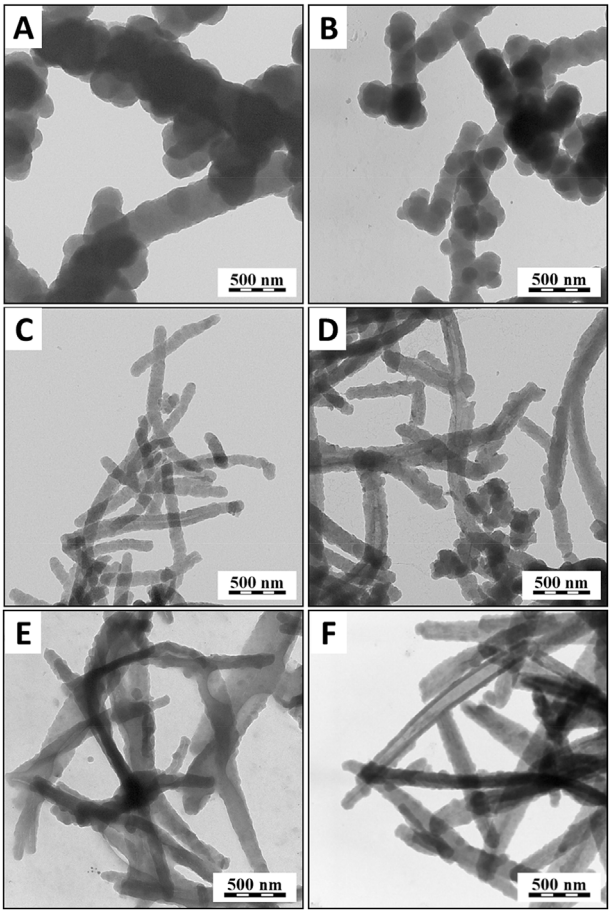

Fig. 3. TEM micrographs of polypyrrole prepared in the presence of safranin with different concentrations: (A) 0.5 mM, (B) 2 mM, (C) 4 mM, (D) 10 mM, (E) 20 mM, and (F) 40 mM.

Among reported PPy morphology modifications, nanotubes have the highest conductivity reaching $\approx 100\ S\ cm^{-1}$ [21]. Moreover, they were found to retain most of their conductivity under the neutral or even alkaline conditions [22] which cannot be achieved in the case of globular PPy.

Various PPy nanostructures have been used in many applications in variety of fields extending from adsorbents [23], chemical sensors [24], biosensors [25], actuators [26], drug delivery systems [27], electrocatalysis [28], supercapacitors [29] to electrode material for batteries [30].

In the present work, PPy nanofibers or nanotubes have been synthesized by the oxidation of pyrrole with iron chloride in the presence of a cationic dye, safranin or chemically similar phenosafranin, (Scheme 1). The influences of the dye chemical structure, dyes concentration, and oxidant-to-monomer mole ratio on morphology and conductivity have been studied to elucidate the role of the dye in the pyrrole polymerization.

2. Experimental section

2.1. Chemicals and reagents

Pyrrole (≥98%), iron(III) chloride hexahydrate, safranin (3,7-diamino-2,8-dimethyl-5-phenylphenazinium chloride; Safranin T, Basic Red 2) and phenosafranine (3,7-diamino-5-phenylphenazinium chloride) were purchased from Sigma-Aldrich. All chemicals were used as received without any further purification.

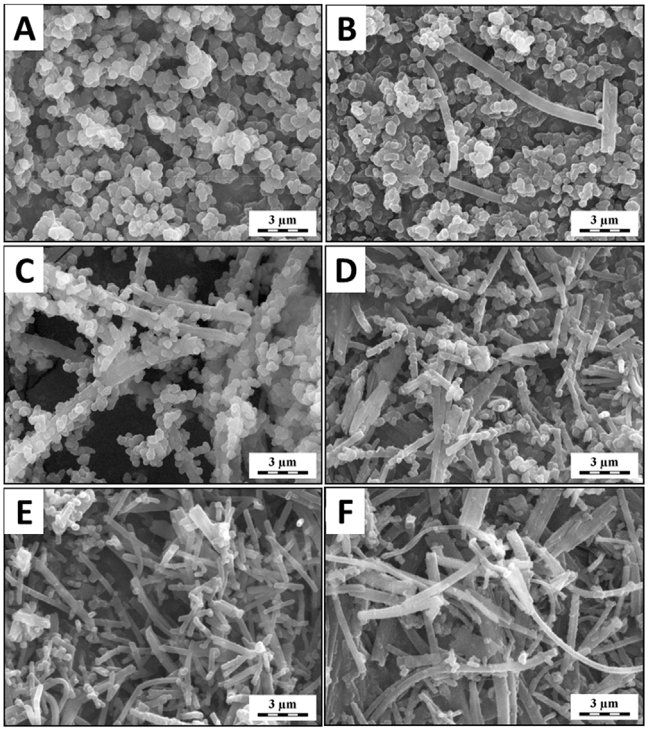

Fig. 4. SEM micrographs of polypyrrole prepared in the presence of different concentrations of phenosafranin: (A) 0.5 mM, (B) 2 mM, (C) 4 mM, (D) 10 mM, (E) 20 mM, and (F) 40 mM.

2.2. Synthesis of PPy in the presence of safranin or phenosafranin

Polypyrrole was prepared by mixing 50 mL of 0.4 M pyrrole (1.34 g of monomer) solution with safranin or phenosafranin (a series of dye concentrations from 0 to 40 mM), then a separately prepared 50 mL aqueous solution of 1 M iron(III) chloride hexahydrate (13.52 g of oxidant) was added. The resulting reaction mixture thus contained 0.2 M pyrrole and 0.5 M iron(III) chloride, i.e. the oxidant/pyrrole mole ratio ([Ox]/[Py]) was 2.5, and a selected concentration of a dye. The polymerization mixtures were stirred for a few seconds and kept for 24 h at room temperature (20 ± 2 °C) without disturbance. The precipitates were collected by vacuum filtration, washed with an excess of 0.2 M hydrochloric acid, followed by ethanol, left to dry in air, and then transferred into desiccators with silica gel until constant weight was achieved.

In order to study the effect of [Ox]/[Py] ratio on the conductivity and morphology of PPy, another series of samples was prepared in the presence of fixed 4 mM safranin and 0.2 M pyrrole concentrations. Iron (III) chloride concentration was varied to obtain [Ox]/[Py] ratios from 1 up to 15.

2.3. Characterization

The morphology of powders was characterized using a VEGATescan scanning electron microscope (SEM) and TECNAI G2 SPIRIT transmission electron microscope (TEM).

PPy pellets with a 13 mm diameter and 1 ± 0.05 mm thickness were compressed with a manual hydraulic press (Trystom H-62) for the conductivity measurements using van der Pauw method. A Keithley 230 Programmable Voltage Source in serial connection with a Keithley 196 System DMM, and a Keithley 181 Nanovoltmeter (Keithley, USA) were used for current and potential drop measurement, respectively. The conductivity value was obtained as an average value from the measurements in two perpendicular directions measured under constant environmental conditions at 23 ± 1 °C and relative humidity

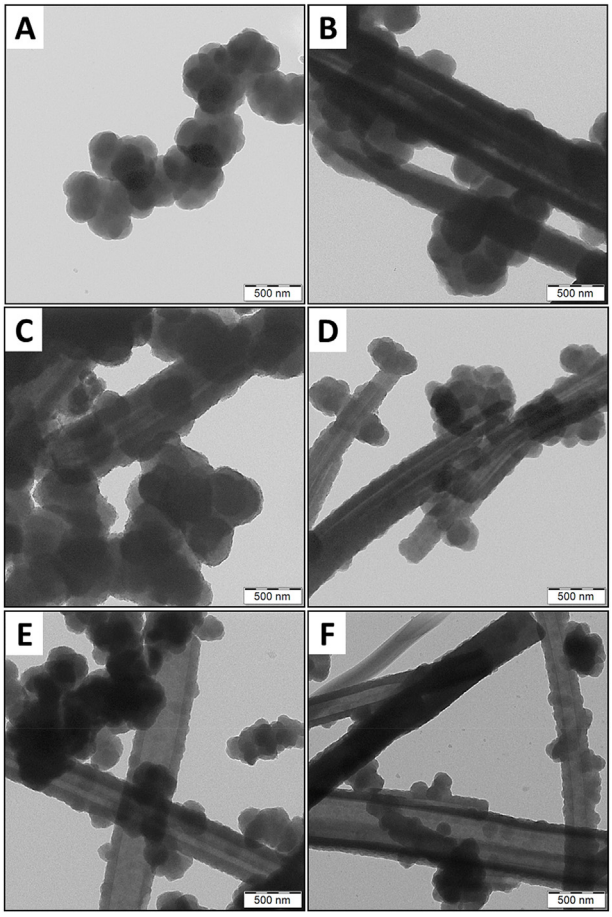

Fig. 5. TEM micrographs of polypyrrole prepared in the presence of different concentrations of phenosafranin: (A) 0.5 mM, (B) 2 mM, (C) 4 mM, (D) 10 mM, (E) 20 mM and (F) 40 mM.

35 ± 5%. The current was kept below 1 mA to avoid heat dissipation in the sample.

Fourier-transform infrared (FTIR) spectra of the powders dispersed in potassium bromide pellets have been registered using a Thermo Nicolet NEXUS 870 FTIR Spectrometer with a DTGS TEC detector in 400–4000 cm^{-1} wavenumber region. Raman spectra were recorded with a Renishaw InVia Reflex Raman microspectrometer. The spectra were obtained using excitation by an argon-ion laser line at 514 nm and analyzed with a spectrograph equipped with a holographic grating 2400 lines mm^{-1}. A research-grade Leica DM LM microscope was used to focus the laser beam. A Peltier-cooled CCD (Charge-coupled device) detector (576 × 384 pixels) registered the dispersed light.

3. Results and discussion

3.1. Template formation

Polypyrrole (Scheme SA) is prepared by the oxidation of pyrrole with a suitable oxidant, such as iron(III) chloride and obtained as a powder with distinct globular morphology. When the oxidation takes place in the presence of suitable organic dyes, one-dimensional morphologies, such as nanotubes or nanofibers, may be obtained [20]. This happens if an organized phase involving a dye is generated in the course of pyrrole oxidation and serves as a template for the surface deposition of PPy [6,31]. The organic dyes have been reported to produce one-dimensional J-aggregates [32] of stacked molecules stabilized by π–π interactions that could serve as templates. Safranin and phenosafranin alone, however, were reported to produce only dimeric

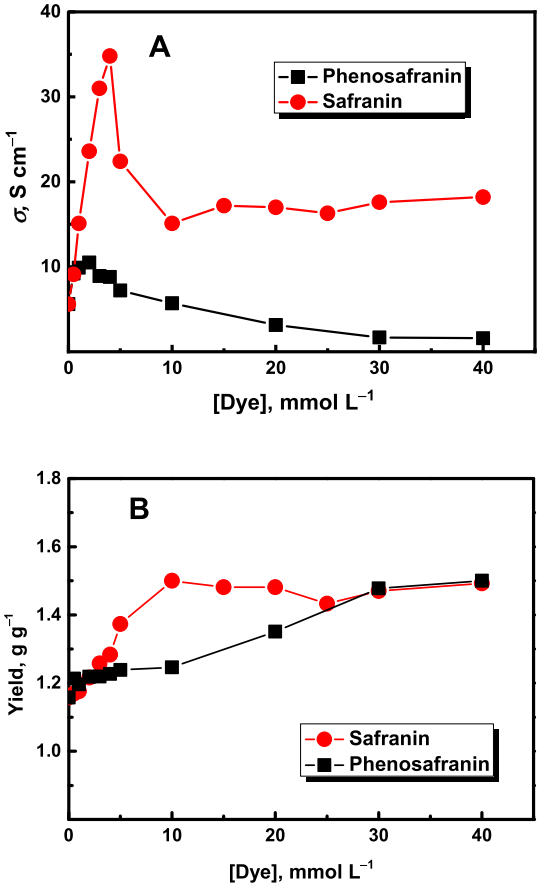

Fig. 6. The dependence of (A) conductivity and (B) yield per gram of pyrrole on molar concentration of safranin or phenosafranin used in the synthesis.

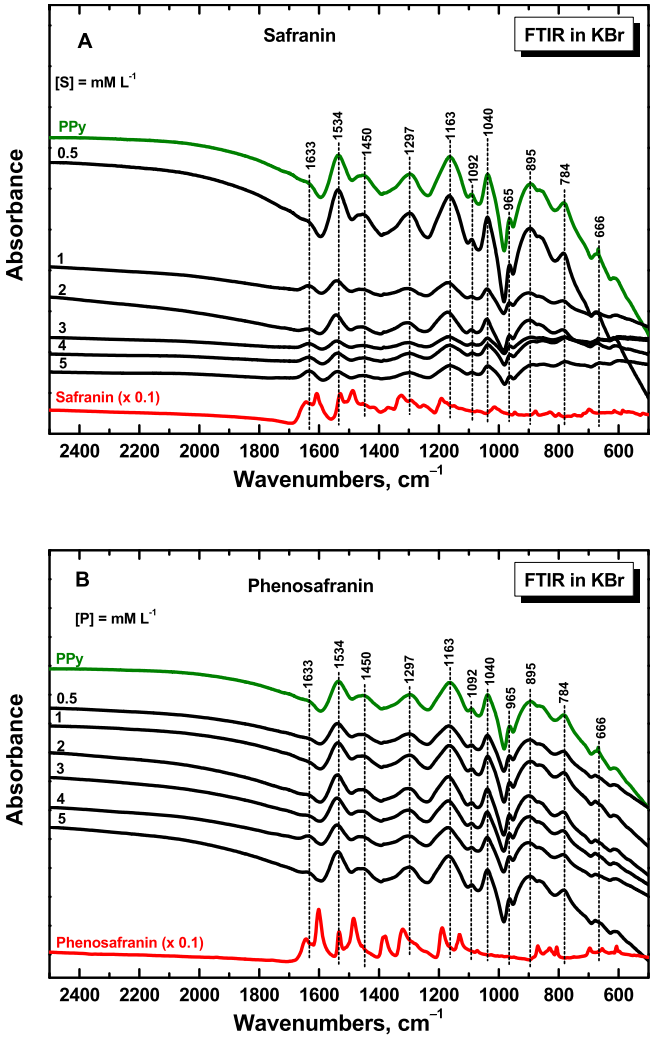

Fig. 7. FTIR spectra of polypyrrole prepared at various concentrations 0.5–5 mM of (A) safranin and (B) phenosafranin.

aggregates [33] that could hardly fulfill such a role.

Turbid solutions have been formed after mixing aqueous solutions of safranin or phenosafranin with iron(III) chloride before addition of pyrrole. Optical microscopic images show the formation of two different types of insoluble solids (Fig. 1). Small fibrillar particles were observed in the case of safranin (Fig. 1A), while phenosafranin produced relatively large microcubes (Fig. 1B). This experiment illustrates the generation of solid phase in the reaction mixture. During the oxidation of pyrrole, such solid objects are prevented to grow to macroscopic dimensions, when pyrrole oligomers adsorb on the surface of emerging solids, now templates, and stimulate following growth of polypyrrole chains [31]. The template formation could be a result of the complex between a dye and iron(III) chloride [34] but the oligomerization of phenosafranin [35] (Scheme SB) or its polymerization [36] yielding insoluble products would be more likely explanation.

To sum up, there are two processes that produce the insoluble solids: (1) the oxidation of pyrrole to polypyrrole (Scheme SA), and (2) the oxidation of phenosafranin or safranin dye to corresponding oligomers (Scheme SB). Depending on the reaction conditions, both reactions proceed simultaneously or in succession as discussed below.

3.2. Effect of dyes concentration on morphology

The conventional PPy obtained with the absence of any dyes has the well-known globular morphology (Fig. S1). The SEM analysis of a series of PPy prepared in the presence of various safranin concentrations shows the significant effect of the safranin, even at very low concentration, on the PPy morphology. At the lowest concentration, 0.5 mM of safranin, the mixture of globules and nanorods is found (Fig. 2A). This might happen if the generation of PPy preceded the formation of a template or if all template dye molecules were depleted in the course of nanorod formation and remaining PPy was therefore produced in globular form. The second explanation is more plausible.

By increasing the safranin concentration nanofibers with different dimensions were obtained (Fig. 2B–F). TEM analysis (Fig. 3) was used to distinguish between fibers and tubes; the results demonstrate the formation of a mixture of nanotubes and nanofibers but no exclusive nanotubes have been observed even at high safranin concentration. At low safranin concentrations (Fig. 3A and B) no tubes cavity was observed while the cavity of the PPy nanotubes increased by increasing the safranin concentration. We can speculate that thicker templates were available for deposition of PPy when the concentration of a dye was higher.

On the other side, SEM micrographs of PPy prepared in the presence of phenosafranin suggest that any fibers have been accompanied with globules (Fig. 4). Moreover, the aspect ratio of the formed fibers is smaller compared to fibers prepared with safranin. By increasing the phenosafranin concentration, the tubular morphology became prominent. TEM analysis (Fig. 5) confirms the formation of nanotubes with rough surfaces and bigger size compared to PPy with safranin. It is worth to mention that the dimensions of the formed nanotubes, about 500 nm in diameter, did not significantly change with the phenosafranin concentration. All these facts indicate that, due to the tendency of phenosafranin to produce larger template compared with safranin (Fig. 1), the phenosafranin dye becomes soon unavailable for the

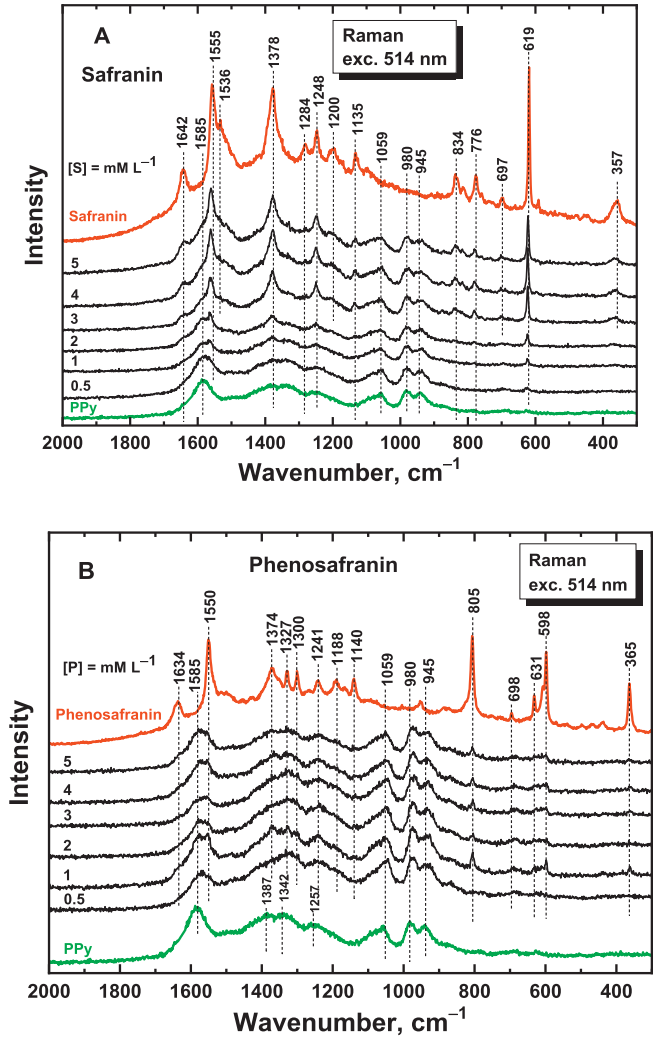

Fig. 8. Raman spectra of polypyrrole prepared in the presence of safranin (A) and phenosafranin (B) at various dye concentrations, 0.5–5 mM.

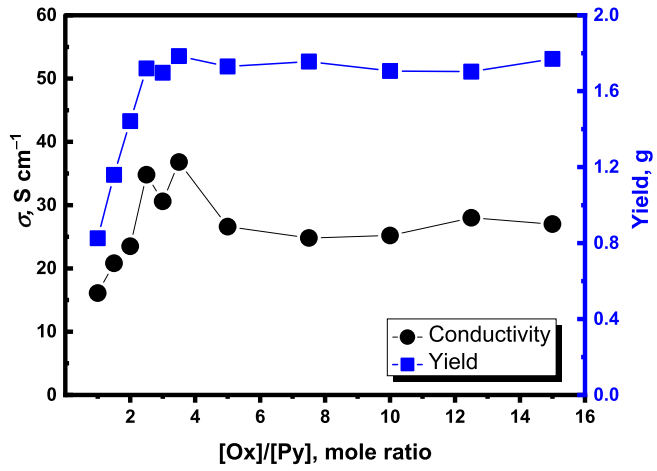

Fig. 9. Dependence of the conductivity and yield of polypyrrole per gram of pyrrole on the iron(III) chloride to pyrrole mole ratio, [Ox]/[Py]. Safranin concentration was 4 mM.

generation of new nanotubes and separate or adhering PPy globules are therefore produced as the polymerization of pyrrole proceeds.

3.3. Conductivity and yield

The DC conductivity of two series of PPy prepared with varied concentrations of safranin or phenosafranin were determined. It is known from the literature that the conductivity of templates composed of oligomeric dyes is low, $\sigma \sim 10^{-9}$ S cm^{-1} [35], and it cannot contribute to the overall conductivity of PPy/dye nanostructured system. PPy prepared in the presence of safranin or phenosafranin has higher conductivity than the conventional globular PPy, $\sigma \sim 5$ S cm^{-1}, prepared in the dye absence. With increasing the safranin concentration, the conductivity increased steadily, reaching a maximum 35 S cm^{-1} at 4 mM dye concentration (Fig. 6A), then the conductivity decreased. The similar trend was found in the case of phenosafranin, where conductivity reached the maximum value 10.5 S cm^{-1} at the concentration 2 mM (Fig. 6B). Compared to our previous results on PPy chains grown at the template surface [37], the increase in the conductivity has been assigned to a better organization of PPy in nanotubular structures compared to the reduced chain-ordering in the globules. Nanotubular structure is also more favorable for the dopant distribution in the bulk of the sample which also leads to the conductivity enhancement. The correlation between conductivity and specific surface areas reported in the literature [38] also points in this direction. By increasing the concentration of dyes and, consequently, the fraction of non-conducting oxidation products [35], the conductivity of composites decreased.

The yield in both cases of dye template used, safranin or phenosafranin, slightly increased with dye concentration (Fig. 6B) as expected. Theoretically 1 g of pyrrole produces 1.3 g of PPy hydrochloride and, as the yield of oxidation product per 1 g of pyrrole is much higher than the theoretical value, the dyes oxidized to insoluble oligomers have to be present as a substantial part of the products. To address this issue, the products have been analyzed with spectroscopic methods.

3.4. FTIR spectroscopy

The infrared spectra of PPy prepared in the presence of various concentrations of safranin (Fig. 7A) and phenosafranin (Fig. 7B) confirm the PPy structure. In the case of safranin the samples prepared with higher dye concentrations were difficult to disperse in potassium bromide pellets. For that reason, infrared absorption spectra were very poorly resolved, and only the bands of stretching and bending vibrations of water molecules at about 3436 cm^{-1} (not shown in Figure) and 1633 cm^{-1} were detected in the spectra. Only low concentrations of dyes from 0.5 mM to 5 mM are presented. For phenosafranin, the samples were better dispersed and the spectra were of good quality. In both cases, we detect the main bands of PPy [20] with maxima at 1534 cm^{-1} (C–C stretching vibrations in the pyrrole ring), at 1450 cm^{-1} (C–N stretching vibrations in the ring), the broad band with maximum at about 1297 cm^{-1} (C–H or C–N in-plane deformation modes), and a local absorption maximum located at 1163 cm^{-1} (breathing vibrations of the pyrrole rings). The band at 1040 cm^{-1} corresponds to the C–H and N–H in-plane deformation vibrations and the peaks at lowest part of the spectrum to the C–H out of plane deformation vibrations of the ring. The peaks typical for safranin or phenosafranin (their spectra are shown in Fig. 7 for comparison) have not been detected in the PPy spectra. This may be due to their low concentrations.

3.5. Raman spectra

The presence of safranin and phenosafranin, however, is well documented by the Raman spectra recorded with a 514 nm excitation wavelength, which is close to the absorbance maximum at 538 nm in UV–visible spectra of these dyes [35] and hence the Raman spectra are

resonantly enhanced (Fig. 8). The spectral features are more pronounced in the case of safranin at 1642, 1555, 1536, 1378, 1284, 1248, 1200, 1135, 834, 776, 697, 619 and 357 cm^{-1}. They are slightly detectable for phenosafranin at 1634, 1550, 1374, 1327, 1300, 1188, 1140, 805, 698, 631, and 365 cm^{-1} at higher dye concentrations. The bands of PPy with maxima at 1585 cm^{-1} (C = C stretching vibrations of PPy backbone), 1387 and 1342 cm^{-1} (bands of ring-stretching vibrations), 1257 cm^{-1} (antisymmetric C–H deformation vibrations), 1059 cm^{-1} (C − H out-of-plane deformation vibrations) and double peak at 980 and 945 cm^{-1} (ring-deformation vibrations of neutral polypyrrole and ring-deformation vibrations in bipolaron units) have also been detected in the spectra. They correspond to the protonated form of PPy [20].

We can conclude from the infrared spectra that PPy was produced in its salt form (Scheme SA), and Raman spectra confirm the presence of dyes in the samples. The spectroscopy, however, is not able to discriminate between the dyes and oligomers produced from these dyes upon oxidation. It is not possible to decide within the present study if the dyes are located inside of the PPy nanostructure or at its surface [38].

3.6. Effect of oxidant/monomer mole ratio

In order to get additional insight into the generation and properties of PPy nanostructures, a series of syntheses with variable oxidant-to-monomer mole ratios, [Ox]/[Py], at fixed 0.2 M pyrrole and 4 mM dye concentrations were carried out. The stoichiometric ratio [Ox]/[Py] = 2.5 was used in experiments discussed in the preceding section. At the ratio reduced to 1, the morphology of PPy was a mixture of fibers and globular particles (Fig. S2). With increasing [Ox]/[Py] ratio up to 3.5, the nanofibers became prominent up to mole ratio equal to 3 (Fig. S2). By further increasing of [Ox]/[Py] mole ratio a mixture of globular and fibrillar morphology with a shape of coral reefs is formed due to the high rate of polymerization at high oxidant concentrations.

The yield as well as the conductivity was found to increase linearly by increasing the oxidant concentration up to [Ox]/[Py] = 2.5 which supplies sufficient amount of oxidant to oxidize all available pyrrole monomers in the reaction mixture. The plateau in the yield is reached at higher ratios (Fig. 9) indicating good stability with respect to over-oxidation. On the other hand, after reaching the maximum value at the concentration [Ox]/[Py] = 3.5 the conductivity decreased to nearly constant 25 S cm^{-1} even at extremely high [Ox]/[Py] ratios. The current use of stoichiometric ratio 2.5 is thus substantiated.

4. Conclusions

Organic cationic dyes, safranin and phenosafranin, have been used in the chemical oxidation of pyrrole for the enhancement of conductivity of polypyrrole and conversion of its globular morphology to nanofibers/nanotubes. Oxidation products of both dyes, i.e. their insoluble oligomers, play a major role as hard templates in directing the morphology of PPy and its aspect ratio. Two processes, (1) the polymerization of pyrrole and (2) the oxidation of dyes to insoluble oligomers proceed simultaneously, and their interplay are responsible for the produced morphology. The highest conductivity of PPy σ = 35 S cm^{-1} and 10 S cm^{-1} were found at 4 mM safranin and 2 mM phenosafranin, respectively, compared with 5 S cm^{-1} of standard globular PPy. Even low concentrations of safranin, 0.5 mM were found to be sufficient to stimulate the growth of one-dimensional morphologies. It is proposed that the PPy chains are better organized in thin one-dimensional structures than in globules and thus nanotubes are more conducting than their globular counterpart. [Ox]/[Py] mole ratio has also significant effect on the conductivity, yield and the morphology of PPy but the currently used value 2.5 affords the products with the best conductivity. The produced PPy can be potentially used in various applications as electrodes materials in supercapacitors, electroactive membranes, etc.

Acknowledgment

The authors wish to thank the Czech Science Foundation (18-04669S) for the financial support.

Appendix A. Supplementary data

Supplementary data to this article can be found online at https://doi.org/10.1016/j.polymer.2019.04.045.

References

[1] A. Malinauskas, Chemical deposition of conducting polymers, Polymer 42 (2001) 3957–3972.
[2] M. Wei, T.Y. Dai, Y. Lu, Controlled fabrication of nanostructured polypyrrole on ion association template: tubes, rods and networks, Synth. Met. 160 (2010) 849–854.
[3] C. Yang, S. Zhang, C. Guan, Polypyrrole nanowires coated with a hollow shell for enhanced electrochemical performance, Mater. Res. Bull. 100 (2018) 116–119.
[4] P. Bober, Y. Li, U. Acharya, Y. Panthi, J. Pfleger, P. Humpolíček, M. Trchová, J. Stejskal, Acid Blue dyes in polypyrrole synthesis: the control of polymer morphology at nanoscale in the promotion of high conductivity and the reduction of cytotoxicity, Synth. Met. 237 (2018) 40–49.
[5] H.D. Tran, K. Shin, W.G. Hong, J.M. D'Arcy, R.W. Kojima, B.H. Weiller, R.B. Kaner, A template-free route to polypyrrole nanofibers, Macromol. Rapid Commun. 28 (2007) 2289–2293.
[6] J. Kopecká, D. Kopecký, M. Vrňata, P. Fitl, J. Stejskal, M. Trchová, P. Bober, Z. Morávková, J. Prokeš, I. Sapurina, Polypyrrole nanotubes: mechanism of formation, RSC Adv. 4 (2014) 1551–1558.
[7] I. Sapurina, Y. Li, E. Alekseeva, P. Bober, M. Trchová, Z. Morávková, J. Stejskal, Polypyrrole nanotubes: the tuning of morphology and conductivity, Polymer 113 (2017) 247–258.
[8] J. Stejskal, I. Sapurina, M. Trchová, E.N. Konyushenko, Oxidation of aniline: polyaniline granules, nanotubes, and oligoaniline microspheres, Macromolecules 41 (2008) 3530–3536.
[9] X.G. Li, A. Li, M.R. Huang, Y. Liao, Y.G. Lu, Efficient and scalable synthesis of pure polypyrrole nanoparticles applicable for advanced nanocomposites and carbon nanoparticles, J. Phys. Chem. C 114 (2010) 19244–19255.
[10] P. Bober, J. Stejskal, I. Šeděnková, M. Trchová, L. Martinková, J. Marek, The deposition of globular polypyrrole and polypyrrole nanotubes on cotton textile, Appl. Surf. Sci. 356 (2015) 737–741.
[11] Y. Li, P. Bober, D.H. Apaydin, T. Syrový, S. Sariciftci, J. Hromádková, I. Sapurina, M. Trchová, J. Stejskal, Colloids of polypyrrole nanotubes/nanorods: a promising conducting ink, Synth. Met. 221 (2016) 67–74.
[12] M. Omastová, P. Bober, Z. Morávková, N. Peřinka, M. Kaplanová, T. Syrový, J. Hromádková, M. Trchová, J. Stejskal, Towards conducting inks: polypyrrole–silver colloids, Electrochim. Acta 122 (2014) 296–302.
[13] S. Ying, W.Q. Zheng, B.R. Li, X. She, H.B. Huang, L. Li, Z.L. Huang, Y.N. Huang, Z.T. Liu, X.H. Yu, Facile fabrication of elastic conducting polypyrrole nanotube aerogels, Synth. Met. 218 (2016) 50–55.
[14] J.S. Jang, H.S. Yoon, Facile fabrication of polypyrrole nanotubes using reverse microemulsion polymerization, Chem. Commun. 6 (2003) 720–721.
[15] M.Q. Xue, F.W. Li, D. Chen, Z.H. Yang, X.W. Wang, J.H. Ji, High-oriented polypyrrole nanotubes for next-generation gas sensor, Adv. Mater. 28 (2016) 8265–8270.
[16] W. Yan, J. Han, Synthesis and formation mechanism study of rectangular-sectioned polypyrrole micro/nanotubules, Polymer 48 (2007) 6782–6790.
[17] J.T. Feng, W. Yan, L.Z. Zhang, Synthesis of polypyrrole micro/nanofibers via a self-assembly process, Microchim. Acta 166 (2009) 261–267.
[18] Y.P. Xue, X.F. Lu, Y. Xu, X.J. Bian, L.R. Kong, C. Wang, Controlled fabrication of polypyrrole capsules and nanotubes in the presence of rhodamine B, Polym. Chem. 1 (2010) 1602–1605.
[19] Y.J. Wang, P. Liu, C. Yang, B. Mu, A.Q. Wang, Improving capacitance performance of attapulgite/polypyrrole composites by introducing rhodamine B, Electrochim, Acta 89 (2013) 422–428.
[20] J. Stejskal, M. Trchová, Conducting polypyrrole nanotubes: a review, Chem. Pap. 72 (2018) 1563–1595.
[21] Y. Li, P. Bober, M. Trchová, J. Stejskal, Polypyrrole prepared in the presence of methyl orange and ethyl orange: nanotubes versus globules in conductivity enhancement, J. Mater. Chem. C 5 (2017) 4236–4245.
[22] J. Stejskal, M. Trchová, P. Bober, Z. Morávková, D. Kopecký, M. Vrňata, J. Prokeš, M. Varga, E. Watzlová, Polypyrrole salts and bases: superior conductivity of nanotubes and their stability towards the loss of conductivity by deprotonation, RSC Adv. 6 (2016) 88382–88391.
[23] B. Boukoussa, A. Hakiki, S. Moulai, K. Chikh, D.E. Kherroub, L. Bouhadjar, D. Guedal, K. Messaoudi, F. Mokhtar, R. Hamacha, Adsorption behaviors of cationic and anionic dyes from aqueous solution on nanocomposite polypyrrole/SBA-15, J. Mater. Sci. 53 (2018) 7372–7386.
[24] A. Karimi, S.W. Husain, M. Hosseini, P.A. Azar, M.R. Ganjali, Rapid, sensitive detection of hydrogen peroxide in milk by enzyme-free electrochemiluminescence

sensor based on a polypyrrole-cerium oxide nanocomposite, Sens. Actuator B 271 (2018) 90–96.
[25] D.M.G. Preethichandra, E.M.I. Mala Ekanayake, M. Onoda, K. Kaneto, Performance enhancement of polypyrrole based nano-biosensors by different enzyme deposition techniques, in: S. Mukhopadhyay, K. Jayasundera, O. Postolache (Eds.), Modern Sensing Technologies. Smart Sensors, Measurement and Instrumentation, vol. 29, Springer, Cham, 2019.
[26] J.R. Hagler, B.N. Peterson, A.R. Murphy, J.M. Leger, Performance of biocompatible silk-polypyrrole actuators under biologically relevant conditions, J. Appl. Polym. Sci. 136 (2019) 46922.
[27] M. Sharma, G.I. Waterhouse, S.W. Loader, S. Garg, D. Svirskis, High surface area polypyrrole scaffolds for tunable drug delivery, Int. J. Pharm. 443 (2013) 163–168.
[28] K. Bouzek, K.M. Mangold, K. Jüttner, Electrocatalytic activity of platinum modified polypyrrole films for the methanol oxidation reaction, J. Appl. Electrochem. 31 (2001) 501–507.
[29] K. Jurewicz, S. Delpeux, V. Bertagna, F. Beguin, E. Frackowiak, Supercapacitors from nanotubes/polypyrrole composites, Chem. Phys. Lett. 347 (2001) 36–40.
[30] H.K. Song, G.T.R. Palmore, Redox-active polypyrrole: toward polymer-based batteries, Adv. Mater. 18 (2006) 1764–1768.
[31] J. Stejskal, Strategies towards the control of one-dimensional polypyrrole nanomorphology and conductivity, Polym. Int. 67 (2018) 1461–1469.
[32] F. Würthner, T.E. Kaiser, C.R. Saha-Möller, J-aggregates: from serendipitous discovery to supramolecular engineering of functional dye materials, Angew. Chem. Int. Ed. 50 (2011) 3376–3410.
[33] R. Pauliukaite, A. Selskiene, A. Malinauskas, C.M.A. Brett, Electrosynthesis and characterisation of poly (safranine T) electroactive polymer films, Thin Solid Films 517 (2009) 5435–5441.
[34] X.M. Yang, Z.X. Zhu, T.Y. Dai, Y. Lu, Facile fabrication of functional polypyrrole nanotubes via a reactive self-degraded template, Macromol. Rapid Commun. 26 (2005) 1736–1740.
[35] G. Ćirić-Marjanović, N.V. Blinova, M. Trchová, J. Stejskal, Chemical oxidative polymerization of safranines, J. Phys. Chem. 111 (2007) 2188–2199.
[36] D. Sarkar, P. Das, A. Girigoswami, N. Chattopadhyay, Spectroscopic characterization of phenazinium dye aggregates in water and acetonitrile media: effect of methyl substitution on the aggregation phenomenon, J. Phys. Chem. A 112 (2008) 9684–9691.
[37] U. Acharaya, P. Bober, M. Trchová, A. Zhigunov, J. Stejskal, J. Pfleger, Synergistic conductivity increase in polypyrrole/molybdenum disulfide composite, Polymer 150 (2018) 130–137.
[38] M. Trchová, J. Stejskal, Resonance Raman spectroscopy of conducting polypyrrole nanotubes: disordered surface versus ordered body, J. Phys. Chem. A 122 (2018) 9298–9306.

Journal of Materials Chemistry C

ROYAL SOCIETY OF CHEMISTRY

PAPER

View Article Online
View Journal | View Issue

Cite this: J. Mater. Chem. C, 2020, 8, 12140

Highly conducting 1-D polypyrrole prepared in the presence of safranin†

Islam M. Minisy, [ab] Udit Acharya,[ac] Libor Kobera, [a] Miroslava Trchová,[ad] Christoph Unterweger, [e] Stefan Breitenbach,[e] Jiří Brus, [a] Jiří Pfleger, [a] Jaroslav Stejskal [a] and Patrycja Bober *[a]

Received 15th June 2020,
Accepted 22nd July 2020

DOI: 10.1039/d0tc02838j

rsc.li/materials-c

A facile preparation of a conducting one-dimensional polypyrrole nanostructure (1-D PPy) was achieved in the presence of safranin dye. The polymerization temperature has a significant effect on the conductivity, specific surface area and morphology of PPy. A decrease in the polymerization temperature leads to a significant increase in the conductivity. The highest conductivity was obtained by frozen polymerization (−24 °C) with a value of 175 ± 4 and 23.7 ± 2.9 S cm^{-1} for 1-D PPy and globular PPy, respectively. The temperature dependence of the conductivity of 1-D PPy prepared at −24 °C revealed a semiconducting behaviour with a 3-D variable range hopping charge transfer mechanism. Raman spectroscopy results suggested that the high conductivity can be attributed to the high protonation level of 1-D PPy. Nuclear magnetic resonance spectroscopy has been used to study the chemical structure of 1-D PPy and the incorporation of safranin into the polymer matrix.

Introduction

Enhancing the electrical conductivity and mechanical properties of conducting polymers is an important prerequisite to improve the performance of soft electronics. Different approaches have been used to increase the conductivity of conducting polymers, such as the synthesis of composites with noble metals,[1,2] graphene,[3] dyes,[4] or doping with an anionic polyelectrolyte such as polystyrene sulfonate.[5] Among the various conducting polymers, polypyrrole (PPy) has attracted attention due to its unique physico-chemical properties and broad spectrum of applications, such as batteries,[6] supercapacitors,[7] chemical sensors,[8] biosensors,[9] conductive textiles,[10,11] antistatic coatings,[12] oxidation–reduction reactions,[13] dye removal,[14] drug delivery systems,[15] ion selective membranes[16,17] and tissue engineering.[18] Polypyrrole can be easily synthesized chemically or electrochemically by the oxidative polymerization of pyrrole.[19] Chemical synthesis allows for a low-cost mass production.

Polypyrrole can be obtained in different forms such as powders,[4] thin films,[20] colloids[21] and cryo- or aerogels,[22,23] and it can exhibit a conductivity of up to 100 S cm^{-1}.[24] Various types of nano-morphologies can be obtained by polymerization processes in which different templates are used as morphology-guiding agents. For example, organic dyes have been used as hard templates to produce PPy nanotubes[24] or nanofibers.[25] Recently, safranin, an organic cationic dye, has been used to obtain one dimensional (1-D) PPy with enhanced conductivity (35 S cm^{-1}) compared to conventional globular PPy (1–5 S cm^{-1}).[26]

The polymerization conditions applied during the preparation can strongly affect the morphology and conductivity of the resulting conducting polymers.[27] Although many reports studied the effect of the polymerization temperature of polyaniline (PANI) in a wide range of temperatures (−50 to +50 °C)[28–32] or that of PPy in the range of 0 to 60 °C,[33,34] to the best of our knowledge, no one has studied the chemical polymerization of pyrrole to PPy nanostructures in frozen medium. Polyaniline was prepared chemically at −24 °C,[31] which leads to an increase in the molecular weight followed by an increase in conductivity, and it even showed metallic character compared to the semiconductor behaviour obtained at room temperature. Reducing the temperature of PANI preparation to −40 °C led to the formation of a higher-molecular-weight product.[24] Stejskal *et al.*[29] reported the influence of the polymerization temperature of PANI in the range of −50 to +50 °C on its molecular weight, crystallinity, and electrical conductivity. They concluded that as the reaction temperature decreases, both the molecular weight of PANI and its crystallinity increase, but the conductivity improved only marginally. Similar to PANI, it was found that

[a] Institute of Macromolecular Chemistry, Academy of Sciences of the Czech Republic, 162 06 Prague 6, Czech Republic. E-mail: bober@imc.cas.cz
[b] Charles University, Faculty of Science, 128 43 Prague 2, Czech Republic
[c] Charles University, Faculty of Mathematics and Physics, 121 16 Prague 2, Czech Republic
[d] University of Chemistry and Technology Prague, 166 28 Prague 6, Czech Republic
[e] Wood K Plus – Kompetenzzentrum Holz GmbH, 4040 Linz, Austria

† Electronic supplementary information (ESI) available. See DOI: 10.1039/d0tc02838j

the conductivity of electrochemically prepared PPy increased with decreasing temperature of the preparation, the highest conductivity being 26.3 S cm^{-1} of PPy prepared at 1 °C compared to 0.04 S cm^{-1} obtained at 60 °C. The conductivity may be enhanced due to the higher doping level, longer conjugated chains and higher charge-carrier hopping frequency.[33]

In spite of the different approaches taken to improve the conductivity of PPy, the challenge remains to develop a low cost and scalable method to get highly conducting PPy. Recently, safranin has been used to enhance the conductivity of PPy prepared at room temperature.[26] In the present paper, we study the effect of polymerization temperature on the conductivity and the morphology of PPy in a wide range of temperatures from −80 to +50 °C. Safranin was used as a morphology-guiding agent to produce 1-D PPy. Various analytical techniques have been used to characterize the PPy prepared in the presence or absence of safranin. The morphology, conductivity and specific surface area of all the samples were examined. In addition, Raman and ssNMR spectroscopy were used to study the molecular structures of PPy in both its protonated and deprotonated forms, respectively.

Experimental

Chemicals and reagents

Pyrrole, iron(III) chloride hexahydrate, safranin (3,7-diamino-2,8-dimethyl-5-phenylphenazinium chloride; Safranin T, Basic Red 2) and ammonia solution (NH_4OH) 25% were obtained from Sigma-Aldrich. All chemicals were used as received.

Synthesis of polypyrrole

Polypyrrole was prepared by the polymerization of pyrrole (0.2 M, 1.34 g) with iron(III) chloride (0.5 M, 13.5 g) as the oxidant in the presence of an organic dye, safranin (4 mM, 0.14 g), or in its absence at various temperatures (from −80 to 50 °C). The total volume of the polymerization mixture was 100 mL. In a water/ethylene glycol bath adjusted to the desired temperature (−24 to 50 °C), 50 mL of a precooled aqueous solution of pyrrole with safranin was mixed with 50 mL of precooled oxidant solution. The mixtures were allowed to polymerize for 24 h at the particular temperatures. For the preparation of PPy at −50 °C, the polymerization mixture was frozen in a solid carbon dioxide/cyclohexanone bath for 30 min before leaving it to polymerize for one week in a freezer adjusted to −50 °C, while a carbon dioxide/ethanol bath was used for the preparation of PPy at −80 °C, and the reaction mixture was kept for 2 weeks in a freezer at −80 °C. Polypyrrole without safranin was prepared in the same manner. The obtained PPy powders were collected after thawing *via* vacuum filtration, rinsed with 0.2 M HCl solution, then with ethanol, and dried in air and in a desiccator over silica gel until constant weights were obtained.

A part of the samples was converted to the PPy base (deprotonated) form by suspension in 1 M or 16 M NH_4OH for 24 h, washed with acetone and left to dry in a desiccator over silica gel until constant weights were obtained.

Characterization

The morphology of PPy powders was characterized by using a MIRA3 TESCAN scanning electron microscope (SEM) and TECNAI G2 SPIRIT transmission electron microscope (TEM).

The DC conductivity was determined by employing the van der Pauw method on compressed pellets having a diameter of 13 mm and thickness of 1.0 ± 0.2 mm prepared under a pressure of 540 MPa using a hydraulic press (Trystom H-62, Trystom, Czech Republic). A Keithley 230 Programmable Voltage Source in serial connection with a Keithley 196 System DMM was used as a current source; the potential difference between the potential probes was measured using a Keithley 181 Nanovoltmeter (Keithley, USA) under constant ambient conditions (23 ± 1 °C and relative humidity 35 ± 5%). The conductivity of each sample was measured at least three times. For studying the temperature dependence of the DC electrical conductivity, the van der Pauw method was used using the same setup as described above, where the samples were mounted in the cryostat (Novocontrol, Germany) and the temperature (in the range of −160 to +160 °C) was controlled using a Novocontrol Quatro 4.0 temperature controller under a gas flow from the liquid nitrogen source. The measurements were taken after at least 30 min of temperature stabilization. Before taking the measurements, the samples were kept in the cryostat in a N_2 atmosphere at 60 °C for 3 h to remove residual humidity. The conductivity values were calculated as the average value of the measurements in two perpendicular directions.

The specific surface area of the samples was determined using physisorption measurements on an automatic volumetric sorption analyser (Autosorb-iQ, Anton Paar QuantaTec Inc.) with nitrogen at 77 K. 40–50 mg of the samples was outgassed for 2 h at 200 °C before the adsorbed gas volume was measured at a relative pressure of 0.1 to 0.4. Using the Brunauer–Emmett–Teller (BET) method, the specific surface areas of the samples were calculated.

Raman spectra were collected on a Renishaw inVia Reflex Raman spectrometer equipped with a near-infrared diode 785 nm laser (holographic grating 1200 lines mm^{-1}) and an argon-ion laser at 514 nm (2400 lines mm^{-1}). A research-grade Leica DM LM microscope with an objective of magnification 50× was used to focus the laser beam on the sample placed on an X–Y motorized sample stage. A Peltier-cooled CCD detector (576 × 384 pixels) registered the dispersed light.

Chemical structural studies on the deprotonated PPy samples were performed using ^{13}C and ^{15}N Magic Angle Spinning Nuclear Magnetic Resonance Spectroscopy (MAS NMR). Solid-state NMR (ssNMR) spectra were recorded under an 11.7 T magnetic field using an AVANCE III HD spectrometer, at Larmor frequencies $\nu(^{13}C)$ = 125.783 MHz and $\nu(^{15}N)$ = 202.478 MHz using 3.2 mm and 4 mm cross-polarization (CP) magic angle spinning (MAS) probes, respectively. The ^{13}C and ^{15}N CP/MAS NMR spectra were recorded at 20 kHz and 5 kHz MAS spinning speeds. The ^{13}C and ^{15}N NMR isotropic chemical shifts were calibrated using α-glycine (^{13}C: 176.03 ppm; carbonyl signal and ^{15}N: 11.59 ppm; amine signal) as the external

standard. The ^{15}N NMR chemical shift of the glycine amine signal is usually referenced to 34.35 ppm;[35] however, different ^{15}N shift values were used in agreement with literature data[32] for easier comparison of experimental results. The ^{13}C CP/MAS NMR spectra were measured with a recycle delay of 2 s. The number of scans was 5–25k at an 800 μs spin lock. The ^{15}N CP/MAS NMR experiment was recorded with a recycle delay of 5 s. The number of scans was 48k at a spin lock of 800 μs. The contact time for the cross-polarization experiment was used according to literature data.[36,37] The SPINAL64 decoupling sequence was applied for suppression of strong dipolar interactions in all cases. Frictional heating of the spinning samples was compensated by active cooling[38] and the dried samples were placed into ZrO_2 rotors. All NMR spectra were processed and fitted using the Top Spin 3.5 pl2 software package.

Results and discussion

Yield

The yield was found to increase linearly upon increasing the polymerization temperature from −80 °C to room temperature (Fig. 1), where the maximum yield was obtained. Upon further increasing the polymerization temperature up to 50 °C, a slight decrease of yield was observed due to the exothermic nature of the PPy polymerization reaction. Generally, the high yield of PPy (more than 100%) is attributed to the presence of chloride counter-ions in the polypyrrole chain (Scheme 1A), the hygroscopic nature of PPy, which contains water molecules, and oxygen uptake during the polymerization.[39,40] On the other hand, 1-D PPy prepared in the presence of safranin has a higher yield than globular PPy due to the incorporation of safranin molecules during the polymerization. The very low yield obtained at −80 °C in both cases, in the presence or absence of safranin, suggests the formation of pyrrole oligomers due to the restriction of long polymer chain formation under these conditions.

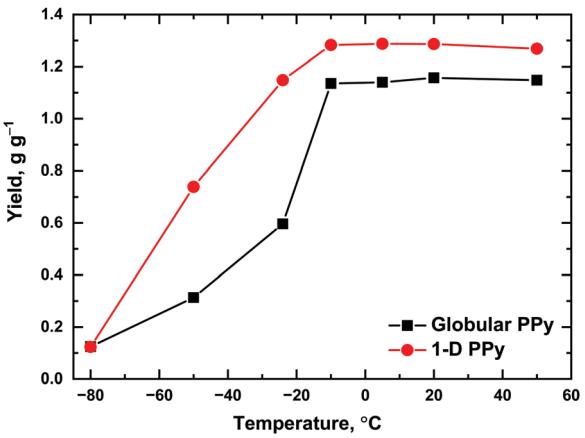

Fig. 1 The influence of the polymerization temperature on the yield of 1-D polypyrrole prepared in the presence of safranin and the globular (dye-free) polypyrrole. The yield was calculated in grams per gram of pyrrole.

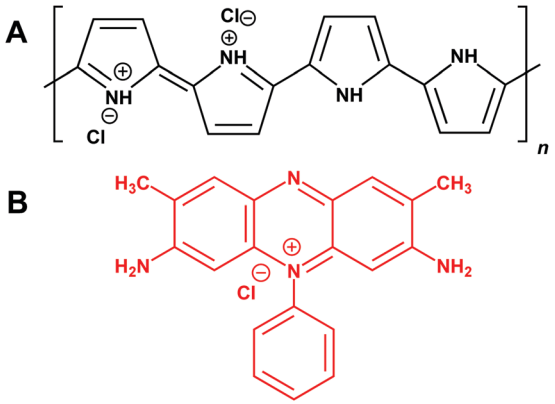

Scheme 1 Chemical formulae of polypyrrole (A) and safranin (B).

Morphology of the obtained polypyrrole

Dye-free PPy has a characteristic globular morphology; however, the addition of safranin into the polymerization medium leads to the formation of a 1-D morphology (Fig. 2). Safranin acts as a morphology-guiding agent. When mixed with iron(III) chloride, it precipitates as fibrillary aggregates (Fig. S1, ESI†), which act as a template for the deposition of PPy.[26] Such formation of fibrillar aggregates could be a consequence of complex formation between safranin and iron(III) chloride, or simply the oligomerization of safranin.[42] The polymerization temperature has a crucial impact on the morphology of PPy (Fig. 1 and Fig. S2, ESI†). The polymerization at 50 °C in the

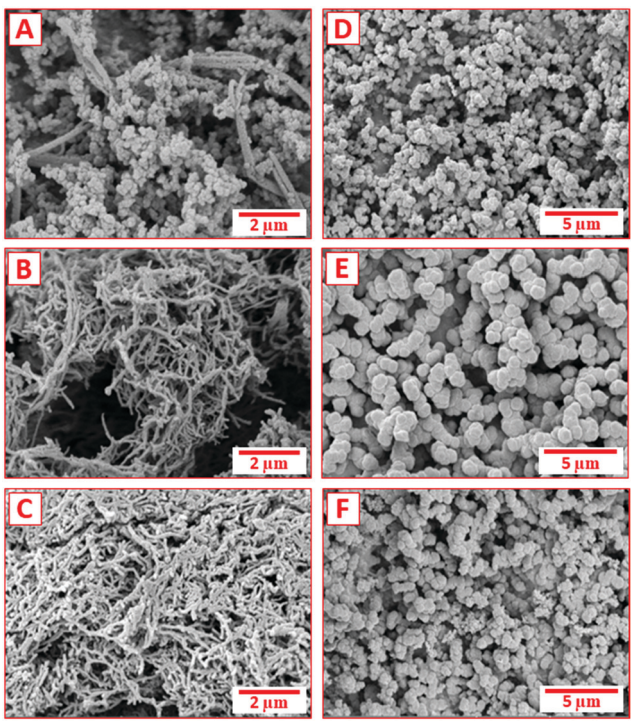

Fig. 2 SEM micrographs of 1-D polypyrrole obtained in the presence of safranin (A–C) and globular polypyrrole formed in its absence (D–F). Polymerization temperature: 50 °C (A and D), 5 °C (B and E) and −24 °C (C and F).

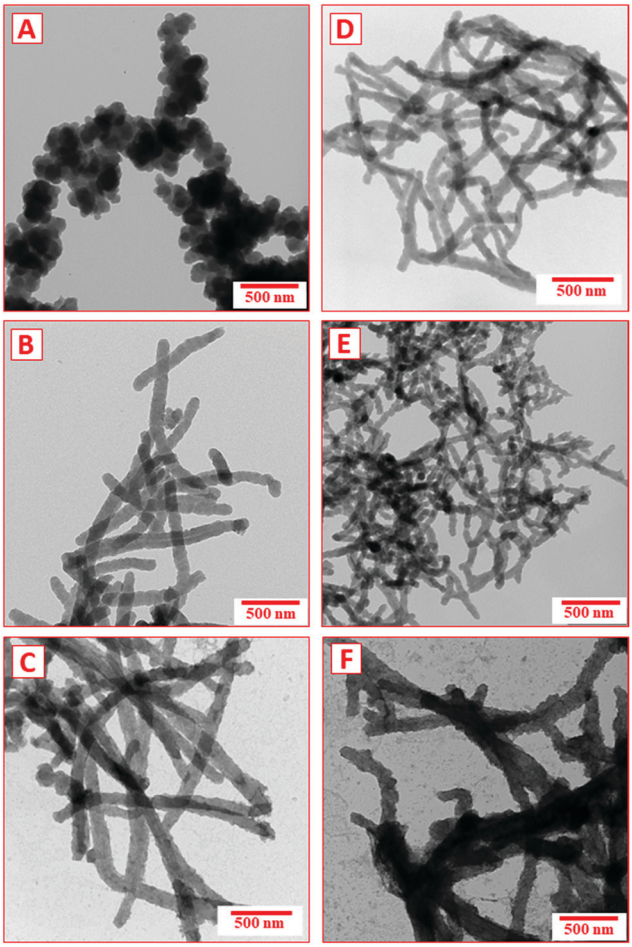

Fig. 3 TEM micrographs of 1-D polypyrrole prepared in the presence of safranin at 50 °C (A), 20 °C (B), 5 °C (C), −10 °C (D), −24 °C (E), and −50 °C (F).

presence of safranin led to the formation of a mixture of globular and fibrillary particles, probably due to the fast nature of the reaction and there being not enough time for the formation of the template facilitating the 1-D morphology. When the same polymerization was performed at room temperature, well-organized PPy nanofibers were formed (Fig. S2, ESI†). It should be noted that the polymerization temperature has a significant effect on the dimensions of the PPy fibres (Fig. 3). Under frozen polymerization conditions, at −24 °C, the produced PPy nanofibers are more interconnected and with smaller dimensions. Further decreasing the polymerization temperature to −50 °C led to the formation of thicker 1-D fibres, while polymerization at −80 °C led to the formation of a mixture of irregular flakes and nanotubes (Fig. S2 and S3, ESI†). On the other hand, all PPy samples prepared in the absence of safranin have a typical globular morphology, with the particle sizes strongly depending on the polymerization temperature. The smallest globular particles were formed at 50 °C and the largest particle size was obtained at −10 °C (Fig. 2).

Specific surface area

Polypyrrole with a 1-D morphology, prepared in the presence of safranin, had a higher specific surface area (S_{BET}) compared to the polymers with a globular morphology, similar to the trend reported in the literature.[4] The results of S_{BET} analysis (Table 1) correlated well with the morphology of the obtained PPy (see SEM and TEM images). A decrease in the polymerization temperature led to an increase in specific surface area of the 1-D PPy from 35.8 ± 6.4 $m^2 g^{-1}$ at 50 °C to 73.6 ± 7.5 $m^2 g^{-1}$ at −80 °C. In the case of the globular PPy, this trend was not observed. The specific surface area, S_{BET}, however, correlates with the particle size: the smaller the particle size, the higher the specific surface area. The highest S_{BET} for globular PPy was 66.8 $m^2 g^{-1}$. The largest surface area being achieved for 1-D PPy (73.6 ± 7.5 $m^2 g^{-1}$), obtained by polymerization at −80 °C, can be explained by the formation of oligomers and nanotubular structures.

Table 1 BET specific surface area, S_{BET}, of globular and 1-D polypyrrole prepared at various temperatures

Polymerization temperature, °C	Globular PPy S_{BET}, $m^2 g^{-1}$	1-D PPy S_{BET}, $m^2 g^{-1}$
50	37.6 ± 9.5	35.8 ± 6.4
20	13.5 ± 0.4	52.4 ± 2.5
5	18.2 ± 8.8	53.2 ± 8.8
−10	8.8 ± 3.5	65.7 ± 3.5
−24	24.4 ± 4.5	72.3 ± 2.5
−50	23.0 ± 4.7	49.6 ± 0.2
−80	66.8 ± 0.0	73.6 ± 7.5

Conductivity

The dependence of the electrical conductivity on the polymerization temperature was markedly different for PPy prepared with and without the safranin template. Whereas both forms of PPy polymerized at high temperature (50 °C) had nearly the same conductivity, with decreasing temperature of preparation, there was a much more pronounced increase of conductivity in 1-D PPy compared to the globular one, which showed only a small increase. When polymerized in a frozen state at −24 °C, both forms of PPy show a maximum but the conductivity value of 1-D PPy, polymerized in the presence of safranin, is almost one order of magnitude higher, reaching 175 S cm^{-1} compared to 23.7 S cm^{-1} found for globular PPy (Fig. 4A). With a further decrease in the polymerization temperature, the conductivity of globular PPy remained almost completely unchanged but the conductivity of 1-D PPy decreased, approaching the conductivity of the globular one when both were prepared at −80 °C. The much higher conductivity of 1-D PPy prepared at −24 °C can be attributed to a higher level of protonation, as evidenced by the Raman spectra (see below) and better rearrangement of the polymer chains resulting in thinner fibres with a higher specific surface area (Table 1). As has been published previously,[4] PPy polymerized in the presence of various dyes is composed of nanofibrils having a well-organized crystalline core surrounded by a disordered shell. The thickness of the core is limited, whereas the thickness of the disordered shell grows with increasing thickness of the fibrils. As can be seen from Fig. 2 and Fig. 3, 1-D PPy prepared at −24 °C, which exhibits the highest conductivity, also has the thinnest fibrils with a higher degree of protonation, as proved by Raman spectroscopy (see below).

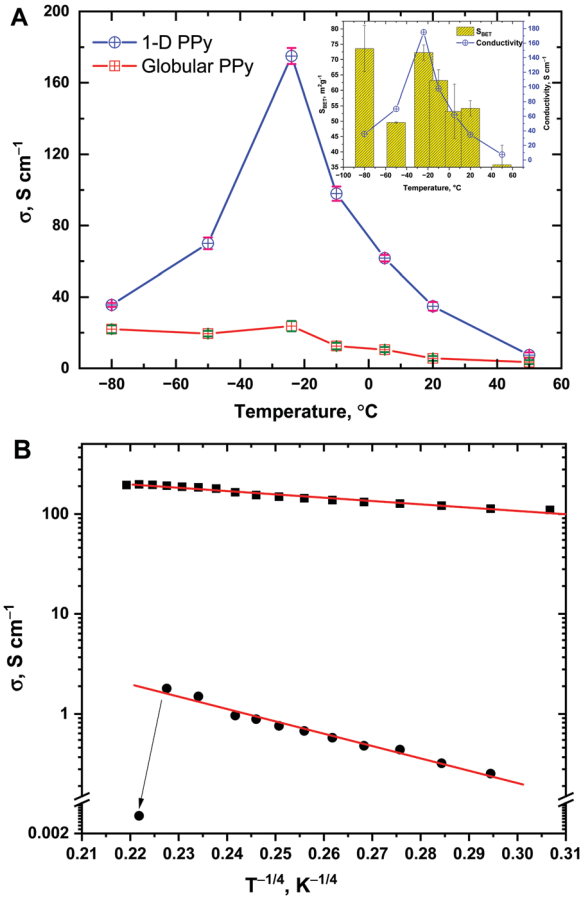

Fig. 4 The influence of the polymerization temperature on the conductivity of the 1-D polypyrrole prepared in the presence of safranin and the globular polypyrrole prepared without safranin; the inset shows the correlation between conductivity and specific surface area of 1-D polypyrrole (A). Temperature dependence of the conductivity of 1-D polypyrrole prepared at −24 °C (full squares) and globular polypyrrole (full circles, data obtained from ref. 41) as a function of $T^{-1/4}$ (B).

In order to get a better insight into the nature of the charge transport in the highly conductive 1-D PPy, the temperature dependence of conductivity was measured and compared to that of previously studied globular PPy[41] (Fig. 4B). The temperature dependence of conductivity of 1-D PPy shows a semiconducting behaviour with increasing conductivity when temperature increases in the range from −160 to 140 °C (113 to 413 K) but with a markedly smaller slope compared to that of the globular PPy. A slight decrease of conductivity was observed above 140 °C, which can be attributed to the deprotonation of the polypyrrole due to the release of HCl (dopant). This only small decrease is in contrast to the large drop in conductivity observed in the globular PPy and serves as another piece of evidence that the dopant is better anchored in the central part of the PPy fibrils. The conduction mechanism of PPy is mostly discussed within the framework of Mott's variable range hopping, using eqn (1).

$$\sigma_T = \sigma_0 \exp\left(-\frac{T_0}{T}\right)^{1/(n+1)} \quad (1)$$

where σ_0 is the preexponential factor resembling the high temperature limit of conductivity, σ_T is conductivity at temperature T, T_0 is the Mott characteristic temperature, indirectly proportional to the density of states at the Fermi level and to the localization length of the wave function of localized charge carriers, and n is the dimension in which the charge transport takes place. The conductivity *vs.* $(1/T)^{1/n}$ plot was fitted for different values of n using the least squares fit procedure. The data were well fitted with $n = 3$, pointing to 3-D variable range hopping. The smaller value of the T_0 obtained from the temperature dependence of the conductivity of 1-D PPy compared to the globular one agrees well with a longer delocalization of carriers and a higher level of doping in the molecularly well-ordered domains. Also, the frequency independent AC conductivity result (Fig. S4, ESI†) confirms that the charge transport proceeds through homogeneous and relatively compact grains.

The conductivity of all deprotonated 1-D PPy (under mild basic conditions, 1 M NH_3 solution) samples showed a decrease of their original conductivity by 5 orders of magnitude. For example, the conductivity of 1-D PPy prepared at −24 °C decreased from 175 to 1.3×10^{-3} S cm^{-1} while that of 1-D PPy prepared at 50 °C decreased from 7.5 to 5.7×10^{-5} S cm^{-1}. However, deprotonation under harsh conditions (16 M NH_3 solutions) led to fully deprotonated PPy samples with the same conductivity for all 1-D PPy samples with the value $\approx 2 \times 10^{-6}$ S cm^{-1}. Re-doping with 0.2 M HCl did not fully recover the original conductivity but it led to an increase by just 2 orders of magnitude for all the PPys prepared at different temperatures. During the deprotonation, the chain ordering is disturbed by the mass loss resulting in volume reduction and consequently shrinking of the chains. This factor limits the full recovery of PPy conductivity.[46]

Raman spectroscopy

Raman spectra provide information on the molecular structure of a polymer and on the charge distribution on the chains. They differ depending on the laser excitation line used.[43] The spectra recorded with a 785 nm excitation wavelength are in resonance with the electronic transitions in PPy. In the spectrum of standard globular PPy (Fig. 5A), which was earlier described in the literature,[43–48] the peak observed at 1595 cm^{-1} corresponds to the backbone stretching mode of C=C bonds and the inter-ring C–C mode in the backbone of the polaron structure. The band with a maximum at 1488 cm^{-1} is assigned to the skeletal, or C–C and C–N stretching vibrations. The shape of two peaks situated at 1380 cm^{-1} (antisymmetrical inter-ring stretching C–N vibration of oxidized, protonated PPy) and 1328 cm^{-1} (inter-ring stretching C–C vibration mode in neutral states of PPy) corresponds to the spectrum of protonated PPy. The band with a maximum at 1242 cm^{-1} is assigned to the antisymmetrical C–H in-plane bending vibrations. The shape of the double peaks observed at 1079 cm^{-1} (C–H in-plane deformation with oxidized, protonated species) and 1052 cm^{-1} (non-protonated PPy units) also corresponds to the spectrum of the protonated state of the prepared samples of PPy. The bands at 976 and 933 cm^{-1} can be assigned to the ring in-plane

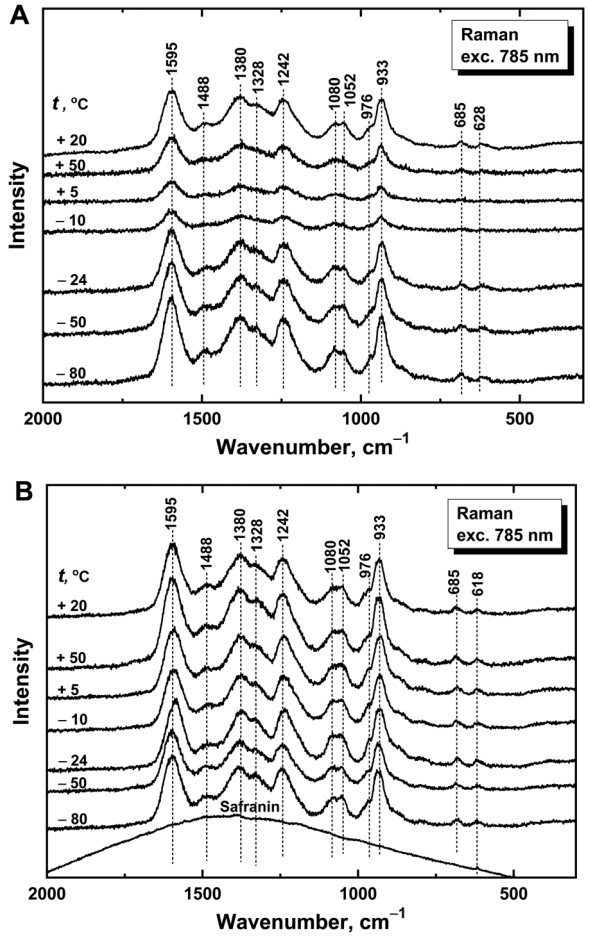

Fig. 5 Raman spectra of polypyrroles prepared without (A) and in the presence (B) of safranin at various temperatures. Laser excitation wavelength: 785 nm.

deformation associated with the polaron and bipolaron states of PPy, respectively.[45]

In the Raman spectra of PPy prepared in the presence of safranin (Fig. 5B), we do not observe any peaks of safranin when using the 785 nm laser excitation line. As this excitation line falls in the polaron absorption band of PPy, it is strongly absorbed and the penetration depth is only several nanometres, *i.e.* close to the surface.[49,50]

The energy of the 514 nm laser excitation line is close to the electronic absorption in safranin dye, which has maximum optical absorption at 538 nm.[42] In the Raman spectra of PPy prepared with safranin, we detect resonantly enhanced peaks of safranin, as marked with asterisks (see Fig. 6). Beside them, we detect peaks at 976 and 933 nm belonging to the polaron and bipolaron states of PPy, respectively. These peaks correspond to PPy in the interior of the nanostructures, which is in contact with the dye, because the energy of the laser excitation 514 nm is not in resonance with the electronic absorption band of PPy and the penetration depth is higher. From the ratio of the bands corresponding to polarons/bipolarons, we can conclude that PPy, which is inside the nanotubes or nanofibers and in contact with the safranin template, is in a more protonated

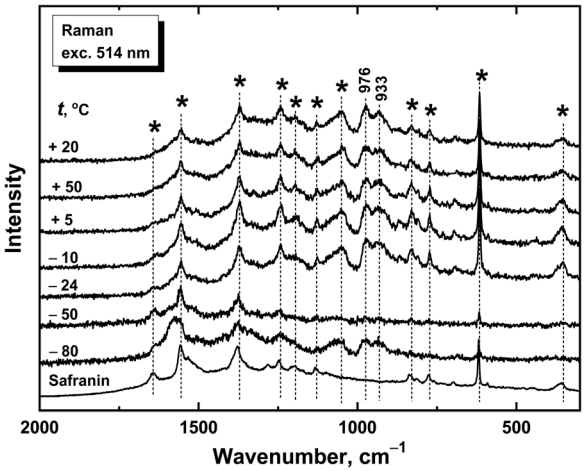

Fig. 6 Raman spectra of 1-D polypyrrole prepared in the presence of safranin at various temperatures. Laser excitation wavelength: 514 nm.

(polaronic) state. This correlates with the higher conductivity of these samples. This effect has been recently described in the literature.[43]

Solid-state NMR analysis

^{13}C and ^{15}N CP/MAS NMR spectroscopy was used for investigation of deprotonated 1-D PPy prepared at different polymerization temperatures. It is problematic to study conducting polymers, especially those possessing high conductivity, using the ssNMR technique, as with increasing conductivity, the signal broadens and loses intensity in addition to a very long time being needed to get an acceptable resolution.[51] The main goal of ssNMR analysis was to study the chemical structure of PPy prepared with safranin at different temperatures and to estimate the quantity of incorporated safranin.

The ^{13}C CP/MAS NMR spectra of deprotonated 1-D PPy (Fig. 7) clearly confirm the formation of the PPy structure with different residual amounts of safranin in all cases. The main signal consists of two peaks at 114 and 129 ppm, which were attributed to the =CH carbon and quaternary carbon of an aromatic form.[37,52] Moreover, the absence of the peak at 143 ppm in all spectra suggests that quinonoid structures are missing. Two relatively broad peaks at 165 ppm and 50 ppm were detected and attributed to the air-oxidized phase.[36] According to the literature, the existence of this phase can be identified using ^{15}N CP/MAS NMR spectroscopy by the presence of a ^{15}N NMR signal at 90 ppm. This signal, however, was not found in the present ^{15}N CP/MAS NMR spectrum, although only one sample (polypyrrole prepared at 5 °C, see Fig. S5, ESI†) was measured due to the long experimental time (72 h). Furthermore, the ^{15}N CP/MAS NMR spectrum was collected for the sample at natural isotopic abundance, in contrast to the spectrum referred to in the literature. Thus, an air-oxidized phase still has to be considered. However, a plausible alternative to the signal assignment reported by Korusu[53] for the resonances at 165 ppm and 50 ppm in the ^{13}C CP/MAS NMR spectra can also be made, namely that the signals belong

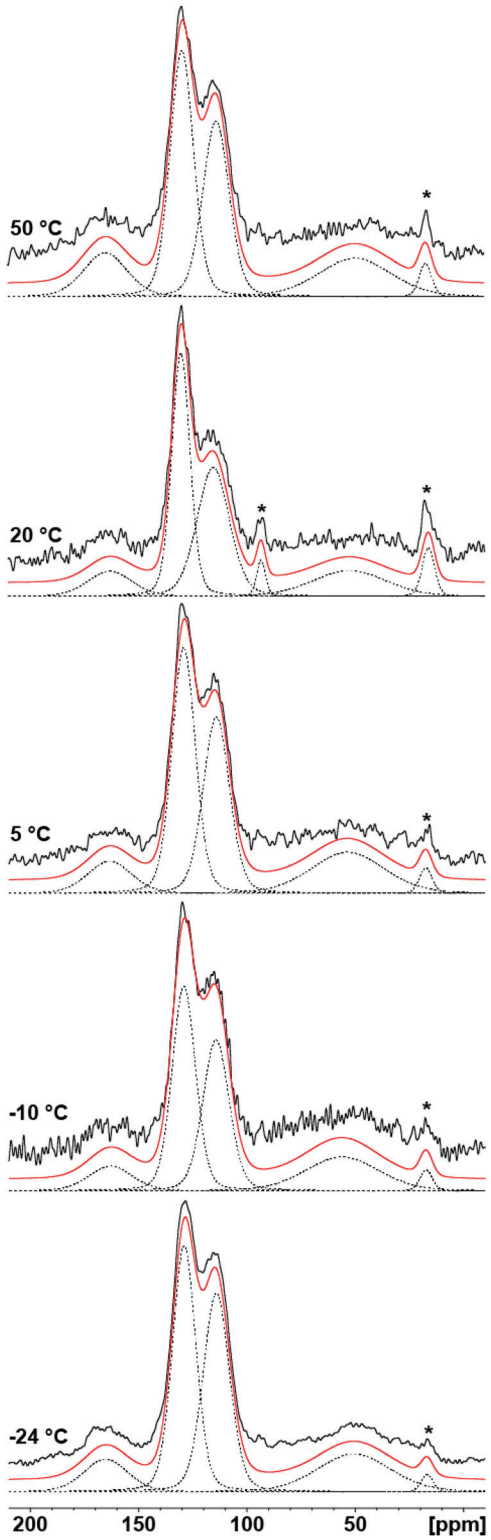

Fig. 7 Experimental ^{13}C CP/MAS NMR spectra (black solid line), simulations of the individual carbon atoms (dashed lines) and their sum (red solid line) of deprotonated 1-D polypyrrole prepared at various temperatures. The star symbol denotes resonance(s) corresponding to safranin.

to the disordered –N=**C**< and –NH-**CH**– groups[54] formed during pyrrole polymerization in the presence of safranin.

Table 2 The content of safranin (mol%) determined from the deconvolution of ^{13}C CP/MAS NMR spectra for the samples prepared at various temperatures. I_{CH}(polypyrrole) = 1

Polymerization temperature, °C	I_{CH_3}(safranin)	Safranin, mol% $(I_{CH3} \times 100)/(I_{CH3} + I_{CH})$
50	0.09	8.3
20	0.15	13.0
5	0.07	6.5
−10	0.07	6.5
−24	0.04	3.9

Furthermore, the right shoulder of the resonance at 165 ppm can be attributed to the NH_2–**C**< groups from safranin. The presence of safranin in the prepared systems is clearly confirmed by a sharp peak at 17 ppm (Fig. S6, ESI†). Additional information (mol% of safranin can be roughly estimated) was extracted from the deconvolution of the ^{13}C CP/MAS NMR spectra, from the ratio of integral areas of the methyl peak of safranin (17 ppm) to the CH carbon of PPy (114 ppm), since these peaks are basically unaffected. The resulting compositions in mol% are listed in Table 2, from which an increasing amount of safranin present in PPy with increasing temperature is evident. The results obtained from the NMR data indicate that with increasing polymerization temperature, the amount of safranin present in PPy increases. This finding also suggests that a higher amount of safranin can be associated with a reduced conductivity of PPy due to increasing the concentration of dyes and, consequently, the fraction of the non-conducting component in the 1-D PPy.[26]

Conclusions

Polypyrrole with a 1-D morphology was easily prepared by the addition of safranin into the polymerization medium. Polypyrrole prepared without the addition of safranin had, in contrast, a globular form. The dimensions of the PPy fibres in 1-D PPy or of the globules in PPy prepared without safranin, as well as conductivity and specific area of the as-prepared products were influenced by the polymerization temperature. Frozen polymerization (at −24 °C) resulted in polymers with the highest conductivity, reaching 175 S cm^{-1} and 23.7 S cm^{-1} for 1-D PPy and globular PPy, respectively. The high-conducting PPy samples possessed thinner fibres, a high specific surface area and a high level of protonation, as evidenced by TEM, BET measurements, and Raman spectroscopy. Raman spectroscopy and ssNMR analysis demonstrated the incorporation of safranin into the PPy fibres, which, in turn, facilitated a higher level of protonation. The mol% of safranin incorporated in deprotonated PPy was found to decrease upon decreasing the polymerization temperature.

Conflicts of interest

There are no conflicts to declare.

Acknowledgements

The authors wish to thank the Czech Science Foundation (18-04669S) for the financial support. Part of this work was carried out within the project BioCarb-K, co-financed by the European Regional Development Fund (EFRE) and the province of Upper Austria through the programme IWB 2014-2020.

Notes and references

1 L. V. Oliveira and F. F. Camilo, *Synth. Met.*, 2019, **247**, 219.
2 P. Bober, M. Trchová, J. Prokeš, M. Varga and J. Stejskal, *Electrochim. Acta*, 2011, **56**, 3580.
3 A. Liu, C. Li, H. Bai and G. Shi, *J. Phys. Chem. C*, 2010, **114**, 22783.
4 J. Stejskal and M. Trchová, *Chem. Pap.*, 2018, **72**, 1563.
5 T. M. Wu, H. L. Chang and Y. W. Lin, *Polym. Int.*, 2009, **58**, 1065.
6 J. Wang, J. Chen, K. Konstantinov, L. Zhao, S. H. Ng, G. X. Wang, Z. P. Guo and H. K. Liu, *Electrochim. Acta*, 2006, **51**, 4634.
7 L. Z. Fan and J. Maier, *Electrochem. Commun.*, 2006, **8**, 937.
8 G. Lisak, M. Wagner, C. Kvarnström, J. Bobacka, A. Ivaska and A. Lewenstam, *Electroanalysis*, 2010, **22**, 2794.
9 J. Wang and M. Musameh, *Anal. Chim. Acta*, 2005, **539**, 209.
10 M. Barakzehi, M. Montazer, F. Sharif, T. Norby and A. Chatzitakis, *Electrochim. Acta*, 2019, **305**, 187.
11 P. Bober, J. Stejskal, I. Šeděnková, M. Trchová, L. Martinková and J. Marek, *Appl. Surf. Sci.*, 2015, **356**, 737.
12 Ö. Yavuz, M. K. Ram, M. Aldissi, P. Poddar and H. Srikanth, *Synth. Met.*, 2005, **151**, 211.
13 I. M. Minisy, N. Gavrilov, U. Acharya, Z. Morávková, C. Unterweger, M. Mičušík, S. K. Filippov, J. Kredatusová, I. A. Pašti, S. Breitenbach and G. irić-Marjanović, *J. Colloid Interface Sci.*, 2019, **551**, 184.
14 M. M. Ayad, W. A. Amer, S. Zaghlol, I. M. Minisy, P. Bober and J. Stejskal, *Chem. Pap.*, 2018, **72**, 1605.
15 M. Sharma, G. I. Waterhouse, S. W. Loader, S. Garg and D. Svirskis, *Int. J. Pharm.*, 2013, **443**, 163.
16 M. Akieh-Pirkanniemi, G. Lisak, J. Arroyo, J. Bobacka and A. Ivaska, *J. Membr. Sci.*, 2016, **511**, 76.
17 J. Arroyo, M. Akieh-Pirkanniemi, G. Lisak, R. M. Latonen and J. Bobacka, *J. Membr. Sci.*, 2019, **581**, 50–57.
18 M. Talikowska, X. Fu and G. Lisak, *Biosens. Bioelectron.*, 2019, **135**, 50–63.
19 S. Demoustier-Champagne, J. Duchet and R. Legras, *Synth. Met.*, 1999, **101**, 20.
20 J. Kim, D. Sohn, Y. Sung and E. R. Kim, *Synth. Met.*, 2003, **132**, 309.
21 M. Omastová, P. Bober, Z. Morávková, N. Peřinka, M. Kaplanová, T. Syrový, J. Hromádková, M. Trchová and J. Stejskal, *Electrochim. Acta*, 2014, **122**, 296.
22 P. Bober, Z. Capáková, U. Acharya, B. A. Zasońska, P. Humpolíček, J. Hodan, J. Hromádková and J. Stejskal, *Synth. Met.*, 2019, **252**, 122.
23 H. An, Y. Wang, X. Wang, L. Zheng, X. Wang, L. Yi, L. Bai and X. Zhang, *J. Power Sources*, 2010, **195**, 6964.
24 Y. Li, P. Bober, M. Trchová and J. Stejskal, *J. Mater. Chem. C*, 2017, **5**, 4236.
25 P. Bober, Y. Li, U. Acharya, Y. Panthi, J. Pfleger, P. Humpolíček, M. Trchová and J. Stejskal, *Synth. Met.*, 2018, **237**, 40.
26 I. M. Minisy, P. Bober, U. Acharya, M. Trchová, J. Hromádková, J. Pfleger and J. Stejskal, *Polymer*, 2019, **174**, 11.
27 H. Kang and K. E. Geckeler, *Polymer*, 2000, **41**, 6931.
28 P. N. Adams and A. P. Monkman, *Synth. Met.*, 1997, **87**, 165.
29 J. Stejskal, A. Riede, D. Hlavatá, J. Prokeš, M. Helmstedt and P. Holler, *Synth. Met.*, 1998, **96**, 55.
30 M. Gholamian and A. Q. Contractor, *J. Electroanal. Chem. Interfacial Electrochem.*, 1988, **252**, 291.
31 P. Bober, J. Stejskal, M. Trchová and J. Prokeš, *J. Solid State Electrochem.*, 2011, **15**, 2361.
32 M. Blaha, M. Varga, J. Prokeš, A. Zhigunov and J. Vohlídal, *Eur. Polym. J.*, 2013, **49**, 3904.
33 A. Kassim, Z. B. Basar and H. E. Mahmud, *J. Chem. Sci.*, 2002, **114**, 155.
34 W. Liang, J. Lei and C. R. Martin, *Synth. Met.*, 1992, **52**, 227.
35 P. Bertani, J. Raya and B. Bechinger, *Solid State Nucl. Magn. Reson.*, 2014, **61**, 15.
36 H. Kurosu, M. Kikuchi and I. Ando, *J. Polym. Sci., Part B: Polym. Phys.*, 1995, **33**, 769.
37 M. Forsyth and V. T. Truong, *Polymer*, 1995, **36**, 725.
38 J. Brus, *Solid State Nucl. Magn. Reson.*, 2000, **16**, 151.
39 M. Salmon, K. K. Kanazawa, A. F. Diaz and M. Krounbi, *J. Polym. Sci., Polym. Lett. Ed.*, 1982, **20**, 187.
40 E. Jakab, E. Mészáros and M. Omastová, *J. Therm. Anal. Calorim.*, 2007, **88**, 515.
41 U. Acharya, B. Bober, M. Trchova, A. Zhigunov, J. Stejskal and J. Pfleger, *Polymer*, 2018, **150**, 130.
42 G. Ćirić-Marjanović, N. V. Blinova, M. Trchová and J. Stejskal, *J. Phys. Chem. B*, 2007, **111**, 2188.
43 M. Trchová and J. Stejskal, *J. Phys. Chem. A*, 2018, **122**, 9298.
44 Y. Furukawa, S. Tazawa, Y. Fuji and A. Harada, *Synth. Met.*, 1988, **24**, 329.
45 F. Chen, G. Q. Shi, M. X. Fu and L. G. Qu, *Synth. Met.*, 2003, **132**, 125.
46 S. Gupta, *J. Raman Spectrosc.*, 2008, **39**, 1343.
47 J. Stejskal, M. Trchová, Z. Morávková, P. Bober, D. Kopecký, J. Kopecká, E. Watzlová, M. Varga and J. Prokeš, *RSC Adv.*, 2016, **6**, 88382.
48 Ishpal and A. Kaur, *J. Nanopart. Res.*, 2013, **15**, 1637.
49 G. Gouadec and P. Colomban, *Cryst. Growth Charact. Mater.*, 2007, **39**, 1.
50 P. Colomban, S. Folch and A. Gruger, *Macromolecules*, 1999, **32**, 3080.
51 A. Mahun, S. Abbrent, P. Bober, J. Brus and L. Kobera, *Synth. Met.*, 2020, **259**, 116250.
52 M. Forsyth, V. T. Truong and M. E. Smith, *Polymer*, 1994, **35**, 1593.
53 H. Kurosu, M. Kikuchi and I. Ando, *J. Polym. Sci., Part B: Polym. Phys.*, 1995, **33**, 769.
54 E. Pretsch, P. Buehlmann, C. Affolter, E. Pretsch, P. Bhuhlmann and C. Affolter, *Structure determination of organic compounds*, Springer-Verlag, Berlin, 2000, p. 108.

polymers

MDPI

Article

Iron (II) Metallo-Supramolecular Polymers Based on Thieno[3,2-*b*]thiophene for Electrochromic Applications

Andrei Chernyshev [1,†], Udit Acharya [2,3,†], Jiří Pfleger [2], Olga Trhlíková [2], Jiří Zedník [1] and Jiří Vohlídal [1,*]

[1] Faculty of Science, Department of Physical and Macromolecular Chemistry, Charles University, Hlavova 2030, 128 40 Prague 2, Czech Republic; andrei.chernyshev@natur.cuni.cz (A.C.); zednik@natur.cuni.cz (J.Z.)
[2] Institute of Macromolecular Chemistry, Czech Academy of Sciences, Heyrovského nám. 2, 162 06 Prague 6, Czech Republic; acharya@imc.cas.cz (U.A.); pfleger@imc.cas.cz (J.P.); trhlikova@imc.cas.cz (O.T.)
[3] Faculty of Mathematics and Physics, Charles University, 121 16 Prague 2, Czech Republic
* Correspondence: vohlidal@natur.cuni.cz
† Both co-authors contributed equally to this work.

Abstract: Four new bis(*tpy*) unimers with different linkers between the thieno[3,2-*b*]thiophene-2,5-diyl central unit and terpyridine-4′-yl (*tpy*) end-groups: no linker (**Tt**), ethynediyl (**TtE**), 1,4-phenylene (**TtPh**) and 2,2′-bithophene-5,5′-diyl (**TtB**) are prepared, characterized, and assembled with Fe^{2+} ions to metallo-supramolecular polymers (Fe-MSPs). The Fe-MSP films prepared by spin-casting on Indium Tin Oxide (ITO) glass are characterized by atomic force microscope (AFM) microscopy, cyclic voltammetry, and UV/vis spectroscopy and studied for their electrochromism and effect of the unimer structure on their electrochromic performance. Of the studied MSPs, **Fe-Tt** shows the highest optical contrast as well as coloration efficiency (CE = 641 cm^2 C^{-1}) and the fastest optical response. This makes it an excellent candidate for possible use in electrochromic devices.

Keywords: electrochromism; field responsive polymer; metallo-supramolecular polymer; self-assembly; terpyridine; unimer; gel electrolyte

Citation: Chernyshev, A.; Acharya, U.; Pfleger, J.; Trhlíková, O.; Zedník, J.; Vohlídal, J. Iron (II) Metallo-Supramolecular Polymers Based on Thieno[3,2-*b*]thiophene for Electrochromic Applications. *Polymers* **2021**, *13*, 362. https://doi.org/10.3390/polym13030362

Academic Editor: Tzi-yi Wu
Received: 31 December 2020
Accepted: 20 January 2021
Published: 23 January 2021

1. Introduction

Electrochromism is an electro-optic effect consisting of a reversible change in the material color or transparency in response to or a change in the applied electric field. Electrochromic (EC) materials are used in optical displays, smart windows, optical switching devices, camouflage objects, and in the thermal management of spacecrafts or in architecture [1,2]. In the last years, electrochromic devices are also gaining application in the field of flexible technologies such as robotics, flexible electronics, smart textiles, etc. [3]. Materials of various types, such as transition metal oxides [4,5], polyoxometalates [5], coordination compounds [5,6], conjugated polymers [2,7–10], and also some metallo-supramolecular polymers (MSPs) [7,11–13] are known to show this phenomenon.

A macromolecule of an MSP is composed of small or oligomeric molecules with chelate end-groups, referred to as unimers [11], which are reversibly linked into chains by coordination of the end-groups to metal ions (so-called ion couplers) [12–14]. Of particular interest are MSPs with reversible coordination linkages, which thus exhibit constitutional dynamics. They are polymeric in the solid-state but dissociated to oligomeric fragments in solutions and/or at elevated temperature, which gives them processing benefits.

The color and properties of MSP are tuned through the structure of the unimer and the selection of ionic couplers [13,14]. Conjugated MSPs containing ions that can be reversibly switched between different oxidation states are attractive as EC materials. They mostly operate on the basis of light absorption. MSPs assembled from bis(*tpy*) unimers (*tpy* stands for 2,2′:6′,2″-terpyridin-4′-yl end-group) and iron ions are known as high-contrast EC materials of this type. They change color by switching between oxidation state Fe(II) with intense absorption centered at ca 550 to 630 nm related to the Metal to

Ligand Charge Transfer (MLCT), and Fe(III) without the MLCT band [13–17]. MSPs with cobalt(II) [14,18,19] and ruthenium(II) [14,18,20] ions show weaker EC effect. Another type of electrochromism exhibit the MSP composed of asymmetric bis(*tpy*) unimer and Fe^{2+} and Eu^{3+} ions in alternating arrangement [21,22]. The Eu^{3+} ions emit luminescence when iron ions are oxidized to Fe(III) state in which the MLCT is absent, while the luminescence is quenched if iron ions are switched to the state Fe(II) and the intense MLCT occurs.

MSPs derived from α,ω-bis(*tpy*) unimers with short oligophenylene [19] or oligothiophene [15,16] central units represent a significant portion of already reported electrochromic MSPs. Those derived from unimers with oligothiophene central units have been the subject of our studies [23–26] that we later on extended to include phosphole [27] and thieno[3,2-*b*]thiophene [28] central units. These new unimers and their MSPs exhibited redshifted absorption (narrower energy bandgap) and increased fluorescence quantum yield compared to the counterparts with central units composed exclusively of thiophene-2,5-diyl units. The effect of phosphole unit was attributed to the decreased aromaticity of phosphole ring while the effect of thieno[3,2-*b*]thiophene unit to its rigid coplanar structure allowing better conjugation compared to the thiophene rings linked by a single bond [29]. In this study, we present new MSPs derived from bis(tpy) unimers with thieno[3,2-*b*]thiophene central unit and various linkers (none, ethynediyl, 1,4-phenylene, and 2,2′-bithophene-5,5′-diyl), in particular the effect of the linker on the optical and redox properties of corresponding Fe-MSPs with the emphasis on electrochromism.

2. Materials and Methods

2.1. Materials

Tetrakis(triphenylphosphane)palladium(0), triphenylphosphane, palladium(II) acetate, 2,5-bis(trimethylstannyl)thieno[3,2-*b*]thiophene, 2,2′-bithiophene-5-boronic acid pinacol ester, iron(II) perchlorate hydrate, copper(I) iodide, propylene carbonate (all Merck, KGAA, Darmstadt, Germany), tetrabutylammonium hexafluorophosphate (≥99.0%, NBu_4PF_6) lithium perchlorate (both Fluka, VWR International, Stribrna Skalice. Czech Republic), poly(methyl methacrylate) (≥99%), *N*-bromosuccinimide (NBS) (98%), tetrahydrofurane (≥99.9%THF) (all Sigma Aldrich, Prague, Czech Republic), ethynyltrimethylsilane, thieno[3,2-*b*]thiophene (both ABCR, Karlsruhe, Germany), 1,1,1,3,3,3-hexafluoropropan-2-ol (HFP) (Fluorochem, Hadfield, Derbyshire, UK), piperidine (Acros Organics, Thermo-Fisher, Prague, Czech Republic), 4′-bromo-2,2′:6′,2″-terpyridine, 4′-(4-bromophenyl)-2,2′:6′,2″-terpyridine (both TCI, Tokyo, Japan), N,N-dimethylformamide and toluene (both of the HPLC grade, VWR International, Stribrna Skalice. Czech Republic), potassium carbonate (Lach-Ner, Neratovice, Czech Republic), acetonitrile (ACN) (Uvasol, Germany, VWR International, Stribrna Skalice, Czech Republic) and Indium Tin Oxide (ITO) (20 Ω/square, Ossila Ltd., Sheffield, UK) were used as received.

2.2. Methods

NMR spectra were recorded on a Bruker Avance III 600 MHz instrument in 1,1,2,2-tetrachloroethane-d_2 (TCE-d_2) at 110 °C, referenced to the solvent signals (6.0 ppm for ^1H and 73.8 ppm for ^{13}C) and deciphered using the first-order analysis. UV/vis spectra were recorded on a Shimadzu UV-2401PC instrument (Shimadzu, Prague, Czech Republic) at room temperature using quartz cuvettes of a 0.4 cm optical path. IR spectra were recorded on a Thermo Nicolet 7600 FTIR spectrometer equipped with a Spectra Tech InspectIR Plus microscopic accessory (Thermo-Fisher, Prague, Czech Republic) using KBr-diluted samples and the diffuse reflectance technique (DRIFT). Atomic absorption spectra (AAS) of ACN solutions of $Fe(ClO_4)_2$ hydrate were measured on a Perkin Elmer AAS spectrometer (model 3110) (Rodgau, Germany) using a hollow cathode lamp emitting a spectrum specific to Fe and a commercial standard (Analytika spol. s.r.o., Prague, Czech Republic) for external calibration.

MALDI-TOF mass spectra were acquired using an UltrafleXtreme (Bruker Daltonics, Bremen, Germany) in the positive ion reflectron mode (sum of 25,000 shots with a DPSS

Nd: YAG laser (355 nm, 2000 Hz) and external calibration for molecular weight assignment. About 1 mg of ground sample was deposited on the ground-steel target plate, pressed with a spatula, overlaid by 1 µL matrix solution of trans-2-[3-(4-*tert*-butylphenyl)-2-methyl-2-propenylidene]malonitrile (≥98.0%, Sigma–Aldrich, Prague, Czech Republic) in THF (10 mg mL^{-1}) and dried at ambient atmosphere.

The topography of Fe^{2+}-MSP films deposited by spin coating on indium tin oxide coated glass substrates was studied in the air using a Nanoscope IIIa (Veeco Instruments New York, NY, USA)) atomic force microscope (AFM) operating in the tapping mode (OTESPA-R3, Bruker silicon tips with spring constant of k = 26 N/m and resonance frequency of 300 kHz). The scans of 2 × 2 µm were acquired with scan rates of 0.7 Hz. The NanoScope Analysis software was used to process raw images and to estimate the root mean squared roughness. AFM was used to measure the thickness and surface roughness of spin-cast films.

Spectro-electrochemical and kinetic studies were performed using UV-Vis-near-infrared (NIR) Lambda 950 spectrometer (Perkin Elmer, Beaconsfield, UK) in combination with Bio-logic potentiostat/galvanostat VSP300. Three-electrode setup was used: spin-cast Fe-MSPs on fluorine doped ITO glass as working electrode, and a platinum wire and Ag/Ag^+ electrodes were used as counter and pseudo-reference electrodes. The measurements were performed in an ACN solution of NBu_4PF_6 (0.1 M) in a quartz cuvette (1 cm) at room temperature. Potentials versus the Ag/Ag^+ pseudo-reference electrode are reported.

2.3. Synthesis of Unimers

Prepared unimers are depicted in Scheme 1 including numbering related to the NMR assignment.

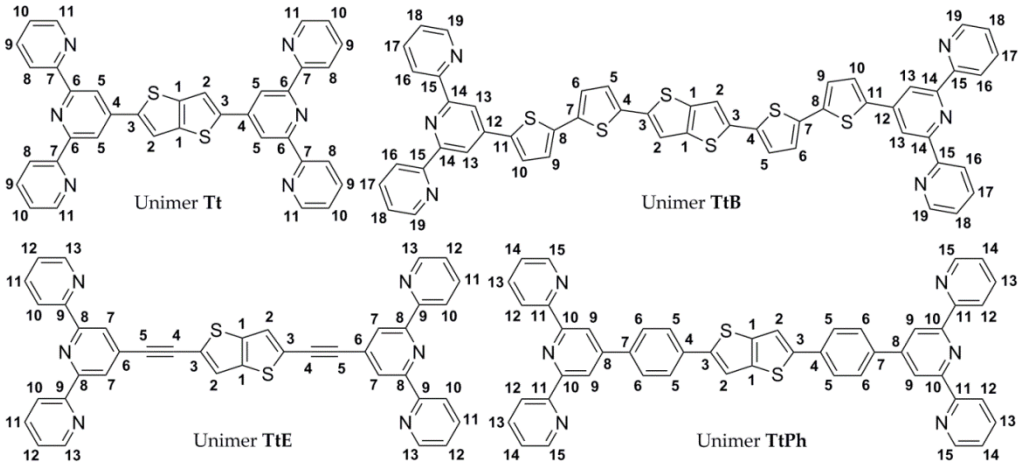

Scheme 1. Prepared unimers including a numbering for NMR assignment.

General Procedure for the Stille Coupling Reactions

A measured amount (2 equivalents, eq) of a given bromo-derivative was added to a solution of 2,5-bis(trimethylstannyl)thieno[3,2-*b*]thiophene (1 eq) in DMF (7 mL) and the resulting solution was bubbled with argon for 15 min. Then $Pd(PPh_3)_4$ (0.1 eq) was added under argon stream and the mixture heated and kept under stirring at 110 °C overnight. After that the reaction mixture was cooled in a freezer and the obtained sediment was filtered, washed with distilled water (3 × 25 mL), *n*-hexane (3 × 25 mL), toluene (3 × 25 mL) and finally dried for a few days to obtain the desired product as a colored powder in the isolated yield of 72 to 82%.

Tt—*2,5-bis(2,2′:6′,2″-terpyridine-4′-yl)thieno[3,2-b]thiophene*

Green powder (211 mg, 82%).
IR (DRIFT): see Figure S1 in ESI.

^{1}H NMR (600 MHz, TCE-d_2, 110 °C) δ 8.84–8.79 (m, 8H, H^5+H^8), 8.68 (d, J = 7.9 Hz, 4H, H^{11}), 8.03 (s, 2H, H^2), 7.92 (td, J_1 = 7.7 Hz, J_2 = 1.7 Hz, 4H, H^9), 7.42–7.38 (m, 4H, H^{10}) (see Figure S2 in Electronic Supporting Information, ESI).

^{13}C NMR (151 MHz, TCE-d_2, 110 °C) δ 156.4 (4C, C^6), 156.0 (4C, C^7), 149.1 (4C, C^{11}), 144.9 (2C, C^1), 143.3 (2C, C^3), 140.7 (2C, C^4), 136.4 (4C, C^9), 123.6 (4C, C^{10}), 121.1 (4C, C^8), 118.1 (2C, C^2), 117.2 (4C, C^5) (see Figure S3 in ESI).

MALDI-TOF MS found m/z: 603.17; theory for $C_{36}H_{22}N_6S_2$ $[M + H]^+$: 603.13.

TtPh—*2,5-bis{4-(2,2′:6′,2″-terpyridine-4′-yl)-phenyl}thieno[3,2-b]thiophene*

Orange powder (185 mg, 76%).

IR (DRIFT: see Figure S1 in ESI.

^{1}H NMR (600 MHz, TCE-d_2, 110 °C) δ 8.84 (s, 4H, H^9), 8.80 (d, J = 3.9 Hz, 4H, H^{12}), 8.71 (d, J = 7.9 Hz, 4H, H^{15}), 8.01 (d, J = 8.2 Hz, 4H, H^5), 7.92 (td, J_1 = 7.7 Hz, J_2 = 1.6 Hz, 4H, H^{13}), 7.86 (d, J = 8.2 Hz, 4H, H^6), 7.65 (s, 2H, H^2), 7.41–7.38 (m, 4H, H^{14}) (see Figure S4, ESI).

^{13}C NMR (151 MHz, TCE-d_2, 110 °C) δ 156.3 (4C, C^{10}), 156.2 (4C, C^{11}), 149.2 (2C, C^8), 149.0 (4C, C^{15}), 145.5 (2C, C^3), 139.9 (2C, C^1), 138.0 (2C, C^7), 136.4 (4C, C^{13}), 135.3 (2C, C^4), 127.8 (4C, C^6), 126.2 (4C, C^5), 123.4 (4C, C^{14}), 121.1 (4C, C^9), 118.6 (4C, C^{12}), 116.0 (2C, C^2) (see Figure S5, ESI).

MALDI-TOF MS found m/z: 755.20; theory for $C_{48}H_{30}N_6S_2$ $[M + H]^+$: 755.20.

TtB—*2,5-bis{5-(2,2′:6′,2″-terpyridine-4′-yl)-2,2′-bithiophen-5′-yl}thieno[3,2-b]thiophene*

Dark-red powder (116 mg, 72%).

IR (DRIFT): see Figure S1 in ESI.

^{1}H NMR (600 MHz, TCE-d_2, 110 °C) δ 8.81 (ddd, J_1 = 4.7 Hz, J_2 = 1.6 Hz, J_3 = 0.8 Hz, 4H, H^{16}), 8.75 (s, 4H, H^{13}), 8.68 (d, J = 7.9 Hz, 4H, H^{19}), 8.02 (s, 2H, H^2), 7.93 (td, J_1 = 7.7 Hz, J_2 = 1.7 Hz, 4H, H^{17}), 7.75 (d, J = 3.8 Hz, 2H, H^{10}), 7.42-7.40 (m, 4H, H^{18}), 7.33 (d, J = 3.8 Hz, 2H, H^9), 7.29 (d, J = 3.8 Hz, 2H, H^5), 7.25 (d, J = 3.8 Hz, 2H, H^6) (see Figure S6 in ESI).

^{13}C NMR (151 MHz, TCE-d_2, 110 °C) δ 156.2 (4C, C^{14}), 156.0 (4C, C^{15}), 148.9 (4C, C^{19}), 142.8 (2C, C^1), 141.0 (2C, C^{12}), 139.0 (2C, C^3), 138.7 (2C, C^{11}), 138.4 (2C, C^7), 137.0 (2C, C^8), 136.5 (4C, C^{17}), 136.4 (2C, C^4), 126.6 (2C, C^2), 125.0 (2C, C^9), 124.8 (2C, C^6), 124.8 (2C, C^5), 123.6 (4C, C^{18}), 121.2 (4C, C^{16}), 117.0 (4C, C^{13}), 115.9 (2C, C^{10}) (see Figure S7 in ESI).

MALDI-TOF MS found m/z: 931.05; theory for $C_{52}H_{30}N_6S_6$ $[M + H]^+$: 931.09.

TtE—*2,5-bis{1-(2,2′:6′,2″-terpyridine-4′-yl)-ethyn-2-yl}thieno[3,2-b]thiophene*

Red powder (198 mg, 38%).

TtE was prepared using Sonogashira coupling. 4′-Bromo-2,2′:6′,2″-terpyridine (497 mg, 1.59 mmol) was added to a solution of 2,5-bis(ethynyl)thieno[3,2-*b*]thiophene (150 mg, 0.79 mmol) in piperidine (10 mL), the obtained solution was bubbled with argon for 10 min and $Pd(PPh_3)_4$ (92.0 mg, 0.079 mmol) and CuI (15.0 mg, 0.079 mmol) were added. Then the reaction mixture was again bubbled with argon for 10 min, heated, and kept at 100 °C overnight. After that the reaction mixture was cooled in a freezer, the obtained sediment was filtered, washed with distilled water (3 × 25 mL), *n*-hexane (3 × 25 mL), toluene (3 × 25 mL) and finally dried for a few days to obtain the desired product as a red powder in the isolated yield of 198 mg (38%).

IR (DRIFT): see Figure S1 in ESI.

^{1}H NMR (600 MHz, TCE-d_2, 110 °C) δ 8.79 (d, J = 4.0 Hz, 4H, H^{10}), 8.67–8.63 (m, 8H, H^7+H^{13}), 7.92 (td, J_1 = 7.7 Hz, J_2 = 1.7 Hz, 4H, H^{11}), 7.58 (s, 2H, H^2), 7.40 (ddd, J_1 = 7.4 Hz, J_2 = 4.7 Hz, J_3 = 1.0 Hz, 4H, H^{12}) (see Figure S8 in ESI).

^{13}C NMR (151 MHz, TCE-d_2, 110 °C) δ 155.7 (4C, C^8), 155.6 (4C, C^9), 149.1 (4C, C^{13}), 140.1 (2C, C^1), 136.6 (4C, C^{11}), 132.3 (2C, C^6), 126.3 (2C, C^3), 125.0 (2C, C^2), 123.7 (4C, C^7), 122.4 (4C, C^{12}), 121.1 (4C, C^{10}), 94.0 (2C, C^5), 87.1 (2C, C^4) (see Figure S9 in ESI).

MALDI-TOF MS found m/z: 651.17; theory for $C_{40}H_{22}N_6S_2$ $[M + H]^+$: 651.13.

3. Results and Discussion

3.1. Synthesis of Unimers

Synthetic pathways to prepared unimers are depicted in Scheme 2. Unimers **Tt, TtPh,** and **TtB** were prepared from commercially available 2,5-bis(trimethylstannyl)-thieno[3,2-*b*]thiophene by using Stille coupling. Commercially available bromo derivatives were used for the syntheses of Tt and TtPh unimers while the bromo derivative necessary for preparing **TtB** unimer [4′-(5-bromo-2,2′-bithiophen-5′-yl)-2,2′:6′,2″-terpyridine] was prepared according to the procedure described earlier [24]. Unimer **TtE** was prepared using the Sonogashira coupling approach. The necessary precursor: 2,5-bis(ethynyl)thieno[3,2-*b*]thiophene was prepared according to the procedure described in [30] and used immeditely after preparation, or stored in a freezer so that it does not decompose after spontaneous deprotection (which is the reason for the lower yield of unimer TtE).

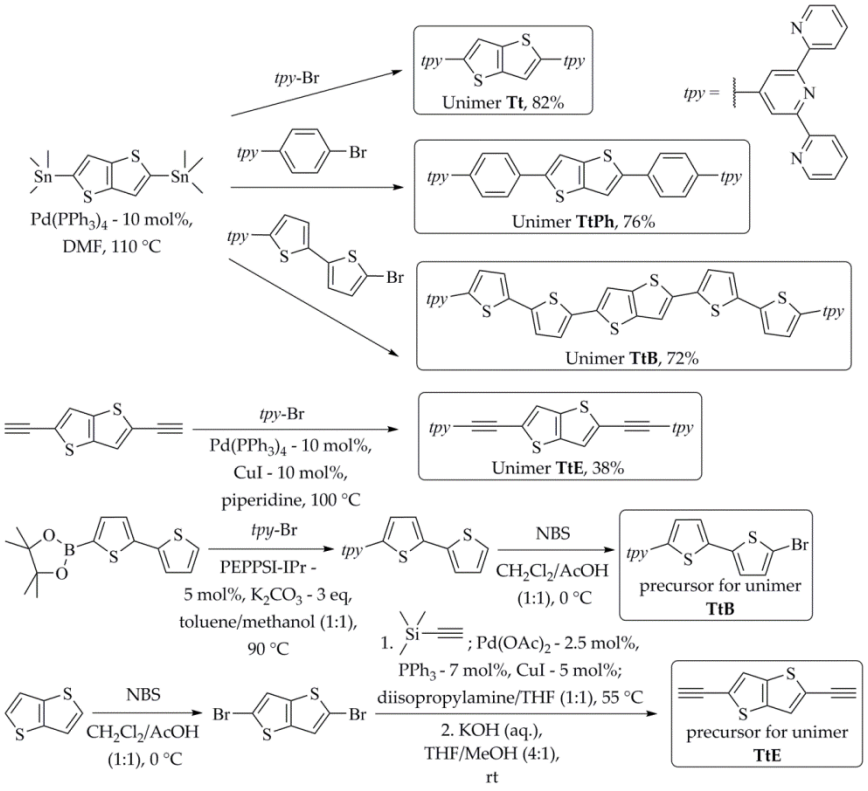

Scheme 2. Synthesis of unimers and their precursors.

The prepared unimers have been obtained as powdered solids of low solubility in common organic solvents, which made their isolation easy. Their insolubility can be attributed to π-stacking of unsubstituted aromatic subunits. 1,1,1,3,3,3-Hexafluoropropan-2-ol (HFP) and its mixtures with acetonitrile (ACN) were found as good solvents of unimers, as well as related MSPs at room temperature, which might be due to acidity of HFP [31] providing effective reversible interactions with nitrogen atoms of *tpy* groups. As indicated in the Experimental section, unimers have been characterized by the MALDI-TOF MS, IR, ^{1}H and ^{13}C NMR (Figures S1–S9 in ESI), and UV/vis spectroscopies.

3.2. Self-Assembly of Fe-MSPs from Unimers and Fe^{2+} Ions in HFP/ACN Solutions

Thermodynamically driven assembly of Fe-MSPs (Scheme 3) in HFP/ACN mixed solvent (4/1 by vol.) was monitored by UV/vis spectroscopy at room temperature using the following procedure.

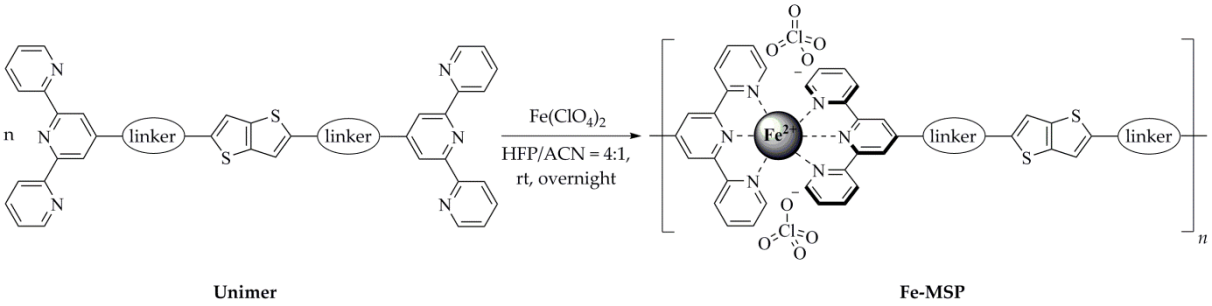

Scheme 3. Self-assembly of Fe^{2+}-MSPs (metallo-supramolecular polymers) from unimers and Fe^{2+} ions.

A series of 13 solutions of practically the same unimer concentration (2×10^{-5} M) and the Fe^{2+} ions-to-unimer mole ratio $r = [Fe^{2+}]/[U]$ increasing stepwise from 0 to 3 was prepared for each unimer by mixing 2 mL of the unimer stock solution (2×10^{-5} M) in the HFP/ACN mixed solvent with a calculated volume (from 2 to 60 µL) of an $Fe(ClO_4)_2$ solution in ACN (2×10^{-3} M). Dilution caused by the added $Fe(ClO_4)_2$ solution was up to 3%, which can be considered negligible. Since $Fe(ClO_4)_2$ hydrate is hygroscopic and therefore contains an undefined amount of water, the exact concentration of Fe^{2+} in its stock ACN solution was determined by atomic absorption spectrometry (AAS). Preparation of the unimer stock solutions was finalized by ultrasonication, immersing a flask with the solution into an ultrasound bath for 5 min. The prepared solutions were allowed to equilibrate for at least half a day before their spectra were measured.

The UV/vis spectra of prepared solutions of different mole ratios r (i.e., of different compositions) are shown in Figure 1 together with photos of vials filled with the respective solutions. Changes in color are visible by the naked eye and they clearly show the great effect of linkers connecting chelate groups to the central unit on the optical spectrum of particular MSPs (see also Figure S10). The observed red color of **Fe-TtPh** is quite atypical because the $Fe^{2+}(tpy)_2$ complexes with an MLCT band are usually blue or green [12,32]. The UV/vis spectrum indicates that the red color stems from the relatively high intensity of the bands contributed with electronic transitions in *tpy* end-groups (around 280 nm) and in the linkers and central unit unimeric units (ranging from 300 to ca 500 nm) and the relatively low intensity of the MLCT band (see the comparison in Figure S11). Of course, this effect might be used for fine color tuning of similar MSP systems.

The spectral changes in response to the increasing r ratio show three stages. The first stage for r from 0 to 0.5 is characterized by the redshift of the band unimeric units (U band) with a maximum at the wavelength λ_U in the range from 400 to 500 nm, and by appearance and enhancement of the MLCT band, whose apex wavelength, λ_{MLCT}, is a function of the linker structure (see Figure 2 and Figure S11). These features correspond to the formation of the species U-Fe^{2+}-U, called 'butterfly dimers' [32]. The observed slight redshift of the MLCT bands in this stage is caused by the broadening and redshift of a particular U-band.

The second stage occurs for r from 0.5 to 1.0, and is characterized by a further slight redshift of λ_U as well as λ_{MLCT} and significant enhancement of the MLCT band. These features prove the assembling of butterfly dimers and Fe^{2+} ions into polymeric chains, whose degree of polymerization should be the highest for the composition ratio r equal to approximately one. The total redshift λ_U from unimer ($r = 0$) to the ideal MSP ($r = 1$) is about 20 nm for all MSPs (see Table 1).

The third stage occurs for r values above 1 and is usually characterized by a blue shift and attenuation of the MLCT band with increasing r, which mostly accompanies partial dissociation of longer MSP chains to the shorter ones end-capped with Fe^{2+} ions [24–26,33]. However, **Fe-TtB** showed the great exception: continuing redshift and amplification of the MLCT band, which is most likely due to the large overlap of the MLCT and U bands in this MSP. It is worth noting that according to the optical absorption spectrum this unimer clearly shows the highest extent of electron delocalization among all unimers in this study.

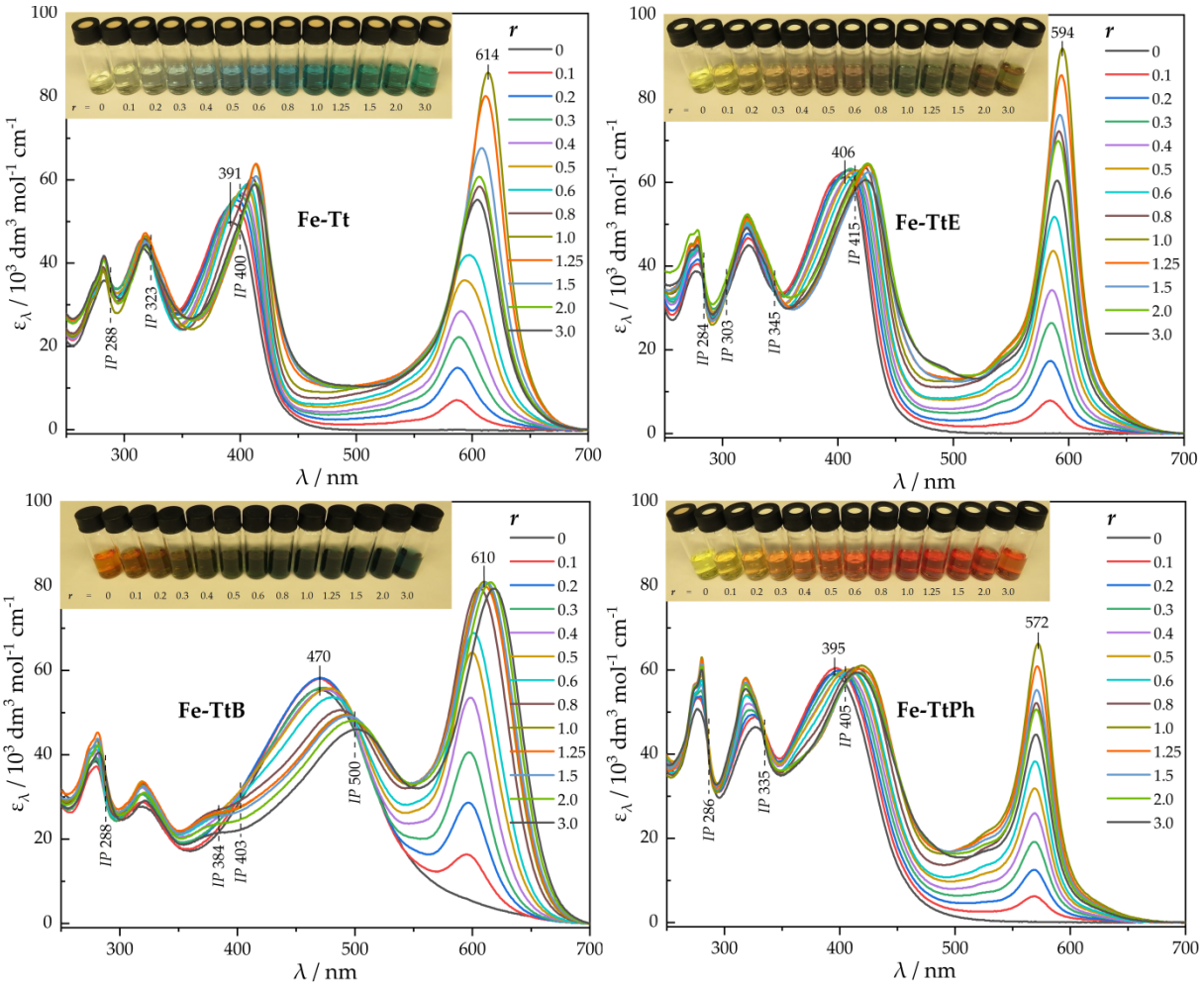

Figure 1. Changes in the UV/vis spectra accompanying stepwise transformation of studied unimers into Fe-MSPs in the HFP/ACN (4:1 by vol.) mixed solvent in response to increasing compositional ratio of solutes $r = [Fe^{2+}]/[U]$. Unimer concentration $[U] = 2 \times 10^{-5}$ mol/L in all solutions.

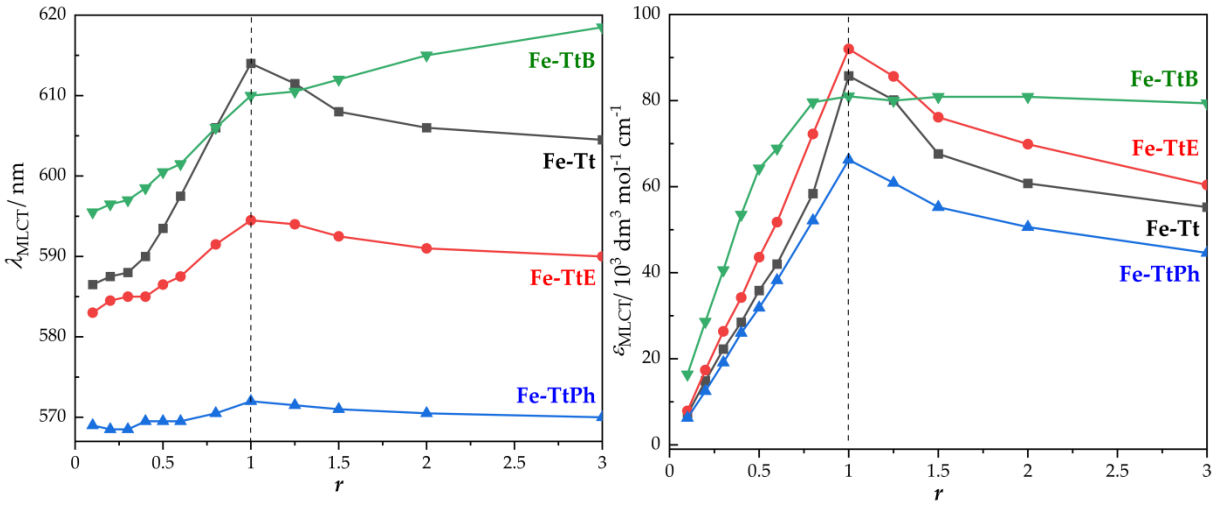

Figure 2. The wavelength (λ_{MCLT}, left) and the molar absorption coefficient (ε_{MLCT}, right) of the Metal to Ligand Charge Transfer (MLCT) band of unimer solutions with added Fe^{2+} ions as a function of the ratio $r = [Fe^{2+}]/[U]$.

Table 1. Positions of UV/vis absorption bands of Fe-MSPs (r = 1.0) in the solid-state and in the 1,1,1,3,3,3-Hexafluoropropan-2-ol (HFP)/acetonitrile (ACN) solution. λ_U and λ_{MLCT} are the characteristic wavelengths of the absorption bands of unimeric units and MLCT, respectively.

MSP	λ_U * Solution nm	λ_U (nm) Solid State 0 V (Fe^{2+})	1.4 V (Fe^{3+})	λ_{MLCT} Solution nm	λ_{MLCT} Solid State nm
Fe-Tt	391 → 412	420	475	614	632
Fe-TtE	406 → 426	432	483	594	612
Fe-TtPh	395 → 418	428	452	572	590
Fe-TtB	470 → 495	502	$(520)_{WEAK}$ 1045_{NIR}	610	620

* The first number (typed in a smaller font) indicates λ_U for corresponding free unimer and the arrow indicates that the change in λ_U is due to unimer assembling to corresponding MSP.

3.3. Preparation and Characterization of Fe-MSP Films

The films were prepared by casting from Fe-MSP solutions (2.6 g/L) in HFP/ACN mixed solvent, which were prepared by mixing the solutions containing equimolar amounts of the components. The solutions were allowed to equilibrate until the next day. Prior to the film casting, a particular solution was treated in an ultrasound bath for 5 min and filtered. Then it was spin-casted (500 rpm, 30 s) onto a rectangular ITO substrate and dried in air. The morphology, roughness, and thickness of spin-cast Fe-MSP films were analyzed by the AFM method. A relatively rough surface was observed for all films (see Figure S12 in ESI). The surface roughness was found to increase with the increased length of the linker of the respective unimer. The smoothest (least coarse) film showed **Fe-Tt** with the difference between the highest and the lowest point of the surface equal to 23 nm. The average film thickness was determined to vary from 35 to 40 nm (see Table 2).

Table 2. Characteristics of Fe-MSP films spin-coated on ITO substrate. R_q is the root mean square roughness; R_a the average roughness and R_{max} the maximum height.

Fe-MSP	Surface Area Scanned μm^2	R_q nm	R_a nm	R_{max} nm	Thickness nm
Fe-Tt	4.1	2.8	2.2	22.9	40 ± 5
Fe-TtE	4.4	3.2	2.5	48.8	40 ± 5
Fe-TtPh	4.1	3.9	3.0	40.6	35 ± 5
Fe-TtB	4.3	5.6	4.1	50.0	35 ± 3

The redox behavior of Fe-MSP films was determined by cyclic voltammetry using an oxygen-free solution of NBu_4PF_6 (0.1 M) in ACN as the electrolyte and the scan rate ranged from 20 to 1000 mV/s (see Figure 3). A single reversible redox wave corresponding to the transformation between Fe^{2+} and Fe^{3+} ions has been observed for all MSPs, in good agreement with the behavior of related systems [8]. The observation that the separation between the anodic and cathodic peaks increases with the increasing scanning speed suggests that the redox reaction is quasi-reversible [11,12]. The insets in Figure 3 show that the peak current density is directly proportional to the square root of the scan speed for all MSPs, which indicates a diffusion control of the redox process in all systems regardless of the linker structure. The noticeable smaller decrease in the proportionality constant of this dependence with increasing linker size can be attributed to the larger volume of unimer units and thus to the lower concentration of Fe ions in the corresponding systems.

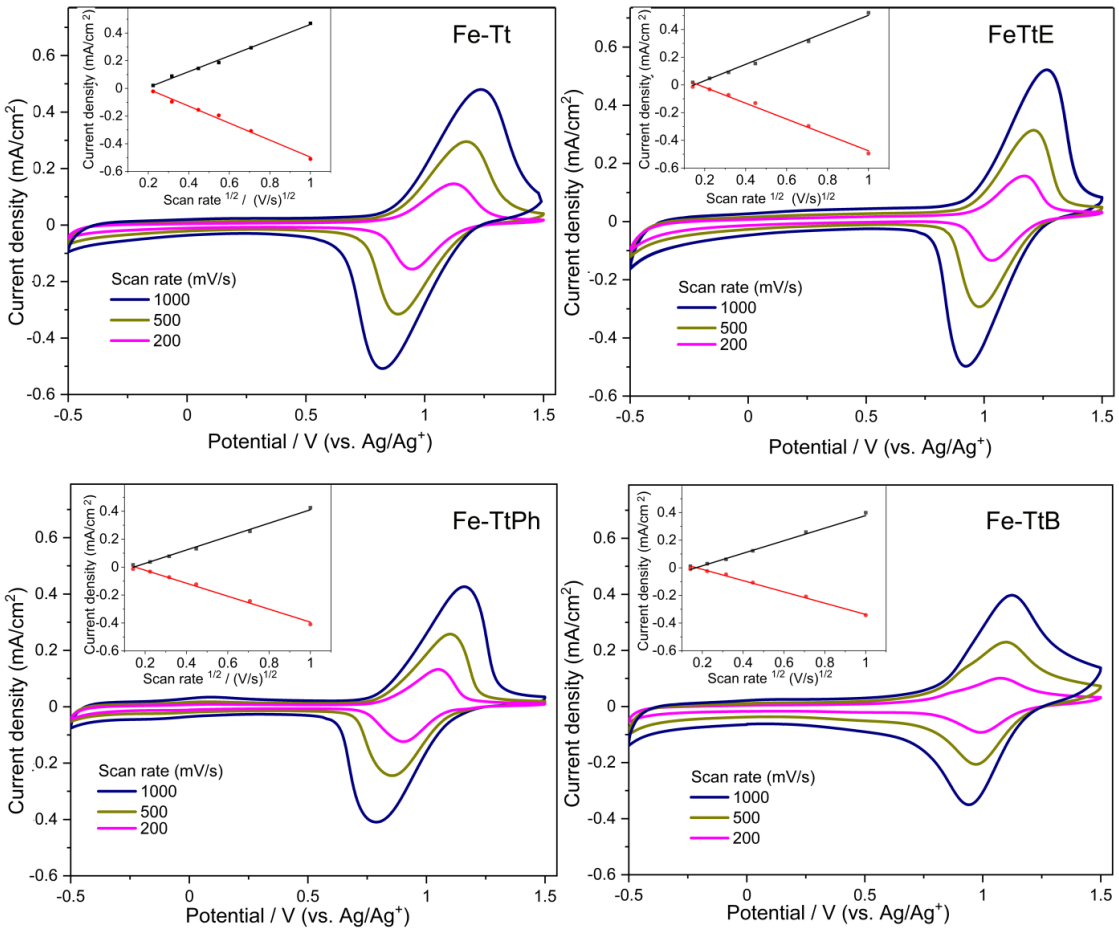

Figure 3. Cyclic voltammetry records of Fe-MSP films taken with different scanning rates. Insets show the dependences of the anodic and cathodic peak currents on the square root of scanning rate.

3.4. Electrochromism of Prepared MSPs

The UV/vis to near-infrared (NIR) absorption spectra of Fe-MSP films as well as photos of the films taken prior and after oxidation of Fe^{2+} ions are shown in Figure 4. Relating spectral data are summarized in Table 2. It can be seen that, after the electrochemical oxidation of Fe^{2+} to Fe^{3+}, the MLCT band almost disappeared and the unimer band was red-shifted significantly. The color of the oxidized film is dominantly controlled by the U band, which, although shifted, remained clearly distinguished and intense only in Fe-MSPs with no or a short linker. In the oxidized Fe-MSPs with longer conjugated linkers, the U band is strongly broadened. In the Fe^{3+}-TtB spectrum, this band is almost invisible. Another interesting feature of the Fe^{3+}-TtB film is an intense absorption band in the NIR region with a maximum at about 1045 nm.

The MLCT band is almost fully reversible, giving upon reduction the film in its original color. The results of responsivity tests during periodic cycling of the applied voltage between 0 and 1.4 V are shown in Figure 5 and the results of chronoamperometry measurements in Figure 6.

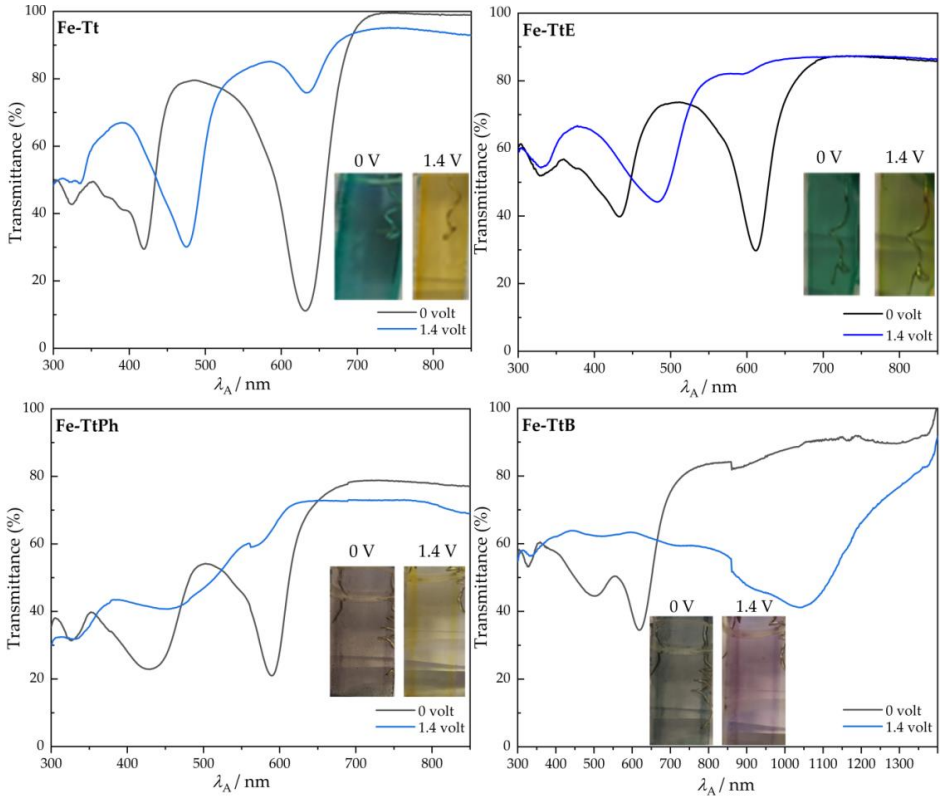

Figure 4. UV/vis to near-infrared (NIR) absorption spectra of Fe-MSP films in the colored (black curve, 0 V) and bleached (blue curve, 1.4 V) state. Insets: The photographs of Fe-MSPs in colored and bleached states.

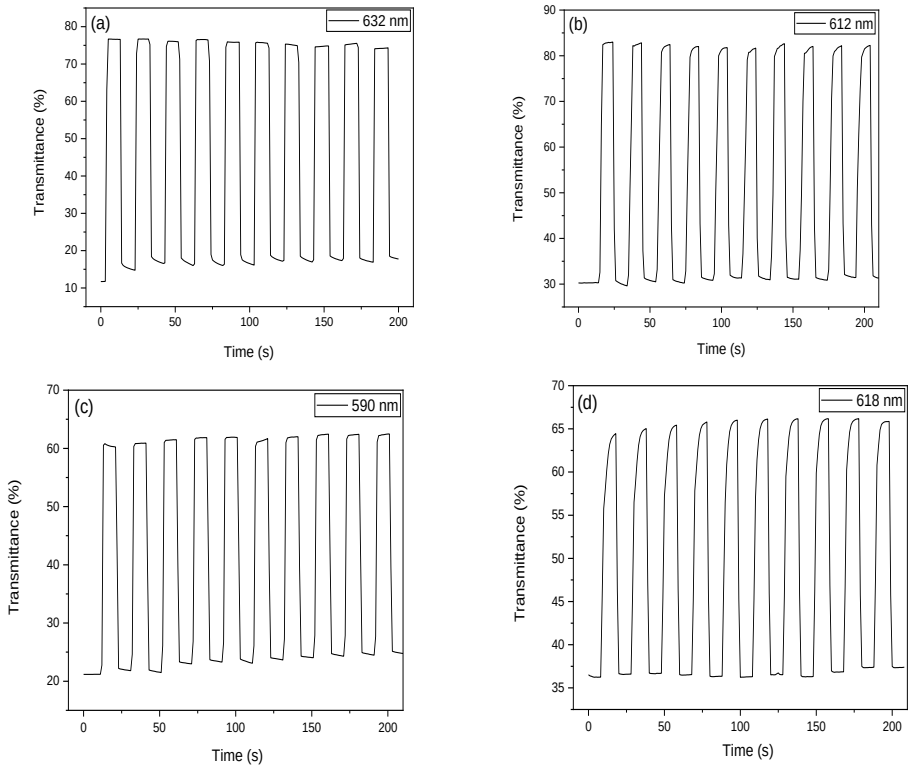

Figure 5. Optical response of (**a**) **Fe-Tt** (**b**) **Fe-TtE** (**c**) **Fe-TtPh** and (**d**) **Fe-TtB** films to the periodic cycling of the applied voltage between 0 and 1.4 V. Absorption recorded at indicated wavelengths.

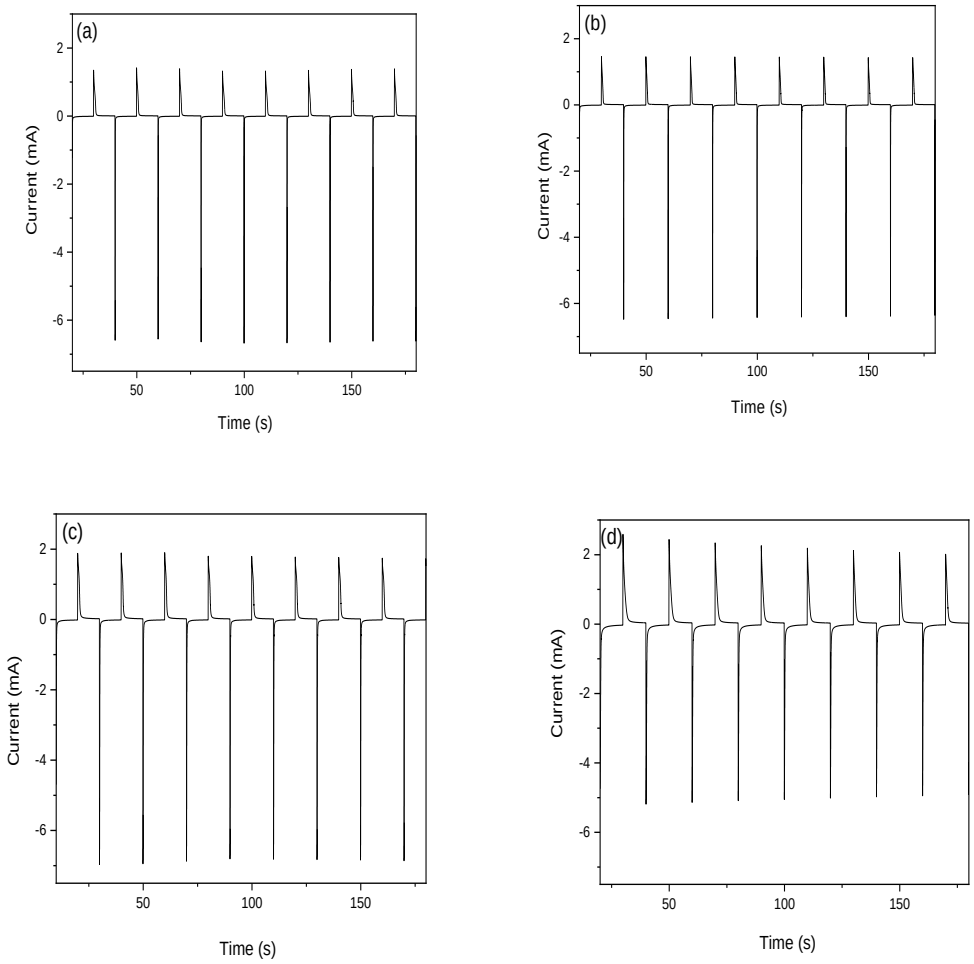

Figure 6. Chronoamperometry of (**a**) **Fe-Tt** (**b**) **Fe-TtE** (**c**) **Fe-TtPh** and (**d**) **Fe-TtB** films with a 10 s delay between 0 V and 1.4 V.

The optical contrast (ΔT) measured at corresponding wavelengths (Table 3) was found to be 29.0% for **Fe-TtB** and increased to 64.5% for **Fe-Tt**. For comparison, Zhu et al. reported for electrochromic conjugated polymers based on thieno[3,2-*b*]thiophene the optical contrast values 19.15% and 13.36% in a similar spectral region [34]. The film **Fe-TtB** also showed optical contrast at 1041 nm with ΔT = 48% and ΔOD = 0.35, but it disappeared after few repetition cycles. Bleaching and coloring times reported in Table 3 are the times required for reaching 95% of the final transmittance at given wavelengths after switching the applied voltage (see Figure S13 in ESI). The coloring time, t_c, (reduction process) was nearly the same (1.7 to 1.8 s) for all Fe-MSPs, while the bleaching time, t_b, (oxidation process) differed up to more than fourfold. The linear dependences shown in the insets of Figure 3 correspond to the Randles-Sevcik equation [35,36] (see page 9 in ESI). Slopes of these dependences decreased from the Fe-Tt to Fe-TtB with increasing size of the parent unimer (with only one exception, see Table 3). This decrease can therefore be tentatively attributed to the gradually decreasing concentrations of the active redox species in the EC material. However, these dependencies do not provide an explanation for the substantially prolonged bleaching times of Fe-TtE and Fe-TtB. Furthermore, there is no correlation between bleaching time and surface roughness of the EC layer. Thus, the differences in bleaching time between different Fe-MSPs are most likely due to differences in the rate of diffusion of counter-ions into polymer films during their oxidation and the ion/charge transport between EC film and electrolyte [37]. The reverse diffusion of counter-ions out of partly swollen film during the reduction process should be easier, which might explain the observed similarity of t_c values.

Table 3. Electrochromic performance of Fe-MSPs films: λ_{MLCT}—the wavelength of the MLCT band, ΔT—optical contrast, ΔOD—change in optical density, t_b—bleaching time (neutral to oxidized state), t_c—coloring time (oxidized to neutral state), *CE*—coloration efficiency.

MSP	λ_{MLCT} nm	ΔT (%)	ΔOD	t_b s	t_c s	*CE* $cm^2\ C^{-1}$	Oxidation Peak Slope	Reduction Peak Slope
Fe-Tt	632	64.5	0.82	1.1	1.8	641	2.12	−2.29
Fe-TtE	612	54.5	0.42	3.7	1.8	229	2.2	−2.14
Fe-TtPh	590	43.0	0.44	1.8	1.8	332	1.79	−1.74
Fe-TtB	618	29.0	0.25	4.6	1.7	173	0.8	−0.73

One of the most important parameters for the characterization of EC materials is coloration efficiency, $CE = \Delta OD/Q$, defined as the difference in optical density $\Delta OD = \log(T_b/T_c)$ per unit charge density Q measured at the λ_{max} of the optical absorption band [38–40]. We adopted the approach suitable for not fully bleached EC materials [41] and used the Q values needed to achieve a 95% final transmittance change to calculate the CE values (see Figure S14). The remaining 5% is barely visible to the naked eye. The Q values were calculated directly by the instrument used for chrono-coulometric measurements as the time integral of the current across the corresponding interval.

The highest coloration efficiency, 641 $cm^2\ C^{-1}$, was found for **Fe-Tt** film. This value is very competitive compared to other materials reported in the literature for electrochromic devices. For example, Mondal [40] and Kuai [41] reported CE values between 12.84 and 230 $cm^2\ C^{-1}$ for their Fe(II) coordination nanosheets, Kuo et al. [38] achieved CE = 372.7 $cm^2\ C^{-1}$ for copolymer composed of carbazole and indole-6-carboxylic acid.

3.5. Fabrication of Electrochromic Devices

The solid-state electrochromic device has been designed, constructed, and its operation has been proven (see Figure 7). Here we present the device based on **Fe-Tt,** the MSP with the fastest EC response (Table 3) and the highest change in transmittance. An **Fe-Tt** film spin-casted on ITO glass was covered with the gel electrolyte layer (thickness of 1 mm) prepared by mixing poly(methyl methacrylate) (3.5 g), propylene carbonate (10 mL), and $LiClO_4$ (1.5 g) according to [14], and stacked with other ITO substrates (see Figure 7). The ionic conductivity of the gel electrolyte was found to be 2.3×10^{-3} S/cm, in good agreement with the earlier reported values [42]. This value has been determined by the broadband impedance spectroscopy from the plateau of the frequency dependence of the real part of the conductivity above 10^3 Hz (Figure S15) and confirmed by the Nyquist plot considering Randles circuit. The UV/vis transmittance spectra of the device (Figure 8) showed optical contrast of around 60% at 637 nm, which is lower than the value listed in Table 3 for an **Fe-Tt** film in a liquid electrolyte. Longer coloration and bleaching times can be attributed to the lowered conductivity of ions in the gel electrolyte compared to that of the liquid electrolyte. On the other hand, the gel electrolyte provides higher stability to the electrochromic cell during cycling.

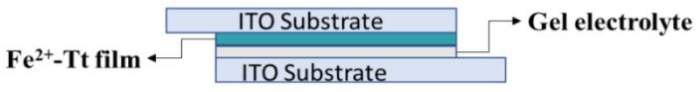

Figure 7. Scheme of the electrochromic device with a gel electrolyte.

The Fe-MSP films showed good stability for a few months when stored in the air under ambient conditions. However, the Fe-MSP device with liquid electrolyte showed signs of degradation after 20 working cycles, especially delamination of the EC layer and obvious signs of its partial dissolution. Degradation could be only partially limited by covering the Fe-MSP layer with Nafion. In contrast, the Fe-MSP based device with the gel electrolyte showed markedly high stability during electrochromic cycling: no change was detected during 100 cycles. We should also note that some degradation over the long-term may occur due to increasing resistance of the ITO layer during repeated redox cycling.

Fluorine-doped tin oxide (FTO) would therefore be a better choice for long term working devices.

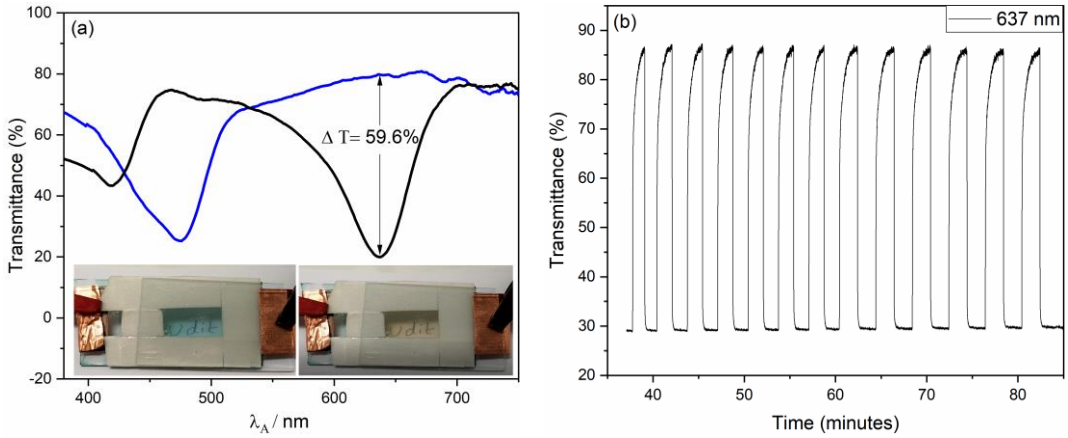

Figure 8. (**a**) Photographs and UV/vis transmittance spectra of Fe-MSP electrochromic device in the reduced colored state (black curve, 0 V) and oxidized bleached state (blue curve, 1.4 V); (**b**) optical response of the device to periodic voltage cycling.

4. Conclusions

The results obtained clearly show how the optical spectral properties of ditopic unimers and particularly spectral and electrochromic properties of related Fe-MSPs can be simply tuned via the choice of linkers connecting chelate end-groups to the unimer central unit. The presented four new unimers of the a,w-bis(*tpy*) family with thieno[3,2-*b*]thiophene-2,5-diyl central unit differed only in the linkers (none, ethynediyl, 1,4-phenylene, and 2,2′-bithophene-5,5′-diyl). The unimers are easily assembled with Fe^{2+} ions to give electrochromic Fe-MSPs of ground colors ranging from blue-green to gray-green, red, and deep purple. The red color of Fe-MSPs is rather surprising because the "generic" color of MSPs with $[Fe(tpy)_2]^{2+}$ centers is blue due to the very intense MLCT band occurring at 550 nm and above [12,32]. Nevertheless, it is also well known that this MLCT band is significantly contributed by transitions in the central parts of unimeric units [24–27]. This interesting feature can potentially help in easy color tuning the EC devices based on bis(*tpy*) Fe-MSPs because their electrochromism is closely related to the color changes accompanying the MSP assembling, which are easy to determine.

One can see that the linker-less **Fe-Tt** provided the Fe-MSP with the highest optical contrast, fastest response, and the highest coloration efficiency (CE = 641 cm^2 C^{-1}) of all examined Fe-MSPs. To the best of our knowledge, its properties are comparable to the highest values reported for MSPs in the literature, which makes **Fe-Tt** an excellent candidate for possible applications in electrochromic devices. On the other hand, **Fe-TtB** possessing the largest linkers (2,2′-bithiofen-5,5′-diyl) exhibited the worst of both of these characteristics, but showed a rare color change (green to dark purple) and, in addition, showed rather high NIR electrochromism (optical contrast about 50% at 1100 cm^{-1}), though only during the first few cycles.

It should be noted here that the Fe-MSP films derived from conjugated bis(*tpy*) unimers cannot be turned to a fully transparent state. Unsubstituted bis(*tpy*) complexes of metal ions absorb in the near UV region (band edge around 350 nm) and small conjugated substituents attached to *tpy* redshift the band edge of the complex to the UV-visible border 12,32]. In addition Fe ions show a weak band centered at 370 nm contributed by transitions at Fe atoms [43]. Considering conjugated Fe-MSPs, the redox process taking place in $[Fe(tpy)_2]^{2+}$ centers always affects optical transitions in unimeric units which significantly contribute to the MLCT band [24–27]. Besides, eventual simultaneous changes in populations of polaronic and bipolaronic states enable optical transitions that make a fully bleached state principally unattainable and the design of organic EC devices difficult. On the other hand, these materials require a mostly lower amount of charge compared to inorganic EC

materials to achieve the same color change, because of the higher oscillator strengths of the associated electronic transitions.

Supplementary Materials: The following are available online at https://www.mdpi.com/2073-4360/13/3/362/s1, The file contains fifteen figures. Figure S1: IR spectra of unimers and corresponding Fe-MSPs. Figures S2–S9: ^{1}H NMR and ^{13}C NMR spectra of all unimers prepared and studied. Figure S10: photographs of solutions showing color changes during assembly of MSPs. Figure S11: A comparison of the MLCT bands of all Fe-MSPs. Figure S12 3D AFM images of Fe-MSP films (tapping mode), Figures S13 and S14: Determination of the bleaching and coloring time of electrochromic films. Figure S15: Frequency dependence of the real part of the conductivity of gel electrolyte. Randles-Ševčik Equation.

Author Contributions: Conceptualization, J.P. and J.V.; methodology, J.Z., A.C. and U.A.; validation, J.V., J.Z. and J.P.; formal analysis U.A., A.C. and J.Z.; investigation, A.C., U.A., J.Z. and O.T.; resources, A.C., J.V. and J.P.; data curation, J.Z., J.P. and J.V.; writing—original draft preparation, A.C., U.A. and J.Z.; writing—review and editing, J.V. and J.P. All authors have read and agreed to the published version of the manuscript.

Funding: Financial supports of the Grant Agency of Charles University (project 1110119) and the Czech Science Foundation (project 17-03984S) are greatly acknowledged.

Institutional Review Board Statement: Not applicable.

Informed Consent Statement: Not applicable.

Data Availability Statement: We have no depository of publicly archived datasets analyzed or generated during the study. Data are available on request; contact please authors on their E-mail addresses.

Acknowledgments: The authors thank Zdeněk Tošner, Head of the NMR laboratory, Faculty of Science, Charles University, for advanced NMR measurements on unimers and Ivana Sloufova (affiliation [1]) for FT-IR measurements.

Conflicts of Interest: The authors declare no conflict of interest.

References

1. Invernale, M.A.; Acik, M.; Sotzing, G.A. Thiophene-Based Electrochromic Materials. In *Handbook of Thiophene-Based Materials: Applications in Organic Electronics and Photonics—Chapter 20*; Perepichka, I.F., Perepichka, D.F., Eds.; Wiley: Hoboken, NJ, USA, 2009; p. 757.
2. Kim, J.; Remond, M.; Kim, D.; Jang, H.; Kim, E. Electrochromic Conjugated Polymers for Multifunctional Smart Windows with Integrative Functionalities. *Adv. Mater. Technol.* **2020**, *5*, 1900890. [CrossRef]
3. Macher, S.; Schott, M.; Sassi, M.; Facchinetti, I.; Ruffo, R.; Patriarca, G.; Beverina, L.; Posset, U.; Giffin, G.A.; Loebmann, P. New Roll-to-Roll Processable PEDOT-Based Polymer with Colorless Bleached State for Flexible Electrochromic Devices. *Adv. Funct. Mater.* **2020**, *30*, 1906254. [CrossRef]
4. Wu, W.; Wang, M.; Ma, J.; Cao, Y.; Deng, Y. Electrochromic Metal Oxides: Recent Progress and Prospect. *Adv. Electron. Mater.* **2018**, *4*, 1–19. [CrossRef]
5. Celiesiute, R.; Ramanaviciene, A.; Gicevicius, M.; Ramanavicius, A. Electrochromic Sensors Based on Conducting Polymers, Metal Oxides, and Coordination Complexes. *Crit. Rev. Anal. Chem.* **2019**, *49*, 195–208. [CrossRef] [PubMed]
6. Laschuk, N.O.; Ebralidze, I.I.; Poisson, J.; Egan, J.G.; Quaranta, S.; Allan, J.T.S.; Cusden, H.; Gaspari, F.; Naumkin, F.Y.; Easton, E.B.; et al. Ligand Impact on Monolayer Electrochromic Material Properties. *ACS Appl. Mater. Interfaces* **2018**, *10*, 35334–35343. [CrossRef] [PubMed]
7. Neo, W.T.; Ye, Q.; Chua, S.-J.; Xu, J. Conjugated polymer-based electrochromics: Materials, device fabrication and application prospects. *J. Mater. Chem. C* **2016**, *4*, 7364–7376. [CrossRef]
8. Amb, C.M.; Dyer, A.L.; Reynolds, J.R. Navigating the Color Palette of Solution-Processable Electrochromic Polymers. *Chem. Mater.* **2011**, *23*, 397–415. [CrossRef]
9. Zhang, A.; Xiao, C.; Wu, Y.; Li, C.; Ji, Y.; Li, L.; Hu, W.; Wang, Z.; Ma, W.; Li, W. Effect of Fluorination on Molecular Orientation of Conjugated Polymers in High Performance Field-Effect Transistors. *Macromolecules* **2016**, *49*, 6431–6438. [CrossRef]
10. Otley, M.T.; Zhu, Y.; Zhang, X.; Li, M.; Sotzing, G.A. Color-Tuning Neutrality for Flexible Electrochromics Via a Single-Layer Dual Conjugated Polymer Approach. *Adv. Mater.* **2014**, *26*, 8004–8009. [CrossRef] [PubMed]
11. Ciferri, A. Supramolecular polymerizations. *Macromol. Rapid Commun.* **2002**, *23*, 511–529. [CrossRef]
12. Winter, A.; Schubert, U.S. Synthesis and characterization of metallo-supramolecular polymers. *Chem. Soc. Rev.* **2016**, *45*, 5311–5357. [CrossRef] [PubMed]

13. Vohlídal, J.; Hissler, M. Metallo-Supramolecular Polymers. In *Smart Inorganic Polymers: Synthesis, Properties, and Emerging Applications in Materials and Life Sciences—Chapter 6*; Hey-Hawkins, E., Hissler, M., Eds.; Wiley: Hoboken, NJ, USA, 2019; pp. 141–162.
14. Higuchi, M. *Metallo-Supramolecular Polymers: Synthesis, Properties, and Device Applications*; Springer: Berlin/Heidelberg, Germany, 2019.
15. Liang, Y.; Strohecker, D.; Lynch, V.; Holliday, B.J.; Jones, R.A. A Thiophene-Containing Conductive Metallopolymer Using an Fe(II) Bis(terpyridine) Core for Electrochromic Materials. *ACS Appl. Mater. Interfaces.* **2016**, *8*, 34568–34580. [CrossRef] [PubMed]
16. Pai, S.; Moos, M.; Schreck, M.H.; Lambert, C.; Kurth, D.G. Green to red electrochromic Fe(II) metallo-supramolecular polyelectrolytes self-assembled from fluorescent 2,6-bis(terpyridyl)pyrimidine bithiophene. *Inorg. Chem.* **2017**, *56*, 1418–1432. [CrossRef] [PubMed]
17. Han, F.S.; Higuchi, M.; Kurth, D.G. Metallo-supramolecular polymers based on functionalized bis-terpyridines as novel electrochromic materials. *Adv. Mater.* **2007**, *19*, 3928–3931. [CrossRef]
18. Pai, S.; Schott, M.; Niklaus, L.; Posset, U.; Kurth, D.G. A study of the effect of pyridine linkers on the viscosity and electrochromic properties of metallo-supramolecular coordination polymers. *J. Mater. Chem. C* **2018**, *6*, 3310–3321. [CrossRef]
19. Takada, K.; Sakamoto, R.; Yi, S.-T.; Katagiri, S.; Kambe, T.; Nishihara, H. Electrochromic Bis(terpyridine)metal Complex Nanosheets. *J. Am. Chem. Soc.* **2015**, *137*, 4681–4689. [CrossRef] [PubMed]
20. Hu, C.-W.; Sato, T.; Zhang, J.; Moriyama, S.; Higuchi, M. Multi-colour electrochromic properties of Fe/Ru-based bimetallo-supramolecular polymers. *J. Mater. Chem. C* **2013**, *1*, 3408–3413. [CrossRef]
21. Sato, T.; Higuchi, M. An alternately introduced heterometallo-supramolecular polymer: Synthesis and solid-state emission switching by electrochemical redox. *Chem. Commun.* **2013**, *49*, 5256. [CrossRef]
22. Duerrbeck, A.; Gorelik, S.; Hobley, J.; Wu, J.E.; Hor, A.; Long, N. Highly emissive, solution-processable and dynamic Eu(III)-containing coordination polymers. *Chem. Commun.* **2015**, *51*, 8656–8659. [CrossRef]
23. Svoboda, J.; Štenclová, P.; Uhlík, F.; Zedník, J.; Vohlídal, J. Synthesis and photophysical properties of α,ω-bis(terpyridine)oligothiophenes. *Tetrahedron* **2011**, *67*, 75–79. [CrossRef]
24. Štenclová, P.; Šichová, K.; Šloufová, I.; Zedník, J.; Vohlídal, J.; Svoboda, J. Alcohol- and water-soluble bis(tpy)quaterthiophenes with phosphonium side groups: New conjugated units for metallo-supramolecular polymers. *Dalton Trans.* **2016**, *45*, 1208–1224. [CrossRef] [PubMed]
25. Štenclová-Bláhová, P.; Svoboda, J.; Šloufová, I.; Vohlídal, J. Alcohol-soluble bis(tpy)thiophenes: New building units for constitutional dynamic conjugated polyelectrolytes. *Phys. Chem. Chem. Phys.* **2015**, *17*, 13743–13756. [CrossRef] [PubMed]
26. Bláhová, P.; Zedník, J.; Šloufová, I.; Vohlídal, J.; Svoboda, J. Synthesis and photophysical properties of new α,ω-bis(tpy)oligothiophenes and their metallo-supramolecular polymers with Zn2+ ion couplers. *Soft Matter.* **2014**, *12*, 214–229. [CrossRef]
27. Vitvarova, T.; Svoboda, J.; Hissler, M.; Vohlidal, J. Conjugated Metallo-Supramolecular Polymers Containing a Phosphole Unit. *Organometallics* **2017**, *36*, 777–786. [CrossRef]
28. Hladysh, S.; Vaclavkova, D.; Vrbata, D.; Bondarev, D.; Havlicek, D.; Svoboda, J.; Zedník, J.; Vohlídal, J. Synthesis and characterization of metallo-supramolecular polymers from thiophene-based unimers bearing pybox ligands. *RSC Adv.* **2017**, *7*, 10718–10728. [CrossRef]
29. Cinar, M.E.; Ozturk, T. Thienothiophenes, Dithienothiophenes, and Thienoacenes: Syntheses, Oligomers, Polymers, and Properties. *Chem. Rev.* **2015**, *115*, 3036–3140. [CrossRef]
30. Li, P.; Ahrens, B.; Feeder, N.; Raithby, P.R.; Teat, S.J.; Khan, M.S. Luminescent digold ethynyl thienothiophene and dithienothiophene complexes; their synthesis and structural characterization. *Dalton Trans.* **2005**, *5*, 874–883. [CrossRef]
31. Filler, R.; Schure, R.M. Highly acidic perhalogenated alcohols. A new synthesis of perfluoro-tert-butyl alcohol. *J. Org. Chem.* **1967**, *32*, 1217–1219. [CrossRef]
32. Vitvarova, T.; Zednik, J.; Blaha, M.; Vohlidal, J.; Svoboda, J. Effect of Ethynyl and 2-Thienyl Substituents on the Complexation of 4′-Substituted 22′:6′,2″-Terpyridines with Zn^{2+} and Fe^{2+} Ions, and the Spectroscopic Properties of the Ligands and Formed Complex Species. *Eur. J. Inorg. Chem.* **2012**, *2012*, 3866–3874. [CrossRef]
33. Schwarz, G.; Hasslauer, I.; Kurth, D.G. From terpyridine-based assemblies to metallo-supramolecular polyelectrolytes (MEPEs). *Adv. Colloid Interface Sci.* **2014**, *207*, 107–120. [CrossRef]
34. Zhu, X.; Zhu, Y.; Murtaza, I.; Shi, J.; He, Y.; Xu, P.; Zhu, M.; Goto, O.; Meng, H. Thieno [3, 2-b]thiophene based electrochromic polymers: Experimental and theoretical appraisal of the EDOT position. *RSC Adv.* **2016**, *6*, 75522–75529. [CrossRef]
35. Randles, J.E.B. Cathode-ray polarograph. II. Current-voltage curves. *Trans. Faraday Soc.* **1948**, *44*, 327–338. [CrossRef]
36. Ševčík, A. Oscillographic polarography with periodical triangular voltage. *Collect. Czech. Chem. Commun.* **1948**, *13*, 349–377. [CrossRef]
37. Zhu, Y.; Otley, M.T.; Alamer, F.A.; Kumar, A.; Zhang, X.; Mamangun, D.M.D.; Li, M.; Arden, B.G.; Sotzing, G.A. Electrochromic properties as a function of electrolyte on the performance of electrochromic devices consisting of a single-layer polymer. *Org. Electron.* **2014**, *15*, 1378–1386. [CrossRef]
38. Kuo, C.-W.; Hsieh, T.-H.; Hsieh, C.-K.; Liao, J.-W.; Wu, T.-Y. Electrosynthesis and Characterization of Four Electrochromic Polymers Based on Carbazole and Indole-6-Carboxylic Acid and Their Applications in High-Contrast Electrochromic Devices. *J. Electrochem. Soc.* **2014**, *161*, D782–D790. [CrossRef]

39. Nie, G.; Wang, L.; Liu, C. High performance electrochromic devices based on a polyindole derivative, poly(1H-benzo[g] indole). *J. Mater. Chem. C* **2015**, *3*, 11318–11325. [CrossRef]
40. Mondal, S.; Ninomiya, Y.; Yoshida, T.; Mori, T.; Bera, M.K.; Ariga, K.; Higuchi, M. Dual-Branched Dense Hexagonal Fe(II)-Based Coordination Nanosheets with Red-to-Colorless Electrochromism and Durable Device Fabrication. *ACS Appl. Mater. Interfaces* **2020**, *12*, 31896–31903. [CrossRef] [PubMed]
41. Kuai, Y.; Li, W.; Dong, Y.; Wong, W.-Y.; Yan, S.; Dai, Y.; Zhang, C. Multi-color electrochromism from coordination nanosheets based on a terpyridine-Fe(II) complex. *Dalton Trans.* **2019**, *48*, 15121–15126. [CrossRef]
42. Stephan, A.M. Review on gel polymer electrolytes for lithium batteries. *Eur. Polym. J.* **2006**, *42*, 21–42. [CrossRef]
43. Schubert, U.S.; Hofmeier, H.; Newkome, G.R. *Modern Terpyridine Chemistry*; Wiley-VCH Verlag GmbH: Weinheim, Germany, 2006.

polymers

MDPI

Article

Synthesis and Impedance Spectroscopy of Poly(*p*-phenylenediamine)/Montmorillonite Composites

Udit Acharya [1,2], Patrycja Bober [1], Muhammed Arshad Thottappali [1,2], Zuzana Morávková [1], Magdalena Konefał [1] and Jiří Pfleger [1,*]

[1] Institute of Macromolecular Chemistry, Czech Academy of Sciences, 162 06 Prague, Czech Republic; acharya@imc.cas.cz (U.A.); bober@imc.cas.cz (P.B.); thottappali@imc.cas.cz (M.A.T.); moravkova@imc.cas.cz (Z.M.); magdalenakonefal@imc.cas.cz (M.K.)

[2] Faculty of Mathematics and Physics, Charles University, 121 16 Prague, Czech Republic

* Correspondence: pfleger@imc.cas.cz

Abstract: Poly(*p*-phenylenediamine)/montmorillonite (PPDA/MMT) composites were prepared by the oxidative polymerization of monomers intercalated within the MMT gallery, using ammonium peroxydisulfate as an oxidant. The intercalation process was evidenced by X-ray powder diffraction. The FT-IR and Raman spectroscopies revealed that, depending on the initial ratio between monomers and MMT in the polymerization mixture, the polymer or mainly oligomers are created during polymerization. The DC conductivity of composites was found to be higher than the conductivity of pristine polymer, reaching the highest value of 10^{-6} S cm^{-1} for the optimal MMT amount used during polymerization. Impedance spectroscopy was performed over wide frequency and temperature ranges to study the charge transport mechanism. The data analyzed in the framework of conductivity formalism suggest different conduction mechanisms for high and low temperature regions.

Keywords: poly(*p*-phenylenediamine); montmorillonite; conductivity mechanism; impedance spectroscopy

Citation: Acharya, U.; Bober, P.; Thottappali, M.A.; Morávková, Z.; Konefał, M.; Pfleger, J. Synthesis and Impedance Spectroscopy of Poly(*p*-phenylenediamine)/Montmorillonite Composites. *Polymers* **2021**, *13*, 3132. https://doi.org/10.3390/polym13183132

Academic Editor: Jacek Ulanski

Received: 27 August 2021
Accepted: 13 September 2021
Published: 16 September 2021

1. Introduction

Composite materials based on polymers and inorganic materials have attracted increasing attention recently, thanks to the possibility of achieving superior properties by a combination of physical and chemical properties of the constituting components [1,2]. Such organic–inorganic composites are often applied as electrode materials in batteries [3,4] and supercapacitors [5]. Recently, composites composed of conjugated polymers or oligomers and clay fillers gained significant research interest due to their improved electrical, optical and mechanical properties, as well as corrosion resistance [6,7]. Montmorillonite (MMT) is a 2D layered phyllosilicate clay built of two tetrahedral and one octahedral sheet, which has been widely used in the preparation of nanocomposites due to its low cost, abundance in nature, zero toxicity, high specific surface area, swelling abilities and ion-exchange properties [8,9]. Various MMT composites with polyaniline [8,10], polypyrrole [11,12], poly (3,4-ethylenediaoxythiophene) [13] and polyphenylenediamine [14,15] were prepared by chemical [8,12] or electrochemical [13] polymerization and have been used as electrode material for oxygen reduction [16], anticorrosion coatings [6,11], sensors [17,18], conducting fillers [19], adsorbents [20] and supercapacitors [7].

In recent years, growing interest in the development of polyphenylenediamine composites can be observed [14,21–25]. Polyphenylenediamine is a conjugated polymer with a structure closely related to polyaniline; however, it possesses a higher nitrogen content and better solubility together with good redox properties, salt–base transition and environmental stability [23,26,27]. Nascimento et al. prepared poly(*p*-phenylenediamine)/MMT composites via oxidative polymerization and confirmed the successful formation of the polymer within the MMT gallery by extensive structural characterizations [14]. Ramya

et al. studied the nonlinear optical properties of chitosan/*o*- or *p*-phenylenediamine/MMT composites by the Z-scan technique with picosecond and femtosecond laser pulses and revealed properties that make this material suitable for optical limiters [15]. Khelifa et al. examined the electrochemical properties of poly (*o*-phenylenediamie)/clay composites by cyclic voltammetry [28]. However, polyphenylenediamine/clay composites have still been described in the literature to a limited extent and impedance spectroscopy of them has not been yet reported. The conductivity of these composites can be contributed by electronic and ionic contribution, differing in their sensitivity to temperature, humidity and frequency response. Impedance spectroscopy is an important tool to elucidate the charge transport mechanism and the type of charge carriers in complex systems. For this, various formalisms are offered: conductivity, dielectric loss and modulus [29,30]. Knowing the conductivity mechanism is important for the development of the next generation of electronic devices, electrorheological fluids, as well as anticorrosive coatings, and optimizing their properties [31].

In this work, a series of poly(*p*-phenylenediamine)/montmorillonite (PPDA/MMT) composites with various monomer to clay ratios has been prepared by in situ chemical oxidation of monomers within the MMT gallery (Scheme 1). Their structure and morphology were investigated by FT-IR and Raman spectroscopies, X-ray powder diffraction (XRD) and scanning electron microscopy (SEM). The impedance was measured in a wide frequency and temperature range and the AC conductivity mechanism was elucidated. We present here a detail impedance characterization to understand the conduction mechanism at different temperature regions. For the first time, the synergic effect in electrical, thermal, dielectric, impedance and modulus properties of PPDA/MMT composites has been investigated.

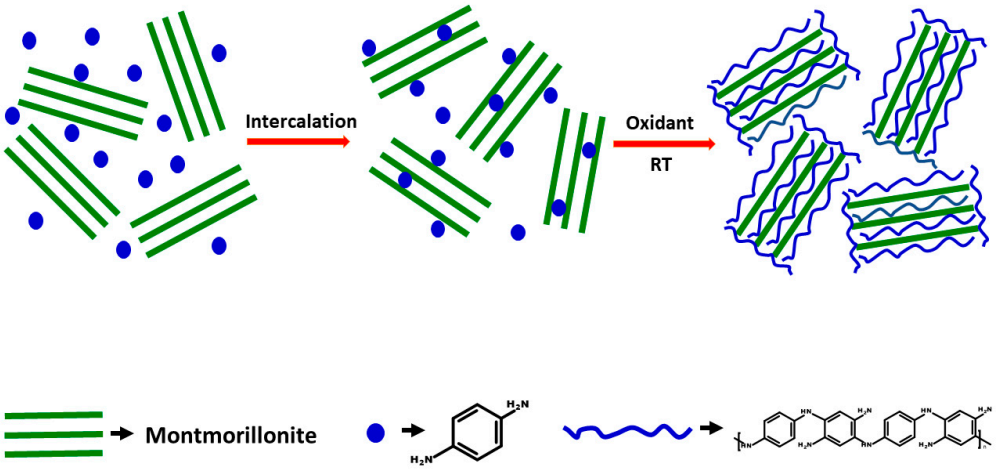

Scheme 1. Schematic diagram of the preparation of PPDA/MMT composites.

2. Materials and Methods

2.1. Preparation of Composites

p-Phenylenediamine dihydrochloride (≥98%) was purchased from Sigma-Aldrich (Buchs, Switzerland), ammonium peroxydisulfate from Lach:Ner (Neratovice, Czech Republic) and montmorillonite (Cloisite-Na^+) from Southern Clay Products (Gonzales, TX, USA). All chemicals were used as received without any further purification.

In a typical process, 3.62 g of *p*-phenylenediamine dihydrochloride (PDA) was dissolved in 50 mL of deionized water. Various amounts of MMT (0 g, 2 g, 5 g, 10 g, 15 g, 25 g, 35 g and 50 g, respectively) were added into the PDA solution, and the mixture was sonicated for 5 h. The amount of 5.71 g of ammonium peroxydisulfate was dissolved in 50 mL deionized water and added to the PDA/MMT dispersion under magnetic stirring. The total concentration of monomer and oxidant in each polymerization mixture was 0.2 M and 0.25 M, respectively. After 1 h of intense stirring, the mixture was left

undisturbed to polymerize for 24 h. The obtained precipitates were filtered and washed with deionized water and ethanol to remove by-products. The final products, poly(*p*-phenylenediamine)/montmorillonite (PPDA/MMT) composites with different amounts of MMT, were labeled as PPDA-X, where X accounts for the amount of MMT added to the reaction mixture.

2.2. Characterization

Morphology of composites was assessed using MAIA3 Tescan scanning electron microscope (Tescan, Brno, Czech Republic).

Thermogravimetric analysis (TGA) of the composites was performed on a Perkin Elmer Pyris 1 (Perkin Elmer, Waltham, MA, USA). Thermogravimetric Analyzer in a temperature range 35–800 °C at a rate of 10 °C min^{-1} with fixed air flow rate at 25 mL min^{-1}.

FTIR spectra in the wavenumber range from 400 to 4000 cm^{-1} were obtained on the composites admixed in KBr pellets using a Thermo Nicolet NEXUS 870 FTIR spectrometer equipped with a DTGS detector. The instrument was purged with dry air. All spectra were corrected for the presence of water vapor and carbon dioxide in the optical path.

Raman spectra were measured with a Renishaw InVia Reflex Raman microspectrometer using 514 nm excitation provided by an Ar-ion laser. The scattered light was registered with a Peltier-cooled CCD detector (576 × 384 pixels) and analyzed by the spectrograph with holographic grating 2400 lines mm^{-1}.

XRD measurements were performed using a pinhole camera (MolMet, Rigaku, Tokyo, Japan, upgraded by SAXSLAB/Xenocs) attached to a micro-focused X-ray beam generator (Rigaku MicroMax 003) operating at 0.6 mA and 50 kV. The camera was equipped with a vacuum version of the Pilatus 300K detector. The sample to detector distance, which was calibrated using a silver behenate powder sample, was 0.190 m. The scattering vector q, defined as $q = 4\pi/\lambda \cdot \sin\Theta$, where λ is the wavelength and 2Θ is the scattering angle, covered the range 0.145–1.41 $Å^{-1}$ (2θ = 2–20°).

The DC conductivity values were obtained on compressed pellets (diameter 13 mm and thickness 1.0 ± 0.2 mm) using van der Pauw method. A Keithley 230 Programmable Voltage Source in serial connection with a Keithley 196 System DMM was used as a current source. The potential difference was measured using a Keithley 617 Programmable electrometer or Keithley 181 nanovoltmeter, respectively, depending on the resistance of the sample. The DC conductivity measurements were carried out at stable ambient conditions at temperature 23 ± 1 °C and relative humidity 35 ± 5%. The frequency and temperature dependences of the impedance were measured in a quasi-steady-state regime using an Alpha-A Analyzer (Novocontrol Technologies, Montabaur, Germany) under applied AC voltage 1 V_{rms} in the frequency range 10^7 to 10^{-2} Hz and temperature range 115 to 435 K with 20 K step in nitrogen atmosphere. For clarity, only curves for selected representative temperatures are shown in the figures. The pellets were placed in the sample holder between the gold-plated brass disk electrodes 13 mm in diameter.

3. Results and Discussion

In the first step of preparation, the *p*-phenylenediamine was intercalated into the MMT gallery, replacing Na^+ cations of Na^+-MMT with *p*-phenylenediamine cations. After the oxidative polymerization with APS, the amount of MMT in the resulting composites, listed in Table 1, was evaluated from TGA analysis (Figure 1). The results clearly demonstrate that even with a significant excess of monomers in the polymerization mixture, just around 7–8 wt% of PDA (Table 1) was intercalated into MMT and the rest remained in the surrounding aqueous medium and was removed later as a by-product during the purification procedure. This can be explained by the limited amount of PPDA that can be formed within the MMT gallery, based on limitations imposed by cation exchange in MMT. Additionally, when an excess of PDA was used, the MMT surface became coated with PPDA film, and the amount of PPDA in the composite reached 18–19 wt% (Table 1). These results are also in good agreement with the previously demonstrated synthesis of polyaniline/MMT

composites [8]. The amount of MMT in the composites reached a plateau of ~93 wt% when less than ~25 wt% of PDA was used in the polymerization mixture; however, the properties and nature of such composites differ and are discussed below.

The morphology of both pristine components, MMT and PPDA, and their composites was investigated by SEM (Figure 2). Pristine MMT consists of flake-like particles of irregular shape (Figure 2a), while PPDA possesses globular morphology (Figure 2b), as already described in the literature [24]. After composite preparation, the morphology of MMT did not show considerable changes even at an excess of monomers (Figure 2c,d). No globular particles of PDPA were observed either. This confirms that the PPDA/MMT composites contain only PDPA embedded within the MMT galleries, or as a thin film covering MMT flakes, which cannot be seen in SEM. Free PPDA precipitate was evidently removed during the washing procedure.

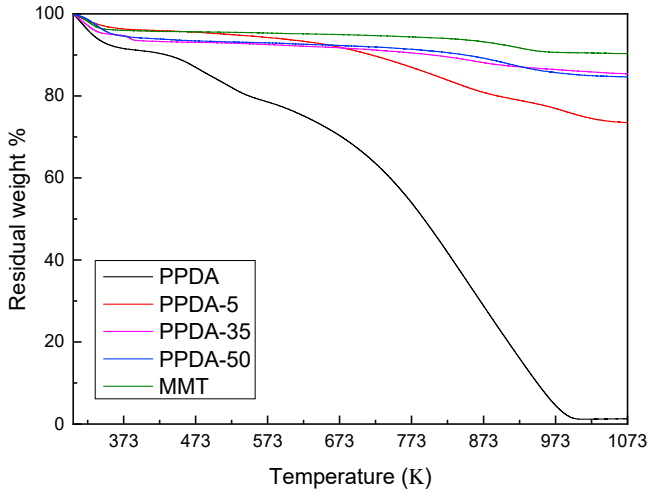

Figure 1. TGA curves of pristine MMT, PPDA and their composites.

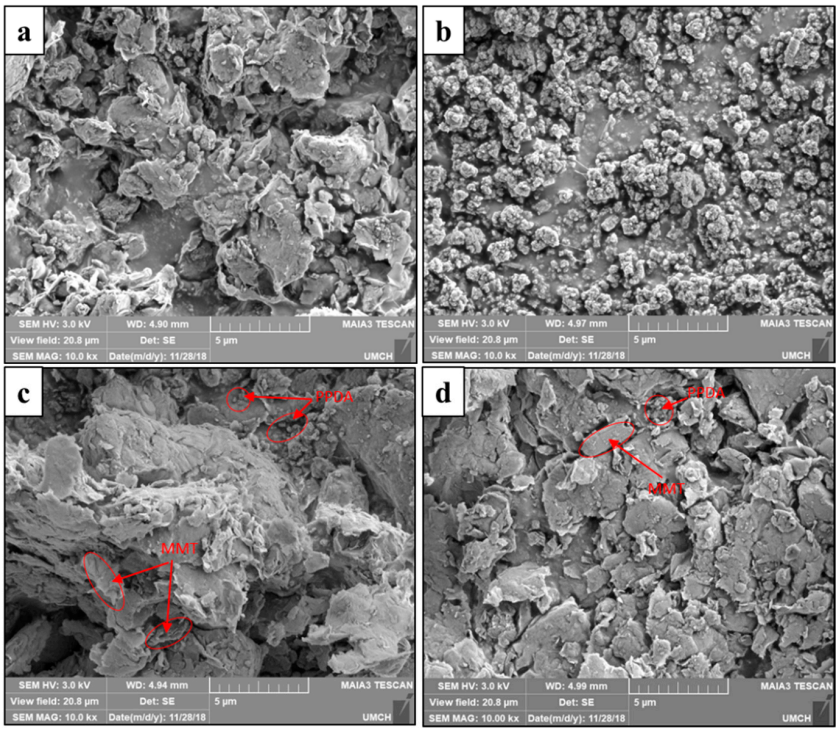

Figure 2. Scanning electron micrographs of pristine (**a**) MMT and (**b**) PPDA, and their composites prepared with various amounts of MMT: (**c**) PPDA-5 and (**d**) PPDA-50.

Table 1. The montmorillonite content and DC conductivity of PPDA/MMT composites.

Sample Code	PDA Content in Polymerization Mixture, wt%	MMT Content in Polymerization Mixture, wt%	PPDA Content in Composites, wt%	MMT Content in Composites, wt%	Conductivity, S cm^{-1} (Measured by Van der Pauw Method)	Activation Energy (Ea) (eV)		
						Evaluated from M″ vs. f	Evaluated from DC Conductivity vs. 1/T	
							High Temperature Region	Low Temperature Region
PPDA	100	0	100	0	7×10^{-11}	0.57	0.64	0.02
PPDA-2	64	36	19	81	3×10^{-11}	-	-	-
PPDA-5	42	58	18	82	1×10^{-11}	0.69	0.58	0.05
PPDA-10	26	74	8	92	2.5×10^{-8}	-	-	-
PPDA-15	19	81	8	92	3.4×10^{-8}	-	-	-
PPDA-25	13	87	7	93	2.2×10^{-7}	-	-	-
PPDA-35	9	91	6	94	1×10^{-6}	0.44	0.34	0.06
PPDA-50	7	93	7	93	9.2×10^{-7}	0.54	0.42	0.12

The DC conductivity (Table 1) of all composites was found to be higher than for pristine PPDA (7×10^{-11} S cm^{-1}), reaching ~10^{-6} S cm^{-1}, the value close to pure MMT, refs. [32,33] for PPDA-35, where a higher amount of MMT was used in the polymerization mixture.

3.1. X-ray Diffraction Analysis

XRD patterns of pristine MMT and PPDA and their composites with different amounts of MMT are presented in Figure 3. For pristine MMT, a well-defined (001) Bragg reflection at 2θ = 8.41° was observed, corresponding to a basal spacing d of 10.5 Å. For the composites, the reflection peaks of the (001) plane were displaced towards the lower 2θ values, which denotes the basal spacing expansion with respect to the pure MMT. The biggest change in basal spacing was observed for samples containing the lowest amount of MMT (PPDA-2 and PPDA-5), for which d = 12.5 Å. The basal spacing expresses the sum of the thickness of one aluminosilicate layer and interlayer spacing, which can be affected by the size and orientation of interlayer ions. Assuming the thickness of the aluminosilicate layer of 9.8 Å [34], the interlayer spacing for PPDA-2 and PPDA-5 composites expanded from 0.7 Å (for pure MMT) to 2.7 Å. This is a consequence of the intercalation process of PPDA chains in between the clay layers. The (001) reflections were in these cases sharp and narrow, indicating that the distribution of PPDA chains in the MMT galleries was uniform. A smaller increase in basal spacing was observed for samples containing a bigger amount of clay, reaching d = 11.7 Å for the PPDA-50 sample. Moreover, the (001) diffraction peaks became much broader and less intense, which may suggest an inhomogeneous distribution of the polymer chains in the interlayers of MMT and possible partial exfoliation of MMT. These results suggest that the swelling of the MMT is related to the amount of PDA able to penetrate into MMT layers. A small signal around $2\theta = 8.7°$, visible in composite patterns, probably came from a small amount of MMT that was not intercalated during the synthesis of PPDA. The shift from 8.41° to 8.7° can be related to a decrease in basal spacing d, caused by the leaching of the interlayer cations [35]. The lack of this peak in the PPDA-50 pattern also suggests the possible partial exfoliation of MMT.

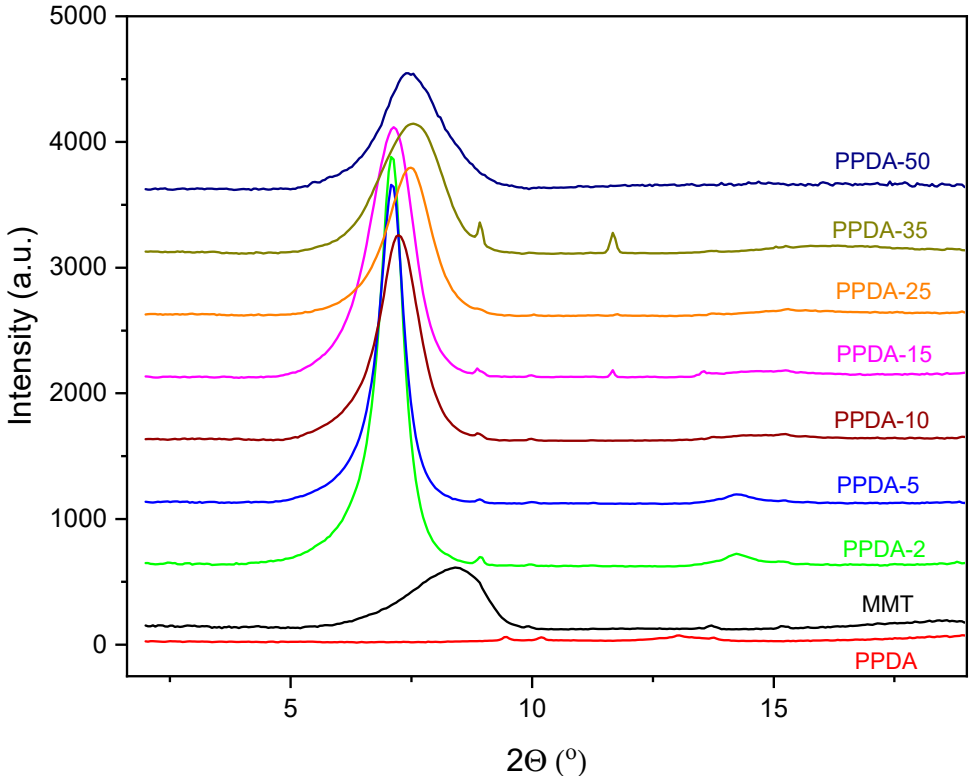

Figure 3. XRD patterns of pristine MMT, PPDA and their composites.

3.2. Infrared and Raman Spectroscopies

The FTIR spectra of the PPDA/MMT composites (Figure 4) mainly display the features of the MMT component: 1440 cm^{-1} (CO3 stretching of calcite impurity), 1035 cm^{-1} (Si–O stretching) with shoulders at 1120 cm^{-1} (Si–O stretching) and 915 cm^{-1} (Al–Al–OH bending), 520 cm^{-1} (Al–O–Si bending) with a shoulder at 625 cm^{-1}, 465 cm^{-1} (Si–O–Si bending) and 1635 cm^{-1} (bending vibrations of water molecules hydrogen bonded to MMT or residual moisture in KBr) [36]. The bands associated with the PPDA component are well resolved only in the spectrum of the composite with the lowest amount of MMT (PPDA-5), and therefore the molecular structure of the PDA oxidation products will be discussed in detail based on Raman spectroscopy. However, let us mention the peak at 1656 cm^{-1} in the spectrum of PPDA-50. We suspect this band can be related to C=O stretching of the benzoquinone structure [37–39].

For the Raman spectroscopy (Figure 5), excitation at 514 nm was chosen to minimize the background caused by MMT fluorescence. The spectrum of the neat PPDA resembles the PANI-like structure reported many times in previous literature. The main bands are observed at 1595 cm^{-1} (C=C stretching in a quinonoid ring), 1530 cm^{-1} (N–H stretching), 1330 cm^{-1} (C~$N^{+\bullet}$ stretching vibration related to a delocalized polaron structure), 1180 cm^{-1} (C–H deformation), 570 cm^{-1}, 500 cm^{-1}, 455 cm^{-1} and 410 cm^{-1} (ring deformations) [8,23,40,41]. The spectra of all composites mainly show peaks related to MMT, but there are also some peaks, visible particularly in the PPDA-50 composite with the highest amount of MMT, which occur neither in PPDA nor in MMT. Namely, the relatively strong and sharp peak at 1686 cm^{-1} observed for the PPDA-50 composite has not yet been observed for any PANI of PPDA-related material. This band can be related to the NH_2 end-groups [42]. The strong peak at 1637 cm^{-1} dominates the spectrum. It was formerly assigned to ring stretching in phenazine-like [43] or oxazine-like structures [44]; however, in detailed spectroscopy studies of phenazine structures [43,45], this peak was only observed in neutral N-phenyl phenazine. However, due to the expected high local acidity in the MMT interlayer area, N-phenyl phenazine should occur there only in protonated form.

The strong peak at 1637 cm^{-1} could also originate in NH deformation vibrations [46] or benzenoid ring stretching [47,48], which seems to be a more likely assignment. The band at 1515 cm^{-1} is assigned to the N–H deformation of the PANI-like structure [49–52]. The bands at 1485 and 1457 cm^{-1} belong to C=N stretching in quinonoid units [53], and N=N stretching in an azobenzene structure can contribute to the latter [54]. The bands at 1393, 1370 and 1345 cm^{-1} can be attributed to C~$N^{+\bullet}$ stretching in polaron structures with varying delocalization lengths [40,55]. The bands at 1265 and 1200 cm^{-1} belong to C–H deformation in quinonoid and benzenoid rings, respectively. The band at 455 cm^{-1} is due to out-of-plane ring deformations [40]. In conclusion, a generally PANI-like structure was observed in the PPDA-50 composite, but given the strong signal of NH_2 groups and the contribution of highly localized polarons, the material intercalated in MMT seems to be of oligomer nature. The Raman spectra of PPDA-35 and PPDA-5 composites reflect both features of the oligomer observed in PPDA-50 and of the PPDA polymer, with the intensity of the above discussed peaks at 1393, 1370, 1686 and 1637 cm^{-1} increasing with the MMT content.

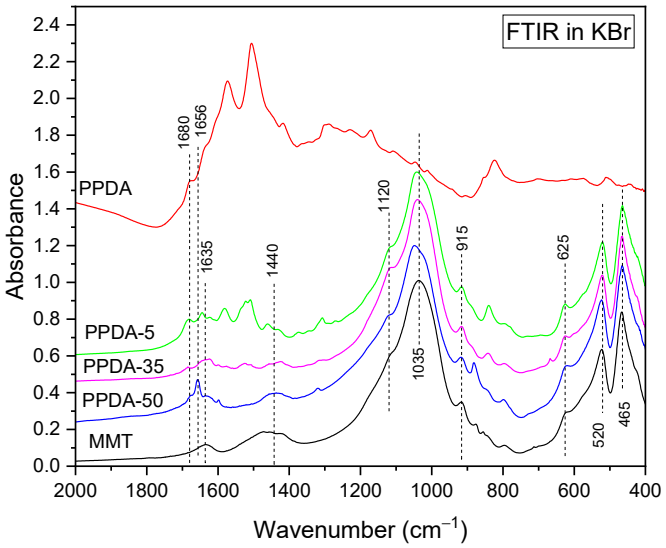

Figure 4. FTIR spectra of selected MMT, PPDA and their composites. The spectra were baseline corrected, normalized and shifted for clarity.

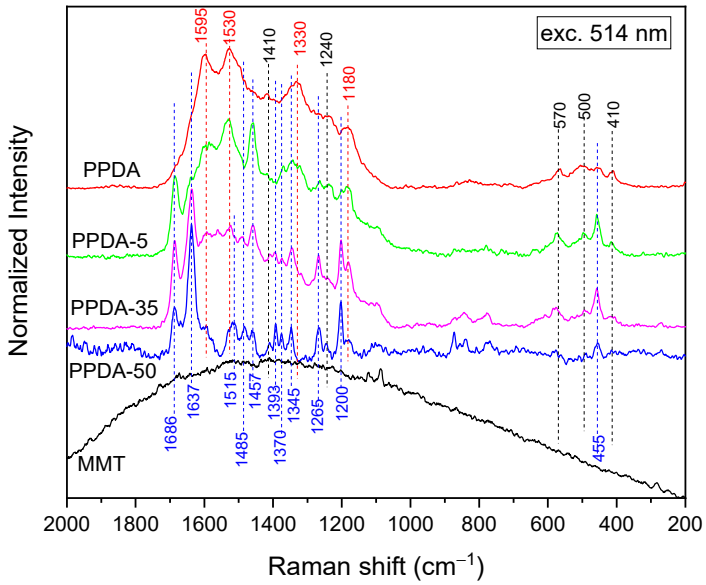

Figure 5. Raman spectra of selected MMT, PPDA and their composites excited with the 514 nm laser line. The spectra were baseline corrected, normalized and shifted for clarity.

3.3. Impedance Spectroscopy

The real part (ε') and imaginary part (ε'') of complex permittivity ε^* ($\varepsilon^* = \varepsilon' - j\varepsilon''$) measured as a function of frequency (10^{-2} Hz to 10^7 Hz) at different temperatures (113 K $\leq$ T $\leq$ 433 K) are shown in Figures 6 and 7. When interpreting these data, we should consider conductivity being contributed by both the electronic and ionic parts. At lower frequencies, an increase in the dielectric constant with decreasing frequency is typical for electrode polarization due to the presence of mobile ions. In lower frequency regions, different values of slopes in ε'' vs. f curves imply ion transport if slope~ -1, whereas slope > -1 means the polarization effect. The decreasing value of slope at a higher frequency represents the caged movement of ions, i.e., ion–ion interactions and short time regime correlations [56]. The Maxwell–Wagner model can be utilized to understand the dielectric response of these materials [57]. These polarizations are also temperature-dependent, as shown in Figure 7. As the temperature increases, ion dissociation takes place, which ultimately results in an increase in dielectric polarization. Moreover, interfacial polarization also occurs because of the buildup of charges at the grain boundaries. At a lower temperature, dissociated ions are not available, and a small value of permittivity is assigned to polarons dominant in PPDA, which are almost in frozen condition. With the gradual increase in temperature, these polarons inside grains separated by grain boundaries result in the Maxwell–Wagner effect at lower frequencies. In the case of PPDA-5, the value of ε' and ε'' is small due to the smaller content of MMT, which is directly proportional to water content since water molecules are captured in between MMT layers and form ionic dipoles [57]. This is also evidenced in Figure 6c,d, where the ε' value decreases after exceeding 353 K since water starts to evaporate [58]. The variation in the dissipation factor ($\tan\delta = \varepsilon''/\varepsilon'$) with temperature at different frequencies decreases with increasing frequency at all temperatures, which is in a good agreement with Koop's phenomenological model [59]. The composites PPDA-35 and PPDA-50 attain a low value of $\tan\delta$, which is due to the partial exfoliation of the MMT gallery as evidenced by XRD.

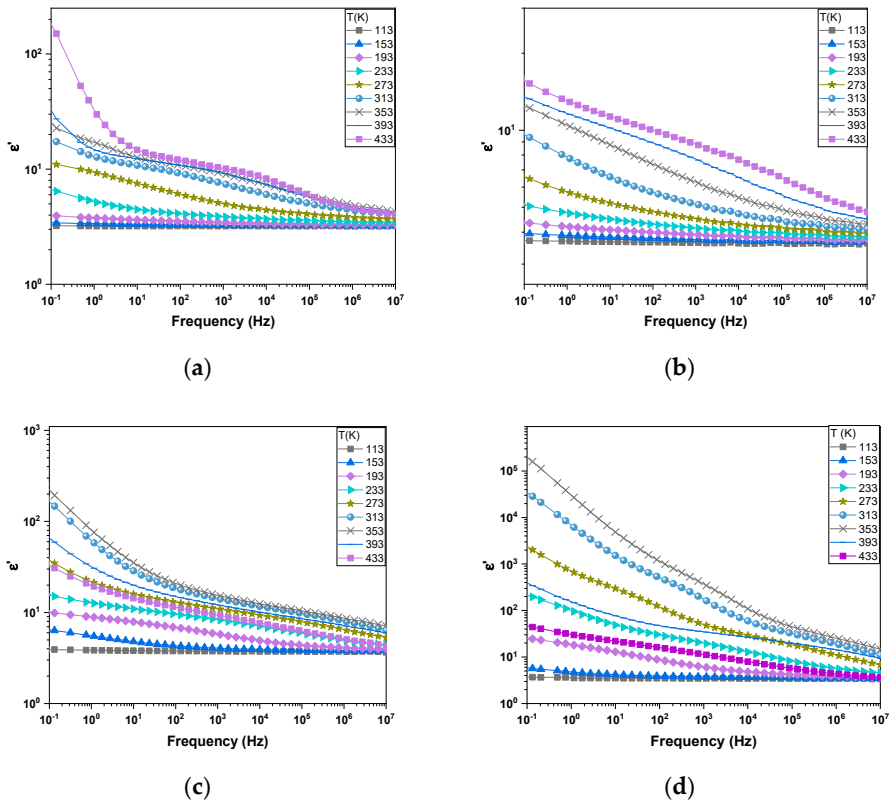

Figure 6. Variations in real part of permittivity with frequency at different temperatures for (**a**) PPDA and PPDA/MMT composites: (**b**) PPDA-5, (**c**) PPDA-35 and (**d**) PPDA-50.

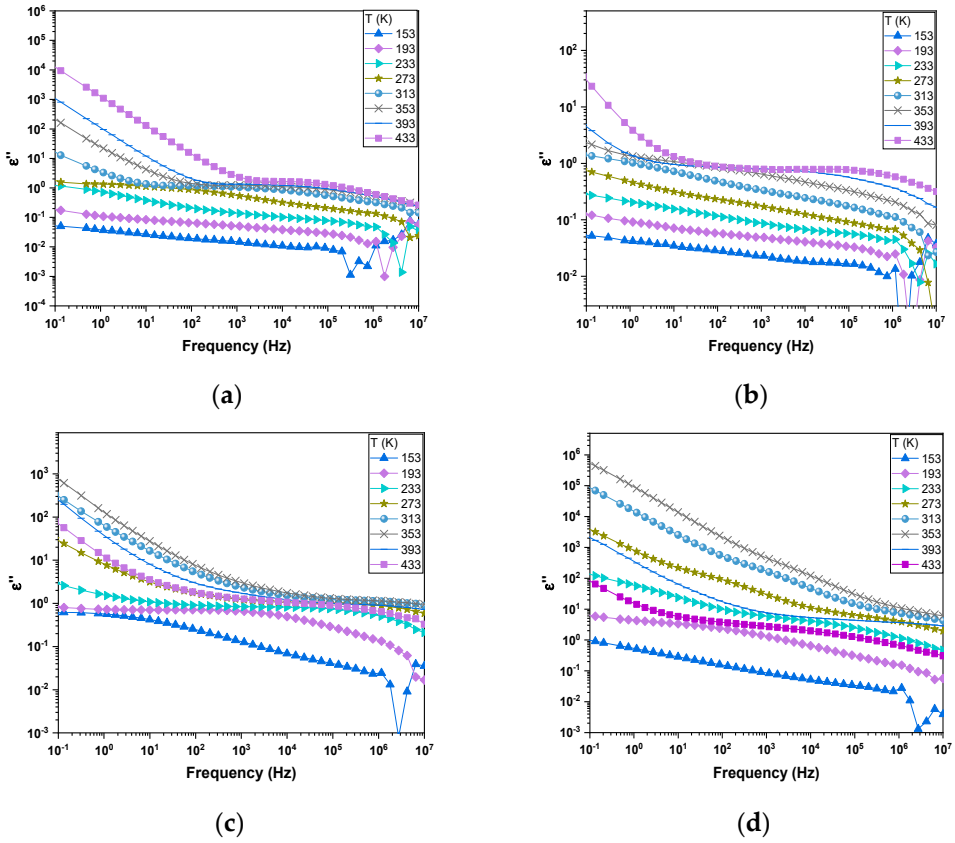

Figure 7. Variations in imaginary part of permittivity with frequency at different temperatures for (**a**) PPDA and PPDA/MMT composites: (**b**) PPDA-5, (**c**) PPDA-35 and (**d**) PPDA-50.

To better discuss relaxation processes of the impedance spectra and suppress the electrode polarization effects, the complex dielectric modulus was obtained from the real and imaginary part of the permittivity.

$$M^* = \frac{1}{\varepsilon^*} = \frac{1}{(\varepsilon - j\varepsilon'')} = M' + jM'' = \frac{\varepsilon'}{(\varepsilon')^2 + (\varepsilon'')^2} + j\frac{\varepsilon''}{(\varepsilon')^2 + (\varepsilon'')^2} \quad (1)$$

where M' and M'' are the real part and imaginary part of the complex dielectric modulus (M*), respectively [60]. Figure 8 shows the frequency dependence of the imaginary part of the modulus at different temperatures. In fact, the low frequency peak corresponds to the long-range migration of ions, whereas the high frequency peak represents spatially confined ions within potential wells and localized short distance motion within the domains [56].

The values of relaxation time $\tau = \frac{1}{w_{max}}$ corresponding to the frequency of the low-frequency maximum f_{max} of the M'' frequency spectrum are plotted in Figure 9 as a function of temperature. This follows an Arrhenius law with the activation energy Ea being 0.56, 0.69, 0.44 and 0.53 eV for pristine poly(*p*-phenylenediamine), PPDA-5, PPDA-35 and PPDA-50, respectively.

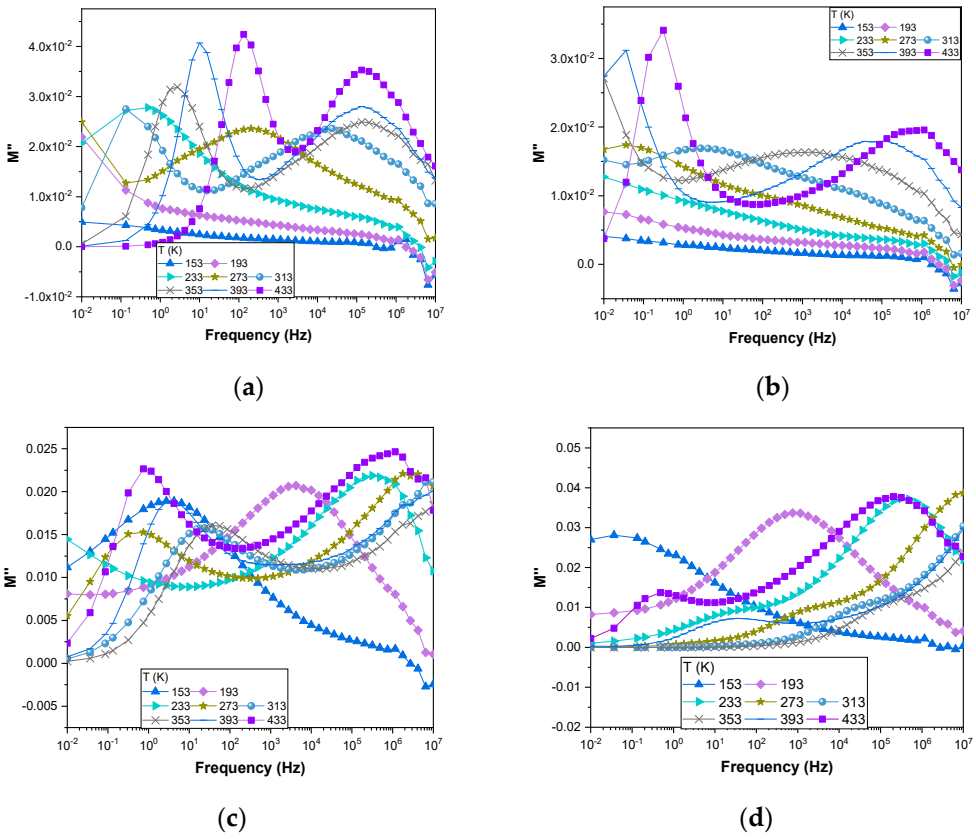

Figure 8. Variations in imaginary part of modulus with frequency with temperature for (**a**) PPDA and PPDA/MMT composites: (**b**) PPDA-5, (**c**) PPDA-35 and (**d**) PPDA-50.

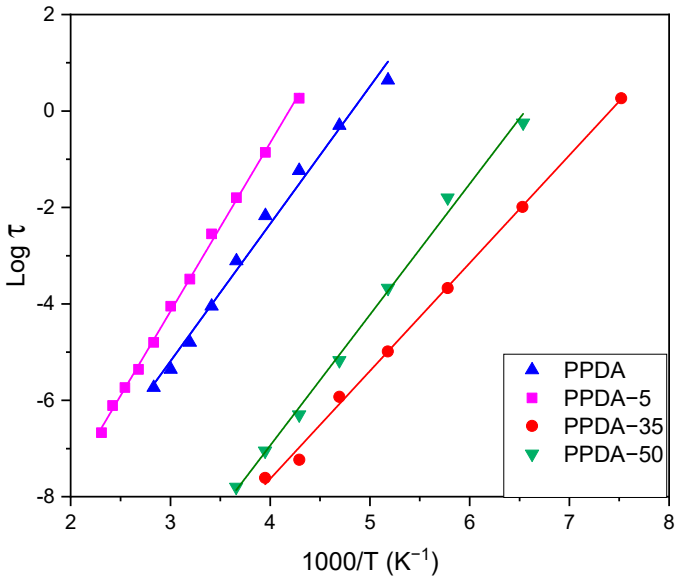

Figure 9. Plot of relaxation time vs. reciprocal temperature for PPDA and PPDA/MMT composites.

The frequency dependences of the real part of conductivity at different temperatures are shown in Figure 10 for the polymer and composites and Figure 11 for montmorillonite. The real part of the conductivity obeys a power law known as Jonscher's law given by Equation (2) within the considered frequency and temperature ranges:

$$\sigma' = \sigma_{dc} + A\omega^s \quad (2)$$

where σ_{dc} is the DC conductivity obtained by extrapolating σ' to the low frequency limit. The term Aw^s is the dispersive component of AC conductivity, which represents the degree of interaction between mobile ions and the lattices. Here, A is the pre-exponential factor describing the strength of the polarizability, and s, which is a power law exponent, within $0 < s < 1$, is a measure of the correlation degree. The behavior of s on temperature provides an insight into the conduction mechanism. The power law dependences point to inhomogeneity in the composites and that the ion transport plays the crucial role. At room temperature and lower frequencies, the composites PPDA-35 and PPDA-50 show a higher value of conductivity than pristine materials. The same is observed in the case of DC conductivity measured with the four-probe van der Pauw method (Table 1). This increase in conductivity is related to the intercalation of PPDA chains between the layers of MMT, which leads to higher ordering in polymer chains causing more a compact structure compared to pristine PPDA. The higher DC conductivity values obtained from the DC four-probe method compared to impedance spectroscopy can be explained by the elimination of the contact resistance in the former case. Figure 12 shows the Arrhenius plots of σ_{dc} against $1/T$ for all the samples according to Equation (3):

$$\sigma_{dc} = \sigma_0 \exp\left(-\frac{E_{dc}}{k_B T}\right) \quad (3)$$

The calculated values of activation energy (E_{dc}) are listed in Table 1. It is seen that different activation energies exist at high and low temperatures, which indicates the dissociation of ions with an increase in temperature, hence increasing the conductivity at high temperatures, but at a low temperature, the ions do not have enough energy to hop to neighboring sites and remain caged. For the sample PPDA-35 and PPDA-50, the change in the slope of the curve occurs at 200 K, which is attributed to the motion of the water–polymer complex in the amorphous region [61], whereas for pristine PPDA and PPDA-5 it is at 273 K, revealing the existence of phase transition that might be associated with alternation in local structures. The lowest activation energy is found for the sample PPDA-35, which means less energy is required to migrate the ions from the binding coordinating site to another site. The decrease in conductivity for PPDA-35 and PPDA-50 above 353 K is again associated with the evaporation of intercalated water. For the low temperature region where the mobile charge carriers are mainly polarons but not ions, the activation energies are sufficiently low and following the opposite trend compared to that in the higher temperature region. Pristine PPDA has the lowest and the composites with more MMT content have higher values of activation energy since the movements of polarons inherited in the polymer are hindered with the addition of MMT, and DC conductivity is thus not only a function of temperature as expressed by the Arrhenius equation [62]. Additionally, pristine PPDA shows intermediate activation energy, which is attributed to the contribution of polymer segmental motion.

From Figure 12, it is clearly seen that two different activation energies exist at different temperature regions. This suggests that two conduction mechanisms prevail, one at lower temperature (polaronic) and another at high temperature (ionic). The temperature dependences of s values obtained from the linear fit of the σ_{ac} frequency dependencies at the linear region are plotted in Figure 13 for the lower temperature region. To study the conduction mechanism at lower temperatures, various models have been proposed in the literature to explain the predominant conduction mechanisms according to the shape of the temperature dependence of exponent s. For the case of s increasing with increasing temperature, a small polaron conduction mechanism has been suggested, whereas if s decreases with increasing temperature then the mechanism is called correlated barrier hopping. If s is independent with temperature, then quantum mechanical tunneling is expected [63]. In our case, the exponent s decreases as the temperature increases, which is attributed to

correlated barrier hopping (CBH) of polarons. The frequency dependence according to the CBH model can be expressed by Equation (2), with s given by Equation (4) [64].

$$s = 1 - \frac{6k_BT}{\left[W_M - k_BTln\left(\frac{1}{\omega\tau_0}\right)\right]} \tag{4}$$

where W_M is the polaron binding energy, τ_0 is the characteristic relaxation time and k_B is the Boltzmann's constant. For large W_M/K_BT, Equation (4) can be deduced as:

$$W_M = \frac{6k_BT}{1-s} \tag{5}$$

The values of W_M calculated at the low temperature region are shown in the inset of Figure 13 using the experimental values of s. The values obtained indicate that single polarons are the major charge carriers but not bipolarons since for bipolaronic transport values of W_M must be almost four times higher [64]. It is seen that at the lowest measured temperature, these single polarons have a higher binding energy for pristine PPDA and PPDA-5 than in the composites PPDA-35 and PPDA-50, but after the gradual increase in temperature similar values are attained.

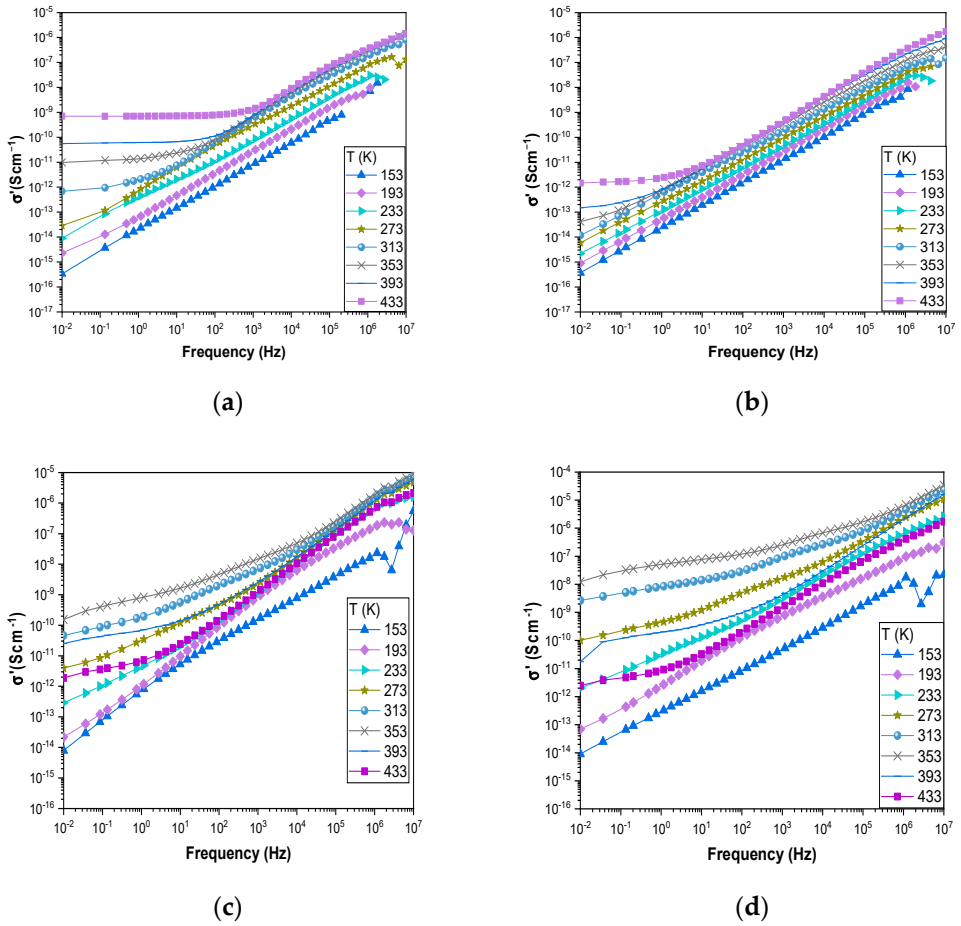

Figure 10. Variations in real part of AC conductivity with frequency at different temperatures for (**a**) PPDA and PPDA/MMT composites: (**b**) PPDA-5, (**c**) PPDA-35 and (**d**) PPDA-50.

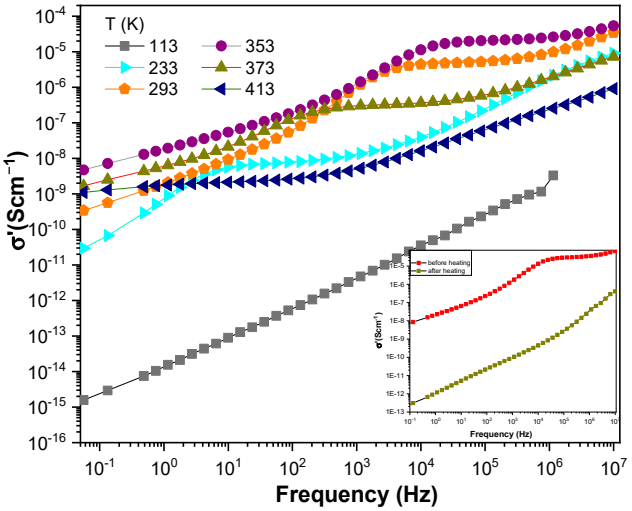

Figure 11. Variations in real part of AC conductivity with frequency at different temperatures for the pure montmorillonite. Inset shows the variation in conductivity at 293 K before and after heating to 433 K.

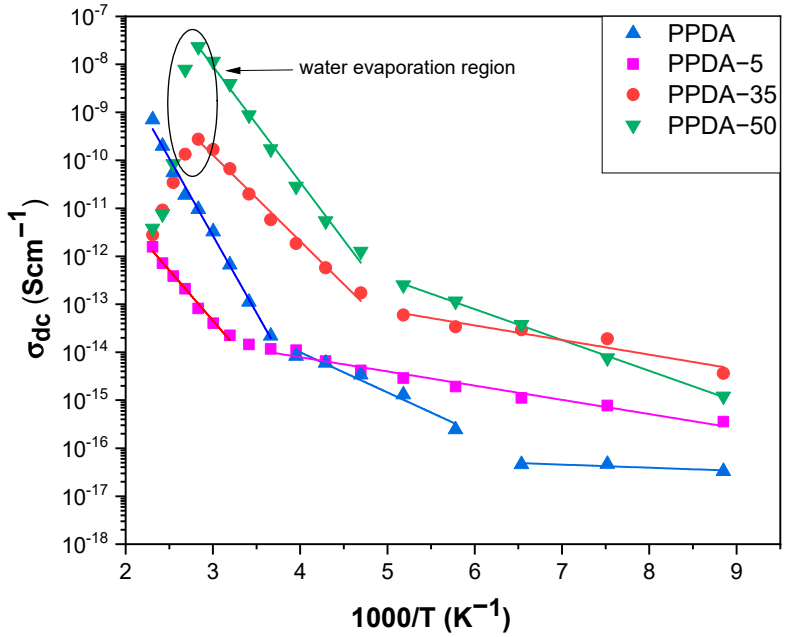

Figure 12. Variation in DC conductivity with reciprocal temperature. The solid lines represent fitting according to Arrhenius equation.

As seen in Figure 11, the dependence of the real part of conductivity shows the plateau that allows the determination of DC conductivity of ~10^{-6} S/cm, which is in a good agreement with values reported in the literature [32,33]. The conductivity decreases above 353 K due to the evaporation of intercalated water. This is similar to the behavior described above for the composites with a higher content of MMT. The conductivity decreases drastically after heating to 433 K, referring to the humidity dependence of montmorillonite and ions playing a dominant role in the conduction mechanism [65,66].

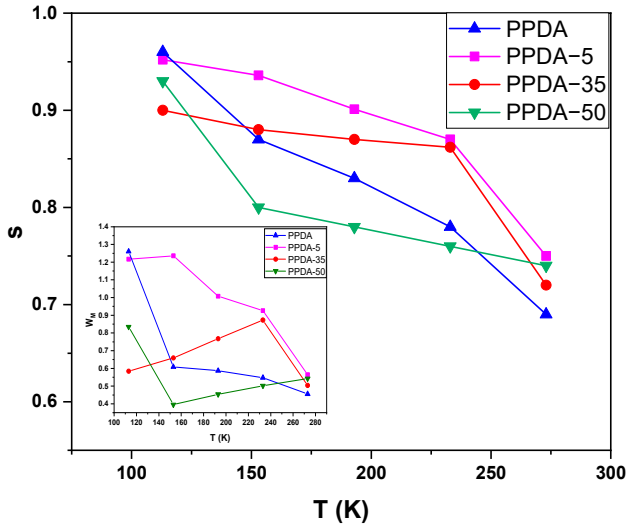

Figure 13. Variation in exponent parameter s with temperature for PPDA and PPDA/MMT composites. The solid lines are drawn for clarity. Inset shows the variation in W_M with temperature.

4. Conclusions

PPDA/MMT composites were successfully synthesized by a two-step procedure, viz., the intercalation of monomers, followed by oxidative polymerization. Even though, contrary to the initial expectations, the introduction of various amounts of MMT into the polymerization mixture led to similar amounts of the MMT in obtained composites, the variation in the initial monomer-to-MMT ratio allowed us to obtain series of composites with diverse conductivity. Spectroscopy characterization revealed that such composites differ in the polymeric or oligomeric nature of the organic part. Both AC and DC conductivities of composites were found to be higher than the corresponding polymer. Impedance spectroscopy studied over a wide range of frequency and temperature points to the change in the conduction mechanism from polaronic conduction arising from the polymer in low temperatures to ionic conduction in higher temperatures inherited in MMT. Such composites can be applied as anticorrosion coatings, sensors, electromagnetic shielding or in electrorheology.

Author Contributions: Conceptualization, U.A., P.B. and J.P.; methodology, U.A. and J.P.; formal analysis, U.A. and M.A.T.; investigation, U.A., Z.M. and M.K.; resources, P.B. and J.P.; writing—original draft preparation, U.A.; writing—review and editing, U.A., P.B. and J.P.; visualization, U.A. and M.A.T.; supervision, J.P.; funding acquisition, P.B. All authors have read and agreed to the published version of the manuscript.

Funding: The authors wish to thank the Czech Science Foundation (21-01401S) for the financial support.

Data Availability Statement: We have no depository of publicly archived datasets analyzed or generated during the study. Data are available on request; please contact authors on their e-mail addresses.

Acknowledgments: The authors acknowledge Wei Lyu and Markéta Karbusická for sample preparation and TGA measurement, respectively.

Conflicts of Interest: The authors declare no conflict of interest.

References

1. Faustini, M.; Nicole, L.; Ruiz-Hitzky, E.; Sanchez, C. History of Organic–Inorganic Hybrid Materials: Prehistory, Art, Science, and Advanced Applications. *Adv. Funct. Mater.* **2018**, *28*, 1704158. [CrossRef]
2. Kenane, A.; Galca, A.-C.; Matei, E.; Yahiaoui, A.; Hachemaoui, A.; Benkouider, A.M.; Bartha, C.; Istrate, M.C.; Galatanu, M.; Rasoga, O.; et al. Synthesis and Characterization of Conducting Aniline and O-Anisidine Nanocomposites Based on Montmorillonite Modified Clay. *Appl. Clay Sci.* **2020**, *184*, 105395. [CrossRef]

3. Li, S.; Fan, Z. Encapsulation Methods of Sulfur Particles for Lithium-Sulfur Batteries: A Review. *Energy Storage Mater.* **2021**, *34*, 107–127. [CrossRef]
4. Li, S.; Leng, D.; Li, W.; Qie, L.; Dong, Z.; Cheng, Z.; Fan, Z. Recent Progress in Developing Li2S Cathodes for Li–S Batteries. *Energy Storage Mater.* **2020**, *27*, 279–296. [CrossRef]
5. Li, S.; Fan, Z. Nitrogen-Doped Carbon Mesh from Pyrolysis of Cotton in Ammonia as Binder-Free Electrodes of Supercapacitors. *Microporous Mesoporous Mater.* **2019**, *274*, 313–317. [CrossRef]
6. Hosseini, M.G.; Raghibi-Boroujeni, M.; Ahadzadeh, I.; Najjar, R.; Seyed Dorraji, M.S. Effect of Polypyrrole–Montmorillonite Nanocomposites Powder Addition on Corrosion Performance of Epoxy Coatings on Al 5000. *Prog. Org. Coat.* **2009**, *66*, 321–327. [CrossRef]
7. Oraon, R.; De Adhikari, A.; Tiwari, S.K.; Nayak, G.C. Enhanced Specific Capacitance of Self-Assembled Three-Dimensional Carbon Nanotube/Layered Silicate/Polyaniline Hybrid Sandwiched Nanocomposite for Supercapacitor Applications. *ACS Sustain. Chem. Eng.* **2016**, *4*, 1392–1403. [CrossRef]
8. Bober, P.; Stejskal, J.; Špírková, M.; Trchová, M.; Varga, M.; Prokeš, J. Conducting Polyaniline–Montmorillonite Composites. *Synth. Met.* **2010**, *160*, 2596–2604. [CrossRef]
9. De León-Almazán, C.M.; Estrada-Moreno, I.A.; Olmedo-Martínez, J.L.; Rivera-Armenta, J.L. Semiconducting Elastomers Based on Polyaniline/Clay Nanocomposites and SEBS Obtained by an Alternative Processing Technique. *Synth. Met.* **2020**, *268*, 116460. [CrossRef]
10. Kazim, S.; Ahmad, S.; Pfleger, J.; Plestil, J.; Joshi, Y.M. Polyaniline–Sodium Montmorillonite Clay Nanocomposites: Effect of Clay Concentration on Thermal, Structural, and Electrical Properties. *J. Mater. Sci.* **2012**, *47*, 420–428. [CrossRef]
11. Contri, G.; Barra, G.M.O.; Ramoa, S.D.A.S.; Merlini, C.; Ecco, L.G.; Souza, F.S.; Spinelli, A. Epoxy Coating Based on Montmorillonite-Polypyrrole: Electrical Properties and Prospective Application on Corrosion Protection of Steel. *Prog. Org. Coat.* **2018**, *114*, 201–207. [CrossRef]
12. Vilímová, P.; Kulhánková, L.; Peikertová, P.; Mamulová Kutláková, K.; Vallová, S.; Koníčková, H.; Plaček, T.; Tokarský, J. Effect of Montmorillonite/Polypyrrole Ratio and Oxidizing Agent on Structure and Electrical Conductivity of Intercalated Nanocomposites. *Appl. Clay Sci.* **2019**, *168*, 459–468. [CrossRef]
13. Aradilla, D.; Estrany, F.; Azambuja, D.S.; Casas, M.T.; Puiggali, J.; Ferreira, C.A.; Alemán, C. Conducting Poly(3,4-Ethylenedioxythiophene)-Montmorillonite Exfoliated Nanocomposites. *Eur. Polym. J.* **2010**, *46*, 977–983. [CrossRef]
14. Do Nascimento, G.M.; Sestrem, R.H.; Temperini, M.L.A. Structural Characterization of Poly-Para-Phenylenediamine–Montmorillonite Clay Nanocomposites. *Synth. Met.* **2010**, *160*, 2397–2403. [CrossRef]
15. Ramya, E.; Rajashree, C.; Nayak, P.L.; Narayana Rao, D. New Hybrid Organic Polymer Montmorillonite/Chitosan/Polyphenylene diamine Composites for Nonlinear Optical Studies. *Appl. Clay Sci.* **2017**, *150*, 323–332. [CrossRef]
16. Rajapakse, R.M.G.; Murakami, K.; Bandara, H.M.N.; Rajapakse, R.M.M.Y.; Velauthamurti, K.; Wijeratne, S. Preparation and Characterization of Electronically Conducting Polypyrrole-Montmorillonite Nanocomposite and Its Potential Application as a Cathode Material for Oxygen Reduction. *Electrochim. Acta* **2010**, *55*, 2490–2497. [CrossRef]
17. de Barros, A.; Constantino, C.J.L.; da Cruz, N.C.; Bortoleto, J.R.R.; Ferreira, M. High Performance of Electrochemical Sensors Based on LbL Films of Gold Nanoparticles, Polyaniline and Sodium Montmorillonite Clay Mineral for Simultaneous Detection of Metal Ions. *Electrochim. Acta* **2017**, *235*, 700–708. [CrossRef]
18. Zheng, H.; Liu, M.; Yan, Z.; Chen, J. Highly Selective and Stable Glucose Biosensor Based on Incorporation of Platinum Nanoparticles into Polyaniline-Montmorillonite Hybrid Composites. *Microchem. J.* **2020**, *152*, 104266. [CrossRef]
19. Špírková, M.; Bober, P.; Kotek, J.; Stejskal, J. Bi-Hybrid Coatings: Polyaniline-Montmorillonite Filler in Organic-Inorganic Polymer Matrix. *Chem. Pap.* **2013**, *67*, 1020–1027. [CrossRef]
20. Ben Ali, M.; Wang, F.; Boukherroub, R.; Lei, W.; Xia, M. Phytic Acid-Doped Polyaniline Nanofibers-Clay Mineral for Efficient Adsorption of Copper (II) Ions. *J. Colloid Interface Sci.* **2019**, *553*, 688–698. [CrossRef] [PubMed]
21. Pham, Q.L.; Haldorai, Y.; Nguyen, V.H.; Tuma, D.; Shim, J.-J. Facile Synthesis of Poly(p-Phenylenediamine)/MWCNT Nanocomposites and Characterization for Investigation of Structural Effects of Carbon Nanotubes. *Bull. Mater. Sci.* **2011**, *34*, 37–43. [CrossRef]
22. Lakouraj, M.M.; Zare, E.N.; Moghadam, P.N. Synthesis of Novel Conductive Poly(p-Phenylenediamine)/Fe_3O_4 Nanocomposite via Emulsion Polymerization and Investigation of Antioxidant Activity. *Adv. Polym. Technol.* **2014**, *33*, 21385:1–21385:7. [CrossRef]
23. Magdziarz, P.; Bober, P.; Trchová, M.; Morávková, Z.; Bláha, M.; Prokeš, J.; Stejskal, J. Conducting Composites Prepared by the Reduction of Silver Ions with Poly(p-Phenylenediamine). *Polym. Int.* **2015**, *64*, 496–504. [CrossRef]
24. Minisy, I.M.; Zasońska, B.A.; Petrovský, E.; Veverka, P.; Šeděnková, I.; Hromádková, J.; Bober, P. Poly(p-Phenylenediamine)/Maghemite Composite as Highly Effective Adsorbent for Anionic Dye Removal. *React. Funct. Polym.* **2020**, *146*, 104436. [CrossRef]
25. Wang, Y.; Wang, H.; Zhang, T.C.; Yuan, S.; Liang, B. N-Doped Porous Carbon Derived from RGO-Incorporated Polyphenylenediamine Composites for CO_2 Adsorption and Supercapacitors. *J. Power Sources* **2020**, *472*, 228610. [CrossRef]
26. Stejskal, J. Polymers of Phenylenediamines. *Prog. Polym. Sci.* **2015**, *41*, 1–31. [CrossRef]
27. Bláha, M.; Trchová, M.; Morávková, Z.; Humpolíček, P.; Stejskal, J. Semiconducting Materials from Oxidative Coupling of Phenylenediamines under Various Acidic Conditions. *Mater. Chem. Phys.* **2018**, *205*, 423–435. [CrossRef]

28. Khelifa, I.; Belmokhtar, A.; Berenguer, R.; Benyoucef, A.; Morallon, E. New Poly(o-Phenylenediamine)/Modified-Clay Nanocomposites: A Study on Spectral, Thermal, Morphological and Electrochemical Characteristics. *J. Mol. Struct.* **2019**, *1178*, 327–332. [CrossRef]
29. Nath, A.K.; Kumar, A. Scaling of AC Conductivity, Electrochemical and Thermal Properties of Ionic Liquid Based Polymer Nanocomposite Electrolytes. *Electrochim. Acta* **2014**, *129*, 177–186. [CrossRef]
30. Dong, Y.Z.; Kim, H.M.; Choi, H.J. Conducting polymer-based electro-responsive smart suspensions. *Chem. Pap.* **2021**, *75*, 5009–5034. [CrossRef]
31. Ates, M. A Review on Conducting Polymer Coatings for Corrosion Protection. *J. Adhes. Sci. Technol.* **2016**, *30*, 1510–1536. [CrossRef]
32. Slade, R.C.T.; Barker, J.; Hirst, P.R.; Halstead, T.K.; Reid, P.I. Conduction and Diffusion in Exchanged Montmorillonite Clays. *Solid State Ion.* **1987**, *24*, 289–295. [CrossRef]
33. Nj, G.; Jc, B. Conductivity in Na+-Montmorillonite and Li+-Montmorillonite as a Function of Equilibration Humidity. *Solid State Ion.* **1996**, *92*, 139–143.
34. Wu, L.; Cao, S.; Lv, G. Influence of Energy State of Montmorillonite Interlayer Cations on Organic Intercalation. *Adv. Mater. Sci. Eng.* **2018**, *2018*, 3489720. [CrossRef]
35. Krupskaya, V.V.; Zakusin, S.V.; Tyupina, E.A.; Dorzhieva, O.V.; Zhukhlistov, A.P.; Belousov, P.E.; Timofeeva, M.N. Experimental Study of Montmorillonite Structure and Transformation of Its Properties under Treatment with Inorganic Acid Solutions. *Minerals* **2017**, *7*, 49. [CrossRef]
36. Hayati-Ashtiani, M. Use of FTIR Spectroscopy in the Characterization of Natural and Treated Nanostructured Bentonites (Montmorillonites). *Part. Sci. Technol.* **2012**, *30*, 553–564. [CrossRef]
37. Becker, E.D. Raman Spectra of Isotopic Derivatives of *p*-Benzoquinone: Revised Vibrational Assignments. *J. Phys. Chem.* **1991**, *95*, 2818–2823. [CrossRef]
38. Stammreich, H.; Sans, T.T. Molecular Vibrations of Quinones. IV. Raman Spectra of P-Benzoquinone and Its Centrosymmetrically Substituted Isotopic Derivatives and Assignment of Observed Frequencies. *J. Chem. Phys.* **1965**, *42*, 920–931. [CrossRef] [PubMed]
39. Bláha, M.; Marek, F.; Morávková, Z.; Svoboda, J.; Brus, J.; Dybal, J.; Prokeš, J.; Varga, M.; Stejskal, J. Role of P-Benzoquinone in the Synthesis of a Conducting Polymer, Polyaniline. *ACS Omega* **2019**, *4*, 7128–7139. [CrossRef]
40. Trchová, M.; Morávková, Z.; Šeděnková, I.; Stejskal, J. Spectroscopy of Thin Polyaniline Films Deposited during Chemical Oxidation of Aniline. *Chem. Pap.* **2012**, *66*, 415–445. [CrossRef]
41. do Nascimento, G.M.; Constantino, V.R.L.; Landers, R.; Temperini, M.L.A. Spectroscopic Characterization of Polyaniline Formed in the Presence of Montmorillonite Clay. *Polymer* **2006**, *47*, 6131–6139. [CrossRef]
42. Baibarac, M.; Baltog, I.; Scocioreanu, M.; Ballesteros, B.; Mevellec, J.Y.; Lefrant, S. One-Dimensional Composites Based on Single Walled Carbon Nanotubes and Poly(o-Phenylenediamine). *Synth. Met.* **2011**, *161*, 2344–2354. [CrossRef]
43. Sestrem, R.H.; Ferreira, D.C.; Landers, R.; Temperini, M.L.A.; do Nascimento, G.M. Synthesis and Spectroscopic Characterization of Polymer and Oligomers of Ortho-Phenylenediamine. *Eur. Polym. J.* **2010**, *46*, 484–493. [CrossRef]
44. Brolo, A.G.; Sanderson, A.C. Surface-Enhanced Raman Scattering (SERS) from a Silver Electrode Modified with Oxazine 720. *Can. J. Chem.* **2011**, *82*, 1474–1480. [CrossRef]
45. Trchová, M.; Morávková, Z.; Dybal, J.; Stejskal, J. Detection of Aniline Oligomers on Polyaniline–Gold Interface Using Resonance Raman Scattering. *ACS Appl. Mater. Interfaces* **2014**, *6*, 942–950. [CrossRef]
46. Anto, P.L.; Panicker, C.Y.; Varghese, H.T.; Philip, D. Potential-Dependent SERS Profile of Orthanilic Acid on Silver Electrode. *J. Raman Spectrosc.* **2006**, *37*, 1265–1271. [CrossRef]
47. de Santana, H.; Quillard, S.; Fayad, E.; Louarn, G. In Situ UV–Vis and Raman Spectroscopic Studies of the Electrochemical Behavior of N,N′-Diphenyl-1,4-Phenylenediamine. *Synth. Met.* **2006**, *156*, 81–85. [CrossRef]
48. Boyer, M.I.; Quillard, S.; Louarn, G.; Froyer, G.; Lefrant, S. Vibrational Study of the FeCl3-Doped Dimer of Polyaniline; A Good Model Compound of Emeraldine Salt. *J. Phys. Chem. B* **2000**, *104*, 8952–8961. [CrossRef]
49. Cochet, M.; Louarn, G.; Quillard, S.; Boyer, M.I.; Buisson, J.P.; Lefrant, S. Theoretical and Experimental Vibrational Study of Polyaniline in Base Forms: Non-Planar Analysis. Part I. *J. Raman Spectrosc.* **2000**, *31*, 1029–1039. [CrossRef]
50. Cochet, M.; Louarn, G.; Quillard, S.; Buisson, J.P.; Lefrant, S. Theoretical and Experimental Vibrational Study of Emeraldine in Salt Form. Part II. *J. Raman Spectrosc.* **2000**, *31*, 1041–1049. [CrossRef]
51. Quillard, S.; Louam, G.; Buisson, J.P.; Boyer, M.; Lapkowski, M.; Pron, A.; Lefrant, S. Vibrational Spectroscopic Studies of the Isotope Effects in Polyaniline. *Synth. Met.* **1997**, *84*, 805–806. [CrossRef]
52. Louarn, G.; Lapkowski, M.; Quillard, S.; Pron, A.; Buisson, J.P.; Lefrant, S. Vibrational Properties of PolyanilineIsotope Effects. *J. Phys. Chem.* **1996**, *100*, 6998–7006. [CrossRef]
53. do Nascimento, G.M.; Kobata, P.Y.G.; Millen, R.P.; Temperini, M.L.A. Raman Dispersion in Polyaniline Base Forms. *Synth. Met.* **2007**, *157*, 247–251. [CrossRef]
54. Do Nascimento, G.M.; Constantino, V.R.L.; Landers, R.; Temperini, M.L.A. Aniline Polymerization into Montmorillonite Clay: A Spectroscopic Investigation of the Intercalated Conducting Polymer. *Macromolecules* **2004**, *37*, 9373–9385. [CrossRef]
55. Morávková, Z.; Dmitrieva, E. The First Products of Aniline Oxidation—SERS Spectroelectrochemistry. *Chem. Sel.* **2019**, *4*, 8847–8854. [CrossRef]

56. Kumar, M.; Tiwari, T.; Chauhan, J.K.; Srivastava, N. Understanding the Ion Dynamics and Relaxation Behavior from Impedance Spectroscopy of NaI Doped Zwitterionic Polymer System. *Mater. Res. Express* **2014**, *1*, 045003. [CrossRef]
57. Soltane, L.; Sediri, F. Hydrothermal Synthesis, Characterization and Electrical Investigation of Poly(Para-Phenylenediamine)/Vanadium Oxide Nanocomposite Nanosheets. *Mater. Sci. Eng. B* **2013**, *178*, 502–510. [CrossRef]
58. Ali, A.; Mohamed, N.S.; Sani, N.A.M.; Abdullah, M.A.A. Preparation and Properties of Alkylphosphonium Modified Montmorillonites. *Int. J. Appl. Chem.* **2016**, *12*, 6.
59. Chand, J.; Kumar, G.; Kumar, P.; Sharma, S.K.; Knobel, M.; Singh, M. Effect of Gd3+ Doping on Magnetic, Electric and Dielectric Properties of MgGdxFe2−xO4 Ferrites Processed by Solid State Reaction Technique. *J. Alloys Compd.* **2011**, *509*, 9638–9644. [CrossRef]
60. Lvovich, V.F. *Impedance Spectroscopy: Applications to Electrochemical and Dielectric Phenomena*, 1st ed.; John Wiley & Sons, Inc.: Hoboken, NJ, USA, 2012; pp. 1–19.
61. Einfeldt, J.; Meißner, D.; Kwasniewski, A. Polymerdynamics of Cellulose and Other Polysaccharides in Solid State-Secondary Dielectric Relaxation Processes. *Prog. Polym. Sci.* **2001**, *26*, 1419–1472. [CrossRef]
62. Aziz, S.B.; Abidin, Z.H.Z. Electrical Conduction Mechanism in Solid Polymer Electrolytes: New Concepts to Arrhenius Equation. *J. Soft Matter.* **2013**, *2013*, 323868. [CrossRef]
63. Megdiche, M.; Perrin-pellegrino, C.; Gargouri, M. Conduction Mechanism Study by Overlapping Large-Polaron Tunnelling Model in $SrNiP_2O_7$ Ceramic Compound. *J. Alloys Compd.* **2014**, *584*, 209–215. [CrossRef]
64. Elliott, S.R. A.c. Conduction in Amorphous Chalcogenide and Pnictide Semiconductors. *Adv. Phys.* **1987**, *36*, 135–217. [CrossRef]
65. Salles, F.; Devautour-Vinot, S.; Bildstein, O.; Jullien, M.; Maurin, G.; Giuntini, J.-C.; Douillard, J.-M.; Van Damme, H. Ionic Mobility and Hydration Energies in Montmorillonite Clay. *J. Phys. Chem. C* **2008**, *112*, 14001–14009. [CrossRef]
66. Su, P.-G.; Chen, C.-Y. Humidity Sensing and Electrical Properties of Na- and K-Montmorillonite. *Sens. Actuators B Chem.* **2008**, *129*, 380–385. [CrossRef]

Progress in Organic Coatings 163 (2022) 106666

Contents lists available at ScienceDirect

Progress in Organic Coatings

journal homepage: www.elsevier.com/locate/porgcoat

Tuning of hydrophobicity of conducting films cast from polyaniline-phytic acid-poly(*N*-vinylpyrrolidone) dispersions

Konstantin A. Milakin [a], Udit Acharya [a,b], Islam M. Minisy [a], Doebner Von Tumacder [a,c], Zuzana Morávková [a], Oumayma Taboubi [a], Tomáš Syrový [d,e], Lucie Syrová [d], Jiří Pfleger [a], Patrycja Bober [a,*]

[a] Institute of Macromolecular Chemistry, Czech Academy of Sciences, 162 06 Prague, Czech Republic
[b] Faculty of Mathematics and Physics, Charles University, 121 16 Prague, Czech Republic
[c] Faculty of Science, Charles University, 128 43 Prague, Czech Republic
[d] Department of Graphic Arts and Photophysics, University of Pardubice, Pardubice, Czech Republic
[e] Center of Materials and Nanotechnologies, Faculty of Chemical Technology, University of Pardubice, Cs. Legii square 565, 53002 Pardubice, Czech Republic

ARTICLE INFO

Keywords:
Polyaniline
Phytic acid
Colloidal dispersion
Film coating
Hydrophobicity

ABSTRACT

Colloidal dispersions of polyaniline (PANI) doped by phytic acid (PA) and stabilized with poly(*N*-vinylpyrrolidone) (PVP) were prepared by oxidative polymerization of aniline and compared to the dispersions prepared under similar conditions in the absence of phytic acid. UV–vis and Raman spectroscopies confirmed the formation of protonated PANI in all the cases. According to dynamic light scattering, the dispersions prepared in the presence of PA had a bigger average particle size (~360 nm) compared to the PANI-HCl-PVP dispersions (~300 nm). The long-term stability of all colloids was confirmed for up to 530 days. The prepared dispersions were used for the film deposition by spiral bar technique resulting in transparent and uniform coatings, which consisted of spherical particles (110–200 nm). The highest conductivity values of 5×10^{-3} and 7×10^{-5} S cm^{-1} for PANI-HCl-PVP and PANI-PA-PVP, respectively, were achieved at 1 wt% of PVP. At 1 wt% of PVP, PANI-PA-PVP showed hydrophobic properties (θ=102°), which decreased with increasing PVP content, while PANI-HCl-PVP had hydrophilic properties (θ=10°) decreasing with increasing PVP fraction. Cyclic voltammetry of drop-cast films showed that PANI-PA-PVP had significantly higher areal capacitance retention (97%) compared to PANI-HCl-PVP (61%). Such conducting coatings with tunable surface characteristics can be useful for electrochemical applications.

1. Introduction

Polyaniline (PANI) is one of the most studied conducting polymers with unique physicochemical characteristics [1]. Its optical and electrochemical properties can be easily controlled by oxidation-reduction and acid-base interactions. PANI is widely used in the preparation of sensors [2–7], actuators [8–11], electrochemical storage devices [12–16], electrochromic devices [17–20], etc. Most of these applications, however, require PANI inherent insolubility in common solvents and overall poor processability to be overcome. Preparation of aqueous colloidal dispersions of PANI [21,22] offers a convenient way of manufacturing PANI-based films and coatings by a wide range of printing and coating techniques with potentially easy upscaling and applicability in sensors [5,23] and biomedical field [24].

Polyaniline-based colloidal dispersions are usually synthesized by oxidative polymerization of aniline in the presence of a water-soluble polymer, such as poly(*N*-vinylpyrrolidone) (PVP) [25,26], poly(vinyl alcohol) [25,27] or gelatin [24], acting as a stabilizer. Depending on the composition of reaction medium and chemical nature of the polymer used, conductivity and morphology of the obtained dispersions can be easily tuned. For example, oxidation of aniline by ammonium peroxydisulfate in the presence of gelatin leads to the formation of spindle-like PANI particles while oxidation by silver nitrate results in fibrillar morphology of PANI [24]. Introduction of *p*-phenylenediamine into copolymerization with aniline in the presence of PVP was shown as another approach to change conventional globular morphology to nanofibrillar and increase the conductivity of the materials by ~3 orders of magnitude [26].

* Corresponding author.
E-mail address: bober@imc.cas.cz (P. Bober).

https://doi.org/10.1016/j.porgcoat.2021.106666
Received 4 October 2021; Received in revised form 22 November 2021; Accepted 3 December 2021
Available online 16 December 2021

Phytic acid is a cyclic molecule containing six dihydrogen phosphate groups and was previously used as a dopant for PANI [28–37]. Due to its multifunctional nature, phytic acid is utilized as a gelator leading to the formation of porous hydrogels during the aniline polymerization or cryopolymerization [28,29,38]. These phytic acid-doped PANI materials can be used for adsorption [29,31,32], photodegradation [30] and sensing [33] of metal ions and dyes or after carbonization as P-doped electrode materials for electrochemical capacitors [34] and electrocatalysts [35,36].

Wettability is an important parameter of PANI-based films and coatings, crucial for their potential applications, for instance, in anticorrosion protection [39], where higher hydrophobicity was found to enhance the protective barrier effect against water. In contrast, high hydrophilicity of the electrode coating films may facilitate penetration of water into the material [39]. Penetration of water is also one of the factors, which determine capacitive performance of PANI-based electrodes. It is known that better accessibility of the material surface for the electrolyte allows improvement of capacitance values [40,41]. At the same time, hydrolysis of PANI chains by water molecules is one of the reasons for capacitance degradation during cycling [42], which can be overcome by shielding of the chains, for example, by anionic surfactants [43]. Therefore, it is important to balance these opposite effects for optimal and stable electrochemical performance and prepare materials with tuned hydrophobicity.

Phytic acid is usually known to be used in the preparation of superhydrophilic surfaces [44,45] due to high density of phosphate groups. However, Kim et al. [46] reported that addition of phytic acid can also lead to the increase of hydrophobicity of conducting polymer-based material due to crosslinking. Moreover, PVP, which was chosen as a stabilizer in the present work, shows amphiphilic properties [47,48] depending on the polarity of the medium, which can affect wettability of the prepared materials. Thus, taking into account complexity of the multicomponent system, containing both phytic acid and PVP, complex nature of their influence on the material hydrophobicity and potential mutual interactions, it is important to study their combined effect on the wettability of the films cast from the prepared colloidal dispersions.

In the present paper, we synthesized novel colloidal dispersions of PANI doped with phytic acid and stabilized by PVP by facile and cost-effective one-step strategy. The colloids were studied in terms of morphology and long-term stability. Furthermore, hydrophobic films have been successfully prepared by spiral bar coating directly from colloidal dispersion and their properties have been evaluated.

2. Materials and methods

2.1. Materials

Aniline (Penta, Czech Republic), aniline hydrochloride (Penta, Czech Republic), ammonium peroxydisulfate (Lach-Ner, Czech Republic), poly (*N*-vinylpyrrolidone) ($M_w \sim 360{,}000$, Sigma-Aldrich, China) and phytic acid (50 wt% solution, Sigma-Aldrich, Japan) were used as received.

2.2. Preparation

2.2.1. Preparation of polyaniline-based colloidal dispersions

Polyaniline-phytic acid colloidal dispersions (PANI-PA-PVP) were prepared by the oxidative polymerization of aniline by ammonium peroxydisulfate in an aqueous solution of poly(*N*-vinylpyrrolidone) (PVP) containing phytic acid. For the typical synthesis, PVP (1–4 wt%) was dissolved in 0.2 M aqueous solution of phytic acid. Then aniline (1.82 ml) and ammonium peroxydisulfate (5.7 g) were dissolved separately in 50 ml of aqueous solution of PVP. After mixing the monomer and the oxidant solutions, the polymerization mixture was left undisturbed for 24 h at room temperature.

For comparison, the PANI-HCl-PVP dispersions were prepared in similar conditions without phytic acid. Aniline hydrochloride (2.59 g) and ammonium peroxydisulfate (5.7 g) were dissolved separately in 50 ml of aqueous solution of PVP (1–4 wt%). The resulting solutions were mixed and the reaction was left undisturbed for 24 h at room temperature.

2.2.2. Deposition of films from polyaniline-based colloidal dispersions

The TQC spiral bar coater AB 3120 was used for the deposition of films from the prepared colloidal dispersions. PET Melinex ST504 foil with thickness 175 μm was used as a substrate; prior to the deposition, its surface was cleaned and treated by corona Alhbrandt for improvement of surface free energy. Before the deposition, the prepared colloids were sonicated in Bandelin Sonorex ultrasonic DT 103 H bath and then were filtered through 1 μm glassy fiber filter. The deposition was performed at a coating speed 20 mm s^{-1} with the 50 μm spiral bar. The coated layers were left to dry at 90 °C for 15 min.

2.3. Characterization

2.3.1. Characterization of polyaniline-based colloidal dispersions

Particle size of the colloidal dispersions diluted by water was characterized by dynamic light scattering (DLS) (Malvern AutoSizer Lo-C) at 25 °C. Presented results are averages of at least 5 measurements. Transmission electron microscopy (TEM) was performed with Tecnai G2 Spirit electron microscope. Ultraviolet-visible (UV–vis) spectra of the prepared dispersions diluted by water were recorded using Perkin Elmer Lambda 950 spectrophotometer.

2.3.2. Characterization of the films deposited from polyaniline-based dispersions

Linear four probe method with equal spacing between electrodes (1.42 mm) was employed to measure electrical conductivity of the films. A Keithley 230 Programmable Voltage Source in serial connection with a Keithley 196 System DMM was used as a current source; the potential difference between the potential probes was measured with a Keithley 617 Programmable Electrometer at constant ambient conditions at 23 ± 1 °C and relative humidity 35 ± 5%. The conductivity (σ) was calculated as:

$$\sigma = \frac{I}{2\pi s F V} \quad (1)$$

where I is current, V is potential drop between inner electrodes, F is correction factor and s is probe spacing. Since the thickness of all the films (as listed in Table 1) was appreciably smaller than the probe spacing and the area of the sample was much larger compared to the probes spacing, correction factor (F) given by Eq. (2) was used [49], which is also valid for non-conducting bottom substrate foil.

Table 1
Thickness, conductivity, contact angle and roughness of PANI-PA-PVP and PANI-HCl-PVP films.

PVP concentration, wt %	Thickness, μm	Conductivity, S cm^{-1}	Contact angle, degree	Roughness (R_a), nm
PANI-PA-PVP				
1	2.8	7×10^{-5}	102	92
2	0.8	4×10^{-5}	99	81
3	1.1	9×10^{-6}	85	52
4	2.2	5.9×10^{-6}	71	17
PANI-HCl-PVP				
1	1.3	5×10^{-3}	10	64
2	1.7	1×10^{-3}	15	60
3	1.5	1×10^{-5}	26	33
4	1.5	4×10^{-6}	38	27

$$F = \frac{\frac{t}{s}}{2ln\left(\frac{sinh\left(\frac{t}{s}\right)}{sinh\left(\frac{t}{2s}\right)}\right)} \quad (2)$$

where t is the film thickness. Since $t \ll 0.4$ and using approximation $sinh(x) \approx x$ for $x \ll 1$, Eq. (1) can be simplified as

$$\sigma = \frac{ln2}{\pi}\frac{I}{Vt} \quad (3)$$

Thickness of the films was determined using a KLA Tencor P-10 Profilometer. The static water contact angle of sessile drop (3 μl) was measured by a contact angle goniometer OCA 20 (Dataphysics) equipped with SCA 21 software where the profile was fitted with the Young–Laplace equation. At least three measurements were done at different positions of each sample and average value is reported. Surface topography and average roughness of the films were studied in air at a Nanoscope IIIa atomic force microscope (Digital Instruments/Veeco) operated in the tapping mode using OTESPA-R3 silicon tips (Bruker) with spring constant (k) 26 N m^{-1} and resonance frequency around 300 kHz. The 20 μm scans were acquired with scan rate of ~0.7 Hz. NanoScope software was used to process the raw AFM images and to determine the roughness average values. Morphology of the films was studied using scanning electron microscope (SEM) MAIA3 Tescan.

Raman spectra were measured with a Renishaw InVia Reflex Raman microspectrometer. The spectra were excited with a 785 nm diode laser. The scattered light was registered with a Peltier-cooled CCD detector (576 × 384 pixels) and analyzed by the spectrograph equipped with holographic grating 1200 lines mm^{-1}. The spectra were obtained at 3 spots of each sample to verify the film homogeneity.

For electrochemical characterization, 1 l of colloidal dispersions was drop-cast onto the glassy carbon electrode and the resulting films were dried at room temperature for at least 2 days.

Electroactivity of PANI-HCl-PVP and PANI-PA-PVP drop-cast films was investigated by cyclic voltammetry (CV) in a 3-electrode cell consisting of a glassy carbon working electrode, Ag/AgCl pseudo reference and a Pt coil as a counter electrode. The voltammograms were recorded using the potential window from −0.1 V to 0.7 V at scan rates of 10, 20, 50, 100 and 200 mV s^{-1} in 1 M HCl. Electrochemical stability of the films was studied in 1 M HCl solution for 1000 cycles at 200 mV s^{-1} scan rate and determined based on the change of their areal capacitance.

The areal capacitance of the films was calculated using Eq. (4):

$$C_{CV} = \frac{\int IdV}{2 \times \nu \times \Delta V \times A} \quad (4)$$

where $\int IdV$ is the area of the CV curve, ν is the scan rate, ΔV is the potential window and A is the electrode surface area equal to 7.07 mm^2.

3. Results and discussion

3.1. Polyaniline-based colloidal dispersions

PANI-PA-PVP colloidal dispersions were synthesized by oxidative polymerization of aniline using ammonium peroxydisulfate in aqueous phytic acid solution in the presence of PVP as a stabilizer. The as-prepared dark green dispersions were characterized by UV–vis spectroscopy (Fig. 1). All recorded UV–vis spectra of PANI-PA-PVP colloidal dispersions are similar to each other at all PVP stabilizer concentrations and, therefore, Fig. 1 shows only the spectrum of PANI-PA-PVP colloidal dispersion stabilized with 4 wt% of PVP. PANI-HCl-PVP dispersions prepared in the absence of phytic acid were also found to have similar spectra, showing no influence of phytic acid on the spectra of the colloids.

All the spectra (Fig. 1) follow the typical spectrum of PANI emeraldine salt and contain a band at around 400 nm and a broad band above

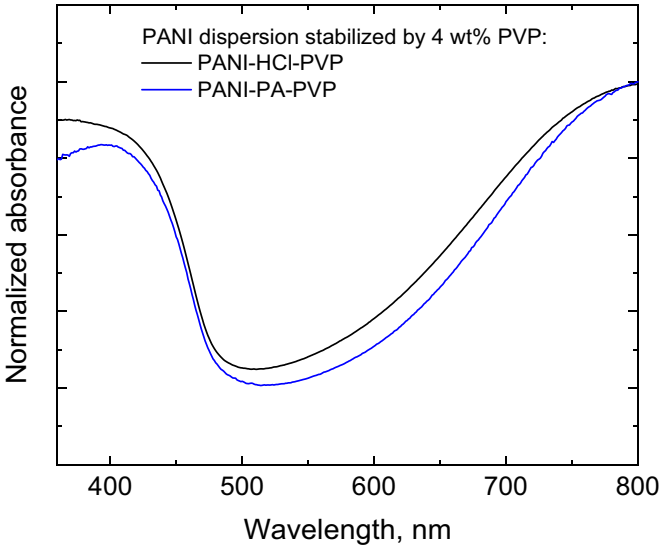

Fig. 1. Typical UV–vis spectra of PANI-PA-PVP and PANI-HCl-PVP colloidal dispersions (4 wt% of PVP).

800 nm, corresponding to polaron-π* and π-polaron transitions, respectively [50]. Thus, in all cases, independent of PVP content or the presence of phytic acid, PANI in the form of emeraldine salt was formed.

TEM micrographs of PANI-PA-PVP and PANI-HCl-PVP dispersions prepared using all studied PVP concentrations are similar within the respective series and only the typical ones (4 wt% of PVP) are shown in Fig. 2. The PANI-PA-PVP dispersions (Fig. 2a) consist of spherical PANI particles with an average diameter of single particles about 150–180 nm. Addition of phytic acid does not lead to the change of PANI globular morphology. The globular particles observed in PANI-HCl-PVP dispersions (Fig. 2b) prepared in the absence of phytic acid have an average diameter 100–130 nm. However, due to the wide particle size distribution the TEM results are not conclusive regarding the influence of phytic acid on the particle size of PANI-based colloids.

Particle size and stability of PANI-PA-PVP dispersions were additionally studied by DLS. The results showed that PANI-PA-PVP dispersions consist of colloidal particles with average size of ≈360 nm and this value does not depend on the concentration of the polymer stabilizer which correlates with the TEM results. The measured value is higher than particle size for PANI-HCl-PVP dispersions prepared without phytic acid (1 wt% of PVP – 321 nm, 2–4 wt% of PVP – ≈285 nm). This might be explained by the fact that adding multifunctional phytic acid into polymerization mixture promotes growth and aggregation of PANI particles due to electrostatic attraction between PANI chains mediated by phytic acid. Average particle sizes measured by DLS are also notably bigger than the corresponding values obtained for single particles from TEM images which is caused by the presence of aggregates in the dispersions and by the contribution of the PVP shell around PANI particles into total particle size.

To evaluate the potential applicability of PANI-PA-PVP dispersions for film preparation using various coating techniques it was important to check long-term stability of the dispersions and evolution of particle size over time Fig. 3a.

Fig. 3a shows the change of PANI-PA-PVP dispersions particle size depending on the storage time. All the dispersions follow the same trend: at first the average particle size of all the samples starts to decrease and then increases which is shown for the samples containing 3 wt% and 4 wt% of PVP. The location of the curve minimum depends on the PVP concentration and shifts to lower number of days with the increase of the stabilizer content. The shape of the curves might be explained by the fact that at first relaxation of PVP shell on the PANI particles surface is observed (initial particle size decrease) with further particle aggregation

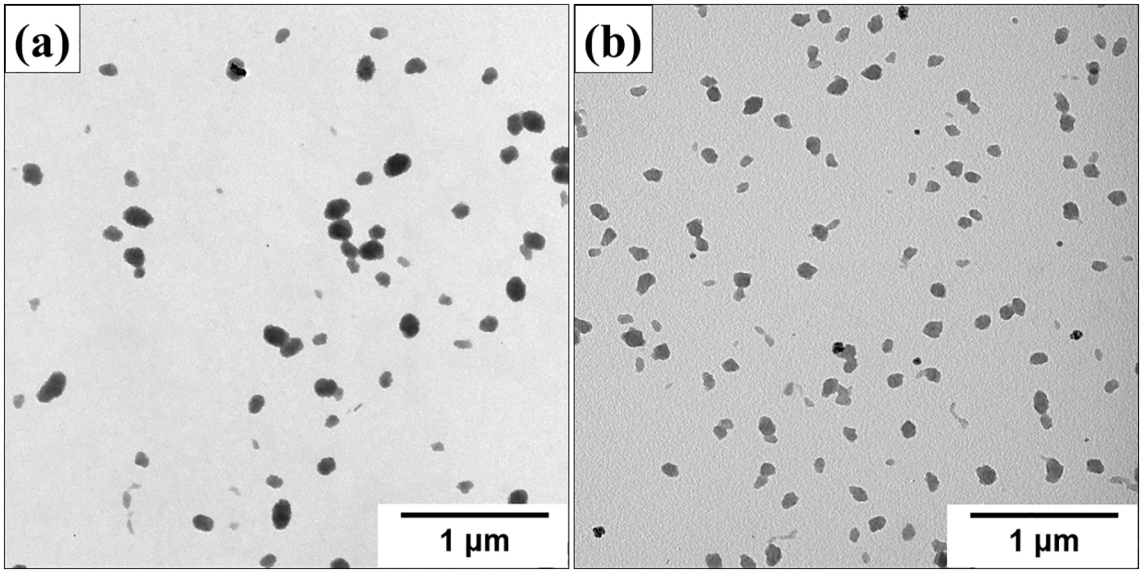

Fig. 2. Typical TEM images of a) PANI-PA-PVP and b) PANI-HCl-PVP colloidal dispersions (4 wt% of PVP).

at higher concentrations of the stabilizer (particle size increase). PANI-HCl-PVP dispersions (Fig. 3b) were found to be stable in the similar time period, which might be connected with more hindered relaxation of PVP shells due to their interaction with PANI in the absence of phytic acid (discussed in more details below regarding the contact angle measurements of the coated films).

3.2. Polyaniline-based thin films

The synthetized colloids were deposited by spiral bar coating technique which allowed preparing PANI layers with high homogeneity (Fig. 4). The given coating technique is scalable from the laboratory level up to the industrial scale, where various functional layers can be prepared with high homogeneity at speed up to 300 mmin^{-1} and for width of the web up to 3 m.

Chemical composition of PANI-PA-PVP and PANI-HCl-PVP films was assessed by Raman spectroscopy excited with 785 nm laser line to resonantly enhance various polaronic structures, allowing to study protonation and oxidation states of PANI (Fig. 5). Several spectra were measured on each film at various locations, showing a good homogeneity over the area.

For all films, the formation of protonated PANI is confirmed by the presence of semiquinonoid ring stretching vibrations of emeraldine salt structure observed at 1590 cm^{-1}, C∼N$^{\bullet+}$ stretching vibration of delocalized polaronic structures at 1340 cm^{-1}, C—N stretching vibration at 1255 cm^{-1}, C—H deformation vibrations at 1173 cm^{-1}, and various skeletal deformation vibrations below 1000 cm^{-1} [51]. The band of the stretching of the quinonoid ring at 1625 cm^{-1}, the N—H deformation band reaching to 1520 cm^{-1}, the C═N stretching band at 1492 cm^{-1} and the bipolaron C∼N^{+} band at 1330 cm^{-1}, as well as skeletal deformation vibrations at 655, 590, 390 and 290 cm^{-1} are connected with pernigraniline salt [51], and, thus, indicate a slight overoxidation of PANI. These bands are significantly stronger in the films containing phytic acid than in PANI-HCl-PVP films.

SEM images (Fig. 6) show that the globular morphology of PANI particles observed in TEM of colloidal dispersions is preserved after coating the films. It is clearly visible that the increase of the PVP stabilizer concentration in the colloidal dispersion and addition of phytic acid make the coated films smoother. At 1 wt% of PVP, PANI-HCl-PVP films (Fig. 6a) also have more porous structure compared to PANI-PA-PVP (Fig. 6c). The average sizes of individual material grains are in the range 110–200 nm, which are similar to the ones measured by TEM (Fig. 2). However, difficulty to distinguish particle boundaries for PANI-HCl-PVP films with higher PVP concentrations (Fig. 6b) and for PANI-PA-PVP films for all used PVP concentrations (Fig. 6c, d) makes a more accurate comparison impossible.

AFM data for both types of films correlate with SEM images (Fig. 7). The PANI-PA-PVP and PANI-HCl-PVP film surface roughness average (R_a) values (Table 1) decrease from 92 to 17 nm and from 64 to 27 nm, respectively, with increasing PVP concentration.

The thickness of the films was found to be independent on the concentration of the stabilizer and phytic acid used for the preparation of the colloids (Table 1). In both series, in the presence and in the absence of phytic acid, the film conductivity (Table 1) increased when lower amount of the stabilizer was used for colloid preparation. This increase is connected to higher amount of conducting fraction in the resulting films. For PANI-PA-PVP and PANI-HCl-PVP-based films the highest conductivity values (1 wt% of PVP) were found to be 7×10^{-5} S cm^{-1} and 5×10^{-3} S cm^{-1}, respectively. The latter value is in the same order with those reported in literature for spray coated PANI hydrochloride colloids stabilized by 2 wt% of PVP [52]. Chemically grown PANI hydrochloride films have conductivity of 4.3×10^{-2} S cm^{-1} [53]. The fact that PANI-HCl-PVP coated films have 2 orders of magnitude higher maximum conductivity than PANI-PA-PVP films containing phytic acid might be attributed to the difference in PANI dopants. It was reported that PANI doped with phytic acid had lower conductivity compared to PANI protonated with conventional hydrochloric acid [54].

Water contact angle measurements (Table 1) showed that the series of the films prepared from the PANI-PA-PVP dispersions have drastically different wettability and an opposite PVP concentration dependence compared to the films coated from PANI-HCl-PVP colloids. PANI-HCl-PVP films have a hydrophilic nature and their contact angle increases with the PVP concentration from 10° (1 wt% of PVP) to 38° (4 wt% of PVP). The obtained values are comparable to the one of PANI hydrochloride film (25° [53]) and the PVP concentration influence on the films contact angle might be explained by the increasing contribution of hydrophobic part of PVP, which is known to be an amphiphilic polymer [47,48]. In contrast to PANI-HCl-PVP films, PANI-PA-PVP films are significantly more hydrophobic and their contact angle decreases from 102° (1 wt% of PVP) to 71° (4 wt% of PVP) with increasing the PVP concentration. The change of hydrophobicity of the films and reversing the PVP concentration trend might be attributed to the amphiphilic nature of PVP and to the change of the polymer conformation induced by addition of phytic acid into the system. Amphiphilic polymer

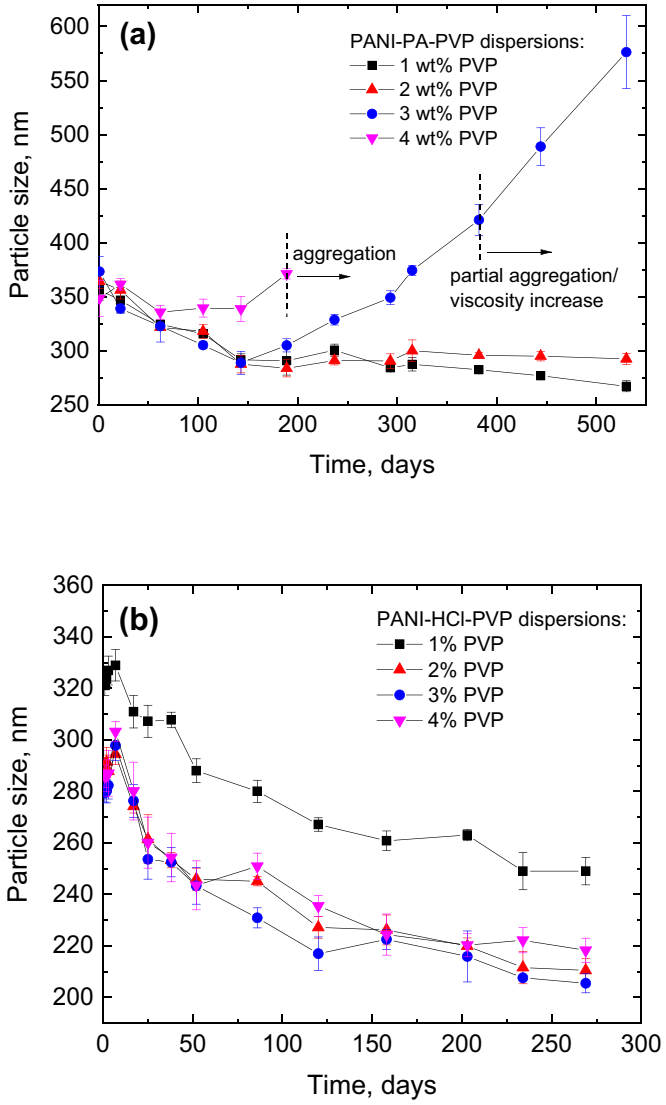

Fig. 3. Evolution of particle size over time of a) PANI-PA-PVP and b) PANI-HCl-PVP dispersions.

components in films are known to rearrange to more favorable conformations based on external factors, such as interaction with water [55,56], leading to dynamic change of their contact angle. It can be assumed that similar changes can occur during film preparation and drying at elevated temperature in air, where the latter can be potentially considered as annealing, which facilitates PVP segmental mobility with water acting as a plasticizer [57]. The PVP conformational freedom is expected to be influenced and limited by various interactions in the multicomponent colloidal dispersion. In the case of PANI-HCl-PVP films, PANI particles are stabilized in water only by PVP and the stabilizer conformation, with hydrophilic segments exposed to water, is expected to be frozen by the interaction with the conducting polymer. It leads to hydrophilic nature of the resulting films. In the case of PANI-PA-PVP dispersions, it is assumed that phytic acid interferes with PANI/PVP interactions leading to more conformational freedom of PVP. It results in flipping its conformation during film deposition and forming more hydrophobic surfaces. This effect is the most pronounced in the film with 1 wt% of PVP, which has the highest hydrophobicity and a relatively small amount of PVP compared to phytic acid.

Electrochemical characterization of PANI-based drop-cast films was performed by CV. For the electrochemical experiments only PANI-HCl-PVP and PANI-PA-PVP dispersions prepared in the presence of 1 wt% of PVP were chosen due to the highest hydrophilicity and hydrophobicity, respectively.

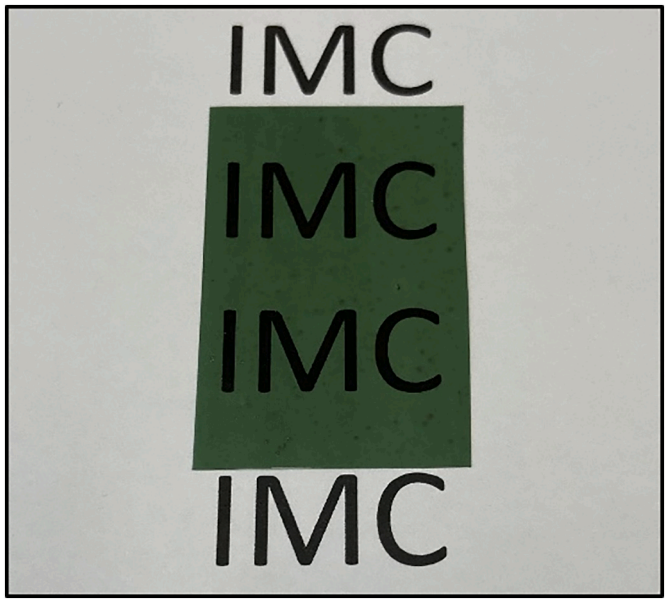

Fig. 4. The typical photo of a cast transparent PANI-based film.

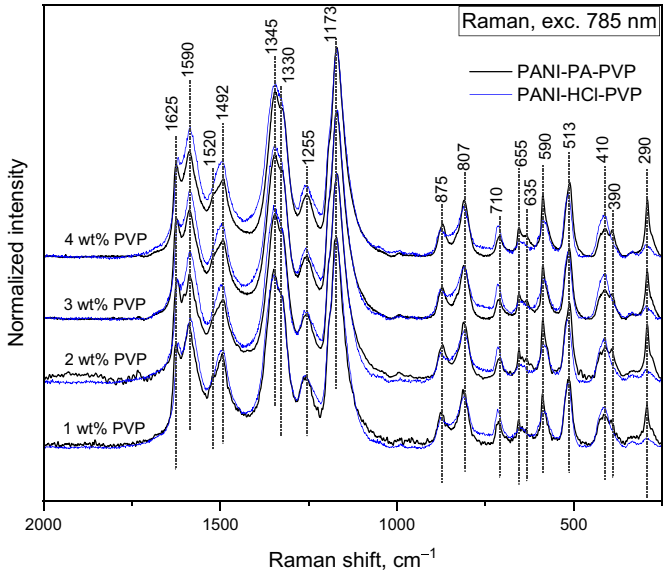

Fig. 5. Raman spectra of PANI-PA-PVP (black) and PANI-HCl-PVP (blue) films. The spectra were baseline corrected, normalized and shifted for clarity. (For interpretation of the references to colour in this figure legend, the reader is referred to the web version of this article.)

According to Fig. 8, PANI-HCl-PVP film shows higher current density at all scan rates compared to PANI-PA-PVP film manifesting higher electroactivity of the former material, which can be connected to its higher conductivity. In the case of PANI-HCl-PVP, the PANI oxidation peak at ≈0.4 V attributed to transition from leucoemeraldine to emeraldine salt is well-resolved. However, in the case of PANI-PA-PVP, it is significantly less distinct and shifted to higher potentials (≈0.5–0.6 V). The observed difference in the peak position is likely to be attributed to phytic acid being a less mobile counterion than chloride.

Although the initial electroactivity of PANI-PA-PVP film was found to be lower compared to PANI-HCl-PVP, its cycling stability was significantly better (Fig. 9). After 1000 cycles PANI-PA-PVP retained

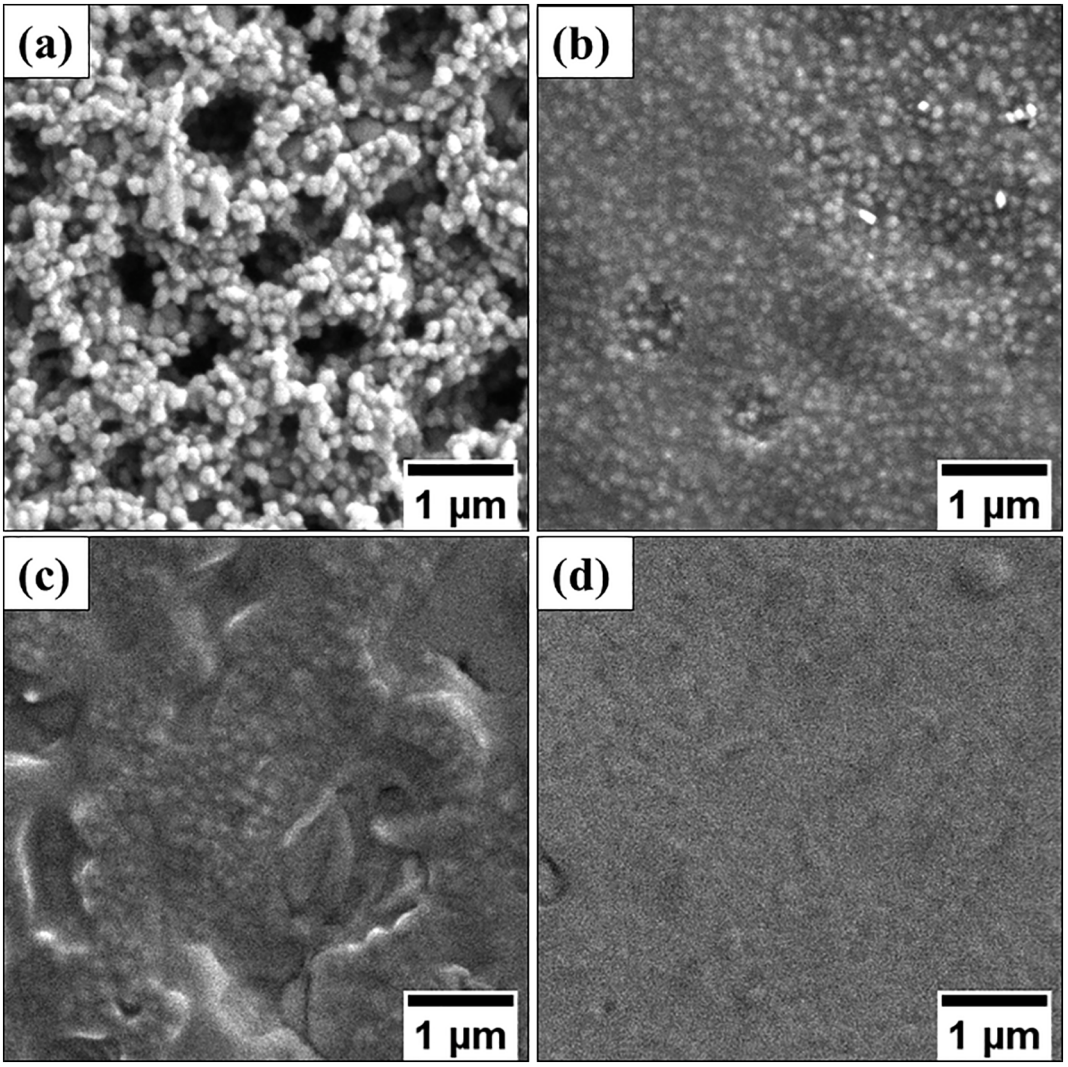

Fig. 6. SEM images of PANI films cast from PANI-HCl-PVP colloids prepared using a) 1 wt%, b) 4 wt% of PVP, and PANI-PA-PVP dispersions prepared with c) 1 wt%, d) 4 wt% of PVP.

97% of its initial capacitance, compared to 61% for PANI-HCl-PVP film. Capacitance loss during electrochemical cycling is connected with PANI degradation, which is mainly caused by nucleophilic attacks of water molecules, leading to hydrolysis of the polymer chains [42]. The presence of phytic acid presumably affects conformation of PVP in PANI-PA-PVP films, leading to more hydrophobic fragments exposed to the film surface that results in higher hydrophobicity of the material compared to PANI-HCl-PVP. Therefore, it can be assumed that the hydrophobic fragments of PVP can have the shielding effect for PANI chains, hindering the hydrolysis and improving capacitance retention. Moreover, according to SEM images (Fig. 6a,c), PANI-HCl-PVP films are visibly more porous compared to PANI-PA-PVP, which can facilitate their exposure to water, promoting hydrolysis and capacitance loss. Therefore, a combination of high capacitance retention with hydrophobicity of PANI-PA-PVP films prepared by an easily scalable and low-cost deposition technique make this material promising for electrochemical applications.

4. Conclusions

PANI-based colloidal dispersions with a long-term stability were prepared by oxidative polymerization of aniline in the presence of PVP. Introducing PA as a dopant for PANI was found to be an efficient way to tune surface properties of conducting films cast from the dispersions. A combination of PA with amphiphilic PVP and their interaction allowed varying contact angle of the coatings from θ=10° for PANI-HCl-PVP film to θ=102° for PANI-PA-PVP. PANI-PA-PVP films showed significantly better electrochemical areal capacitance retention compared to PANI-HCl-PVP films. Therefore, the combination of easy processing of dispersions by coating techniques and tunable hydrophobicity of prepared films with good capacitance retention can be beneficial for electrochemical applications.

CRediT authorship contribution statement

Konstantin A. Milakin: Conceptualization, Methodology, Investigation, Writing – original draft, Writing – review & editing. **Udit Acharya:** Investigation, Writing – review & editing. **Islam M. Minisy:** Investigation, Writing – review & editing. **Doebner Von Tumacder:** Investigation, Visualization, Writing – review & editing. **Zuzana Morávková:** Writing – review & editing. **Oumayma Taboubi:** Investigation. **Tomáš Syrový:** Investigation, Writing – review & editing, Funding acquisition. **Lucie Syrová:** Investigation. **Jiří Pfleger:** Writing – review & editing, Funding acquisition. **Patrycja Bober:** Conceptualization, Methodology, Supervision, Writing – review & editing, Funding acquisition.

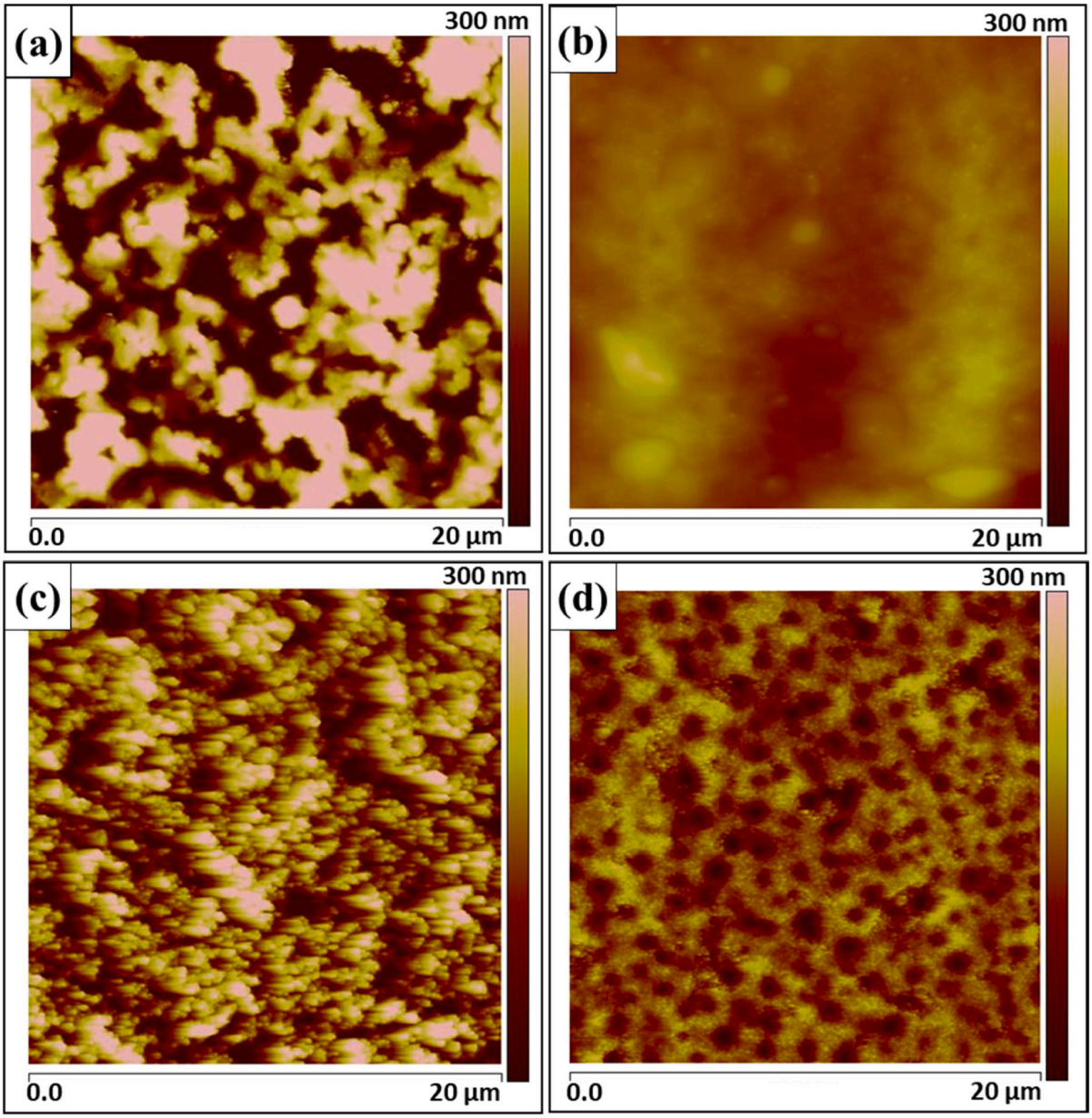

Fig. 7. AFM images of films cast from PANI-PA-PVP dispersions prepared using a) 1 wt% and b) 4 wt% of PVP and PANI-HCl-PVP colloids prepared with c) 1 wt% and d) 4 wt% of PVP.

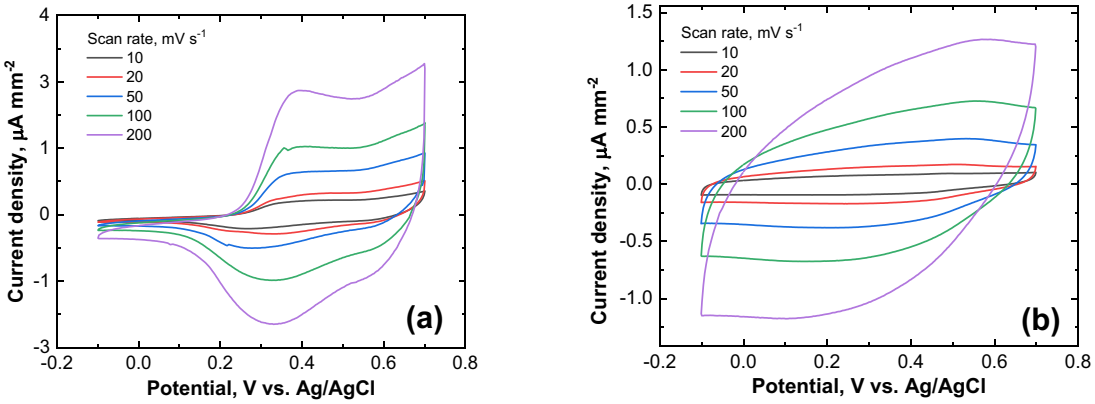

Fig. 8. Cyclic voltammograms of films drop-cast from a) PANI-HCl-PVP and b) PANI-PA-PVP dispersions (1 wt% of PVP) recorded at different scan rates in 1 M HCl.

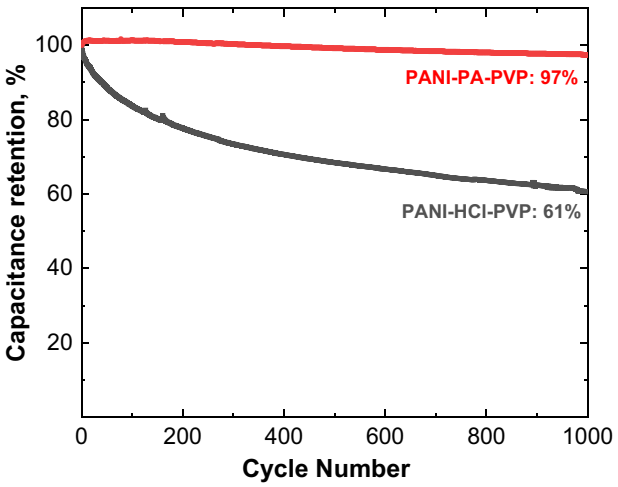

Fig. 9. Cycling stability (1000 cycles) of films drop-cast from PANI-HCl-PVP and PANI-PA-PVP dispersions (1 wt% of PVP).

Declaration of competing interest

The authors declare that they have no known competing financial interests or personal relationships that could have appeared to influence the work reported in this paper.

Acknowledgment

The authors wish to thank the Czech Science Foundation (21-01401S) for the financial support. The paper was created with the support of the project Ministry of Agriculture of the Czech Republic NAZV QK1810010 “SmartField”. Authors appreciate financial support from grant LM2018103 and INTEREXCELLENCE - LTAUSA19066 from The Ministry of Education, Youth and Sports of the Czech Republic. J. Hromádková and M. Karbusická are acknowledged for performing SEM/TEM and TGA measurements, respectively.

References

[1] J. Stejskal, M. Trchová, P. Bober, P. Humpolíček, V. Kašpárková, I. Sapurina, M. A. Shishov, M. Varga, Conducting polymers: polyaniline, in: Encyclopedia of Polymer Science and Technology, Wiley online, 2015, pp. 1–44, https://doi.org/10.1002/0471440264.pst640.

[2] I. Fratoddi, I. Venditti, C. Cametti, M.V. Russo, Chemiresistive polyaniline-based gas sensors: a mini review, Sensors Actuators B Chem. 220 (2015) 534–548, https://doi.org/10.1016/j.snb.2015.05.107.

[3] S. Bilal, W. Ullah, A.U.A. Shah, Polyaniline@CuNi nanocomposite: a highly selective, stable and efficient electrode material for binder free non-enzymatic glucose sensor, Electrochim. Acta 284 (2018) 382–391, https://doi.org/10.1016/j.electacta.2018.07.165.

[4] E. Falletta, P. Costa, C. Della Pina, S. Lanceros-Mendez, Development of high sensitive polyaniline based piezoresistive films by conventional and green chemistry approaches, Sensors Actuators A 220 (2014) 13–21, https://doi.org/10.1016/j.sna.2014.09.004.

[5] T. Syrový, P. Kuberský, I. Sapurina, S. Pretl, P. Bober, L. Syrová, A. Hamáček, J. Stejskal, Gravure-printed ammonia sensor based on organic polyaniline colloids, Sensors Actuators B Chem. 225 (2016) 510–516, https://doi.org/10.1016/j.snb.2015.11.062.

[6] K.A. Milakin, A.N. Korovin, E.V. Moroz, K. Levon, A. Guiseppi-Elie, V.G. Sergeyev, Polyaniline-based sensor material for potentiometric determination of ascorbic acid, Electroanalysis 25 (2013) 1323–1330, https://doi.org/10.1002/elan.201300023.

[7] E. Tomšík, P. Dallas, I. Šeděnková, J. Svoboda, M. Hrubý, Electrochemical deposition of highly hydrophobic perfluorinated polyaniline film for biosensor applications, RSC Adv. 11 (2021) 18852–18859, https://doi.org/10.1039/d1ra02325j.

[8] M. Beregoi, A. Evanghelidis, E. Matei, I. Enculescu, Polyaniline based microtubes as building-blocks for artificial muscle applications, Sensors Actuators B Chem. 253 (2017) 576–583, https://doi.org/10.1016/j.snb.2017.06.128.

[9] S. Mehraeen, S.A. Gursel, M. Papila, F.C. Cebeci, Investigation of electrochemical actuation by polyaniline nanofibers, Smart Mater. Struct. 26 (2017), 095021, https://doi.org/10.1088/1361-665X/aa7718.

[10] E. Smela, W. Lu, B.R. Mattes, Polyaniline actuators - part 1. PANI(AMPS) in HCl, Synth. Met. 151 (2005) 25–42, https://doi.org/10.1016/j.synthmet.2005.03.009.

[11] L. Duan, J.C. Lai, C.H. Li, J.L. Zuo, A dielectric elastomer actuator that can self-heal integrally, ACS Appl. Mater. Interfaces 12 (2020) 44137–44146, https://doi.org/10.1021/acsami.0c11697.

[12] G. Wu, P.F. Tan, D.X. Wang, Z. Li, L. Peng, Y. Hu, C.F. Wang, W. Zhu, S. Chen, W. Chen, High-performance supercapacitors based on electrochemical-induced vertical-aligned carbon nanotubes and polyaniline nanocomposite electrodes, Sci. Rep. 7 (2017) 43676, https://doi.org/10.1038/srep43676.

[13] K.S. Ryu, X.L. Wu, Y.G. Lee, S.H. Chang, Electrochemical capacitor composed of doped polyaniline and polymer electrolyte membrane, J. Appl. Polym. Sci. 89 (2003) 1300–1304, https://doi.org/10.1002/app.12242.

[14] L.M. Santino, Y. Lu, S. Acharya, L. Bloom, D. Cotton, A. Wayne, J.M. D'Arcy, Enhancing cycling stability of aqueous polyaniline electrochemical capacitors, ACS Appl. Mater. Interfaces 8 (2016) 29452–29460, https://doi.org/10.1021/acsami.6b09779.

[15] H. Huang, S.C. Abbas, Q.D. Deng, Y.H. Ni, S.L. Cao, X.J. Ma, An all-paper, scalable and flexible supercapacitor based on vertically aligned polyaniline (PANI) nanodendrites@fibers, J. Power Sources 498 (2021), 229886, https://doi.org/10.1016/j.jpowsour.2021.229886.

[16] M.M. Zhang, A. Nautiyal, H.S. Du, Z. Wei, X.Y. Zhang, R.G. Wang, Electropolymerization of polyaniline as high-performance binder free electrodes for flexible supercapacitor, Electrochim. Acta 376 (2021), 138037, https://doi.org/10.1016/j.electacta.2021.138037.

[17] L. Zhao, L. Zhao, Y.X. Xu, T.F. Qiu, L.J. Zhi, G.Q. Shi, Polyaniline electrochromic devices with transparent graphene electrodes, Electrochim. Acta 55 (2009) 491–497, https://doi.org/10.1016/j.electacta.2009.08.063.

[18] H. Wei, X. Yan, S. Wu, Z. Luo, S. Wei, Z. Guo, Electropolymerized polyaniline stabilized tungsten oxide nanocomposite films: electrochromic behavior and electrochemical energy storage, J. Phys. Chem. C 116 (2012) 25052–25064, https://doi.org/10.1021/jp3090777.

[19] P.R. Somani, S. Radhakrishnan, Electrochromic materials and devices: present and future, Mater. Chem. Phys. 77 (2002) 117–133, https://doi.org/10.1016/S0254-0584(01)00575-2.

[20] X.Y. Huang, Q.Q. Niu, S.N. Fan, Y.P. Zhang, Highly oriented lamellar polyaniline with short-range disorder for enhanced electrochromic performance, Chem. Eng. J. 417 (2021), 128126, https://doi.org/10.1016/j.cej.2020.128126.

[21] C.A. Zimmermann, J.C. Ferreira, S.D.A.D. Ramoa, G.M.D. Barra, Facile approach to produce water-dispersible conducting polyaniline powder, Synth. Met. 267 (2020), 116451, https://doi.org/10.1016/j.synthmet.2020.116451.

[22] R.M. Latonen, A. Maattanen, P. Ihalainen, W. Xu, M. Pesonen, M. Nurmi, C. Xu, Conducting ink based on cellulose nanocrystals and polyaniline for flexographical printing, J. Mater. Chem. C 5 (2017) 12172–12181, https://doi.org/10.1039/c7tc03729e.

[23] M.V. Kulkarni, S.K. Apte, S.D. Naik, J.D. Ambekar, B.B. Kale, Processing and formulation of inkjet printable conducting polyaniline based ink for low cost, flexible humidity sensors using untreated polymeric substrate, Smart Mater. Struct. 21 (2012), 035023, https://doi.org/10.1088/0964-1726/21/3/035023.

[24] P. Bober, P. Humpolíček, T. Syrový, Z. Capáková, L. Syrová, J. Hromádková, J. Stejskal, Biological properties of printable polyaniline and polyaniline–silver colloidal dispersions stabilized by gelatin, Synth. Met. 232 (2017) 52–59, https://doi.org/10.1016/j.synthmet.2017.07.013.

[25] J. Stejskal, P. Kratochvíl, M. Helmstedt, Polyaniline dispersions. 5. Poly(vinyl alcohol) and poly(N-vinylpyrrolidone) as steric stabilizers, Langmuir 12 (1996) 3389–3392, https://doi.org/10.1021/la9506483.

[26] Y. Li, P. Bober, M. Trchová, J. Stejskal, Colloidal dispersions of conducting copolymers of aniline and p-phenylenediamine for films with enhanced conductometric sensitivity to temperature, J. Mater. Chem. C 5 (2017) 1668–1674, https://doi.org/10.1039/c6tc05413g.

[27] C. Dispenza, M.A. Sabatino, D. Chmielewska, C. LoPresti, G. Battaglia, Inherently fluorescent polyaniline nanoparticles in a dynamic landscape, React. Funct. Polym. 72 (2012) 185–197, https://doi.org/10.1016/j.reactfunctpolym.2012.01.001.

[28] R. Yao, Z.J. Yao, J.T. Zhou, Novel multi-configuration aniline/phytic acid based aerogel with directed higher performance, Mater. Lett. 198 (2017) 206–209, https://doi.org/10.1016/j.matlet.2017.03.032.

[29] B. Yan, Z.H. Chen, L. Cai, J.W. Fu, Q. Xu, Fabrication of polyaniline hydrogel: synthesis, characterization and adsorption of methylene blue, Appl. Surf. Sci. 356 (2015) 39–47, https://doi.org/10.1016/j.apsusc.2015.08.024.

[30] H.H. Wu, C.W. Chang, D.L. Lu, K. Maeda, C.C. Hu, Synergistic effect of hydrochloric acid and phytic acid doping on polyaniline-coupled g-C_3N_4 nanosheets for photocatalytic Cr(VI) reduction and dye degradation, ACS Appl. Mater. Interfaces 11 (2019) 35702–35712, https://doi.org/10.1021/acsami.9b10555.

[31] H.J. Kim, S. Im, J.C. Kim, W.G. Hong, K. Shin, H.Y. Jeong, Y.J. Hong, Phytic acid doped polyaniline nanofibers for enhanced aqueous copper(II) adsorption capability, ACS Sustain. Chem. Eng. 5 (2017) 6654–6664, https://doi.org/10.1021/acssuschemeng.7b00898.

[32] R.J. Li, L.F. Liu, F.L. Yang, Removal of aqueous Hg(II) and Cr(VI) using phytic acid doped polyaniline/cellulose acetate composite membrane, J. Hazard. Mater. 280 (2014) 20–30, https://doi.org/10.1016/j.jhazmat.2014.07.052.

[33] H. Huang, W.C. Zhu, X.C. Gao, X.Y. Liu, H.Y. Ma, Synthesis of a novel electrode material containing phytic acid-polyaniline nanofibers for simultaneous determination of cadmium and lead ions, Anal. Chim. Acta 947 (2016) 32–41, https://doi.org/10.1016/j.aca.2016.10.012.

[34] L.J. Yan, D. Li, T.T. Yan, G.R. Chen, L.Y. Shi, Z.X. An, D.S. Zhang, N, P, S-codoped hierarchically porous carbon spheres with well-balanced gravimetric/volumetric

capacitance for supercapacitors, ACS Sustain. Chem. Eng. 6 (2018) 5265–5272, https://doi.org/10.1021/acssuschemeng.7b04922.
[35] C.T. Zhang, Z.H. Pu, I.S. Amiinu, Y.F. Zhao, J.W. Zhu, Y.F. Tang, S.C. Mu, Co_2P quantum dot embedded N, P dual-doped carbon self-supported electrodes with flexible and binder-free properties for efficient hydrogen evolution reactions, Nanoscale 10 (2018) 2902–2907, https://doi.org/10.1039/c7nr08148k.
[36] K. Lv, H. Zhang, S.L. Chen, Nitrogen and phosphorus co-doped carbon modified activated carbon as an efficient oxygen reduction catalyst for microbial fuel cells, RSC Adv. 8 (2018) 848–855, https://doi.org/10.1039/c7ra12907f.
[37] M. Ballabio, T. Zhang, C. Chen, P. Zhang, Z.Q. Liao, M. Hambsch, S.C.B. Mannsfeld, E. Zschech, H. Sirringhaus, X.L. Feng, M. Bonn, R.H. Dong, E. Canovas, Band-like charge transport in phytic acid-doped polyaniline thin films, Adv. Funct. Mater. (2021), 2105184, https://doi.org/10.1002/adfm.202105184 early access.
[38] K.A. Milakin, Z. Morávková, U. Acharya, M. Kašparová, S. Breitenbach, O. Taboubi, J. Hodan, J. Hromádková, C. Unterweger, P. Humpolíček, P. Bober, Enhancement of conductivity, mechanical and biological properties of polyaniline-poly(N-vinylpyrrolidone) cryogels by phytic acid, Polymer 217 (2021), 123450, https://doi.org/10.1016/j.polymer.2021.123450.
[39] H.Y. Chen, H.Z. Fan, N. Su, R.Y. Hong, X.S. Lu, Highly hydrophobic polyaniline nanoparticles for anti-corrosion epoxy coatings, Chem. Eng. J. 420 (2021), 130540, https://doi.org/10.1016/j.cej.2021.130540.
[40] F. Huang, D. Chen, Towards the upper bound of electrochemical performance of ACNT@polyaniline arrays as supercapacitors, Energy Environ. Sci. 5 (2012) 5833–5841, https://doi.org/10.1039/c1ee01989a.
[41] J.L. Zhou, L. Yu, W. Liu, X.D. Zhang, W. Mu, X. Du, Z. Zhang, Y.L. Deng, High performance all-solid supercapacitors based on the network of ultralong manganese dioxide/polyaniline coaxial nanowires, Sci. Rep. 5 (2015) 17858, https://doi.org/10.1038/srep17858.
[42] H.R. Zhang, J.X. Wang, Y.Y. Chen, Z. Wang, S.C. Wang, Long-term cycling stability of polyaniline on graphite electrodes used for supercapacitors, Electrochim. Acta 105 (2013) 69–74, https://doi.org/10.1016/j.electacta.2013.04.114.
[43] M.S. Rahmanifar, M.F. Mousavi, M. Shamsipur, S. Riahi, A study on the influence of anionic surfactants on electrochemical degradation of polyaniline, Polym. Degrad. Stab. 91 (2006) 3463–3468, https://doi.org/10.1016/j.polymdegradstab.2005.12.014.
[44] L.B. Li, G.Y. Zhang, Z.H. Su, One-step assembly of phytic acid metal complexes for superhydrophilic coatings, Angew. Chem. Int. Ed. 55 (2016) 9093–9096, https://doi.org/10.1002/anie.201604671.
[45] Q. Hu, G.M. Li, X.F. Liu, B. Zhu, X.Y. Chai, Q.L. Zhang, J.H. Liu, C.X. He, Superhydrophilic phytic-acid-doped conductive hydrogels as metal-free and binder-free electrocatalysts for efficient water oxidation, Angew. Chem. Int. Ed. 58 (2019) 4318–4322, https://doi.org/10.1002/anie.201900109.
[46] H. Kim, A.P. Tiwari, H.Y. Kim, Fabrication of electrically highly conductive, mechanically strong, and near-infrared responsive phytic acid crosslinked polypyrrole coated korean paper, Mater. Today Commun. 26 (2021), 102081, https://doi.org/10.1016/j.mtcomm.2021.102081.
[47] L.Y. Hao, X.L. Gong, S.H. Xuan, H. Zhang, X.Q. Gong, W.Q. Jiang, Z.Y. Chen, Controllable fabrication and characterization of biocompatible core-shell particles and hollow capsules as drug carrier, Appl. Surf. Sci. 252 (2006) 8724–8733, https://doi.org/10.1016/j.apsusc.2005.12.084.
[48] F. Haaf, A. Sanner, F. Straub, Polymers of N-vinylpyrrolidone - synthesis, characterization and uses, Polym. J. 17 (1985) 143–152, https://doi.org/10.1295/polymj.17.143.
[49] D.K. Schroder, Semiconductor Material and Device Characterization, Third Edition, Wiley, 2015.
[50] A. Gruger, A. El Khalki, P. Colomban, Protonation, sol formation and precipitation of poly- and oligoanilines, J. Raman Spectrosc. 34 (2003) 438–450, https://doi.org/10.1002/jrs.1018.
[51] Z. Morávková, E. Dmitrieva, Structural changes in polyaniline near the middle oxidation peak studied by in situ raman spectroelectrochemistry, J. Raman Spectrosc. 48 (2017) 1229–1234, https://doi.org/10.1002/jrs.5197.
[52] N. Peřinka, M. Držková, D.V. Randjelović, P. Bondavalli, M. Hajná, P. Bober, T. Syrový, Y. Bonnassieaux, J. Stejskal, Characterization of polyaniline-based ammonia gas sensors prepared by means of spray coating and ink-jet printing, Sens. Lett. 12 (2014) 1620–1627, https://doi.org/10.1166/sl.2014.3362.
[53] P. Bober, T. Lindfors, M. Pesonen, J. Stejskal, Enhanced pH stability of conducting polyaniline by reprotonation with perfluorooctanesulfonic acid, Synth. Met. 178 (2013) 52–55, https://doi.org/10.1016/j.synthmet.2013.07.002.
[54] Y. Gawli, A. Banerjee, D. Dhakras, M. Deo, D. Bulani, P. Wadgaonkar, M. Shelke, S. Ogale, 3D polyaniline architecture by concurrent inorganic and organic acid doping for superior and robust high rate supercapacitor performance, Sci. Rep. 6 (2016) 21002, https://doi.org/10.1038/srep21002.
[55] E. Martinelli, S. Menghetti, G. Galli, A. Glisenti, S. Krishnan, M.Y. Paik, C.K. Ober, D.M. Smilgies, D.A. Fischer, Surface engineering of styrene/PEGylated-fluoroalkyl styrene block copolymer thin films, J. Polym. Sci. A Polym. Chem. 47 (2009) 267–284, https://doi.org/10.1002/pola.23151.
[56] S. Krishnan, R. Ayothi, A. Hexemer, J.A. Finlay, K.E. Sohn, R. Perry, C.K. Ober, E. J. Kramer, M.E. Callow, J.A. Callow, D.A. Fischer, Anti-biofouling properties of comblike block copolymers with amphiphilic side chains, Langmuir 22 (2006) 5075–5086, https://doi.org/10.1021/la052978l.
[57] N. Weiss, L. Muller-Meskamp, F. Selzer, L. Bormann, A. Eychmuller, K. Leo, N. Gaponik, Humidity assisted annealing technique for transparent conductive silver nanowire networks, RSC Adv. 5 (2015) 19659–19665, https://doi.org/10.1039/c5ra01303h.